Department of Signal
Theory and Communications

UNIVERSITAT POLITÈCNICA DE CATALUNYA
BARCELONATECH

PAU-Synthetic Aperture: a New Instrument to Test Potential Improvements for Future Interferometric Radiometers

PhD Thesis Dissertation

by
Isaac Ramos Pérez
Signal Theory and Communications Dpt.
Universitat Politècnica de Catalunya
isaacramos@tsc.upc.edu

Submitted to the Universitat Politècnica de Catalunya (UPC)
in partial fulfillment on the requirements for the degree of

DOCTOR OF PHILOSOPHY

Barcelona, February 2012

Supervised by
Prof. Adriano José Camps Carmona
Signal Theory and Communications Dpt.
Universitat Politècnica de Catalunya
camps@tsc.upc.edu

ACKNOWLEDGEMENTS

This work has been conducted as part of the award "Passive Advanced Unit (PAU): A Hybrid L-band Radiometer, GNSS Reflectometer and IR-Radiometer for Passive Remote Sensing of the Ocean" made under the European Heads of Research Councils and European Science Foundation European Young Investigator (EURYI) Awards scheme in 2004, it was supported in part by the Participating Organizations of EURYI, and the EC Sixth Framework Program. It has also been supported by the Spanish National Research and EU FEDER Project TEC2005- 06863-C02-01 (FPI grant BES-2006-11578, 2006-2010), and by the Spanish National Research and EU FEDER Project AYA2008-05906-C02-01/ESP.

First of all I would like to express my gratitude to Prof. Adriano Camps, for give me the possibility to do my thesis in the remote sensing group as well as for his guidance, dedication, advices and funding during these years.

I would like to express my gratitude in a special manner to Joaquim Giner, for the development of the PAU-SA instrument that would not been possible without his enthusiastic support in the project.

I would like to express my gratitude to Merce Vall·llosera to finance the project.

I would like to express my gratitude to Enric, Paolo, Fabio, Marco, and Fran for their contributions in the PAU-SA instrument with their final projects whom I have directed.

I would like to express me special my gratitude to my partner Xavier Bosch for his support during all theses years, and also to Giuseppe Forte for the contribution in the instrument and the support in the measurement campaign.

Thanks to all the people of the Radiometry team especially to: Neri, Xavi, Enric, José Miguel, JuanFer, Talone, Sandra, and the new generation: Alberto, Roger, Fran, Hugo, Dani, and Hyuk for their support.

I would like to thanks my office mates for the great comprehension especially to: Pere, Santi, Marta, Dani, Rene, Vero, Juan Carlos (King and Prince), Raquel, Oscar, Marc, Enrique, and Jordi.

Thanks to the people that have helped and supported me during this time: Ruben Tardio, Albert Marton, Josep Mª Haro, Josep Pastor, Alfredo Cano, Teressa, Aynie, Alicia, Joaquin Fernandez, and José Angel.

Finally I would like to thank you to all the people of the department of Signal Theory and Communications (TSC) for its support during these years.

Dedicado a todos aquellos/as
que persiguen sus objetivos y
no desisten hasta culminarlos,
a pesar de las dificultades
encontradas en el camino.

a mi familia y a Mar por vuestro apoyo y comprensión.

Preface

The Soil Moisture and Ocean Salinity (SMOS) mission is an Earth Explorer Opportunity mission from the European Space Agency (ESA). It was a direct response to the lack of global observations of soil moisture and ocean salinity. Its goal is to produce global maps of these parameters using a dual-polarization L-band interferometric radiometer called the Microwave Imaging Radiometer by Aperture Synthesis (MIRAS). This instrument is a new polarimetric two-dimensional (2-D) Y-shaped synthetic aperture interferometric radiometer based on the techniques used in radio-astronomy to obtain high angular resolution avoiding large antenna structures. MIRAS measures remotely the brightness temperature (T_B) emitted by the Earth's surface, which is not isotropic, since it depends on the incidence angle and polarization, the Soil Moisture (SM) or the Sea Surface Salinity (SSS), the surface roughness etc. among others.

The scope of this doctoral thesis is the study of some potential improvements that could eventually be implemented in future interferometric radiometers. To validate these improvements a ground-based instrument concept demonstrator the Passive Advanced Unit Synthetic Aperture or (PAU-SA) has being designed and implemented. Both MIRAS and PAU-SA are Y-shaped array, but the receiver topology and the processing unit are quite different. This Ph.D. thesis has been developed in the frame of The European Young Investigator Awards (EURYI) 2004 project entitled "Passive Advanced Unit (PAU): A Hybrid L-band Radiometer, GNSS Reflectometer and IR-Radiometer for Passive Remote Sensing of the Ocean", and supported by the European Science Foundation (ESF).

Contents

Chapter 1

Introduction and motivations

The first chapter of this Ph.D. thesis is devoted to present an overview of the scope for the global context in which this Ph.D. thesis has been developed. This framework is the passive microwave remote sensing, which has a relevant importance on the oceanographical, hydrological and climatological studies.

1.1 Importance of the sea surface salinity and the soil moisture retrievals

Soil Moisture (SM) and Sea Surface Salinity (SSS) may seem to be unconnected. However, both variables are intrinsically linked to the Earth's water cycle and the climate system. Nowadays, it is known that these parameters control the continuous exchange of heat between the oceans, the atmosphere, and the land. Water plays a key role in all the geological and biological processes that take place in our planet. Cycling endlessly between oceans, atmosphere, and land, it triggers and supports life, shapes the Earth and drives the weather and the climate. Recalling that oceans account for more than 96 % of water on Earth, for this reason it is important to study the mechanisms that govern the ocean-atmosphere interface. Figure 1.1 shows the importance of the water cycle, which regulates the climate and the Earth heat exchange. Water evaporates from the ocean, resulting in an increase of the SSS, if it rains again over the ocean; it decreases the SSS of the raining area creating a fresh pool. On the other hand, if it rains over the land, SM increases. Land water may evaporate returning to the atmosphere or it is transpired by the vegetation canopies, or it can run off returning to the ocean and the cycle starts again.

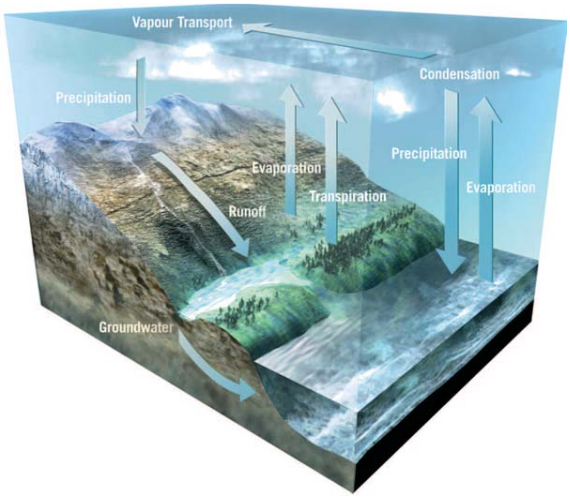

Figure 1.1. The Earth's water cycle [1].

1.2 The sea surface salinity

The SSS is an oceanographic parameter that depends on the balance between precipitation and fresh water river discharge, ice melting, atmospheric evaporation, and mixing and circulation of the ocean surface water with the deep water below. It is usually expressed using the practical salinity unit (psu) of the Practical Salinity Scale of 1978 (PSS-78) (1 psu $\approx$ 1 g of salt in a litre of water). In the open ocean the SSS ranges between 32 psu and 38 psu, with an average value of 35 psu. It is maximum in sub-tropical

latitudes, where evaporation is more important than precipitation. Conversely, the salinity drops below the average around the Equator, where there is more precipitation, and in polar regions, due to ice melting and snowfall. Salinity and temperature are the two variables that control the density of the ocean water, which increases with increasing salinity and decreasing temperature. Density itself is a very important oceanographic parameter, since ocean currents are generated by horizontal differences in density, and also its vertical profile determines the effect that surface winds, heating, and cooling have on subsurface waters. Salinity, through density, also determines the depth of convection at high latitudes. During the formation of sea ice, composed mainly of fresh water, dense cold salty water masses remain in the surface. At some point the water column losses its balance and denser water sinks. This vertical circulation is one of the engines of the global oceanic circulation known as the thermohaline circulation (Fig. 1.2). This kind of oceanic conveyor belt is a key component of the Earth's heat engine, and therefore strongly influences the weather and the climate. Therefore, SSS is directly linked to the climatic cycle. In other words, the stability of the sea water has a dependence with its density, and therefore it is important parameter to retrieve in order to define mixing and circulations of the ocean surface water [2]. Salinity also determines the behavior of the

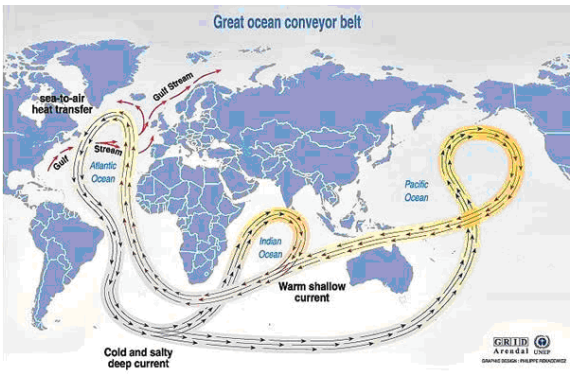

Figure 1.2. Thermohaline circulation acts as a global conveyor belt that redistributes heat throughout the whole planet [3].

ocean-air interface, where gas and heat exchange takes place. The increased precipitation in tropical latitudes can locally create pockets of fresh water where the upper layer is more stable, thus reducing the gas transfer. SSS also influences the vapor pressure of sea water, thus controlling the evaporation rates.

Nowadays, Sea Surface Temperature (SST) along with other oceanographic parameters such as Wind Speed (WS), or sea surface topography is monitored on a regular basis from spaceborne sensors. However, SSS retrieval from space has not been possible until the Soil Moisture and Ocean Salinity (SMOS) mission was launched [4]. Therefore, while ocean circulation models already incorporate satellite SST, WS and altimetry, they lack of accurate SSS data. To overcome this limitation usually temperature-salinity correlations are used, based on the density conservation principle over a certain water volume [5]. However, the validity of this principle is seriously questioned at the surface, where heat and gas exchange between sea and air takes place [6]. This results in modeling errors that hinder the modeling of surface currents. The severity of this lack of data is

clearly understood considering that SSS has never been measured for 42% of the ocean surface, and that it has been measured less than four times over the past 125 years for 88% of the ocean surface [7]. First results of remote sensing from an aircraft to retrieve the sea-surface salinity were made in 1976 [8].

1.3 The soil moisture

On the other hand, the SM parameter is an important variable of the water cycle over the land, since it controls water fluxes between the atmosphere, the surface, and the subsurface. Because a large amount of heat is exchanged when water changes its phase, the water cycle is fundamental to the dynamics of the Earth's energy cycle. Also, since water is the ultimate solvent in the Earth system, biogeochemical cycles such as carbon, nitrogen and methane are embedded in the water cycle. Through these dynamics, SM determines the evolution of weather and climate over continental regions. Hence, global measurements of SM are needed to improve the understanding of water cycle processes. Global SM information will be transformational for the Earth's system science; it will help to characterize the relationship between soil moisture, its freeze/thaw state, and the associated environmental constraints to ecosystem processes including land-atmosphere carbon, water and energy exchange, and vegetation productivity. At the same time, global SM information will enable societal benefit applications such as better water resource assessment, improved weather forecasts, natural hazards mitigation, predictions of agricultural productivity, and enhanced climate prediction, human health and defense services [9].

1.4 Earth observation missions to retrieve the SSS and SM

Thanks to the technological advances, the interest of the scientific community in remotely measuring SSS and SM has been increasing in these last years, spending much effort in this direction. The three main Earth observation contributions are: the European Space Agency (ESA) with the Microwave Imaging Radiometer by Aperture Synthesis (MIRAS) instrument in SMOS mission [10], the National Aeronautics and Space Administration (NASA) with the Aquarius instrument aboard the Argentinean spacecraft Satélite de Aplicaciones Cientificas (SAC-D) [11], and the NASA Soil Moisture Active and Passive (SMAP) [12]. All three missions carry a microwave radiometer as primary instrument. A microwave radiometer is an instrument that measures the spontaneous electromagnetic radiation emitted by all bodies at a physical temperature different from 0 Kelvin. Microwave radiometers where first used in radio-astronomy in the 1930's [13]. Since the 1960's a large number of microwave radiometers have been developed for remote sensing applications to measure a wide range of natural phenomena (for example [14, 15]). The first remote measurements of the SSS using microwave radiometry at L-band were carried out by Miller and Zaitzeff in 1996, using the airborne Scanning Low Frequency Microwave Radiometer (SLFMR), a 6 beam, real aperture radiometer [16]. Traditionally, these radiometers have a limited angular resolution due to the antenna size [17]. In the

early 1980's, LeVine and Good [18] proposed the use of the interferometric aperture synthesis techniques used in radio-astronomy [19] as a way to overcome the limited angular resolution and avoid mechanical scanning especially at low microwave frequencies creating SSS maps using the Electronically Steered Thinned Array Radiometer (ESTAR), the first airborne 1D synthetic aperture radiometer [20].

1.5 The SMOS mission

The spatial resolution of real-aperture radiometers depends on the antenna size. Therefore, they usually have large antennas with narrow beams to scan the Field Of View (FOV). However, the retrieval of some geophysical parameters, such as the SM or the SSS at L-band (1,400-1,427 MHz), has demanding requirements on the spatial resolution (10-20 km), which implies antenna sizes on the order of 20 m of diameter from a Low Earth Orbit (LEO) satellite, not possible to implement today with the required parameters (main bean efficiency, side lobes...). The aperture synthesis approach allows for lighter structures composed of small antennas that effectively 'synthesize' a larger one, able to meet the required spatial resolution [21, 22]. The drawback is the increase in hardware, data processing and calibration complexity. In 1995 the Soil Moisture and Ocean Salinity consultative workshop SMOS was held at the European Space Research and Technology Centre (ESTEC). This workshop concluded two important points. The first one was that microwave radiometry at L-band seemed to be the best technique to recover these geophysical variables. The second one was related to the type of radiometer to be used. For a long time, real aperture microwave radiometers were considered the only feasible technique, but a few years before it had been demonstrated that aperture synthesis radiometry was actually the most promising technique [23]. The SMOS mission was proposed in 1998 by a group of 70 Scientifics led by Yann Kerr in the Centre d'Etudes Spatiales de la BIOsphère (CESBIO), Toulouse, France, and Jordi Font in the Institut de Ciències del Mar (ICM), and the Consejo Superior de Investigaciones Científicas (CSIC), Barcelona, Spain, as an ESA Earth explorer opportunity mission [10]. SMOS, is the first satellite ever launched (2/11/2009) to globally and systematically measure the Earth's SM and SSS by means of L-band microwave radiometry [24,25]. MIRAS, SMOS' payload is an L-band (1,400 - 1,427 MHz) two-dimensional, synthetic aperture radiometer with multi-angular and dual/full-polarimetric imaging capabilities without any mechanical antenna sweeping [26]. SMOS capabilities allow to simultaneously retrieve the SSS, and also the SST and an "effective" wind speed that minimizes the salinity retrieval error. It has a Y-shaped deployable structure, consisting of 3 coplanar arms, 120° apart each other. The total arm length is about 4.5 m with an angular resolution of approximately 2°. The range of incidence angles is variable (spanning from 0° to almost 65°) within the FOV and depends on the distance between the pixel and the sub-satellite path. To achieve an even greater angular excursion and fully exploit its viewing capability the array will be tilted 32° with respect to nadir, (Fig. 1.3) The salinity retrieval algorithms of ESA's SMOS and NASA and the Comisión Nacional de Actividades Espacieales (CONAE) with the Aquarius missions base the sea state correction of the brightness temperature (T_B) on ancillary of data from others sources, or from an on-board scatterometer at a single incidence angle. Both approaches have limitations due to errors, time-space interpolations,

Figure 1.3. MIRAS instrument [1].

and fluctuations of the brightness temperatures. The use of GNSS-R [27] has also been proposed as a source ancillary data, but due to the lack of maturity of these techniques, only a demonstration reflectometer has flown aboard the Surrey Satellite Technology Ltd UK-DMC mission [28]. Significant progress has been achieved in the past few years in determining the dependence between radiometric measurements, sea state, and the GNSS-R observables, a GNSS-R receiver could fly as a secondary payload of an SMOS follow-on mission [29] or as a tandem micro-satellite mission [27]. In any case, these advances can be used for next generation L-band radiometers and/or Global Navigation Satellite System (GNSS)-Reflectometers for ground-based coastal or space-borne ocean monitoring [30].

1.6 Objectives and justifications of this thesis

As previously discussed the collocated measurements of sea brightness temperature and reflected GNSS-R signals can result in a significant improvement of the retrieved SSS. The Passive Advanced Unit for ocean monitoring (PAU) project aims at demonstrating this sensor synergy [31]. Its scientific goals are to perform ocean monitoring by passive remote sensing to improve the knowledge of the relationship of the GNSS-R signal with the sea state, and to improve the knowledge on the relationship between L-band brightness temperature and sea state. To accomplish these goals the PAU sensor consists of three instruments that operate in a synergetic way:

- an L-band radiometer to measure the brightness temperature,
- a reflectometer to measure the sea state using reflected Global Positioning System (GPS) opportunity signals, that shares with the radiometer the same RF front-end, and
- an Infrared Radiometer (IR): to measure the physical sea surface temperature.

As presented in chapter 2, PAU is also a test bed of new technological demonstrators such as real aperture radiometers with digital beamforming and polarization synthesis, fully-

digital synthetic aperture radiometers, etc. In addition to the SSS, SM monitoring using radiometric and GNSS-R signals is another target of the PAU-Project. The scope of this doctoral thesis is to identify the critical elements in the MIRAS's design and introduce and test some potential improvements that could be eventually implemented in future MIRAS's versions of SMOS follow-on missions. Both MIRAS and the synthetic aperture version of the PAU project called PAU-SA are Y shaped arrays, but the instrument altitude, the arm size, the receiver topology, the processing unit in addition to other parts are quite different. For this reason an instrument comparisons is no possible, being this thesis a proposal of a new instrument to test potential improvements for future operational satellite mission to SMOS follow-on missions or other interferometric radiometers. To perform this, a ground-based instrument demonstrator PAU-SA has been designed, implemented, and tested to validate these possible improvements. The tests have been focused in the radiometric part, been the SSS and the SM retrieve part of future studies.

1.7 Organization of the text

This text is structured as follows:

Chapter 2 presents the innovation of the PAU concept as a hybrid of three instruments to retrieve the SSS and the SM. An overview of the different projects developed under the framework of PAU project in the Remote Sensing Lab (RSLab) group of the Univertitat Politècnica de Catalunya are presented.

Chapter 3 reviews the basics concepts of microwave radiometry to retrieve the SSS and SM parameters. Moreover the optimum electromagnetic wavelength for measuring salinity is discussed. Furthermore, the most representative radiometers are presented.

Chapter 4 introduces the fundamentals of interferometric radiometry theory in addition to determine some of the basic parameters such as: the field of view, the angular, the radiometric sensitivity and the space resolution etc.

Chapter 5 presents a general description of the PAU-SA instrument to have a global concept of the instrument. Once the instrument has been described, a comparative description between MIRAS and PAU-SA instruments is introduced, and the most representative parameters are commented. The last part is devoted to quantify the main parameters of the instrument presented in chapter 4.

Chapter 6 describes the PAU-SA's interface. It works in two main modes: simulation and acquisition modes. The first one is an end-to-end simulator (from the noise generation at the surface under observation and the instrument behavior, to the calibration procedures and the image reconstruction), modeling all the system as faithfully as possible. In this part the error sources have been modeled and simulated. Moreover it is possible to change a wide range of parameters and use it as a tool to have a better understanding of the instrument.

Chapter 7 presents the most important parts of the PAU-SA hardware design and its

implementation. The first part is devoted to present a global vision of the instrument and how the different subsystems are interconnected. In the following subsection these subsystems are described one by one, from the antenna element to the mobile unit where the instrument has been installed.

Chapter 8 presents the on-ground tests and measurements performed with PAU-SA. Calibration at baseline level has been tested and the baseline response measured in the anechoic chamber obtaining the optimum integration times through the Allan's variance among other parameters such as the sensibility circles. Several tests with point sources using PRN sequences have been implemented. In order to check the global validation of the instrument image retrieval using point sources has been achieved. To determine the spatial resolution of the instrument two point sources have been used. Moreover the first synthetic aperture images of the moving GPS satellites have been measured. On the other hand, natural extended sources have been measured been necessary debugging the calibration and image recovery algorithms.

Chapter 9 discusses the difficulties encountered in the instrument implementation and its behavior and compares the measurements results with the theoretical ones. Moreover, the future research lines are presented.

Chapter 2

PAU project overview

This chapter is devoted to present the PAU instruments suite and provides a global vision of the projects developed under the framework of PAU project. Although, the scope of this Ph.D. thesis is the synthetic aperture version of PAU, an overview to the other passive remote sensors built in the laboratory are presented as a background.

2.1 PAU concept

As it has been previously said, the scientific community had determined that the best way to retrieve the SSS and SM is by using L-band microwave radiometry. This technique measures changes in the brightness temperature due to the change of the sea water dielectric constant (with respect to the physical temperature, and the surface salinity), and the sea state surface roughness. That is, it is necessary to know well two of the three parameters to retrieve the third one. In the early 2000's, there was not an instrument with all necessary sensors to properly retrieve the sea surface salinity. With this objective a new instrument was conceived.

Within the frame of the European Young Investigator (EURYI) Awards program, in 2003 the PAU project was proposed to the European Science Foundation European Science Foundation (ESF) to test the feasibility of using GNSS-R over the sea surface to make sea state measurements jointly to perform the corrections of the L-band brightness temperature with IR observations to obtain the SST [31]. GNSS-R was originally devised for altimetry applications [32], and in PAU it is extended to try to obtain a direct correction for the sea state, without having to rely neither in numerical sea surface spectra models, nor in scattering and emission models.

The PAU concept [33] merges two different instruments in the same receiver front-end: an L-band radiometer, and a GNSS-R. Due to the availability of integrated receivers in a chip, the radiometer part has been designed to operate at the L1-band of GPS signals, exactly 1,575.42 MHz, instead of the 1,400-1,427 MHz reserved band. This frequency is appropriate for the GPS-reflectometer that will be used to infer the sea state needed to correct the brightness temperatures, while it is also suitable for SSS determination from radiometric measurements. Since the reflectometer part requires continuous data acquisition, the receivers' input cannot be chopped and therefore each linear polarization has its own receiver chain (two receivers chain per antenna element) which simplifies the switch control allowing all-time full-polarimetric mode operation [33]. To achieve this, an innovative pseudo-correlation radiometer topology was conceived, designed and implemented [34] to avoid the classical input switch in a Dicke radiometer. Nowadays, for convenience, to advance in the reflectometer experiments, the radiometer and reflectometer part are working separately.

Although the main topic of this Ph.D. is focused in the radiometry part of the PAU synthetic aperture version, some of the other projects presented are related with the reflectrometry part to measure the sea state. The GNSS-R concept is simple to understand, when the electromagnetic wave is scattered over the sea surface, the scattered signal changes its polarization from Right Hand Circular Polarization (RHCP) and Left Hand Circular Polarization (LHCP), and arriving to the receiver mainly from the specular reflection point, determined by the shortest distance between the transmitting GPS satellite and the receiver, but when the sea is roughed, the scattered signals come from a wider region (known as "glistening zone") that enlarges with increasing sea state (larger roughness) in a similar manner as the Sun reflecting over the sea (Fig. 2.1). When observing the GNSS reflected signals, two points over the sea surface correspond to the same delay and Doppler coordinates, and the point with minimum delay corresponds to the specular reflection point. In the PAU project it was proposed to measure the complete Delay-Doppler Map (DDM)s to perform the sea state correction of the brightness tem-

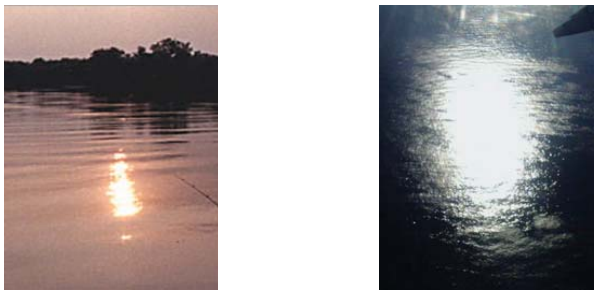

(a) **(b)**

Figure 2.1. Sun glint over the sea for: a) calm, and b) windy conditions [35].

perature required for the salinity retrieval. The DDM is the square of the absolute value of the correlations of the reflected GNSS signals with local replicas of the transmitted signal, but shifted in delay and Doppler [36].

2.2 PAU demonstrator instruments

In order to demonstrate the PAU concept, two main instruments have been developed:

1. PAU-RA instrument [37,38], is a real aperture antenna that synthesizes simultaneously two different beams at two different incidence angles, eventually with different widths and side lobes so as to satisfy different requirements, and

2. PAU-SA instrument, is the synthetic aperture version of PAU project, and the main topic of this Ph.D. thesis used to test potential new technological developments and algorithms for upcoming future SMOS missions [39].

In addition to these two instruments, and in order to advance the scientific studies relating the GNSS-R [40] and the radiometric observables, other PAU demonstrators have been developed:

4. PAU-One Receiver (PAU-OR) with just one element for ground tests and algorithms development, and GPS reflectometer instrument for PAU (griPAU), fully automated improved PAU-OR instrument ,

5. PAU-One Receiver Airborne (PAU-ORA), a lighter version of PAU-OR for aircraft operations from a remote controlled plane,

6. Multi-frequency Experimental Radiometer With Interference Tracking For Experiments Over Land And Littoral (MERITXELL), a classical Dicke radiometer, that includes not only L-band, but S-, C- X-, K-, Ka-, and W-bands, plus a multi-spectral camera, and a camera in addition to the PAU/IR and PAU/GNSS-R units, and

7. Soil Moisture Interference-pattern GNSS Observations at L-band (SMIGOL) instrument is a GNSS Reflectometer that works at the GPS L1 band and implements the Interference Pattern Technique (IPT).

2.3 PAU-RA instrument

PAU-RA is the real aperture version of the PAU project [38]. One of the technological goals of the project is to demonstrate the feasibility of combining in a single hardware two types of sensors: PAU-real aperture RADiometer part (PAU-RAD), the microwave radiometer, and PAU-GNSS-R, the GNSS reflectometer. Detailed information on the receiver design can be found in chapter 7 of this Ph.D. thesis. PAU-RA antenna is a 4 x 4 rectangular antenna array with a spacing between adjacent elements of 0.63 λ (d = 0.63 λ) and triangular illumination in both directions to achieve a Mean Beam Effiency (MBE) $\geq$ 94% at boresight. It is capable to steer the beam up to $\pm$ 20º from the array boresight in 5º steps with a beamwidth of 25º at -3 dB. The conceptual block diagram consists of an analog part that collects the input signals through the antennas. Each antenna of the array is combined by rows using analog techniques. Then, the RF and IF down-conversion from 1,575.42 MHz to 4.039 MHz is performed. The radiometer part differs from other radiometers in the fact that it has been conceived to share the front-end with a GPS reflectometer. Once the signals are at IF, they are digitized using 8 bits, and sent to a FPGA. Inside the FPGA, each channel is down-converted to baseband, which also equalizes phases and amplitudes. Then, the Digital Beam Former (DBF) is implemented and finally, signals are properly correlated in order to obtain the Stokes parameters [41, 42]. Figure 2.2 shows the PAU-RAD instrument without the radome, and measuring an alfalfa during the Palau d'Anglesola field campaign.

(a) **(b)**

Figure 2.2. PAU-RAD instrument a) without radome, and b) measuring an alfalfa field, in the 2010 Palau d'Anglesola field campaign.

2.4 PAU-SA instrument

PAU's Synthetic Aperture version is the so-called PAU-SA instrument. It is the aim of this Ph.D. thesis. Its description and implementation (radiometer part) are presented, in detail chapters 5 and 7 respectively. In order to present the instrument, a summary is introduced here. PAU-SA is composed by a Y-shaped array of 8 antennas per arm plus the one in the center, and an additional dummy antenna at the end of each arm to improve the antenna pattern similarity, 25 antennas for radiometry applications. Moreover, the 4 central antennas plus the 3 additional ones, 7 antennas in total, will be used to create a steerable array for PAU-GNSS-R to point to the specular reflection points (total =

31 dual-polarization antennas). Figure 2.3 shows the PAU-Synthetic Aperture topology, and two pictures taken during the integration. Hardware and simulation details can be found in [43].

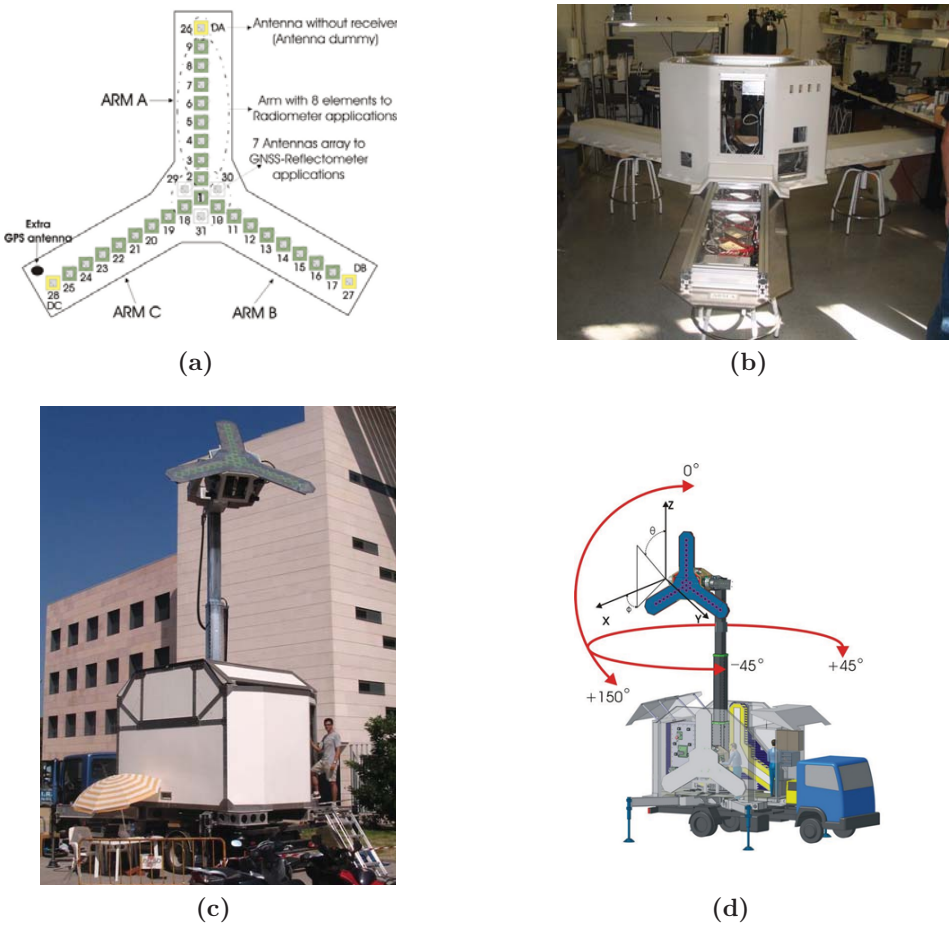

Figure 2.3. PAU-Synthetic Aperture a) PAU- Synthetic Aperture's topology, b) View of the whole instrument with one arm open, c) the PAU - Synthetic Aperture mounted and deployed on its mobile unit, and d) sketch of the functionalities of the PAU-Synthetic Aperture's mobile unit.

2.5 PAU-OR and griPAU instruments

In order to develop the science behind the GNSS-R observables and their relationship with the brightness temperatures while PAU-RA and PAU-SA were finalized, two simplified instruments were developed. They consist of just one LHCP down-looking antenna (a 7 LHCP path hexagonal array), and a RHCP up-looking antenna. Two of these instruments have been built, one for ground based operations (PAU-One Receiver [44,45] and griPAU [46], and another one for airborne operations PAU-ORA.

The griPAU instrument was deployed during the Advanced L-BAnd emissiviTy and Reflectivity Observations of the Sea Surface (ALBATROSS) 2009 field experiment in

the Canary Islands. In this particular implementation of the PAU concept, two 7-patch hexagonal arrays are used: one for a dual polarization radiometer (vertical and horizontal polarizations) at 1,400-1,427 MHz (instead of f_0 = 1,575.42 MHz, B = 2.2 MHz), and the second one for PAU-GNSS-R at L1 of GPS. A smaller up-looking patch antenna in the center is used to track the delay of the direct signal, and fed it to the reflectometer. Figure 2.4 shows the griPAU (PAU-GNSS-R) instrument block diagram and view. This instrument includes an automatic tracking of the specular reflection point of the pre-selected GPS satellite to simplify instrument's operation, while at the same time ensures observations collocated in time and space, exactly in the 1,400-1,427 MHz band used for passive observations.

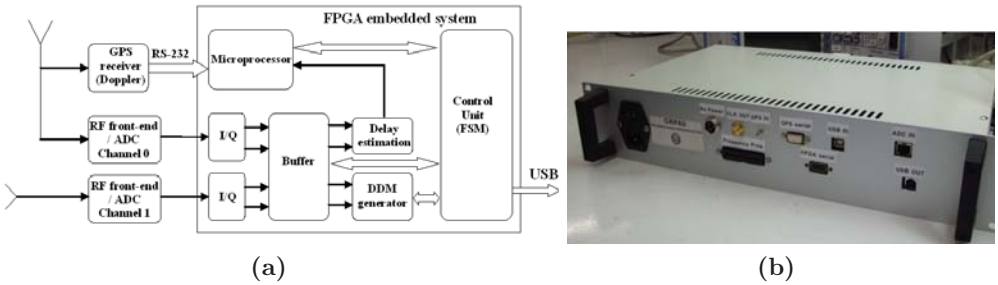

Figure 2.4. griPAU instrument a) block diagram showing: commercial GPS receiver to provide Doppler estimates, up-looking antenna to provide delay estimates (every 5 ms), and down-looking antenna (7 LHCP hexagonal patch array) to collect the reflected signal. The whole system is embedded in a Xilinx Virtex-4 FPGA and has serial USB connectivity, and b) a picture of the processing unit.

2.6 PAU-ORA instrument

Figure 2.5 shows the PAU-ORA located on the cargo bay of a remote controlled aircraft [44]. Details on the control, telemetry, data links and data storage can be found in [47, 48]. Figure 2.5b shows the DDMs measured when the direct (RHCP) and reflected (LHCP) signals are collected simultaneously using two separated antennas connected to the inputs of a non-resistive 2-way power combiner. The left-hand side peak corresponds to the DDM of the direct signal, which has a larger amplitude, while the right-hand side one corresponds to the reflected one, which is attenuated in the scattering process and has suffered a longer signal path. The separation between peaks is 21 samples, which corresponds to $\sim$ 770 m, since in this implementation of the instrument; the sampling frequency is 8.18 MHz. Therefore, since the antenna was pointing to the nadir direction and the GPS satellite was close to the zenith, the estimated height is $\sim$ 385 m, which is very close to the measured flight height (379 m). This design offers several advantages over the previous ones (just measuring the reflected signal) since it intrinsically provides absolute calibration of the scattering coefficient (ratio of peaks between direct and reflected DDM), it offers altimetric capabilities, and sea state determination using the full DDM of the reflected signal.

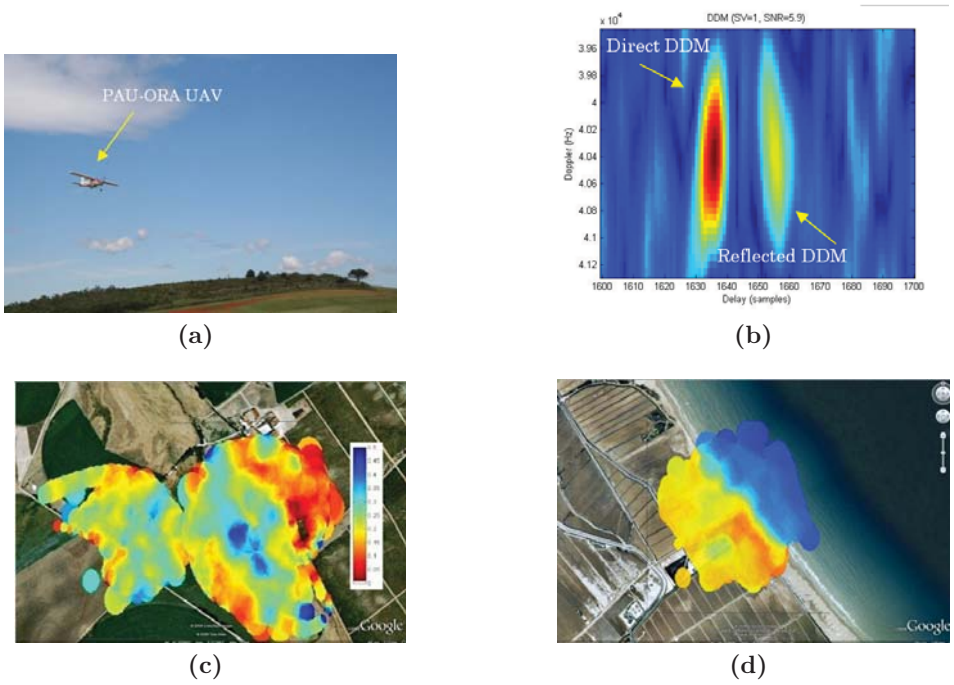

Figure 2.5. PAU-ORA overview a) PAU - One Receiver Airborne instrument block mounted on the bay of a Remote Control aircraft, b) DDMs obtained collecting simultaneously the direct (RHCP) and reflected (LHCP) signals. Brightness temperature maps measured over c) Vadillo de la Guareña (Zamora, Spain) and d) Marquesa Beach (Ebre river mounth, Tarragona, Spain).

2.7 MERITXELL instrument

MERITXELL is a step forward to advance our understanding of the potentials of combining data from several sensors: microwave radiometers, multi-spectral and IR cameras, and GNSS Reflectometers [49]. It will also be used in testing Radio Frequency Interference (RFI) detection and mitigation algorithms for microwave radiometry. The MERITXELL microwave radiometer is a multi-band dual-polarization Dicke radiometer covering eight protected bands used for passive remote sensing: L, S, C, X, K, Ka, and W, Table. 2.1. To add flexibility and simplify the design, a spectrum analyzer is used

Table 2.1. MERITXELL microwave radiometer bands and antenna parameters.

Band	Frequency bounds	Beamwidth	MBE
L	1.400 - 1.427 GHz	~25 °	98 %
S	2.69 - 2.70 GHz	~25 °	98 %
C	7.14 - 7.23 GHz	~25 °	98 %
X	10.6 - 10.7 GHz	~5 °	95 %
K	18.6 - 18.8 GHz	~5 °	95 %
K	23.6 - 24.0 GHz	~5 °	95 %
Ka	36 - 37 GHz	~5 °	95 %
W	86 - 92 GHz	~5 °	95 %

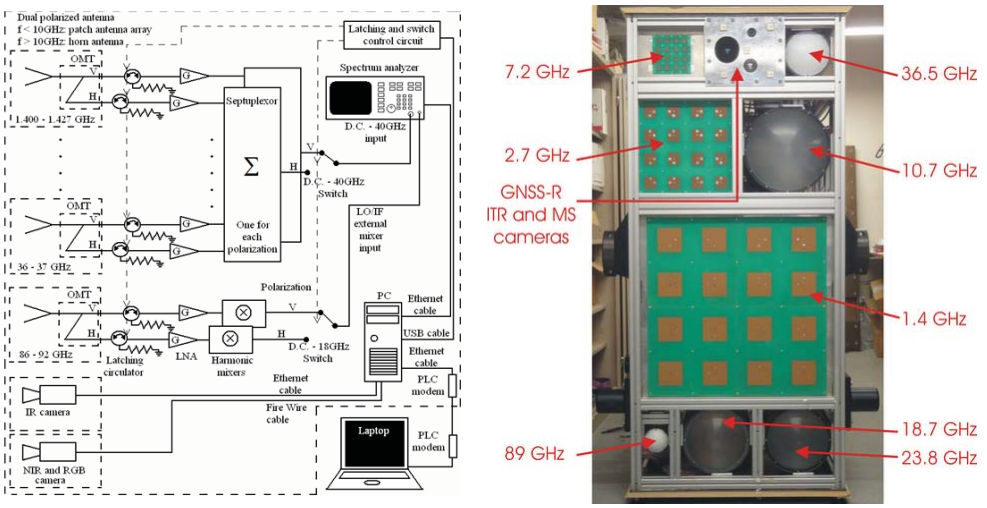

(a) **(b)**

Figure 2.6. a) MERITXELL microwave radiometer schematic, and b) front view.

as IF stage, for filtering and power detection for all bands. This allows an easy reconfiguration of the band and/or frequency response shape, since the antennas and amplifiers response exceed those indicated in Table. 2.1. Antennas are 4 x 4 dual-polarization path arrays at L, S, and C bands, and horn antennas with a lens in the aperture to provide a quasi-Gaussian beam for the other bands. In addition, MERITXELL includes a thermographic camera (320 x 240 pixels) operating in the 8-14 μm range, a multi-spectral camera (640 x 480 pixels) with four spectral bands: red ($\lambda_0 = 0.62$ μm), green ($\lambda_0 = 0.54$ μm), blue ($\lambda_0 = 0.45$ μm) and Near Infra-Red ($\lambda_0 = 0.80$ μm), and a PAU-GNSS-R unit. Figure 2.6a shows the schematic of the MERITXELL microwave radiometer, and Fig. 2.6b shows the front view with the antennas mounted.

2.8 SMIGOL instrument

Soil Moisture Interference-pattern GNSS Observations at L-band (SMIGOL) is a GNSS Reflectometer that works at the GPS L1 band. The SMIGOL-Reflectometer, located pointing to the horizon and using a Vertical polarization (V-pol) patch antenna, measures the interference power between the direct GPS signal and the one reflected over the surface. This technique is called Interference Pattern Technique (IPT). The IPT has been tested by measuring with the SMIGOL -Reflectometer and performing several geophysical parameters retrieval depending on the observed surface:

1. Soil moisture mapping over a bare soil [50] (Fig. 2.7b), vegetation growing retrieved over wheat-covered and barley-covered soils [51], and maize-covered soils [52]. Figure 2.7c shows the vegetation height retrieval over a wheat field during all the growing season, and

2. topography mapping, Fig. 2.7d shows the topography retrieval over a barley field [51].

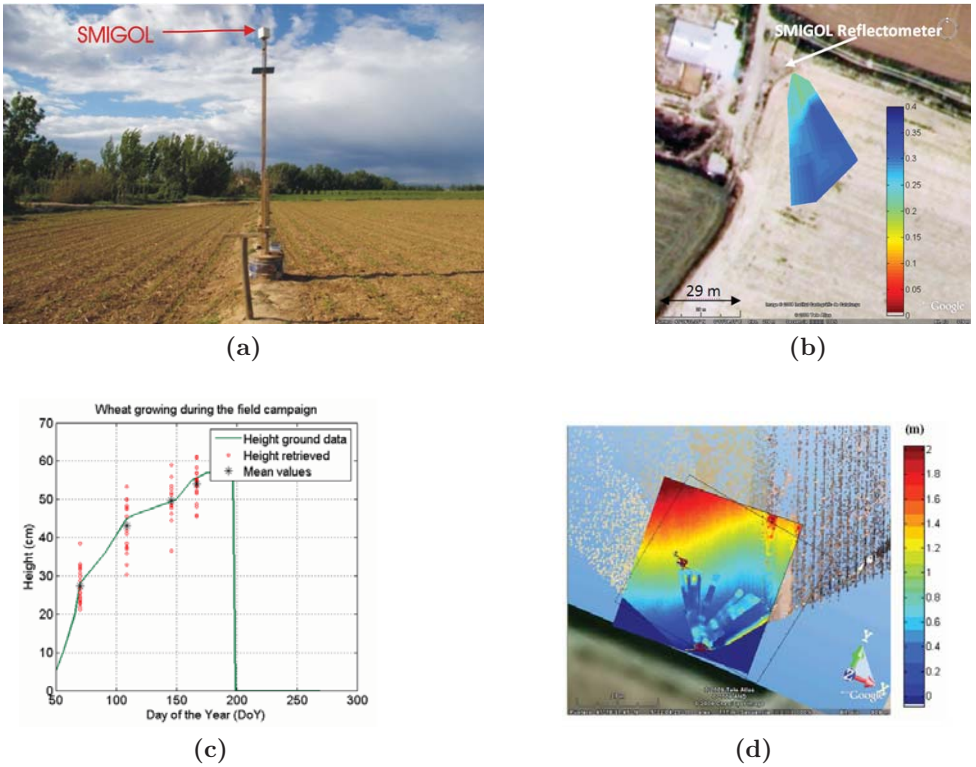

Figure 2.7. Fields observed in the various field experiments: a) SMIGOL -Reflectometer at Palau d'Anglesola, Lleida, (Spain), Jan-Sep 2008 b) Soil moisture retrieval achieved over bare soil at Palau d'Anglesola, c) wheat growing retrieval achieved over wheat-covered soil, both observed at Palau d'Anglesola, Lleida (Spain) during 2008 and d) topography retrieval achieved over barley-covered soil observed at Vadillo de la Guareña, Zamora (Spain) during 2009.

2.9 Field experiments

During May-June 2008 the first PAU-One Receiver was deployed at El Mirador del Balcón, La Aldea de San Nicolás, in the North-West coast of Gran Canaria in the Canary Islands, and gathered for the first time ever collocated L-band radiometric and GNSS-R data, together with oceanographic data (sea surface temperature + sea surface directional spectrum buoys). The field experiment was repeated during the same period of time in 2009 with an improved version of the instrument (griPAU) that collected radiometric and GNSS reflectometric data collocated both in time and space using two antennas with the same 22º beamwidth (Fig. 2.8). Figure 2.9 shows the scatter plot of the measured DDM volume (in arbitrary units) vs. the Significant Wave Height (SWH) for several threshold values. This plot gives an understanding on the relationship between the sea state and the GNSS-R observables DDMs and the changes in the brightness temperature. It can be noticed that increasing the threshold decreases the sensitivity to SWH since a lower volume is being considered. However, this threshold cannot be arbitrarily small, since it has to be above the noise threshold to provide meaningful observations. The correlation of the instantaneous brightness temperature changes and the instantaneous DDM volumes observed during ALBATROSS 2009 is shown in Fig. 2.10 for incidence

Figure 2.8. griPAU deployed during the ALBATROSS 2009 field experiment.

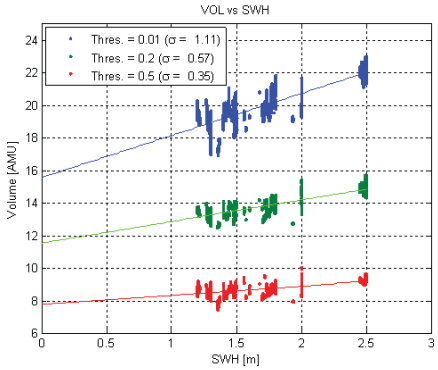

Figure 2.9. DDM-volume dependence on the SWH for three various thresholds [29].

angles larger than 55º, since the cliff already imposed a 45º mask, and incidence angles between 45º and 50º were affected by multi-path.

Despite these encouraging results, there is still a long way to go until meaningful physical quantities that can be successfully extracted from satellite data to be used by the oceanographic communities, and they can be used to perform the sea state correction in sea surface salinity retrievals. More extensive data sets need to be gathered and processed. Following this line, the GPS and the GPS and RAdiometric Joint Observations

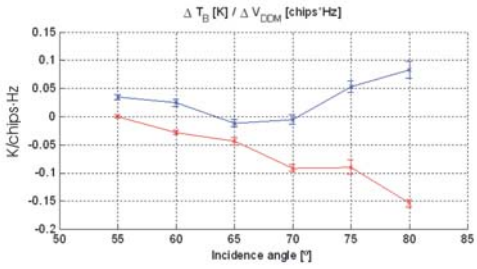

Figure 2.10. Estimated brightness temperature sensitivity to changes in the normalized DDM volume at vertical (red) and horizontal (blue) polarizations respecively.

one-year experiment (GRAJO) was conducted from November 2008 to April 2010 at the REMEDHUS network (Zamora, Spain) [53] (Fig. 2.11). At the plot scale, the goal of

(a) **(b)**

Figure 2.11. GRAJO field campaign: a) L-Band AUtomatic Radiometer (LAURA) and SMIGOL deployed instruments [53], and b) preparing the UAV of PAU-ORA for measuring [54].

this experiment is to jointly use radiometry and GPS-reflectometry data to study: the potential of the GNSS-R techniques measuring SM, the influence of the vegetation on the retrieval of geophysical parameters, and to characterize the effective roughness parameter to be used in the land emission models. The experiment site was located in a farm within the REMEDHUS network located at Vadillo de la Guareña, Zamora, Spain.

The limited GNSS-R data gathered by the UK-DMC satellite and made publicly available [55] showed the potential of this technique, and supported the proposal of a PAU secondary payload in the Spanish Earth Observation Satellite Spanish Earth Observation Satellite (SeoSat)/Ingenio [56]. This proposal went through phase A, but did not succeed to pass into phase B due to the accommodation issues with the primary payload raised after a configuration change. A simplified, lighter and less power consuming payload is currently under development in cooperation with industry and will be available for future launches of opportunity, such as the Instituto Nacional de Tecnica Aeroespacial (INTA) MicroSat-1 (Fig. 2.12).

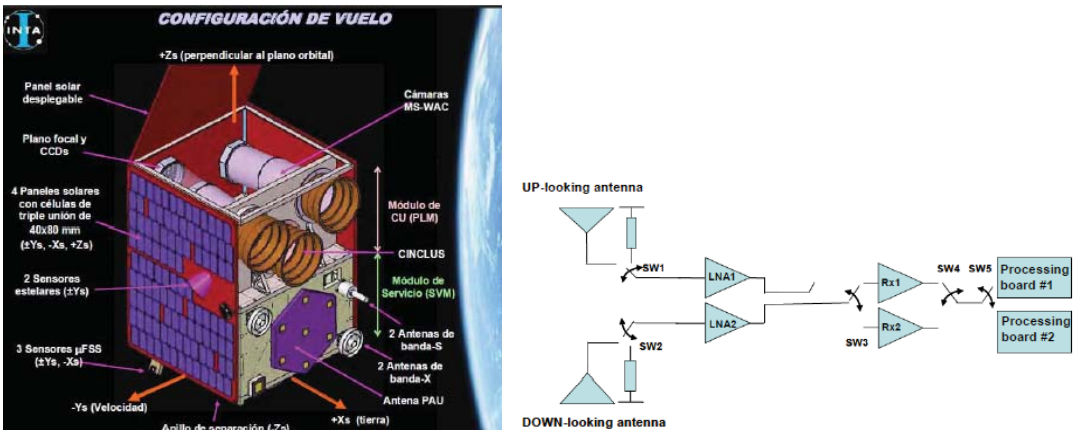

(a) **(b)**

Figure 2.12. a) Artist's view of the INTA MicroSat-1 and b) block diagram of PAU in MicroSat-1.

2.10 Conclusions

The PAU instrument concept for ocean monitoring has been presented. It is a new instrument that combines in a single receiver and without time multiplexing a microwave radiometer at L-band and a GPS-reflectometer which, in conjunction with an infra-red radiometer, will simultaneously provide the sea surface temperature and -more important- the sea state information needed to accurately retrieve the sea surface salinity. Moreover, a set of instruments under the framework of the PAU project that have been or are being developed at the Remote Sensing Lab of the Universitat Politècnica de Catalunya have been presented. These instruments have been developed for two purposes: 1) to analyze the nature of reflectometric observables and their relationship with the brightness temperature at L-band over the sea and the land, and 2) to be technological demostrators of improvements to be applied in future space-borne missions (e.g. SMOS follow-on missions), or secondary payloads that can help in the sea state correction.

Chapter 3

Introduction to radiometry

The first part of this chapter is devoted to present the fundamental concepts of microwave radiometry and emission theory. The second part provides the most typical types of microwave radiometers. Moreover, the most suitable frequency for SSS applications is discussed and the table of the main applications of microwave radiometry and their frequencies of operation is presented.

3.1 Introduction to microwave radiometry

This chapter presents the basic concepts of microwave radiometry. Radiometry is the field of science devoted to the measurement of the thermal electromagnetic energy spontaneously emitted by all bodies at a physical temperature different from 0 K. This technique was born in radio-astronomy to measure the electromagnetic emissions coming from the outer space. Since the 1960's it has became a common and powerful tool for Earth remote sensing. With the study and analysis of the physical processes related with this spontaneous emission, it is possible to infer the parameters that have caused it, such as atmospheric and geophysical parameters. Table 3.1 shows the main microwave radiometry applications and their suitable frequencies being divided in two groups: atmospheric and Earth surface applications. Hence, a radiometer is an instrument that measures this emitted energy or brightness temperature (T_B) with high resolution and accuracy. This chapter presents the basic microwave radiometry concepts, starting from the power collected by an antenna up to the concept of emissivity and brightness temperature. Finally different radiometer types are described: the Total Power Radiometer (TPR), the Dicke Radiometer (DR), the Noise Injection Radiometer (NIR), and the Polarimetric Radiometer (PR).

Table 3.1. Relationship between radiometry applications and their suitable frequencies [22].

Application	Frequency (GHz)
Clouds water content	21, 37, 90
Ice Classification	10, 18, 37
Sea Oil spills tracking	6.6, 37
Rain over soil	18, 37, 55, 90, 180
Rain over the ocean	10, 18, 21, 37
Sea Ice concentration	18, 37, 90
Sea Surface Salinity	**1.4**, 6.6
Sea Surface Temperature	6.6, 10, 18, 21, 37
Sea Surface Wind Speed	10, 18
Snow Coating	6.6, 10, 18, 37, 90
Soil Moisture	**1.4**, 6.6
Atmospheric Temperature Profiles	21, 37, 55, 90, 180
Atmospheric Water Vapor	21, 37, 90, 180

3.2 Thermal radiation

3.2.1 Quantum theory of radiation

All bodies at a finite absolute temperature radiate electromagnetic energy. Gases radiate at discrete frequencies. According to quantum theory, each spectral line corresponds to an electron transition from an atomic energy level ϵ_1 to another one ϵ_2. The radiation is produced at a frequency given by Bohr's equation:

$$f = \frac{\epsilon_1 - \epsilon_2}{h} \qquad [\text{Hz}], \tag{3.1}$$

where h is the Planck's constant, $h = 6.63 \cdot 10^{-34}$ J.

The emission is originated by the collision between particles. The probability of collision is a density function of the particles and the kinetic energy of their random motions. The increase of intensity of the energy radiated by a body is proportional to the increase of its absolute temperature.

3.2.2 Planck's radiation's law

In general, part of the electromagnetic energy incident on a surface is absorbed, and part is reflected. The spectral brightness (brightness for unit bandwidth) is given by Planck's law:

$$B_f = \frac{2hf^3}{c^2} \frac{1}{e^{\frac{hf}{k_B T_{ph}}} - 1} \qquad [\mathrm{Wm^{-2}Hz^{-1}sr^{-1}}], \tag{3.2}$$

where f is the frequency in Hertz, $k_B = 1.38 \cdot 10^{-23} \mathrm{JK^{-1}}$ is the Boltzmann's constant, T_{ph} is the absolute physical temperature in Kelvin and $c \approx 3 \cdot 10^8 \,\mathrm{ms^{-1}}$ is the speed of light in the vacuum. Natural surfaces absorb only a fraction of the incident power,

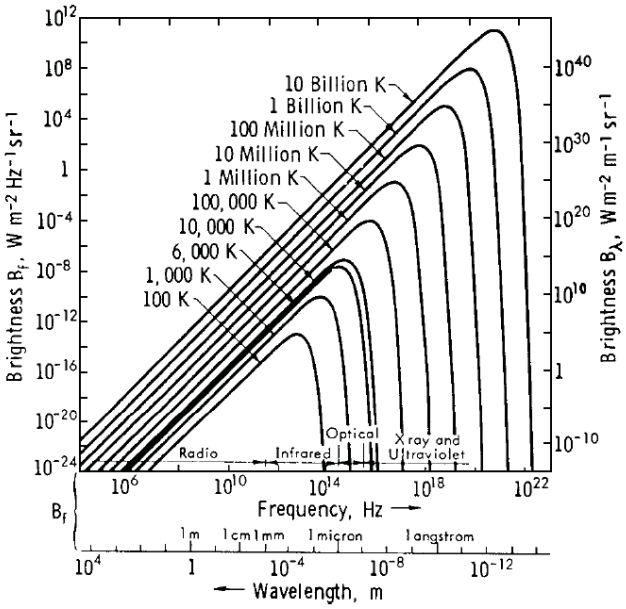

Figure 3.1. Planck's radiation law [57].

the rest being reflected. Applying Taylor's approximation to the exponential function in Eqn. 3.2, where the exponent $hf/k_B T_{ph}$ in the denominator of Planck's law is far smaller than 1 at microwave frequencies, the following approximation can be used to simplify:

$$e^x - 1 = 1 + x + \frac{x^2}{2} + ... - 1 \approx x, \quad \text{for} \quad x << 1. \tag{3.3}$$

At low microwave frequencies the Rayleight-Jeans law can then be used as good approximation of the Planck's law and can be written as:

$$B_f = \frac{2f^2 k_B T_{ph}}{c^2} = \frac{2k_B T_{ph}}{\lambda^2} \qquad [\mathrm{Wm^{-2}Hz^{-1}sr^{-1}}], \tag{3.4}$$

Figure 3.2 compares these two approximations with Planck's law. The higher the physical

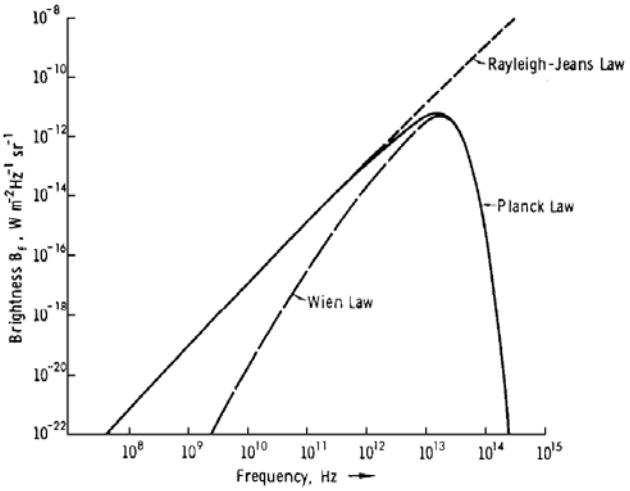

Figure 3.2. Comparison of Planck's law with its low-frequency (Rayleigh-Jeans law) and high frequency (Wien's law) approximations at 300 K [57].

temperature, the higher the brightness and the frequency where the brightness reaches its maximum. The Stefan-Boltzmann law provides an expression for the total brightness and it is obtained by integrating Eqn. 3.2 over all the spectrum:

$$B_{bb} = \int_0^\infty B_f \, df = \frac{\sigma {T_{ph}}^4}{\pi}, \tag{3.5}$$

where $\sigma = 5.673 \cdot 10^{-8}$ [Wm^{-2}K^{-4}sr^{-1}] is the Stefan-Boltzmann constant and the subscript *bb* stands for black body.

At high microwave frequencies the Planck's law reduces to Wien's law:

$$B_f = \frac{2hf^3}{c^2} e^{-\frac{hf}{k_B T_{ph}}} \qquad [\mathrm{Wm^{-2}Hz^{-1}sr^{-1}}]. \tag{3.6}$$

3.2.3 Gray body radiation

A black-body is an idealized body which is a perfect absorber and a perfect emitter. These bodies absorb all the incident energy, and when the thermodynamic equilibrium is reached at a physical temperature T_{ph}, they radiate all the energy omni-directionally. However, real bodies, usually called gray-bodies, emit less energy than a black-body since they do not absorb all the energy incident on them. If the emitted brightness depends on the direction $B(\theta, \phi)$, a similar equation to that of the black body can be written:

$$B(\theta, \phi) = 2\frac{k_B}{\lambda^2} T_B(\theta, \phi) B, \tag{3.7}$$

where $T_B(\theta, \phi)$ is the equivalent temperature associated to the brightness and it is called the brightness temperature. Since the universe is composed of gray-bodies another concept is introduced: the emissivity $e(\theta, \phi)$, that is related to both magnitudes:

$$e(\theta, \phi) = \frac{B(\theta, \phi)}{B_{bb}} = \frac{T_B(\theta, \phi)}{T_{ph}}, \tag{3.8}$$

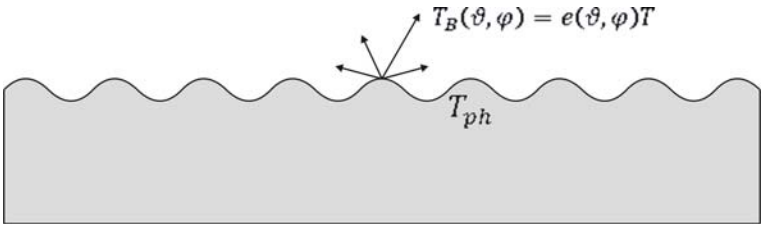

Figure 3.3. Brightness temperature of a semi-infinite medium at a uniform temperature [57].

where B_{bb} is the brightness of the black-body at temperature T_{ph}. The brightness temperature emitted by a black-body coincides with its physical temperature, hence its emissivity is 1. Consequently the brightness temperature emitted by real bodies is less than their physical temperature, and then their range of emissivity values varies between 0 and 1. The emissivity is zero for a perfect reflecting body or a lossless metal, and it is one for a perfect absorber, the black-body.

3.3 Brightness and antenna power

A radiometer is an instrument that measures the brightness, that is, the power emitted by a body by unit solid angle and by unit surface. If the emitting surface radiates with the pattern $F_t(\theta,\phi)$, the brightness $B(\theta,\phi)$ is given by:

$$B(\theta,\phi) = \frac{F_t(\theta,\phi)}{A_t} \qquad [\mathrm{W\,sr^{-1}m^{-2}}], \tag{3.9}$$

where A_t is the total area which is radiating. The power collected by an antenna surrounded by a distribution of incident power $B(\theta,\phi)$ can be computed as:

$$P = F_t\frac{A_r}{R^2} = BA_t\frac{A_r}{R^2} \qquad [\mathrm{W}], \tag{3.10}$$

being A_r the effective area of the antenna and R the distance to the radiating surface. Taking into account that the solid angle Ω_t subtended by the transmitting antenna is defined as:

$$\Omega_\mathrm{t} = \frac{A_t}{R^2}, \tag{3.11}$$

then, the power collected by the antenna can be computed as:

$$P = BA_r\Omega_\mathrm{t} \qquad [\mathrm{W}]. \tag{3.12}$$

Replacing the solid angle by a differential solid angle ($d\Omega$), the corresponding power received by the antenna from an extended source of incident brightness $B(\theta,\phi)$ can be expressed as:

$$dP = A_rB(\theta,\phi)|F_n(\theta,\phi)|^2, \tag{3.13}$$

where $|F_n(\theta,\phi)|^2$ is the normalized antenna radiation pattern. Moreover, if the brightness is not constant with frequency, a new magnitude must be defined: the spectral brightness

density $B_f(\theta,\phi)$, units [$\mathrm{Wm^{-2}Hz^{-1}sr^{-1}}$]. The total power collected by the antenna is then obtained by integrating Eqn. 3.13 over the system's bandwidth and over the space:

$$P = \frac{1}{2} A_r \int_f^{f+B} \iint_{4\pi} B_f(\theta,\phi) |F_n(\theta,\phi)|^2 \, d\Omega \, df \qquad [\mathrm{W}], \tag{3.14}$$

where B is the bandwidth of the receiving system. Since the antenna collects only half of the randomly polarized thermal power emitted, it is multiplied by a factor $\frac{1}{2}$.

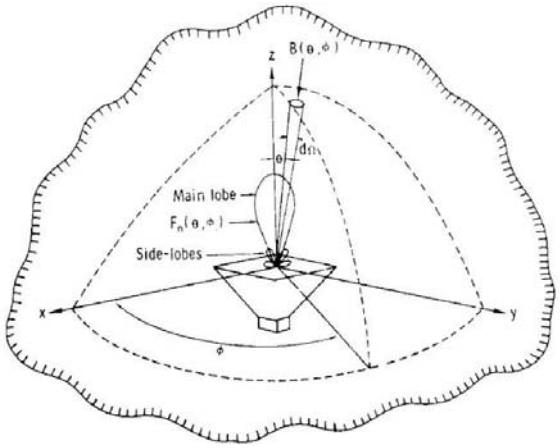

Figure 3.4. Geometry of the radiation incident over the antenna [57].

3.3.1 Antenna surrounded by a black body

The antenna is now surrounded by a black-body at a constant physical temperature T_{ph} as shown in Fig. 3.5.

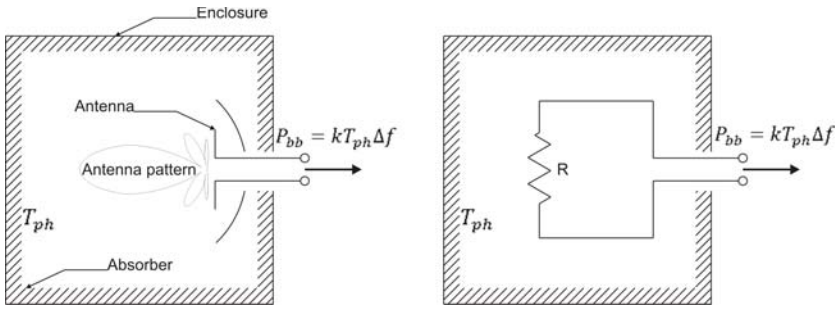

Figure 3.5. Antenna surrounded by an ideal black body has the same delivered power than a resistor maintained at the same T_{ph}, (assuming each one is connected to a matched receiver of bandwidth B) [57].

The power collected by the antenna can be obtained replacing 3.4 into 3.14:

$$P_{bb} = \frac{1}{2} A_r \int_f^{f+B} \iint_{4\pi} \frac{2kT_{ph}}{\lambda^2} |F_n(\theta,\phi)|^2 \, d\Omega \, df \qquad [\mathrm{W}]. \tag{3.15}$$

The detected power will be limited by the antenna and receiver's bandwidth B. If this is small enough to assume that the spectral brightness density is constant over the frequency range, Eqn. 3.15 reduces to:

$$P_{bb} = kT_{ph}B\frac{A_r}{\lambda^2}\iint_{4\pi}|F_n(\theta,\phi)|^2\,d\Omega = kT_{ph}B \qquad \text{[W]}. \tag{3.16}$$

where the antenna solid angle has been expressed as a function of its effective area (Eqn. 3.11). Equation 3.16 establishes a linear relationship between the physical temperature of a body and the power collected by an antenna. In 1928 Nyquist found the same expression for the available power at the terminals of a resistance at a physical temperature T_{ph}. This means that for an ideal receiver of bandwidth B, the antenna delivers to the load the same power as a resistance at a temperature T_A, which is called the antenna temperature.

3.3.2 The apparent temperature

When an antenna is not surrounded by a black body, but by gray bodies, the apparent temperature T_{AP} concept is defined; it is an equivalent temperature related to the total brightness incident over the antenna, $B_i(\theta,\phi)$:

$$B_i(\theta,\phi) = \frac{2k_B}{\lambda^2}T_{AP}(\theta,\phi)B. \tag{3.17}$$

The apparent temperature depends on several terms related to the different sources radiating over the antenna. Figure 3.6 shows the relationship between them: the radiation emitted by the surface (land and sea) reaches the antenna attenuated by the atmosphere, the radiation emitted downwards by the atmosphere and reflected on the sea/ground in the antenna direction and the upwards radiation emitted by the atmosphere:

$$T_{AP} = T_{UP} + \frac{1}{L_a}(T_B + T_{SC}) \qquad \text{[K]}. \tag{3.18}$$

T_B is the brightness temperature of the surface under observation, T_{UP} is the atmospheric upward radiation, and T_{SC} is the atmospheric downward radiation scattered and reflected by the surface and L_a are the atmospheric losses. When the atmospheric losses are high, the apparent temperature T_{AP} is almost equal to the atmospheric physical temperature. It happens at high frequencies or at the absorption peaks of some gases. In the frequency range from 1 GHz to 10 GHz losses for a cloud free atmosphere are very small and can be neglected. Consequently the apparent brightness temperature T_{AP} can be approximated by the brightness temperature T_B. According to the figure and taking into account the normalized antenna pattern $F_n(\theta,\phi)$ and solid angle Ω_p, the antenna temperature without losses is given by:

$$T_A = \frac{1}{\Omega_\mathrm{p}}\iint_{4\pi}T_{AP}(\theta,\phi)|F_n(\theta,\phi)|^2\,d\Omega \qquad \text{[K]}, \tag{3.19}$$

. Since in reality the antenna absorbs a certain amount of the power incident on it, and hence it also radiates, the resultant antenna temperature including losses is given by Eqn. 3.20.

$$T'_A = \eta_\Omega T_A + (1-\eta_\Omega)T_{ph} \qquad \text{[K]}. \tag{3.20}$$

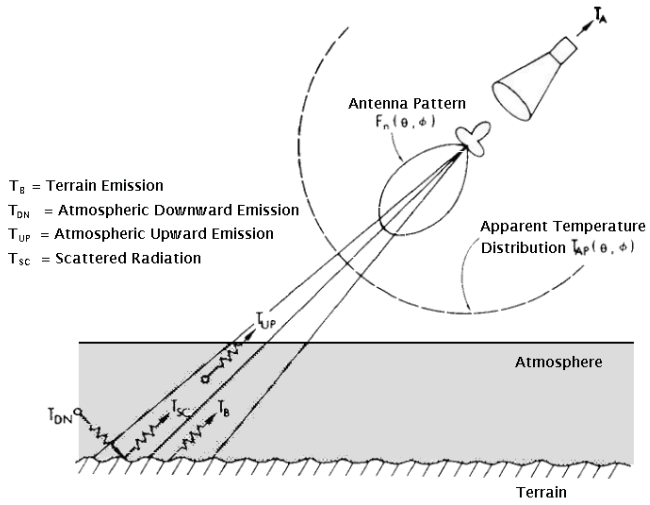

Figure 3.6. Relationship between antenna temperature, apparent temperature and brightness temperature [57].

where T'_A is the equivalent apparent temperature at the antenna output port including losses, η_Ω is the efficiency of the antenna, and T_{ph} is the physical temperature of the antenna.

3.4 Emission theory

If the reflection of the incident wave is not produced over a plane surface, the incident power will be scattered over the space. Some of the scattered power maintains the phase and is reflected in the specular direction, but the rest of the radiation loses its phase characteristics and it is scattered. In a similar way, the power radiated by the medium passes through the surface and it is transmitted over a range of directions. Consequently, $T_B(\theta, p)$ has contributions coming from several directions of the inner part of the body. As it has been previously mentioned, the emissivity links the capability of a surface to emit or absorb radiation. Moreover its value has a dependency with the incidence angle, polarization, and the roughness surface. This section is devoted to present the emissivity of two extreme and idealizes cases: specular surface and completely rough surface, Fig. 3.7. The scattering of a rough surface can be modeled by its cross-section by the unit area as $\sigma^0(\theta_0, \phi_0, \theta_s, \phi_s, p_s)$. This parameter relates the scatter power in the (θ_s, ϕ_s) direction with polarization p_s for an incident plane wave at the (θ_0, ϕ_0) direction with polarization p_0. When the p_0 and p_s are the same, σ^0_{pp} is called horizontal or vertical scattering coefficient, where pp designates the same polarization. If p_0 and p_s are different, σ^0_{pq} is called the cross-polar scattering coefficient, where pq indicates different polarizations (incident wave at p-polarization, scattered wave at q-polarization). The general expression for the emissivity is presented in Eqn. 3.21 [57]:

$$e(\theta_0, \phi_0; p_0) = 1 - \frac{1}{4\pi cos\theta_0} \int_{\phi_s=0}^{2\pi} \int_{\theta_s=0}^{\pi/2} [\sigma^0_{pp} + \sigma^0_{pq}] sin\theta_s d\phi_s d\theta_s. \tag{3.21}$$

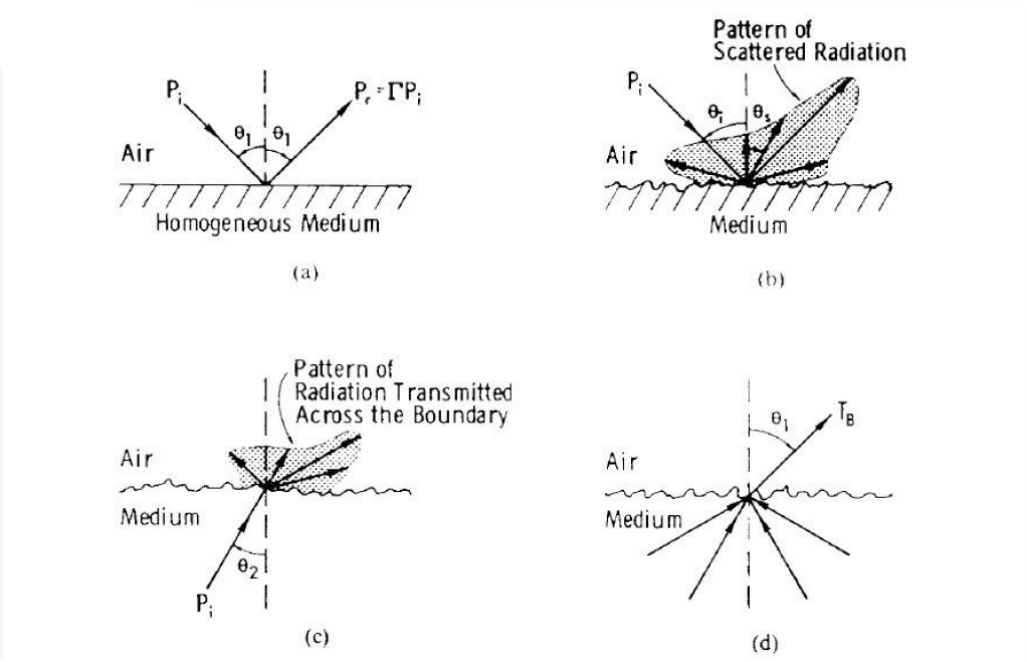

Figure 3.7. Specular and rough surface scattering and emission: a) specular reflection, b) diffuse scattering, c) diffuse emission, and d) contributions to T_B come from many directions [57]

.

3.4.1 Emission from a specular surface

The scattering produced at the specular surface consists of the coherent reflection of the incident wave only. Consequently, the cross-polar scattering coefficient σ^0_{pq} is zero, and the horizontal or vertical polarization scattering coefficients are delta functions:

$$\sigma^0_{pp} = 4\pi\Gamma(\theta_0; p_0)\frac{cos\theta_0}{sin\theta_{sp}}\delta(\theta_s - \theta_{sp})\delta(\phi_s - \phi_{sp}), \tag{3.22}$$

where Γ is the specular reflection coefficient, and the subindex sp in the angles denotes the specular direction:

$$\theta_{sp} = \theta_0 \quad and \quad \phi_{sp} = \pi - \phi_0, \tag{3.23}$$

Substituting Eqn. 3.22 in 3.21 and after some straightforward manipulations the next expression is obtained.

$$e(\theta_0, \phi_0; p_0) = 1 - \Gamma(\theta_0; p_0). \tag{3.24}$$

It is the ideal case, when the reflection is specular, the emissivity can be expressed as a function of the reflection coefficient.

3.4.2 Emission from a perfectly rough surface

When the incident wave is not reflected over plane surface it produces a diffuse scattering and its power is scattered over the space (Fig. 3.7b). Some of the scattered power remains with the same phase and the other part is changed. The extreme case is when the

plane surface is perfectly rough. In this particular case the scattering surface is called a *Lambertian surface*, and the scattering coefficient depends only on the product $cos\theta_0 cos\theta_s$.

$$\sigma^0_{pp} + \sigma^0_{pq} = \sigma^0_0 cos\theta_0 cos\theta_s, \tag{3.25}$$

where σ^0_0 is a constant related to the dielectric properties of the scattering surface. Substituting expressions 3.25 in 3.21 the obtained emissivity is:

$$e(\theta_0, \phi_0; p_0) = 1 - \frac{1}{4\pi cos\theta_0} \int_{\phi_s=0}^{2\pi} \int_{\theta_s=0}^{\pi/2} \sigma^0_0 cos\theta_0 cos\theta_s sin\theta_s d\phi_s d\theta_s sin\theta_s = 1 - \frac{\sigma^0_0}{4}. \tag{3.26}$$

Actually, natural surfaces do not have neither specular, nor Lambertian characteristics. They exhibit a mixed behavior depending on its dielectric properties and the surface roughness compared to the wavelength. Particular cases for natural surfaces can be found in [58].

3.5 Stokes' parameters

Two important phenomena appear when a wave reaches a surface: reflection (change in direction of a wave front at an interface between two dissimilar media so that the wave front returns into the medium from which it originated) and refraction (a wave passes from one medium to another). For every wave (incident, transmitted and reflected) it is possible to distinguish two different orthogonal cases that depend on the polarization: horizontal or vertical. In the first case the electromagnetic field is parallel to the separation surface between the two media; in the second the electromagnetic field is contained in the plane formed by the incidence direction and the normal to the separation surface. A rough surface causes depolarization of reflected and transmitted waves, that means a polarization change of incident waves. The Stokes' vector is defined in polarimetric radiometry and depends on the electromagnetic fields as:

$$\mathcal{S} \propto \begin{bmatrix} \langle E_h {E_h}^* \rangle \\ \langle E_v {E_v}^* \rangle \\ 2\,\Re e \langle E_v {E_h}^* \rangle \\ 2\,\Im m \langle E_v {E_h}^* \rangle \end{bmatrix} \equiv \begin{bmatrix} \langle E_h {E_h}^* \rangle \\ \langle E_v {E_v}^* \rangle \\ I_{45^o} - I_{-45^o} \\ I_{LHCP} - I_{RHCP} \end{bmatrix}, \tag{3.27}$$

where E_h, E_v, I_{45^o}, I_{-45^o}, I_{LHCP}, I_{RHCP} are the electromagnetic field in different polarization. The thermal emission vector resultant $\overline{T}_S$ can be defined with the four Stokes parameters, that characterize the thermal emission:

$$\overline{T}_S = \begin{bmatrix} T_h \\ T_v \\ T_U \\ T_V \end{bmatrix} = \begin{bmatrix} T_h \\ T_v \\ T_{45^o} - T_{-45^o} \\ T_{LHCP} - T_{RHCP} \end{bmatrix} = T_{ph} \begin{bmatrix} e_h \\ e_v \\ e_U \\ e_V \end{bmatrix} = C \begin{bmatrix} \langle E_h {E_h}^* \rangle \\ \langle E_v {E_v}^* \rangle \\ 2\,\Re e \langle E_v {E_h}^* \rangle \\ 2\,\Im m \langle E_v {E_h}^* \rangle \end{bmatrix}, \tag{3.28}$$

where T_h and T_v are the brightness temperature at horizontal and vertical polarizations respectively. T_U and T_V are the third and the fourth Stokes' parameters, that represent the depolarization level of the waves. The third parameter can be also defined as the

difference of two linearly polarized waves with polarization vector angles of $\frac{\pi}{4}$ and $-\frac{\pi}{4}$ with respect to the horizontal vector. The fourth parameter can be defined as the difference between left and right hand circularly polarized waves. The full-polarimetric emission vector $[e_h,\ e_v,\ e_U,\ e_V]$ corresponds to thermal emission vector; C is a constant which depends on instrument parameters and T_{ph} is the temperature of the surface. To measure the four Stokes'parameters is necessary a polarimetric radiometer. Next section presents the radiometer classification as a function of their capacity to measure these parameters.

3.6 Types of microwave radiometers

As it has been seen, if an antenna is pointing to a body, the power that is collected at its output, expressed in terms of the antenna temperature (T_A), is related to the brightness temperature (T_B) of this body. A microwave radiometer is an instrument that measures the T_A with high precision and accuracy. In fact, a microwave radiometer is a well calibrated and high sensitive microwave receiver. The performance of a radiometer is characterized by two main factors: the radiometric resolution and the radiometric accuracy [59]. The first one determines the smallest change in T_A that can be detected by the radiometer output. The second one indicates the correspondence of the measurement of the true value.

In order to illustrate these two aspects, the following example is analyzed; a radiometer is connected to an antenna which is exposed to a temperature including losses $T'_A = 200$ K, and the resolution requirement of the measurement is of 1 K. The noise temperature introduced by the radiometer, has to be taken in account; a typical value will be T_{REC} = 300 K. Then the aim of the radiometer is to perform a measurement which matches with a variation of 1 K over 500 K = 200 K + 300 K. In order to achieve this resolution, a radiometer uses integration techniques. Therefore, if the radiometer's gain G and the noise temperature T_{REC} are added in Eqn. 3.29, the resulting output power is:

$$P = kBG(T'_A + T_{REC}) \qquad \text{[W]}. \tag{3.29}$$

As it is shown, the stability of the power measurement depends on the stability of the factors in Eqn. 3.29: B, G and T_{REC}. Since B is a parameter of the filter (passive device), it is assumed to be rather constant. Back to the previous example, if the required resolution is 1 K, it means that G and T_{REC} have to be stable in an interval of ≤ 0.2 %, which corresponds to about 0.007 dB. Therefore, the following problem appears that it will be difficult to get these requirements from an amplifier. After having seen the two mains problems linked to the design of a radiometer, the main radiometer types and their behavior are presented in term of resolution.

A radiometer block diagram basically consists of an antenna, a super-heterodyne receiver which translates the radio frequency signal to an intermediate frequency, a detector and a low-pass filter. The radiometric resolution of an ideal radiometer, without gain fluctuations, can be defined as [57]:

$$\Delta T = \frac{T'_A + T_{REC}}{\sqrt{B\tau}} \qquad \text{[K]}. \tag{3.30}$$

The radiometer classification can be divided in two groups:

- Measurement of the 1^{st} and the 2^{nd} Stokes'parameters T_h and T_v: are the radiometers that process each polarization independently, therefore only is possible to retrieve the first two Stokes'parameters.
- Measurement of the 3^{rd} and the 4^{th} Stokes'parameters T_U and T_V or $T_{45^o} - T_{-45^o}$ and $T_{LHCP} - T_{RHCP}$ respectively: are the radiometers that combine the polarization or use correlation techniques, obtaining the four Stokes'parameters.

3.7 Radiometers to measure of the 1^{st} and the 2^{nd} Stokes' parameters

There are different types of radiometers that use each polarization independently. The most representatives ones are: Total Power Radiometer (TPR), Dicke Radiometer, (DR) and Noise Injection Radiometer (NIR). Since the PAU-SA's receiver is one of then, a deeper analysis of these radiometers is performed.

3.7.1 Total Power Radiometer (TPR)

The TPR is the most common radiometer used. It is easy to understand and it can illustrate the most important notions of the performance of such instrument. Figure 3.8 is used to explain it with more details.

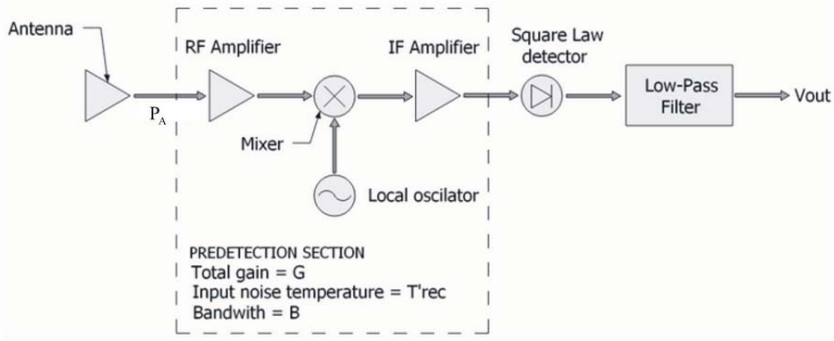

Figure 3.8. Total power radiometer block diagram.

In the radiometer of the Fig. 3.8, the gain G is represented by an amplifier and its bandwidth B with a band-pass filter. To measure the noisy input signal, a square law detector is used. Its output is directly proportional related to the input signal and so to the temperature T'_A. An integrator is used to reduce the fluctuations in the detected signal and therefore to increase the stability of the measurement. Taking into account that the input signal is thermal noise, the voltage output of the IF frequency is a random variable which follows a Gaussian pdf, having 0 mean and an standard deviation which follows a Rayleigh's law (Eqn. 3.31)

$$p(V_e) = \begin{cases} \frac{V_e}{\sigma^2} e^{-\frac{V_e}{2\sigma^2}}, V_e \geq 0 \\ 0, V_e < 0\,, \end{cases} \tag{3.31}$$

So, the mean value of V_e is the available power at the output of the IF amplifies over a unitary resistor:

$$P_{FI} = \overline{V_e^2} = 2\sigma^2 \qquad [\text{W}]. \tag{3.32}$$

Therefore, the relationship between the output and the input of the quadratic law diode can be described as:

$$V_d = C_d V_e^2 \qquad [\text{V}], \tag{3.33}$$

where C_d stands for the power sensibility constant of the power detector, with the units Volts over Watts (V/W). Hence, the mean value of V_d can be expressed as:

$$\overline{V}_d = C_d \overline{V_e}^2 = 2C_d\sigma^2 = C_d P_{FI} = C_d GkBT_{SYS} \qquad [\text{V}]. \tag{3.34}$$

On the other hand, the Low Pass Filter (LPF) output voltage ($\overline{V}_{out}$) depends on two factors, a constant value ($\overline{V}_d$) and a random component ($V_{ac}(t)$). The parameter $V_{ac}(t)$ accounts for the standard deviation of V_d and is related with the uncertainly created by the intrinsic noise of the system (P_{SYS}). The constant value is related with the input power (P_A), thus the radiometric temperature including losses T'_A using the following equation:

$$\overline{V}_{out} = G_{LPF}\overline{V}_d \qquad [\text{V}], \tag{3.35}$$

where G_{LPF} is the gain of the LPF. So that, the output of a TPR is proportional to the radiometric temperature and its value is given by the following equation:

$$V_{out}(t) = \overline{V}_{out} + V_{ac}(t) = G_{LPF}C_d GkBT_{SYS} + V_{ac}(t) = G_s T_{SYS} + V_{ac}(t) \qquad [\text{V}]. \tag{3.36}$$

For a Rayleigh distribution, the squared mean value is equal to its variance, which means that the standard deviation and the mean value at the output of the quadratic law diode are the same:

$$\frac{\sigma_d}{\overline{V}_d} = 1 \rightarrow \sigma_d = \overline{V}_d \qquad [\text{V}]. \tag{3.37}$$

Following Eqn. 3.37, it implies that the measurement uncertainly has the same value of its mean, which invalidates the measurements. The main function of the LPF is to avoid this effect by integrating V_d over a period of time τ (which, in fact is the time constant of the filter). In that way the variance of the measurement is reduced by a factor $N = B \cdot \tau$, where N is the number of independent samples used for the integration. Therefore, the relationship between the standard deviation and the mean value at the LPF filter is:

$$\frac{\sigma_{out}}{\overline{V}_{out}} = \frac{1}{\sqrt{B\tau}} \rightarrow \sigma_{out} = \frac{1}{\sqrt{B\tau}}. \tag{3.38}$$

Hence, assuming that the parameters of Eqn. 3.38 remain constant, this relationship can be re-written as a function of the standard deviation associated to the mean value:

$$\frac{\Delta T_{SYS}}{T_{SYS}} = \frac{1}{\sqrt{B\tau}}, \tag{3.39}$$

where T_{SYS} can be defined by:

$$T_{SYS} = T'_A + T_{REC} \qquad [\text{K}]. \tag{3.40}$$

From Eqn. 3.39 it is possible to infer the radiometric sensibility or resolution (ΔT), which is defined as the minimum input temperature which the radiometer is able to infer a change at its voltage output. The radiometric resolution of a TPR is described as [57]:

$$\Delta T_N \triangleq \Delta T_{SYS} = \frac{T_{SYS}}{\sqrt{B\tau}} = \frac{T'_A + T_{REC}}{\sqrt{B\tau}} \qquad [\mathrm{K}]. \tag{3.41}$$

However, Eqn. 3.41 does not take into account the system gain fluctuations, so all the real fluctuations that occur in a receiver are missing from Eqn. 3.41. The gain uncertainly can be defined as $\Delta G_S/G_S$ witch translates into an uncertainty of the estimated system's temperature:

$$\Delta T_G = T_{SYS}\left(\frac{\Delta G_S}{G_S}\right) \qquad [\mathrm{K}], \tag{3.42}$$

where G_S is the total receiver gain and ΔG_S is the root mean square (rms) variation of the detected power for a constant power input signal. Taking into account that the noise and the gain fluctuations are statistically independent, the final system resolution can be written as:

$$\Delta T = \left[(\Delta T_N)^2 + (\Delta T_G)^2\right]^{\frac{1}{2}} = T_{SYS}\left[\frac{1}{B\tau} + \left(\frac{\Delta G_S}{G_S}\right)^2\right]^{\frac{1}{2}} \qquad [\mathrm{K}]. \tag{3.43}$$

From Eqn. 3.43 it can be inferred that the radiometric resolution of a TPR has a strong dependence on the gain fluctuations. It is important to notice that the best theoretical radiometric resolution can be achieved with a TPR. However due to the gain fluctuations problems, a calibration process is required frequently. As explained in chapter 7, PAU-SA'receiver has been designed with this topology for simplicity hardware reasons.

3.7.2 Dicke Radiometer (DR)

With the aim to correct the stability problems associated to gain fluctuations existing in the TPR, Dicke published in 1946 a radiometer design which is named after him (Fig. 3.9). The Dicke radiometer, instead of measuring directly the antenna temperature, performs the measurement of the difference between T'_A and a known reference temperature T_{REF}. With this method, the noise temperature instability T_{REC} is filtered out and the impact of the gain fluctuations is largely reduced.

As it is shown in Fig. 3.9, a DR is a modified TPR with an input switch that changes of position at a given frequency (f_s) between the antenna and the reference temperature T_{REF} and a synchronous demodulator (± 1 multiplier). Therefore, two different outputs in different time slots are obtained. Depending on the half period, the detector output is:

$$\overline{V}_{dANT} = C_d GKB(T'_A + T_{REC}) \quad \text{for} \quad 0 \le t \le \frac{\tau_s}{2} \qquad [\mathrm{V}], \tag{3.44}$$

$$\overline{V}_{dREF} = C_d GKB(T_{REF} + T_{REC}) \quad \text{for} \quad \frac{\tau_s}{2} \le t \le \tau_s \qquad [\mathrm{V}], \tag{3.45}$$

where T_{REF} is the reference noise temperature, τ_s is the switching period, and T_{REC} is the receivers noise temperature, including the noise of the input switch. On the other

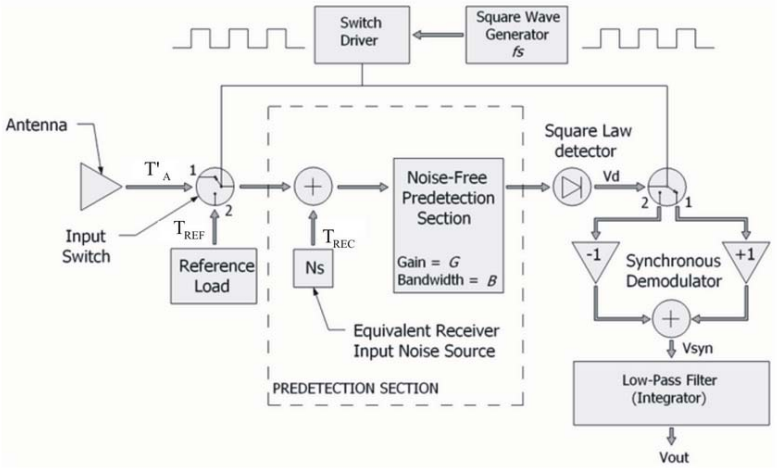

Figure 3.9. Dicke radiometer sketch (adapted from [57]).

hand, the synchronous demodulator has another synchronous switch. This switch, gives the input signal to two unitary gain amplifiers, which have opposed signs, an amplifier has the $\overline{V}_{dANT}$ and the other one has $\overline{V}_{dREF}$. The outputs of these amplifiers are added, and finally low-pass filtered. If the switching frequency f_s is sufficiently fast to consider the parameter T'_A, T_{REF} and G constants during an entire period, and also that the period is smaller than the integration time ($f_s \gg \tau^{-1}$), then the radiometer output can be expressed as:

$$V_{SYN} = \frac{1}{2}(\overline{V}_{dANT} - \overline{V}_{dREF}) = \frac{1}{2}C_d GKB(T'_A - T_{REF}) \qquad \text{[V]}. \tag{3.46}$$

As it can be observed in Eqn. 3.46, the output of the Dike radiometer is proportional to the $(T'_A - T_{REF})$ term. So that, the uncertainly of this new term (T_{REF}) has to be taken into account in the radiometric resolution calculation. The resolution of a Dike radiometer can be expressed as it follows:

$$\Delta T = \left[\frac{(T'_A + T_{REC})^2}{\frac{B\tau}{2}} + \frac{(T_{REF} + T_{REC})^2}{\frac{B\tau}{2}} + \left(\frac{\Delta G_s}{G}\right)^2 (T'_A - T_{REF})^2 \right]^{1/2} \qquad \text{[K]}, \tag{3.47}$$

It is said that a Dicke radiometer is balanced in the ideal case in which the antenna the reference temperatures are identical ($T'_A = T_{REF}$), and then the resolution reduces to:

$$\Delta T = \frac{2(T'_A + T_{REC})}{\sqrt{B\tau}} = 2\Delta T_{TPR} \qquad \text{[K]}. \tag{3.48}$$

where ΔT_{TPR} is the radiometric resolution of a TPR in the total absence of fluctuations. As it can be observed, in this ideal case Eqn. 3.48, there is no gain fluctuations on the radiometric resolution, but the resolution is twice worse than in a TPR, due to the integration time has been split by 2, half the period it is looking to the antenna and the other half the period it is looking to a reference load.

In a real case, when the temperature T_{REF} is chosen close to the antenna temperature T'_A, the impact of G fluctuations is small. Then if $(T'_A - T_{REF}) \ll (T'_A + T_{REC})$ is fulfilled, the DR decreases the accuracy respect to the TPR. Although the stability of the system is improved, by measuring the antenna temperature just half of the time, there is a loss of resolution as compared to a TPR. Indeed, on each half period, the radiometer can be assimilated to a TPR pointing to the antenna or to the reference load, using an integration time of $\tau/2$.

3.7.3 Noise Injection Radiometer NIR

The noise injection radiometer is a particular case of a Dicke radiometer. It has been optimized to ensure that its output is always not dependent on the gain fluctuations and on the receiver noise. To achieve that purpose a NIR has a feedback loop which is shown in Fig. 3.10. The aim of the feedback loop is to balance the radiometer (obtaining the

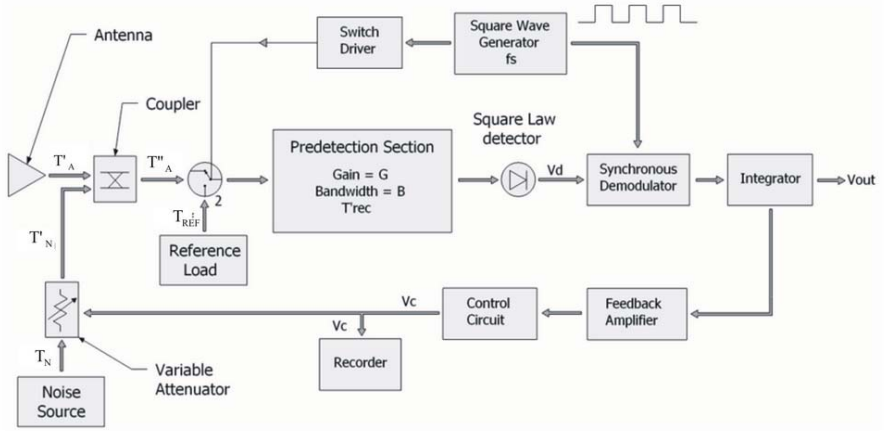

Figure 3.10. NIR radiometer sketch (adapted from [57]).

same result as in the ideal case of a balanced Dike radiometer) by injecting noise in the system input through a directional coupler ensuring that always is fulfilling:

$$T''_A = T_{REF} = 0 \qquad [\mathrm{K}]. \tag{3.49}$$

The amount of injected power is controlled by a variable attenuator, which is controlled by the feedback loop. Thence, the amount of power entering to the system can be calculated as:

$$T''_A = \left(1 - \frac{1}{F_c}\right) T'_A + \frac{T'_N}{F_c} \qquad [\mathrm{K}], \tag{3.50}$$

where F_c is the coupling factor of the directional coupler, and T'_N is the amount of injected noise, attenuated by the variable attenuator. The voltage V_c , that controls the attenuation is proportional to the antenna, and the system physical temperature ($T_{ph} \sim 290\,\mathrm{K}$) difference, and it is given by the following expression:

$$V_C = \frac{F_c - 1}{T_N - T_{ph}} (T_{ph} - T'_A) \qquad [\mathrm{V}], \tag{3.51}$$

Using this technology, the output of the NIR is independent to the gain fluctuations and to the noise of the receiver. The radiometric resolution of a NIR in the case of $T_{ph} = T'_A$ can be described as it follows:

$$\Delta T = \frac{2(T_{ph} + T_{REF})}{\sqrt{B\tau}} = 2\Delta T_{TPR} \qquad \text{[K]}. \tag{3.52}$$

As it can be seen in Eqn. 3.52, the NIR radiometric resolution is the same than a balanced Dicke, but with the advantage that this does not depend on the noise of the receiver.

3.8 Radiometers to measure of the 3^{rd} and the 4^{th} Stokes'parameters

A Polarimetric Radiometer PRis an instrument devoted to the measurement of the four Stokes parameters. It can be classified in two groups: combination of polarization or correlation. Due PAU-SA'receivers is not in this group of radiometers, a brief explanation is performed. A block diagram of a typical PR is shown in Fig. 3.11. The radiometer

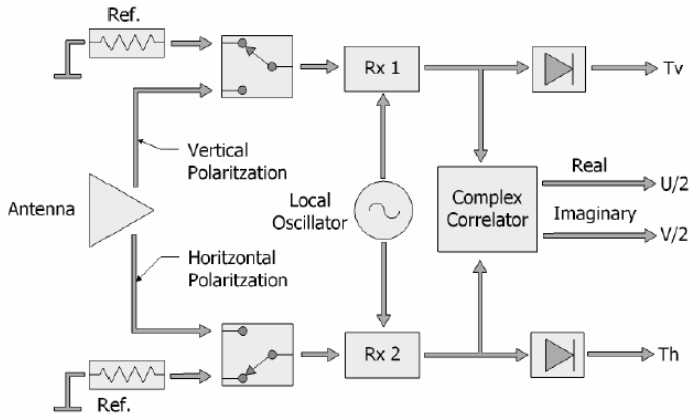

Figure 3.11. Block diagram of a polarimetric radiometer [60].

is a Dicke type, super-heterodyne receiver and the antenna has separate outputs for vertical and horizontal polarizations. The third and fourth Stokes parameters can be obtained in several ways such as with a linear combination of the collected powers at $\pm 45^o$ polarizations or using a complex correlator between the H and the V-polarization signals. In the example shown in Fig. 3.11, a complex correlator provides the third (obtained by in-phase correlation) and the fourth (obtained after a 90^o phase shift) Stokes parameters. The error caused by differences in signal propagation times is minimized using a delay line in one of the correlator channels. The phase differences in different channels are equalized using a phase shifter in the RF-block or some other advanced techniques. The correlator block that multiplies the vertical and horizontal signals is the heart of the PR. The obtained DC component at the correlator output is proportional to the phase difference between the signals.

3.9 Conclusions

In this chapter the fundamentals of microwave radiometry theory have been presented. This technique consists of the principle that matter, when an equilibrium temperature is researched, emits electromagnetic radiation, following Plank's radiation law. The brightness temperature and the apparent temperature concepts have been defined, as well as the black and gray-body relationships through the emissivity. The concept of Stokes' parameter has been presented and a radiometer classification have been performed in two groups in relation to the capacity to measure these parameters. Since PAU-SA's receiver is in the first group, it has been explained in detail. As explain in chapter 7, in order to simplify the hardware architecture, a TPR topology for the PAU-SA'receiver has been chosen. In an ideal temperature controlled environment without gain fluctuations, this topology has the best radiometric resolution been possible to measure for all integration time, like the ideal case. Otherwise the NIR architecture solves the problems of gain fluctuations, but deteriorates, by factor of two the radiometric resolution.

Chapter 4

Introduction to interferometric radiometry

While a real aperture radiometer directly measures the power collected by an antenna in the main beam direction measuring an image pixel by pixel, an interferometric radiometer measures the complex correlation between the signals collected by each pair of antennas recovering the image in a single snapshot. The spatial resolution achievable by a radiometer is limited by its antenna size. That of an interferometric radiometer is limited by the maximum antenna spacing. The measurement of some physical parameters such as the SM or the SSS requires passive measurements at low frequencies with moderate spatial resolution (10-20 km) which requires large antennas, of about 20 m of diameter, at present technologically unfeasible. This is the reason to configure two-dimensional interferometric radiometry as the preferred option over real aperture radiometry due to its lighter structure, but with the drawback of more complex electronic hardware, data processing and calibration procedures. This chapter explains the principles of interferometric radiometry and the relationship between measurements (called "visibilities") and the source temperature. The antenna positions and their radiation voltage patterns, as well as the receiver frequency responses are included. All these relations will be useful to study instrument behavior.

4.1 Principles of operation of an interferometric radiometer

This section summarizes some of the results of [22]. Let us consider a point source located at given coordinates (x_0, y_0, z_0) radiating a random scalar field (symbolized as italic b) $b(x, y, z, t)$ as shown in Fig. 4.1. If the signal in point (x_1, y_1, z_1) is $b_1(t) = b(x_1, y_1, z_1, t)$,

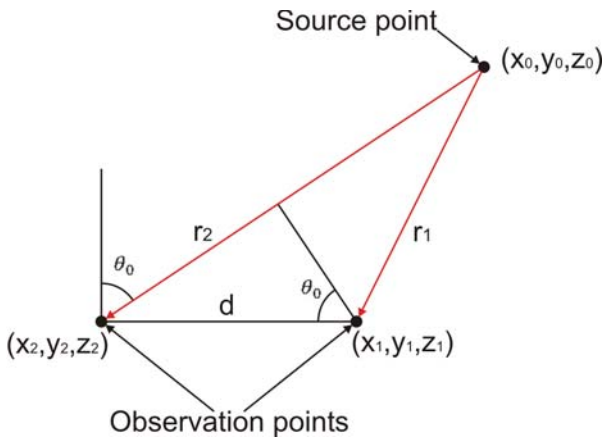

Figure 4.1. A point source and two observation points.

assuming that the process is stationary and ergodic, its mean power (power density of the electromagnetic wave) can be expressed as the self-correlation of the real precess $b_1(t)$ given by:

$$P_1 = \lim_{T\to+\infty} \frac{1}{T} \int_{-T/2}^{T/2} [b_1(t)]^2 \, dt = R_{b1}(0). \tag{4.1}$$

Using the properties of the analytic signal (symbolized as non-italic b), this power can be expressed as:

$$P_1 = \frac{1}{2} \lim_{T\to+\infty} \frac{1}{T} \int_{-T/2}^{T/2} |\mathrm{b}_1|^2 \, dt = \frac{1}{2} E[\mathrm{b}_1 \mathrm{b}_1{}^*] = \frac{1}{2} R_{\mathrm{b}_1}(0), \tag{4.2}$$

where R_{b_1} is the self-correlation function of $\mathrm{b}_1(\mathrm{t})$, the analytic signal of $b_1(t)$. The function $b(x, y, z, t)$ is expressed in the frequency domain as $\beta(x, y, z, f)$. The signal at point (x_1, y_1, z_1) can be expressed as:

$$\beta(x_1, y_1, z_1, f) = \frac{A(f)}{r_1} e^{-jkr_1}, \tag{4.3}$$

where $A(f)$ is now a complex function of frequency and $k = 2\pi f/c$. Alternatively, in the time domain:

$$b_1(t) = b(x_1, y_1, z_1, t) = \int_{-\infty}^{+\infty} \frac{A(f)}{r_1} e^{-j\frac{2\pi f}{c} r_1} e^{j2\pi ft} \, df = \frac{a(t - \frac{r_1}{c})}{r_1}, \tag{4.4}$$

where $a(t)$ is the inverse Fourier transform of $A(f)$. The analytic signal of $b_1(t)$ is obtained easily from the analytic signal of $a(t)$:

$$\mathrm{b}_1(t) = \frac{\mathrm{a}(t - \frac{r_1}{c})}{r_1}, \tag{4.5}$$

From 4.2 the mean power density of the wave at the observation point can be obtained:

$$P_1 = \frac{1}{2}\frac{R_{\mathrm{a}}(0)}{r_1^2}, \tag{4.6}$$

where $R_{\mathrm{a}}(0)$ is the self-correlation function of $\mathrm{a}(t)$, the analytic signal of $a(t)$. The term $\frac{1}{2}R_{\mathrm{a}}(0)$ is defined as the radiation intensity of the source, and will be denoted by P_{a}:

$$P_{\mathrm{a}} = \frac{1}{2}R_{\mathrm{a}}(0). \tag{4.7}$$

In the case of two points (x_1, y_1, z_1) and (x_2, y_2, z_2), in which the sources produce signals, with associated analytic signals $\mathrm{b}_1(\mathrm{t})$ and $\mathrm{b}_2(\mathrm{t})$, respectively. The visibility function (V) can be defined as:

$$V_{12} = \frac{1}{2}E[\mathrm{b}_1(t)\mathrm{b}_2(t)^*] = \frac{1}{2}R_{\mathrm{b}_1\mathrm{b}_2}(0). \tag{4.8}$$

Using now the expression 4.5 for $\mathrm{b}_1(\mathrm{t})$ and a similar one for $\mathrm{b}_2(\mathrm{t})$, it can be concluded that:

$$V = \frac{1}{2}\frac{1}{r_1 r_2}E\left[a\left(t - \frac{r_1}{c}\right)a^*\left(t - \frac{r_2}{c}\right)\right] = \frac{1}{2}\frac{1}{r_1 r_2}R_{\mathrm{a}}\left(\frac{\Delta r}{c}\right), \tag{4.9}$$

being $\Delta r = r_2 - r_1$. V can be expressed in terms of the self-correlation function of the complex envelope of $a(t)$ yielding:

$$V = \frac{1}{r_1 r_2}\widetilde{R}_A\left(\frac{\Delta r}{c}\right)e^{j\omega_0\frac{\Delta r}{c}} = \frac{1}{r_1 r_2}\widetilde{R}_A\left(\frac{\Delta r}{c}\right)e^{jk_0\Delta r}, \tag{4.10}$$

where $\widetilde{R}_A(\tau)$ is the self-correlation function of the complex envelope of a $a(t)$, $k_0 = \omega_0/c$ and ω_0 is an arbitrary frequency, which, for narrow band signals is usually chosen as the mid-band frequency. The function $\widetilde{R}_A(\tau)$ is the inverse Fourier transform of the power spectral density of the complex envelope.

Alternatively, expressing equation 4.10 as a function of the complex degree of coherence of the analytic signal and the complex envelope:

$$V(\Delta r) = \frac{1}{r_1 r_2}P_{\mathrm{a}}r_{\mathrm{a}}\left(\frac{\Delta r}{c}\right) = \frac{1}{r_1 r_2}P_{\mathrm{a}}\widetilde{r}_A\left(\frac{\Delta r}{c}\right)e^{jk_0\Delta r}. \tag{4.11}$$

The term $\widetilde{r}_A(\frac{\Delta r}{c})$ is often called the "Fringe-Wash Function" (FWF) in interferometry terminology. Note that, if the signal bandwidth is reduced to zero, the stochastic noise source becomes a sinusoidal source, the amplitude of the fringe-washing function is constant and the visibility function depends only on the path length difference Δr:

$$V(\Delta r) = \frac{1}{r_1 r_2}P_{\mathrm{a}}e^{jk_0\Delta r}. \tag{4.12}$$

In the case of non-sinusoidal signals, the visibility function has an amplitude effect. Considering $a(t)$ a band-limited point thermal source located at the (ξ_0, η_0) direction Eqn. 4.13.

$$\xi_0 = \frac{x_0}{r_0} \qquad\qquad \eta_0 = \frac{y_0}{r_0} \tag{4.13}$$

where r_0 is the distance of the source and the observation points to an arbitrary origin of coordinates. It has a power spectrum centered on a frequency f_0, and a bandwidth B and zero outside. Then, the power spectral density $S(f)$ can be easily determined as:

$$S(f) = 2k_B T \Pi\left(\frac{f - f_0}{B}\right) \Leftrightarrow \widetilde{R}_A(\tau) = 2k_B T B \,\mathrm{sinc}(B\tau), \tag{4.14}$$

where k_B is the Boltzmann's constant and T is the apparent brightness temperature and being

$$\mathrm{sinc}(x) = \begin{cases} 1 & \text{for } x = 0, \\ \frac{\sin x}{x} & \text{otherwise.} \end{cases} \tag{4.15}$$

From Eqn. 4.10 the visibility function becomes:

$$V(\Delta r) = \frac{k_B T}{r_1 r_2} B \,\mathrm{sinc}\left(b\frac{\Delta r}{c}\right) e^{-jk_0 \Delta r} = \frac{k_B T}{r_1 r_2} B \,\mathrm{sinc}\left(\frac{u\xi_0 + v\eta_0}{W^{-1}}\right) e^{-j2\pi[u\xi_0 + v\eta_0]}, \tag{4.16}$$

where $c \approx 3 \cdot 10^8 m/s$ is the speed of light in vacuum, and W is defined as:

$$W \triangleq \frac{B}{f_0}. \tag{4.17}$$

and the variables (u, v) are called the baseline and are defined as the projections over the (x, y) axes of the distance between the antennas normalized to the wavelength:

$$u = \frac{x_2 - x_1}{\lambda} = \frac{D_x}{\lambda} \qquad\qquad v = \frac{y_2 - y_1}{\lambda} = \frac{D_y}{\lambda} \tag{4.18}$$

If $\Delta r/c$ is much be smaller than $1/B$, the sinc function is approximately equal to one and the result is the same as for the previous case, the sinusoidal function. In other case, the amplitude of the visibility function decreases and vanishes for $\Delta r = c/B$. The time $1/B$ is called the *coherence time* of the signal, and this multiplied by c gives the *coherence length*. So, for an interferometer to perform well, it must satisfy:

$$\Delta r \gg coherence\,length = \frac{c}{B}. \tag{4.19}$$

For a radioastronomy interferometer this effect supposes no limitation since a time delay is added to the receivers so as to have an effective Δr close to 0. This can be done only if the approximate location of a quasi-point source is known a priori. For a wide field of view radiometer this is not possible in general, since the source is extended. This is the main difference between radiometry and other applications of interferometry.

The elemental operation of a synthetic aperture radiometer is the correlation of the signal collected at each pair of antennas or baseline. It is formed by two channels composed of antenna and receiver and a complex correlator as shown in Fig. 4.2 where the $F_{m,n}^{p,q}(\xi, \eta)$ is the normalized antenna pattern at the antennas labeled m and n and the polarization p and q, $(\xi, \eta) = (sin\theta cos\phi, sin\theta sin\phi)$ are the direction cosines defined with respect to the x and y axes, $T_{Am,n}$ is the antenna temperature, $H_{m,n}(f)$ is the frequency response, $G_{m,n}$ is the power gain of the channel, $B_{m,n}$ is the equivalent noise bandwidth,

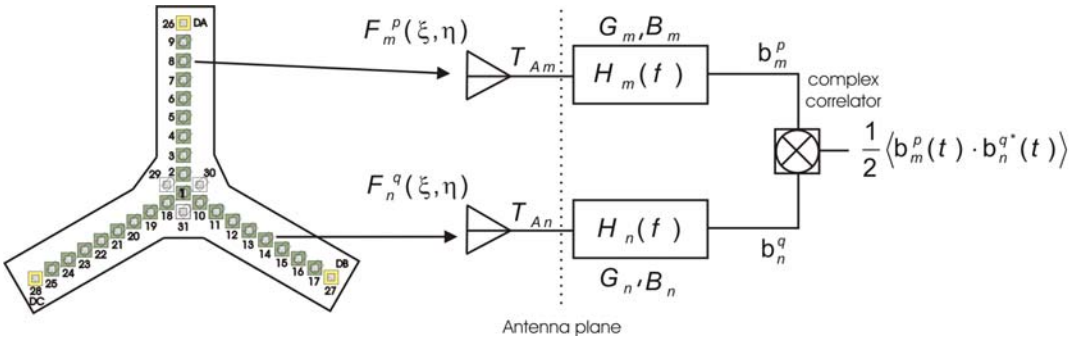

Figure 4.2. Sketch of the elemental operation in an interferometer (baseline level), composed of a pair of receiver channels and a complex correlator.

$\mathrm{b}_{m,n}^{p,q}$ is the analytical signal, and $\langle\rangle$ being the expectation operator, correspond with the time average. A synthetic aperture radiometer measures all the correlations between the incident signal collected by the antennas. The auto-correlation and the cross-correlation of the signals at each receiver output can defined as:

$$\frac{1}{2}\langle|\mathrm{b}_m^p(t)|^2\rangle \triangleq k_B\cdot B_m\cdot G_m\cdot(T_{Am}^p + T_{RECm}), \tag{4.20}$$

$$\frac{1}{2}\langle|\mathrm{b}_n^q(t)|^2\rangle \triangleq k_B\cdot B_n\cdot G_n\cdot(T_{An}^q + T_{RECn}), \tag{4.21}$$

$$\frac{1}{2}\langle\mathrm{b}_m^p(t)\mathrm{b}_n^{q*}(t)\rangle \triangleq k_B\cdot\sqrt{B_m\cdot B_n}\cdot\sqrt{G_m\cdot G_n}\cdot V_{mn}^{pq}(u_{mn},v_{mn}), \tag{4.22}$$

where k_B is the Boltzmann constant, $T_{RECm,n}$ is the equivalent receiver temperature, and V_{mn}^{pq} is the visibility function defined in the spatial frequency (baseline) that depends on the difference of the antenna position normalized to the wavelength $(u_{mn},v_{mn}) \triangleq (x_n - x_m, y_n - y_m)/\lambda_0$, being $\lambda_0 = c/f_0$. According to Eqn. 4.22 the visibility function can be derived as a sample of the cross-correlation function with units of Kelvin.

$$V_{mn}^{pq}(u_{mn},v_{mn}) = \frac{1}{k_B\sqrt{B_m\cdot B_n}\sqrt{G_m\cdot G_n}}\frac{1}{2}\langle b_m(t)b_n^*(t)\rangle. \tag{4.23}$$

assuming that the collected signal is stationary random process (thermal noise radiation) that fulfills the ergodicity property, narrow-band, spatially uncorrelated, and distance between antennas $\gg$ wavelength, then Eqn. 4.23 can be computed in practice using the cross-correlation (time average) of the in-phase and quadrature components $b_m^p = I_m^p(t) + jQ_m^p(t)$ and $b_n^q = I_n^q(t) + jQ_n^q(t)$. From the Van-Cittert Zernicke theorem [61], the visibility function can be related to the brightness temperature distribution [62]:

$$V_{mn}^{pq}(u_{mn},v_{mn}) = R_{I_m^q I_n^p}(0) + jR_{Q_m^q I_n^p}(0), \tag{4.24}$$

$$\begin{aligned} V_{mn}^{qp}(u_{mn},v_{mn}) &= \frac{1}{\sqrt{\Omega_m\Omega_n}}\iint_{\xi^2+\eta^2\le 1}\frac{T_B^{qp}(\xi,\eta) - T_{rec}\delta_{qp}}{\sqrt{1-\xi^2-\eta^2}}F_m^q(\xi,\eta)F_n^{p*}(\xi,\eta) \\ &\quad\cdot\widetilde{r}_{mn}\left(-\frac{u_{mn}\xi + v_{mn}\eta}{f_0}\right)e^{-j2\pi(u_{mn}\xi+v_{mn}\eta)}\,d\xi\,d\eta. \end{aligned} \tag{4.25}$$

where

- Ω_{mn} are the equivalent solid angle of the antennas,
- $T_B^{qp}(\xi,\eta)$ is the T_B of the scene at $p-q$ polarization (E_p and E_q being the electric field at p and q polarization),
- T_{rec} is the physical temperature of the receiver (the Corbella's term) [62],
- δ_{pq} is the Kronecker's delta function: $\delta_{pq}=1$ if $p=q$ and $\delta_{pq}=0$ if $p\neq q$,
- $\widetilde{r}_{mn}\left(-\frac{u_{mn}\xi+v_{mn}\eta}{f_0}\right)$ is the fringe-washing function. This term is related to the differences in the frequency response of the filters in the two receivers within the baseline. Being $\widetilde{r}_{mn}\triangleq\frac{e^{-j2\pi f_0 t}}{\sqrt{B_m B_n}}\int_0^\infty H_m H_n^* e^{j2\pi f_t} d_f$, where $H_{m,n}$ is the normalized frequency response for each channel,
- $1/\sqrt{1-\xi^2-\eta^2}$ is the obliquity factor.

In addition, Eqn. 4.25 is normalized by the terms K_B, $\sqrt{B_m B_n}$, $\sqrt{G_m G_n}$, and $\sqrt{\Omega_m \Omega_n}$ to ensure that the visibility function has units of Kelvin.

4.2 Ideal situations

A simplified version of Eqn. 4.25 is analyzed. Given the narrow bandwidth of PAU-SA (2.2 MHz) and the reduced dimensions of the array (being $\Delta r\approx 2.4$ m the maximum distance between two antennas of the array), the fringe-washing function becomes:

$$\widetilde{r}_{mn}\left(-\frac{u_{mn}\xi+v_{mn}\eta}{f_0}\right)\approx 1, \tag{4.26}$$

The term $T_{rec}\delta_{mn}$ is neglected, all antenna patterns are identical $F_m=F_n$, and the constant terms are normalized to the unity. For an ideal situation, the relationship between the visibility function (V_{mn}), Eqn. 4.27, and the so-called modified brightness temperature (T) Eqn. 4.28, is given by Eqn. 4.29.

$$V_{mn}=\iint_{\xi^2+\eta^2\leq 1} T(\xi,\eta)e^{-j2\pi(u_{mn}\xi+v_{mn}\eta)}\,d\xi\,d\eta, \tag{4.27}$$

$$T(\xi,\eta)=\frac{T_B(\xi,\eta)}{\sqrt{1-\xi^2-\eta^2}}|F_n(\xi,\eta)|^2, \tag{4.28}$$

$$V_{mn}=\mathscr{F}\Big[\frac{T_B^{qp}(\xi,\eta)}{\sqrt{1-\xi^2-\eta^2}}|F_n(\xi,\eta)|^2\Big], \tag{4.29}$$

where $\mathscr{F}$ is the Fourier transform .With this conditions, the modified brightness temperature can be recovered by means of the inverse Fourier transform of the visibility samples, Eqn. 4.30.

$$T(\xi,\eta)=\mathscr{F}^{-1}\left[V_{mn}\right]. \tag{4.30}$$

4.2.1 Total power radiometer

Each type of radiometers can be derived from the general version of the interferometric radiometer [38], expressed in equation 4.25 and taking into account proper considerations. The most simpler case is the TPR radiometer, considering an interferometric radiometer with only the central antenna, that is to say, having only one visibility sample at (u, v) = (0,0). In this case the resultant visibility function becomes:

$$V(0,0) = T_A. \tag{4.31}$$

where T_A is the antenna temperature.

4.3 Interferometric radiometer equation: discretization and G-matrix formulation

In practice, it is not possible to acquire the visibilities continuous manner. The resulting are discrete visibility function samples of the mentioned visibility function. A simplified version of Eqn. 4.25 with the contributions of the fringe-washing function neglected, the visibility function can be discretized and calculated for all the visibilities:

$$V_{mn}(u_{mn}, v_{mn}) \approx \Delta \sum_k \sum_l \frac{T_B(\xi_{kl}, \eta_{kl})}{\sqrt{\Omega_m \Omega_n}\sqrt{1 - {\xi_{kl}}^2 - {\eta_{kl}}^2}} F_m(\xi_{kl}, \eta_{kl}) {F_n}^*(\xi_{kl}, \eta_{kl}) \cdot \widetilde{r}_{mn}\left(- \frac{u_{mn}\xi_{kl} + v_{mn}\eta_{kl}}{f_0} \right) e^{-j2\pi(u_{mn}\xi_{kl} + v_{mn}\eta_{kl})}. \tag{4.32}$$

where (u_{mn}, v_{mn}) points are determined by the array shape, in our case Y-shape, which is optimal in terms of minimum number of samples. (ξ_{kl}, η_{kl}) are the arbitrary samples of the directing cosines. As it is explained in the next section, it can be recognized as an hexagonal Discrete Fourier Transform (DFT) in the ideal case and the brightness temperature pixel area is given by

$$\Delta = \frac{\sqrt{3}\, d^2}{2}. \tag{4.33}$$

Then, considering $(m, n) \triangleq r$ and $(p, q) \triangleq s$, the system of equations becomes:

$$\begin{bmatrix} V_1 \\ V_2 \\ \vdots \\ V_r \end{bmatrix} = \begin{bmatrix} g_{11} & g_{12} & \cdots & g_{1s} \\ g_{21} & g_{22} & \cdots & g_{2s} \\ \vdots & \vdots & \ddots & \vdots \\ g_{r1} & \cdots & \cdots & g_{rs} \end{bmatrix} \begin{bmatrix} T_1 \\ T_2 \\ \vdots \\ T_s \end{bmatrix}, \tag{4.34}$$

or, using matrix notation,

$$\overline{V}_r = \overline{\overline{G}}_{r,s}\, \overline{T}_s, \tag{4.35}$$

where G is the so-called (G matrix) and determine the spatial impulse response of the synthetic aperture radiometer, V is the visibility vector, and the T is the brightness

temperature vector that can be inverted by the Moore-Penrose pseudoinverse. When the G matrix is used to to recovered the image, part of the errors can be corrected. Each element of the $\overline{\overline{G}}$ matrix is given by:

$$g_{rs} = \frac{\sqrt{3}\,d^2}{2} \frac{F_r(\xi_s, \eta_s) {F_r}^*(\xi_s, \eta_s)}{\sqrt{\Omega_r \Omega_r}\sqrt{1 - {\xi_{pq}}^2 - {\eta_{pq}}^2}} \cdot \widetilde{r}_r \left(- \frac{u_r \xi_s + v_{mn} \eta_s}{f_0} \right) e^{-j2\pi(u_r \xi_s + v_r \eta_s)}. \tag{4.36}$$

The solution of Eqn. 4.34 changes depending on the number of unknowns, that is the number of brightness temperature points or pixels. Three situations are possible:

1. the number of unknowns equals the number of visibilities, then:

$$\overline{T} = \overline{\overline{G}}^{-1}\, \overline{V}, \tag{4.37}$$

2. the number of unknowns is smaller than the number of visibilities, then:

$$\overline{T} = \left(\overline{\overline{G}}^H \overline{\overline{G}} \right)^{-1} \overline{\overline{G}}^H\, \overline{V}, \tag{4.38}$$

3. the number of unknowns is greater than the number of visibilities, then there are infinite possible solutions to the system. An analytical solution is given by the Moore-Penrose pseudoinverse:

$$\overline{T} = \overline{\overline{G}}^H \left(\overline{\overline{G}}\, \overline{\overline{G}}^H \right)^{-1} \overline{V}, \tag{4.39}$$

   which provides the so-called minimum norm solution.

This last condition is the usual one, since:

1. there are missing (u, v) points to fill up a complete hexagonal period;

2. the number of temperature pixels is usually chosen much higher than the number of visibilities, in order to stabilize the inversion process by lowering the condition number of the $\overline{\overline{G}}\,\overline{\overline{G}}^H$ matrix [22].

4.4 Determination of the shape array and sample sampling

The main difference between linear arrays and planar arrays consist that the first one needs mechanical scanning to obtain a complete snapshot and the second one can provide it at the same time such as MIRAS and PAU-SA. The spatial frequency coverage or sampling pattern (u, v) depends on the topology configuration, been divided into two groups: rectangular or hexagonal sampling arrays. As mentioned previously, the visibility function have been obtain from data sampling, producing a variety of effects such as

replicas image on the image reconstruction. The relationship between sampling pattern and alias distribution can be defined as:

$$f(n) = f_{analog}(U_n), \tag{4.40}$$

where f is the discrete resultant function, f_{analog} is the continuous raw data function, U is the sampling matrix whose columns are the basis vectors of the sampling pattern and n is an integer to determine the sequence of points. When the image is reconstructed through the inverse Fourier transform, alias replicas are formed on a lattice whose basis vectors are given by the columns. These alias are distributed according to to the inverse of the transpose of the sampling matrix, Eqn. 4.41.

$$(U^T)^{-1}. \tag{4.41}$$

Next sections analyze and quantize the effect of the sampling pattern and the alias distribution of the hexagonal and rectangular patterns respectively.

4.4.1 Hexagonal sampling arrays

Both MIRAS and PAU-SA are two-dimensional arrays sampling band-limited signals (the brightness temperature) using hexagonal sampling. Is known that this type of grid needs the minimum number of samples in the spatial frequency coverage (u, v) to retrieve the image of the brightness temperature [22]. The specified aliasing level depends on the spacing between two adjacent antennas of the array. The most typical configuration with hexagonal sampling coverage are △-shape and Y-shape. Figures 4.3 and 4.4 show these two configurations arrays composed of 15 elements for the △-shape and 16 elements for the Y-shape with their respective spatial frequency coverage. The redundant (u, v) samples are represented in red. As it can noticed, for the similar number of elements, the Y-shape array covers a larger number of points in its spatial frequency coverage, than that the △-shape array, obtaining better spatial resolution. On other hand, the △-shape covers a complete hexagon whereas Y-shape form a star with missing points in the spatial frequency coverage. For this reason the Hexagonal Fast Fourier Transformation (HFFT)

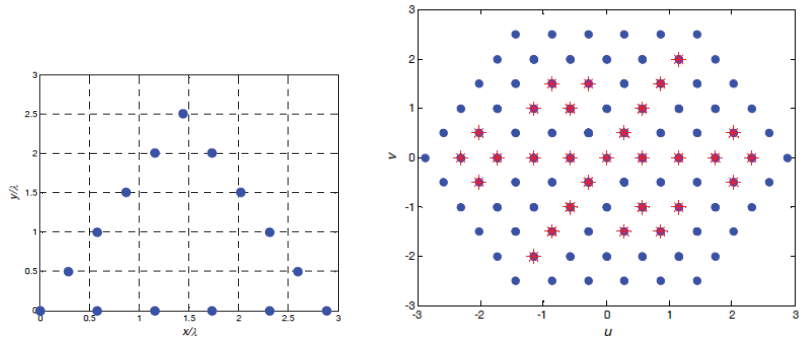

(a) **(b)**

Figure 4.3. (a) △-shape array configuration, and (b) △-shape spatial frequency coverage.

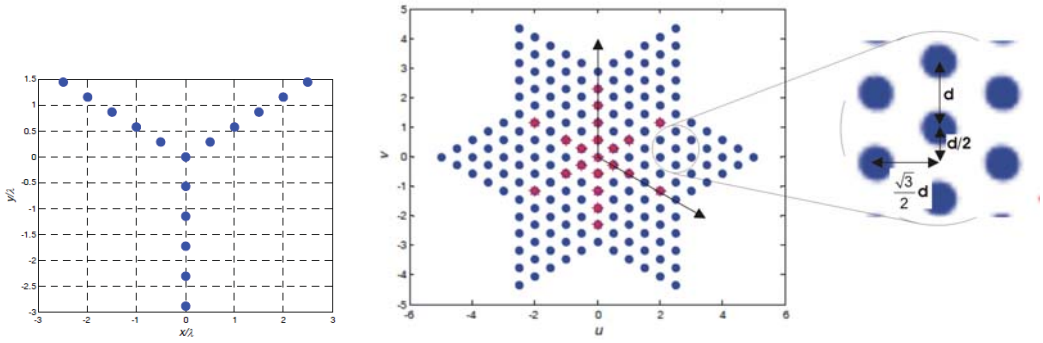

(a) **(b)**

Figure 4.4. (a) Y-shape array configuration, and (b) Y-shape spatial frequency coverage.

algorithms developed by [63, 64] compute directly the outputs points over a rectangular lattice to avoid interpolation strategies.

The periodic extension of the (u, v) hexagonal coverage and their aliases contributions are presented in detail. In the particular case of Y-shape topology, the resultant sample matrix can be obtained from Fig. 4.4b as:

$$U = \begin{bmatrix} \frac{\sqrt{3}}{2}d & 0 \\ \frac{-1}{2}d & d \end{bmatrix}, \tag{4.42}$$

or in an equivalent nomenclature:

$$\begin{aligned} u &= \frac{\sqrt{3}}{2} d\, k_1, \\ v &= \frac{d}{2}(-k_1 + 2k_2), \\ V(u,v) &\triangleq V(k_1, k_2), \qquad\qquad k_1, k_2 = 1, ..., N_T. \end{aligned} \tag{4.43}$$

where $N_T = 3N_{EL}+1$ is the total number of elements of the array and N_{EL} is the number of elements per arm.

The missing (u, v) points can be padded with zeros, producing a smoother spectrum. Moreover, the periodic extension of the spectrum is not unique in band-limited 2-D sequences, as the spectral replicas do not need to be necessarily repeated along the u and v axes. Periodicity is given by the $\overline{\overline{N}}$ matrix [22]:

$$\widetilde{V}(\overline{k}) = \widetilde{V}(\overline{k} + \overline{\overline{N}}\,\overline{r}), \tag{4.44}$$

where $\widetilde{V}(\overline{k})$ is the periodic extension of $\widetilde{V}(\overline{k})$, $\overline{\overline{N}}$ is a non-singular integer matrix called the periodicity matrix, and $\overline{r}$ is a vector of integers. The number of samples in a period is given by $\det(\overline{\overline{N}})$.

All visibilities leading to the same (u, v) points are called redundant. For a Y-shaped array the number of non-redundant visibilities is given by:

$$N_V = 6{N_{EL}}^2 + 6N_{EL} + 1, \tag{4.45}$$

and the number of missing samples to be initially padded with zeros is:

$$N_{V^-} = \det\left(\overline{\overline{N}}\right) - N_V, \tag{4.46}$$

which should be minimized by properly choosing the periodicity matrix $\overline{\overline{N}}$. The choice of $\overline{\overline{N}}$ and of the periodic extension scheme is not unique.

A general approach to choose the periodicity matrix $\overline{\overline{N}}$ is given by the Smith normal decomposition [22], which states that any non-singular integer matrix $\overline{\overline{N}}$ can be diagonalized by pre and post multiplication by unimodular integer matrices $\overline{\overline{E}}$ and $\overline{\overline{F}}$:

$$\overline{\overline{N}} = \overline{\overline{E}}\,\overline{\overline{\Lambda}}\,\overline{\overline{F}}, \tag{4.47}$$

$$\det\left(\overline{\overline{E}}\right) = \det\left(\overline{\overline{F}}\right) = 1, \tag{4.48}$$

where $\overline{\overline{\Lambda}}$ is a diagonal matrix that allows any fundamental period over any arbitrary sample grid to be mapped into a rectangular one, allowing rectangular Fast Fourier Transformation (FFT) routines to be used in the reordered indexes (k_1, k_2) and (n_1, n_2):

$$\begin{aligned} T(\overline{n}) &= T(\xi(n_1,n_2),\eta(n_1,n_2)) = \\ &= \frac{1}{|\det\overline{\overline{N}}|}\sum_{\overline{k}}\widetilde{V}(\overline{k})e^{j2\pi\left(\overline{k}^T\overline{\overline{N}}^{-1}\overline{n}\right)} = \\ &= \frac{1}{|\det\overline{\overline{N}}|}\sum_{\overline{k}}\widetilde{V}(\overline{k})e^{j2\pi\left(\left(\overline{k}^T\overline{\overline{F}}^{-1}\right)\overline{\overline{\Lambda}}^{-1}\left(\overline{\overline{E}}^{-1}\overline{n}\right)\right)} = \\ &= \frac{1}{|\det\overline{\overline{N}}|}\sum_{\overline{k}}\widetilde{V}(\overline{k})e^{j2\pi\left(\overline{k'}^T\overline{\overline{\Lambda}}^{-1}\overline{n'}\right)}, \end{aligned} \tag{4.49}$$

where

$$\overline{k'} \triangleq \left(\overline{\overline{F}}^{-1}\right)^T\overline{k}, \tag{4.50}$$

and

$$\overline{n'} \triangleq \overline{\overline{E}}^{-1}\,\overline{n}. \tag{4.51}$$

It can be demonstrated [22] that the periodic extension of Fig. 4.5:

- minimizes the number of samples in the periodic cell;
- minimizes the number of non-measured visibilities that must be initially padded with zeros;
- allows the use of standard rectangular FFT routines;
- avoids the permutation of indexes required by the Smith normal decomposition of Eqns. 4.50 and 4.51.

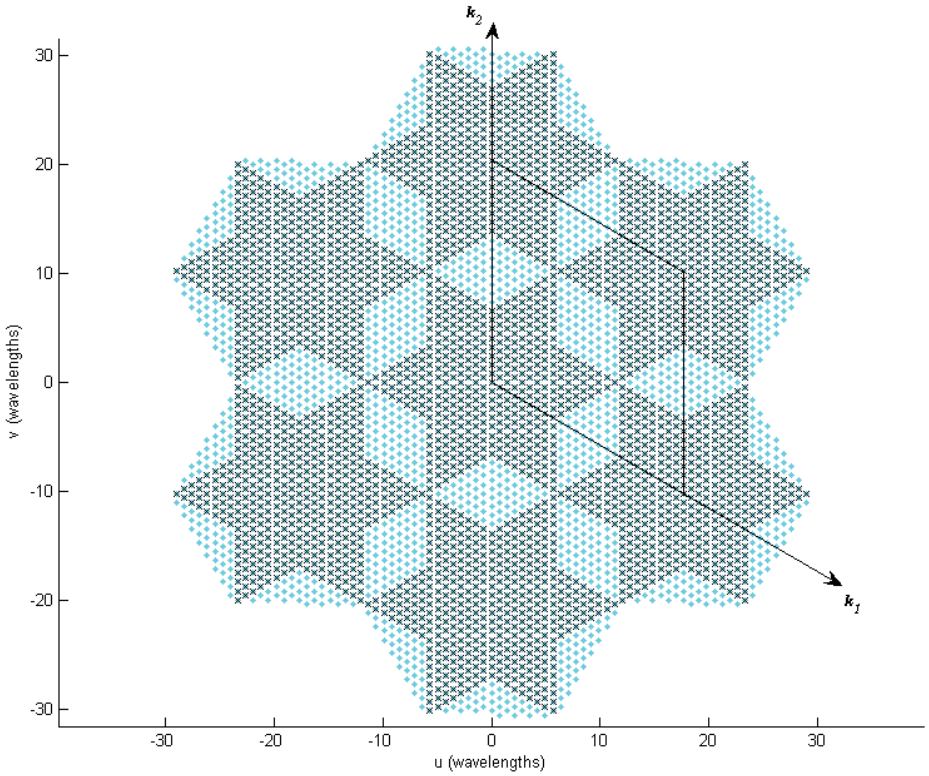

Figure 4.5. Periodic extension of the (u, v) coverage.

The periodicity scheme of Fig. 4.5, where zero-padded points have been added between adjacent periods, is such that:

$$\begin{bmatrix} u' \\ v' \end{bmatrix} = \begin{bmatrix} u \\ v \end{bmatrix} + \overline{\overline{U}} \begin{bmatrix} k_1 \\ k_2 \end{bmatrix}, \tag{4.52}$$

where

$$\overline{\overline{U}} = N_T\, d \begin{bmatrix} 0 & \frac{\sqrt{3}}{2} \\ 1 & -\frac{1}{2} \end{bmatrix}, \tag{4.53}$$

$$\overline{u}_1 = N_T\, d \begin{bmatrix} 0 & 1 \end{bmatrix}^T, \qquad \overline{u}_2 = N_T\, d \begin{bmatrix} \frac{\sqrt{3}}{2} & -\frac{1}{2} \end{bmatrix}^T. \tag{4.54}$$

where $\overline{\overline{U}}$ is a sampling matrix in the (u, v) domain. The $\overline{\overline{U}}$ matrix is not unique, since all the sampling matrices given by:

$$\begin{aligned} \overline{\overline{U}}_1 &= N_T\, d \begin{bmatrix} -\overline{u}_1 & \overline{u}_2 \end{bmatrix}^T, \\ \overline{\overline{U}}_2 &= N_T\, d \begin{bmatrix} \overline{u}_1 & -\overline{u}_2 \end{bmatrix}^T, \\ \overline{\overline{U}}_3 &= N_T\, d \begin{bmatrix} -\overline{u}_1 & -\overline{u}_2 \end{bmatrix}^T, \end{aligned} \tag{4.55}$$

produce the same periodic extension in the (u, v) plane. This choice, however, determines the numbering of the (u, v) and (ξ, η) samples to process them properly. The associated periodicity matrix in the (k_1, k_2) axes is:

$$\overline{\overline{N}} = \begin{bmatrix} N_T & 0 \\ 0 & N_T \end{bmatrix}, \qquad \det\left(\overline{\overline{N}}\right) = {N_T}^2. \tag{4.56}$$

If the sampling points in the (ξ, η) direction cosines are forced to satisfy the relationship

$$\overline{\overline{U}}^T \, \overline{\overline{\Xi}} = \overline{\overline{I}}, \tag{4.57}$$

then:

$$\overline{\overline{\Xi}} = (\overline{\overline{U}})^{-1} = \frac{1}{N_T\, d} \begin{bmatrix} \frac{1}{\sqrt{3}} & \frac{2}{\sqrt{3}} \\ 1 & 0 \end{bmatrix} \triangleq \begin{bmatrix} \overline{\xi}_1 & \overline{\xi}_2 \end{bmatrix}, \tag{4.58}$$

and the Fourier transform kernel becomes separable, even if the (u, v) and (ξ, η) sampling points are not chosen over a rectangular grid. The $[\overline{\xi}_1 \; \overline{\xi}_2]$ indices form the so-called *reciprocal basis* of $[\overline{u}_1 \; \overline{u}_2]$ in the (ξ, η) domain. Hence, the sampled (u, v) and (ξ, η) points are given by:

$$(u, v) = \left(\frac{\sqrt{3}}{2}\, d\, k_1, \;\; \frac{d}{2}(-k_1 + 2k_2) \right), \qquad k_1, k_2 = 0, ..., N_T - 1, \tag{4.59}$$

$$(\xi, \eta) = \left(\frac{1}{\sqrt{3}\, N_T\, d}\, (n_1 + 2n_2), \;\; \frac{1}{N_T\, d} n_1 \right), \qquad n_1, n_2 = 0, ..., N_T - 1. \tag{4.60}$$

Thus, the Inverse Fast Fourier Transformation (IFFT) of the hexagonally sampled $V(u(k_1, k_2), v(k_1, k_2))$ is given by:

$$\begin{aligned} T(n_1, n_2) &= T(\xi(n_1, n_2), \eta(n_1, n_2)) = \\ &= \frac{\sqrt{3}\, d^2}{2} \sum_{n_1=0}^{N_T-1} \sum_{n_2=0}^{N_T-1} V(k_1, k_2) e^{j2\pi[u(k_1,k_2)\xi(n_1,n_2) + v(k_1,k_2)\eta(n_1,n_2)]} \\ &= \frac{\sqrt{3}\, d^2}{2} \sum_{n_1=0}^{N_T-1} \sum_{n_2=0}^{N_T-1} V(k_1, k_2) e^{\frac{2\pi}{N_T}(k_1 n_2 + k_2 n_1)}, \end{aligned} \tag{4.61}$$

Equation 4.61 can be recognized as a standard rectangular FFT with n_1 and n_2 interchanged. The factor $\frac{\sqrt{3}\, d^2}{2}$ is the hexagonal pixel area in the (u, v) domain. The centers of the periodic cells can be found applying the periodicity condition to the argument in the Fourier kernel:

$$\begin{aligned} \frac{2\pi}{N_T}[\overline{u}_1^T(\xi_n, \eta_n) + \overline{u}_2^T(\xi_n, \eta_n)] &= 2\pi \left[\begin{bmatrix} 0 & d \end{bmatrix} (\xi, \eta) + \begin{bmatrix} \frac{\sqrt{3}}{2} & -\frac{d}{2} \end{bmatrix} (\xi, \eta) \right] = 2\pi m, \\ m &= 0, \pm 1, \pm 2, ... \end{aligned} \tag{4.62}$$

whose closest solutions to the origin are:

$$(\xi_n, \eta_n) = \frac{2}{\sqrt{3}d}\left[\ \cos(n\tfrac{\pi}{3}) \quad \sin(n\tfrac{\pi}{3})\ \right], \qquad n = 0, 1, 2, ..., 5. \tag{4.63}$$

If the extension of the modified brightness temperature is the whole unit circle, the (ξ_n, η_n) points must be at distance 2 from the origin to avoid aliasing completely, forcing a maximum antenna spacing of $d \leq \frac{\lambda}{\sqrt{3}}$. Figure 4.6 shows the AF-FOV for a Y-shaped array with equally spaced antennas for $d = \lambda/\sqrt{3}$ and $d = 0.816\lambda$ as in PAU-SA.

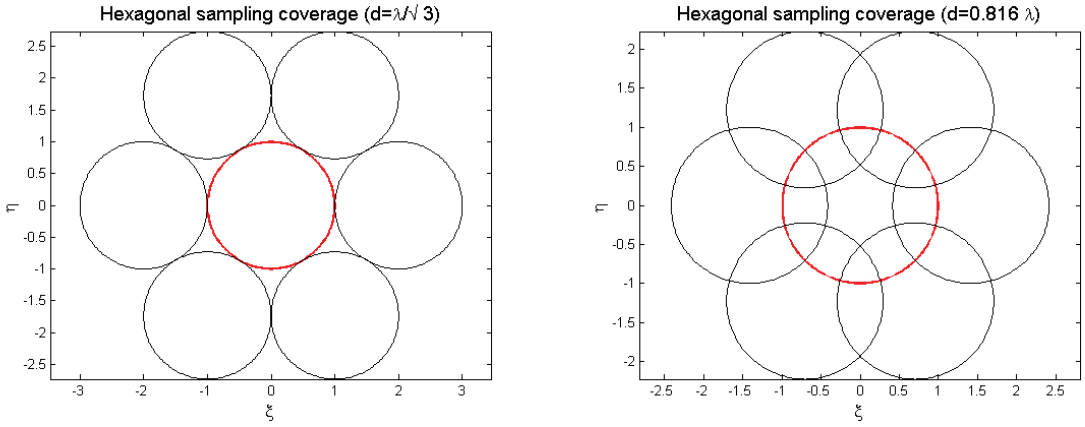

Figure 4.6. Alias-free region for a Y-shape array with (a) $d = \lambda/\sqrt{3}$, and (b) $d = 0.816\lambda$.

4.4.2 Rectangular sampling arrays

The most representative rectangular sampling coverage are: U-shape, T-shape in addition to L-shape [22]. Figures 4.7 and 4.8 show a U-shape and T-shape array configurations and its spatial frequency coverage respectively. In the particular case of U-shape topology

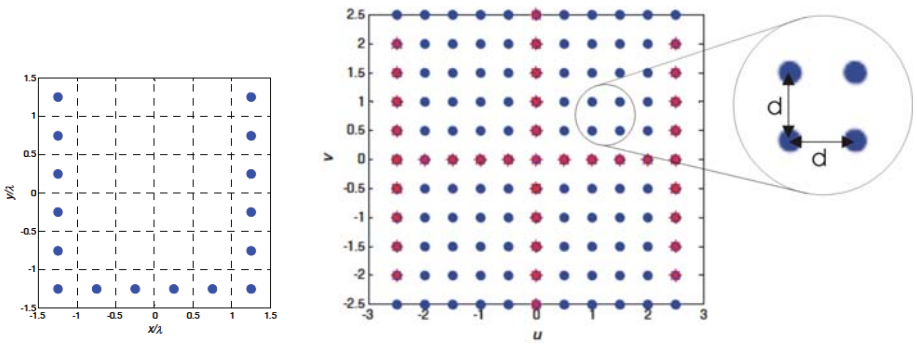

Figure 4.7. (a) U-shape array configuration and (b) U-shape spatial frequency coverage.

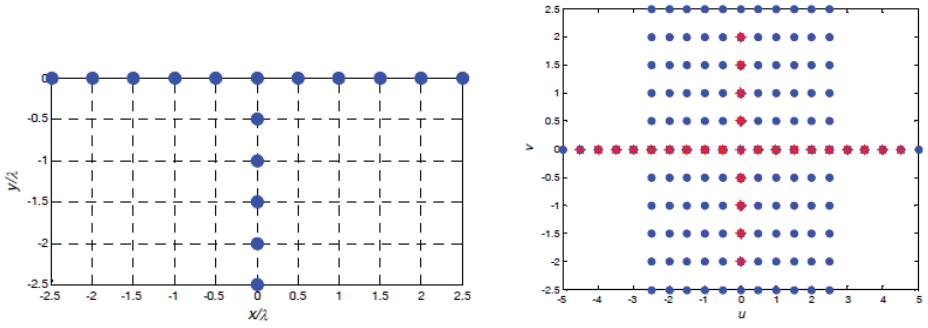

(a) **(b)**

Figure 4.8. T-shape array configuration and (b)T-shape spatial frequency coverage.

Fig. 4.7b, the sample matrix is:

$$U = \begin{bmatrix} d & 0 \\ 0 & d \end{bmatrix}, \tag{4.64}$$

and the resultant rectangular sample:

$$(U^T)^{-1} = \begin{bmatrix} 1/d & 0 \\ 0 & 1/d \end{bmatrix}. \tag{4.65}$$

The whole space maps are composed with by circles. Figure 4.9 presents the case of rectangular sampling, in (blue) the alias located in a rectangular pattern around the true image (in red). Figure 4.9a shows the minimum spacing between adjacent antennas, d to avoid alias. The minimum distance between the true image to the alias is $1/d$, and it should be equal to 2 to avoid an alias replica overlapping with the main image. Therefore, the distance between adjacent antennas must be equal to $d = 0.5\lambda$. Figure 4.9b shows the case of PAU-SA where the value of $d = 0.816\lambda$. Comparing the hexagonal and

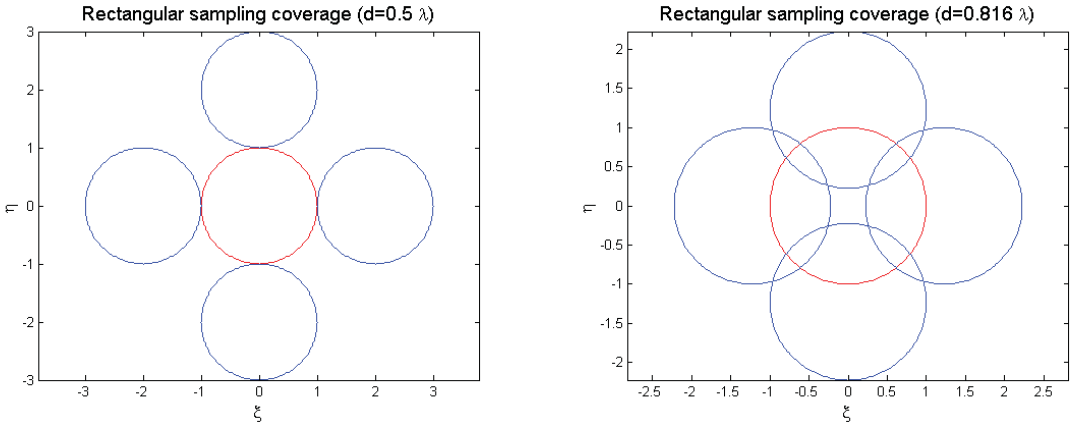

(a) **(b)**

Figure 4.9. Alias-free region for a U-shape array with (a) $d = 0.5\lambda$, and (b) $d = 0.816\lambda$.

rectangular alias-free region for a specific antenna space of $d = 0.816\lambda$, Figs. 4.6b and 4.9b, the rectangular sampling reduces the alias-free region about 13.4 % with respect to the hexagonal sampling.

4.5 Determination of the Alias-Free Field Of View AF-FOV

Once the center of the periodic cells of the alias replicas is determined, the AF-FOV can be computed as:

$$\frac{1}{2}\,\mathrm{AF-FOV} = arcsin\left(\frac{2}{\sqrt{3}d} - 1\right), \tag{4.66}$$

$$\mathrm{AF-FOV} = 2 \cdot \frac{1}{2}\,\mathrm{AF-FOV}. \tag{4.67}$$

Equation. 4.66 can be derived directly from the Fig. 4.10.

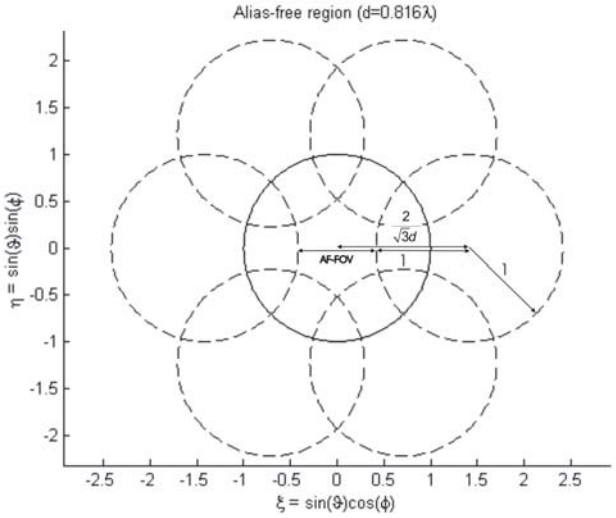

Figure 4.10. Alias-free region for a Y-shaped array with $d = 0.816\lambda$.

4.6 Angular and spatial resolutions

The angular resolution ($\Delta\theta$) of an interferometric radiometer is defined as the capability to measure the angular separation of two point sources that are close together, been inversely proportional to the array size. To achieve an infinite spatial resolution, it would be necessary to use an interferometric radiometer with an infinite number of antennas and therefore, baselines. Obviously, this is impossible in practice, and the array must be designed with a finite size, minimizing the number of baselines to synthesize. This is equivalent to truncating the visibility function. The result is the elimination of abrupt

transitions in the temperature map (smoothing effect) and therefore degrading the angular resolution. Considering an ideal case, and ignoring the constant, filter response, antennas, as well as geometric factors not involved in the angular resolution, in the one-dimensional case we can obtain modifying the limits of the integral according to the variables:

$$V(u) = \int_{-1}^{1} \frac{T(\xi)}{\sqrt{1-\xi^2}} e^{-j2\pi u\xi} d\xi \triangleq \int_{-1}^{1} \overline{T}(\xi) e^{-j2\pi u\xi} d\xi, \tag{4.68}$$

Assuming that the minimum baseline is Δu times the wavelength:

$$\Delta u = \frac{d}{\lambda}, \tag{4.69}$$

where d is the minimum separation between antennas. Therefore, the values of $(V(u))$ are sampled at $u = n\Delta u$ been known this function only in these points.

The finite number of visibility samples, is equivalent to apply a window function to the visibility function, resulting in a maximum length of 2N+1 samples. In the case of rectangular window it results:

$$V_{truncated}(n\Delta u) = V(n\Delta u)W(n\Delta u), \quad \begin{cases} W(n\Delta u) = 1, & \forall |n| \leq N \\ W(n\Delta u) = 0, & \text{rest} \end{cases} \tag{4.70}$$

where $V_{truncated}$ represents the visibility function with a finite number of points and $W(n)$ is the selected windowing type (Table 4.1). In this case, using the rectangular window, the expression obtained for the IFFT determine the temperature is given by

$$\widetilde{T}(\xi) = \sum_{n=N}^{N} V(n) e^{-j2\pi n\Delta u\xi}, \tag{4.71}$$

Substituting Eqn. 4.68 into Eqn. 4.71, Eqn. 4.72 is obtained:

$$\widetilde{T}(\xi) = \sum_{n=-N}^{N} \Big[\int_{-1}^{1} \overline{T}(\xi') e^{-j2\pi u\xi'} d\xi' \Big] e^{j2\pi u\xi}, \tag{4.72}$$

which can be rewritten as:

$$\widetilde{T}(\xi) = \int_{-1}^{1} \overline{T}(\xi') AF(\xi, \xi') d\xi', \tag{4.73}$$

where $AF(\xi, \xi')$ represents the synthesized array factor defined as:

$$AF(\xi, \xi') = \sum_{n=-N}^{N} e^{j2\pi n\Delta u(\xi-\xi')} = \frac{sin[(2N+1)\pi\Delta u(\xi-\xi')]}{sin[\pi\Delta u(\xi-\xi')]}. \tag{4.74}$$

which corresponds to a periodic sinc function. This term is also called the interferometer's "impulse response", since it is the response of a point source. The main difference between a real and a synthetic aperture radiometer is that the first one points the main beam in a single direction being necessary to scan the image pixel by pixel. On the other

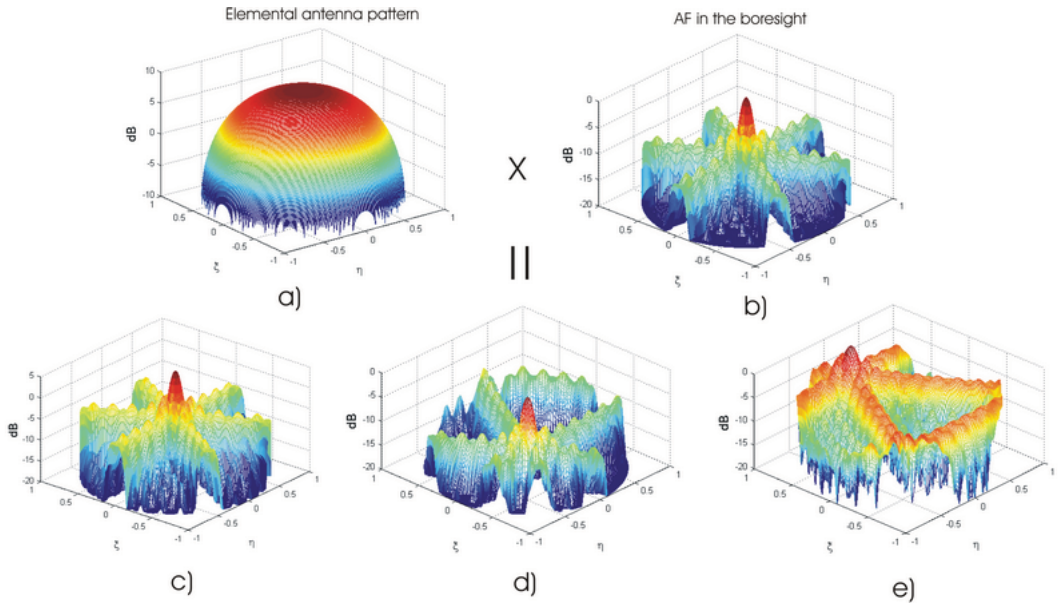

Figure 4.11. Determination of the PAU-SA global array pattern a) Elementary antenna pattern, b) AF in the boresight (rectangular window). Array pattern evaluated at c) ($\xi = 0$, $\eta = 0$), d) ($\xi = 0.4$, $\eta = 0.4$), and e) (ξ = -0.8, η = -0.8).

hand, the second one, recovers a whole image in a single snapshot. By means of a Fourier synthesis process, the Array Factor (AF) or impulse response for all possible directions in the direction cosines are computed at once, and therefore a whole image is acquired in a single snap-shot. The global array pattern is the product of the elementary antenna pattern, weighted by the AF, as shown in Fig. 4.11. The synthesized array factor determines the instrument's angular resolution. This parameter depends on the number of antennas in the arm and the antenna spacing, that is it, on the array size. There are several criteria to define this parameter, depending on the valley to peak ratio of the reconstructed image is a given value or another one. A criterion of -3 dB main beam width is used, since it is the most widely used in antenna theory [65] is given by:

$$\Delta\theta = sin^{-1}\Big[\frac{2\lambda}{\Delta u(2N+1)}\Big] = sin^{-1}\Big[\frac{2\lambda}{\Delta u_{max}}\Big], \tag{4.75}$$

where $\triangle u_{max} = 2\sqrt{3}N_{EL}d$ is the maximum dimension of the synthetic aperture or the distance in the (u, v) complete hexagon plane corresponding twice the distance between the two most separated baselines in the Y-shape array, N_{EL} is the number of antennas per arm without the central one and d is the adjacent antenna spacing in terms of wavelengths. If $\Delta u_{max} \gg 1$, the arcsin can be approximate by its argument and can be written as:

$$\Delta\theta \simeq \frac{2\lambda}{\Delta u_{max}} = \frac{2}{D}. \tag{4.76}$$

where D is the is the maximum dimension of the antenna. In this case, the antenna synthesized with a Y-shape (x, y plane) has a star coverage in the coordinates (u, v), Fig. 4.12. Taken into account that D is the diameter of the antenna, in this case the

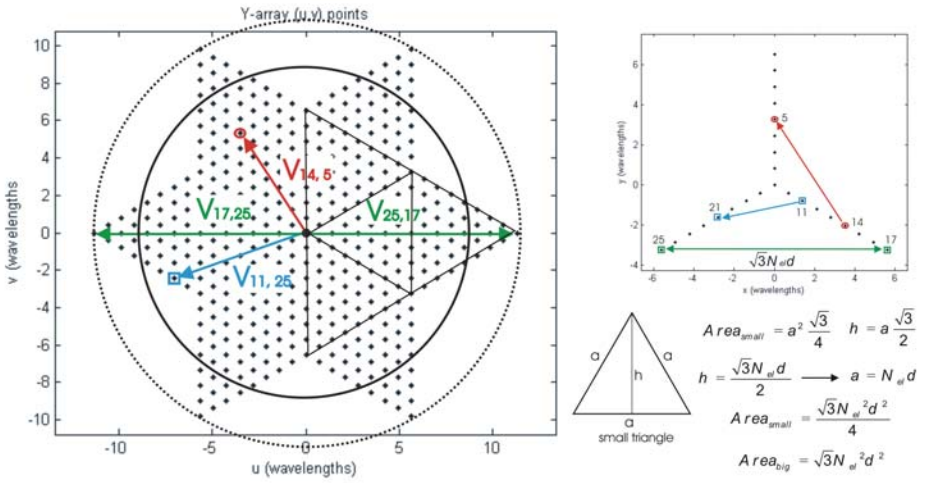

Figure 4.12. Coverage of the synthetic aperture antenna. External circle (ideal case) but non-complete coverage. Internal circle (equivalent) with complete coverage.

external circle is non-completely filled (Fig. 4.12), therefore, it is necessary a conversion factor obtaining a smaller circular antenna with the same (u, v) area as the star area. The angular resolution for a rectangular window can be approximately computed in the direction cosines coordinates as define in [22]:

$$\triangle\xi_{-3dB}^{rect} = \frac{\pi/2}{\triangle u_{max}}, \qquad \epsilon < 10\% \quad if \quad \triangle u_{max} > 15, \tag{4.77}$$

The $\pi/2$ term is the conversion factor found empirically in [22]. This factor relates the area of the external circle (ideal case) with the area of the star.

Computing these terms, a new conversion factor can be found actually, being very similar to the one empirically found.

$$\frac{\text{Area external circle}}{\text{Area star}} = \frac{\pi(\frac{D}{2})^2}{3 \cdot \text{Area}_{\text{big}}} = \frac{\pi 3 N_{EL}^2 d^2}{3\sqrt{3} N_{EL}^2 d^2} = \frac{\pi}{\sqrt{3}}, \tag{4.78}$$

$$\triangle\xi_{-3dB}^{rect} = \frac{\pi/\sqrt{3}}{\triangle u_{max}}, \tag{4.79}$$

It is also possible to reduce the side lobes using other windowing types, (Table 4.1) at the expense of a broadening of the main beam by a factor of:

$$\begin{aligned} \triangle\xi_{-3dB}^{triang} &= 1.24\triangle\xi_{-3dB}^{rect}, \\ \triangle\xi_{-3dB}^{Hamming} &= 1.26\triangle\xi_{-3dB}^{rect}, \\ \triangle\xi_{-3dB}^{Haning} &= 1.33\triangle\xi_{-3dB}^{rect}, \\ \triangle\xi_{-3dB}^{Blackman} &= 1.48\triangle\xi_{-3dB}^{rect}. \end{aligned} \tag{4.80}$$

Finally the spatial resolution(Δx) can be achieved from the angular resolution multiplied by the distance (r) and divided by the inverse of the cosine of the incidence angle as

express in Eqn. 4.81

$$\Delta x = \frac{\Delta\theta \cdot r}{cos\theta_i} \tag{4.81}$$

where r is the distance between the antenna array and the scene of observation, and $\Delta\theta = \Delta\xi$ when the synthetic beam is very narrow.

Table 4.1. Different windowing types [22].

Window Type	Expression
Rectangular	$W(n) = 1$
Tiangular	$W(n) = 1 - \frac{\lvert n \rvert}{N}$
Hanning	$W(n) = cos^2\left(\frac{\pi n}{2N}\right)$
Hamming	$W(n) = 0.54 + 0.46\, cos\left(\frac{\pi n}{N}\right)$
Blackman	$W(n) = 0.42 + 0.5\, cos\left(\frac{\pi n}{N}\right) + 0.08\, cos^2\left(\frac{2\pi n}{N}\right)$

4.7 Number of independent pixels in the AF-FOV

This parameter determines the resolution in 1D of the image. The larger it is, the larger the number of independent point sources that can be distinguished in the AF-FOV. For the same AF-FOV the number of points is inversely proportional with the angular resolution as shown in Eqn. 4.82.

$$\#\quad sources\quad in\quad AF-FOV = \frac{AF-FOV(\xi,\eta)}{\triangle\xi_{-3dB}^{window}}. \tag{4.82}$$

Figure 4.13 shows a example for the case of PAU-SA, with an antenna separation of $d = 0.816\lambda$ $N_{EL} = 8$ and rectangular windows. As it can be noticed, the number of independent sources in the ξ axe is approximately about 10.

4.8 Radiometric imperfections

This section briefly describes the system imperfections and the related errors affecting radiometric resolution. A deep analysis of all system errors and imperfections and a theoretical analysis can be found in [22]. A first error classification is necessary to separate all contributions. Part of these errors can be accurately calibrated, others can be corrected by means of image reconstruction algorithms. Depending on the point in the chain where errors occur, they can be grouped in:

antenna errors, such as gain ripples, antenna coupling and antenna position errors, which require perfectly known scenes to be calibrated or can be ground measured and included in the inversion algorithm. This type of error affects each pixel of the image independently.

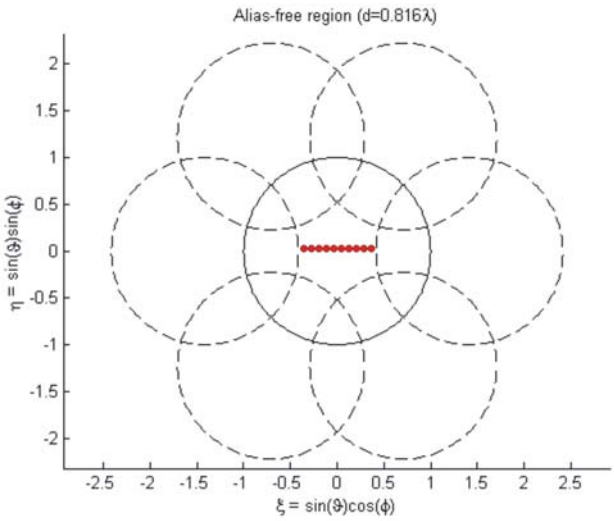

Figure 4.13. PAU-SA's independent pixels in the Alias-free 1D region for a rectangular windows.

channel errors, such as in-phase channel errors, filters phase and time delays. I/Q demodulators quadrature errors also appear in this group but in our case, as demodulators are digital, they can be supposed zero. Channel errors appear as separable factors.

baseline errors, which depend on the pair of antennas/receivers forming the baseline, such as filter response mismatches, channel delay errors appearing in the fringe-wash factor and channel frequency responses. These errors cannot be separated.

Table 4.2 shows a summary of the errors and their correction methods. Quadrature errors and fringe-washing effects are not included in the table, as in the next section demonstrate that they are negligible in PAU-SA. These type of errors can be corrected by internal and external calibrations as shown in Table 4.2. Internal calibrations can by divided in uncorrelated noise source injected at each channel independently through a matched load and correlated noise source injection commonly at two levels (T_{HOT}) and (T_{COLD}) through a noise source and distributed in each channel by a power splitter. External calibration uses known targets. In our case a beacon transmitting a Pseudo-Random Noise (PRN) signal or noise to the center of the array. The second one using the GPS satellites as they are imaged.

In a radiometric system there are three types of errors: radiometric bias, radiometric accuracy and radiometric resolution. For a determined number of snap-shots measuring an absorber with an effective integration time, the spatial average reduces the random errors at each pixel of the brightness temperature image and is the so-called radiometric accuracy map. For this brightness temperature image it is possible to obtain the different radiometric errors.

- The spatial mean value of this brightness temperature minus a reference temperature determines the radiometric bias.

- The rms value of this brightness temperature image determines the radiometric accuracy (assuming infinite integration time). With this method it is possible to eliminate the systematic errors or instrumental errors.

- The spatial standard deviation of this brightness temperature retrieve the radiometric sensitivity or radiometric resolution.

In order to obtain analytically the radiometric resolution, let us assume an instrument with identical antennas and receivers and negligible fringe-wash effects. Equation 4.83 shows the estimated visibility function incorporating the errors in both the real and imaginary part:

$$\widehat{V}(u_n, v_n) = V(u_n, v_n) + \Delta V_r(u_n, v_n) + j\Delta V_i(u_n, v_n), \tag{4.83}$$

where $\widehat{V}(u_n, v_n)$ is the estimated visibility sample, and $V(u_n, v_n)$ the error-free visibility sample. Applying the inverse transform function, it is obtained:

$$\widehat{T}(\xi, \eta) = T(\xi, \eta) + \sum_n W(u_n, v_n)[\Delta V_r(u_n, v_n) + j\Delta V_i(u_n, v_n)]e^{j2\pi(u_n\xi + v_n\eta)}, \tag{4.84}$$

where $T(\xi, \eta)$ is the modified brightness temperature given by Eqn. 4.28, and $W(u_n, v_n)$ is the window used in the image reconstruction process, Table 4.1. As it can be noticed, the visibility function errors propagate to the brightness temperature image. The absolute error can be computed as:

$$\widehat{T}(\xi, \eta) - T(\xi, \eta) = \sum_n W(u_n, v_n)[\Delta V_r(u_n, v_n) + j\Delta V_i(u_n, v_n)]e^{j2\pi(u_n\xi + v_n\eta)}, \tag{4.85}$$

Table 4.2. Errors and calibration methods.

Error type	**Procedure**
Offset errors	Uncorrelated noise + 1/0 unbalance
Non-separable in phase and amplitude errors	Correlated noise injection (centralized)
Separable phase errors	Correlated noise injection (centralized or distributed)
Separable amplitude errors	Correlated noise injection with 2 levels: T_{HOT}/T_{COLD} (centralized or distributed)
Antenna radiation voltage patterns	Anechoic chamber measurements + image reconstruction algorithm
Antenna position errors	Image reconstruction algorithm

and its variance is given by

$$\Delta T_p = E[(\widehat{T}(\xi,\eta) - T(\xi,\eta))(\widehat{T}(\xi,\eta) - T(\xi,\eta))^*]. \tag{4.86}$$

Considering ΔV_r and ΔV_i independent zero-mean random Gaussian variables:

$$\Delta T^2 = \sum_n W^2(u_n, v_n)(E[V_r^2(u_n, v_n)] + E[V_i^2(u_n, v_n)]), \tag{4.87}$$

when the expectation values result developed in [22] are :

$$E\Delta[V_r^2(u_n, v_n)] = \frac{1}{2B_w\tau}[(T'_A + T_{REC})^2 + V_r^2(u_n, v_n) - V_i^2(u_n, v_n)], \tag{4.88}$$

$$E\Delta[V_i^2(u_n, v_n)] = \frac{1}{2B_w\tau}[(T'_A + T_{REC})^2 + V_i^2(u_n, v_n) - V_r^2(u_n, v_n)], \tag{4.89}$$

where T_A is the antenna temperature with losses, and T_{REC} is the receiver noise temperature. Replacing the expectation in Eqn. 4.87, the radiometric resolution can be obtained:

$$\Delta T = \frac{(T'_A + T_{REC})}{\sqrt{B_w\tau}} \sqrt{\sum_n W^2(u_n, v_n)}. \tag{4.90}$$

4.9 Conclusions

The first part of this chapter is devoted to present the principles of operation of interferometric radiometer. An aperture synthesis radiometer measures the correlation between each signal collected by the two spaced antennas or baseline obtaining the visibility function (V) of the brightness temperature under observation (T). The general expression of the visibility function has been presented. For an ideal case, the relationship between $\overline{T}$ and V are related by an inverse Fourier transformation. The determination of the shape array and sample sampling has been presented. In two-dimensional arrays working with band-limited signals, the hexagonal sampling improves the alias-free region about 13.4 % in relation to the rectangular sampling for the same antenna spacing. Both $\triangle$ and Y-arrays are hexagonal sampling arrays, the second one covering a larger number of points in the spatial frequency coverage, and thus obtaining better spatial resolution. Against, Y-shape array form a star coverage in the spatial frequency coverage with missing points in the spatial frequency, whereas a $\triangle$-array covers a complete hexagonal period, simplifying the processing. Moreover other parameters such as: the AF-FOV, the angular resolution ($\Delta\theta$) introducing an alternative definition, the determination of the number of point sources in the AF-FOV, radiometric imperfections etc. have been presented.

Chapter 5

PAU-SA overview

In this chapter a global description of PAU-SA instrument is presented. It is composed of five parts. The first part is devoted to present an overview of the instrument. The second part describes some potential improvements that could be eventually implemented for future MIRAS payloads on SMOS follow-on missions or in other future synthetic aperture radiometer based missions. The third part discusses some instrument parameters such as: frequency of operation, and spatial decorrelation. The fourth part presents an overview of the processing from the correlation matrices coming to the FPGA to the raw visibility function, and the phase and amplitude calibration. The fifth part shows the procedure used for the image reconstruction to understand better the instrument, and finally the PAU-SA's features are presented.

5.1 PAU-SA instrument overview

The purpose of this chapter is to present an overview of the PAU-SA instrument. A detailed description of the hardware instrument is presented in chapter 7. As shown in Fig. 5.1, PAU-SA instrument is composed by a Y-shaped array of 25 antennas array for radiometric applications: 8 antennas per arm plus the one in the center. An additional dummy antenna at the end of each arm is included to improve the antenna pattern similarity. Moreover, at the beginning of the design, the reflectrometer part (PAU-SA-GNSS-R) was going to use the 4 central antennas plus 3 additional ones, (7 antennas in total), to create a steerable array to be able to point to the GNSS signal specular reflection points. Nowadays, this part has been simplified by a single extra antenna plus a GPS receiver front-end and data logger for off-line processing. Each dual-polarization RF front-

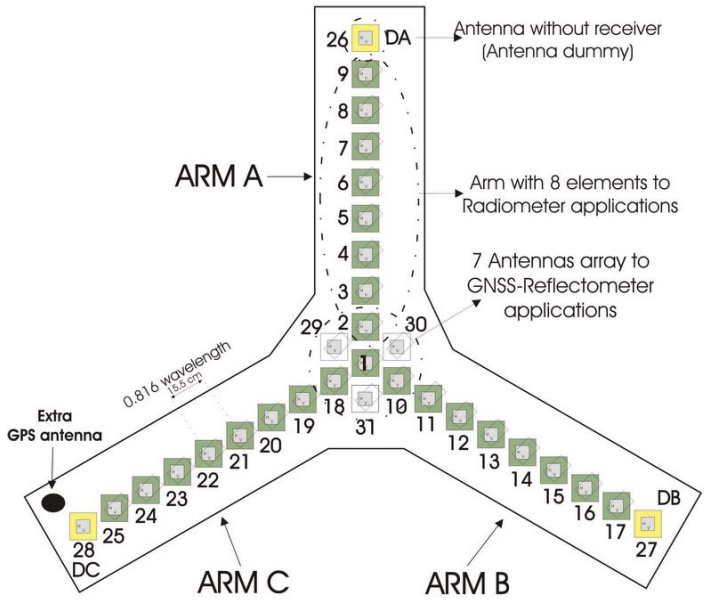

Figure 5.1. Scheme of PAU-SA's array.

end is integrated behind a dual polarization patch antenna. The three main features of this receiver are: simultaneous dual polarization (V & H), frequency of operation (L1 of GPS) the same for both instruments (radiometer, and reflectometer), a three-stage down-converter, and a Local Oscillator (LO) inside each down-converter generated from a 10 MHz reference master clock common to all receivers. In this way, since the LO is generated inside each down-converter, their noise is uncorrelated from receiver to receiver and does not introduce a common correlation offset. Each receiver translates the input signal from 1,575.42 MHz to 4.309 MHz with a gain of approximately 110 dB. The differential IF signal is sent to the ADC unit through a twisted pair (RJ45 grade 5) cable. This signal is digitalized at eight bits using IF sub-sampling techniques. These data enters in a FPGA for digital In-phase and Quadrature (I/Q) down-conversion and digital filtering using 8 bits. Then, all possible correlations between antenna pairs at each polarization are simultaneously performed, using only the sign bit (1 bit). At the same time the 8

bit digitalized signals are squared to compute the signal power, instead of using a power detector diode as in MIRAS. Using digital techniques it is possible to eliminate 3 possible error sources: quadrature errors in the I/Q analog demodulators, thermal drifts in the Power Measurement System (PMS) due to the diodes thermal stability used in analog systems, and quasi-perfect matching of the frequency responses for all receiver's using a digital filter (the only differences are due to the previous analog filters, which are much wider). Once the correlation matrix has been calculated, the data is sent via a Universal Asynchronous Receiver/Transmitter (UART) interface from the FPGA to the internal PC for an off-line post-processing in the external PC. Due to the high volume of data, it is not possible to process it inside the FPGA. The external PC performs three tasks: to undertake the calibration process needed before each acquisition process, to do the off-line post-processing for the image reconstruction and to record the data for off-line post-processing. For calibration purposes, a noise distribution network distributes correlated noise into all receivers at two different noise levels (hot and warm) for phase calibration. Moreover, an uncorrelated load is used inside each receiver for offset estimation.

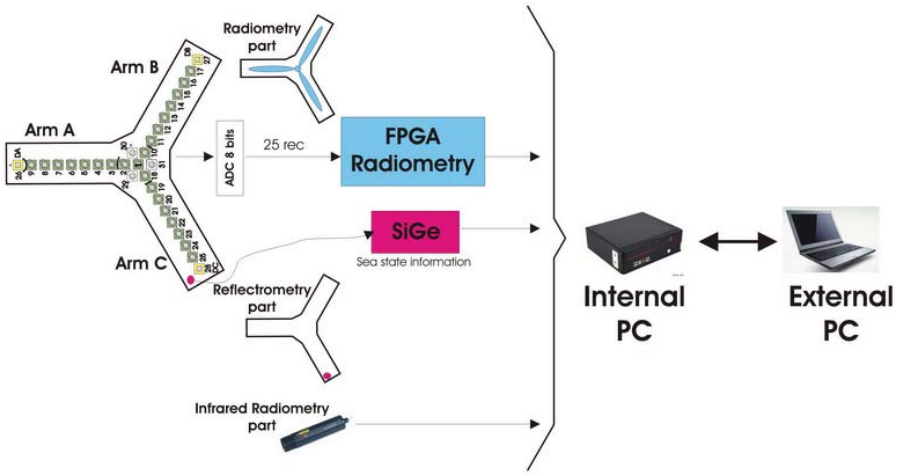

Figure 5.2. Global view of the PAU-SA architecture.

5.2 Comparative table between MIRAS and PAU-SA

In order to detect some possible improvements over the current MIRAS design, Table. 5.1 shows a comparative table between both instruments. One of the main differences between MIRAS and PAU-SA are the altitude and the operation frequency. MIRAS has been designed for global observation from a LEO orbit, with an altitude of 763 km and 3 days revisited time [10]. For convenience, PAU-SA is a ground-based instrument placed in a mobile unit and located in a robotic arm to hold it at eight meters height, with azimuth and elevation movements (Section 7.11). To achieve the best performance, the L-band radiometer should operate in the 1,400-1,427 MHz "reserved" band as in MIRAS. However, PAU-SA is an instrument concept demonstrator, and the GPS reflectometer and the

Table 5.1. Comparative between MIRAS and PAU-SA.

N°	Parameter	MIRAS/SMOS	PAU-SA	Comments
1	Altitude	Global observation, LEO, orbital altitude of 763 km, 3 days equatorial revisit time.	On-ground	
2	Frequency operation	L-band (1,400 – 1,427 MHz) band is protected for passive observations.	L-band (1,575.42 MHz) L1 of GPS signal.	Same frequency for Radiometer and Reflectrometer
3	Bandwidth	19 MHz	2.2 MHz	negligible spatial correlation effects
4	Arm size	4 m	1.3 m	
5	Number of antennas per arm	23	8+1 (dummy)	Additional dummy antenna at the end of each arm to improve antenna pattern inter-similarity
6	Number total antennas	69	31	- 8x3+1=25 for Radiometer. - 3 center plus 3 additional = 7 antennas for Reflectometer. - 3 dummy antenna, 1 at the end of each arm.
7	Antenna type	Patch antenna without dielectric substrate and V & H polarizations (non-simultaneous)	Patch antenna without dielectric substrate and V & H polarizations (simultaneous)	Full-pol (non-sequential)
8	Antenna spacing	0.875 λ at 1,400 MHz, 21 cm wavelength	0.816 λ at 1,575.42 MHz, 19 cm wavelength	Increase the alias-free field of view
9	Receiver type	1 per element	1 per polarization (2 per element)	Full-pol (non-sequential)
10	Topology of the LO down-converter	Distributed LO (groups of 6 elements)	Centralized reference clock + Internal LO generator.	Elimination of correlation offsets
11	Quantization	1 bit IF sampling depending upon the noise uptake level (Inside the LICEF)	8 bit IF sub-sampling using an external ADC	(8 bits) for I/Q conversion and (1 bit) to power measurement
12	I/Q conversion	Analog	Digital	Mass reduction. Elimination quadrature error
13	Frequency response shaped by	Analog RF filter	Digital low- pass filter	Mass reduction, quasi perfect matching, no temperature and frequency drifts
14	Power measurement system (PMS)	Analog, using classical methods (diode)	Digital (FPGA)	Mass reduction, No temperature drifts
15	Digital Correlated Unit	$f_{CLK} = f_{sampling}$	$f_{CLK} >> f_{sampling}$	Allows hardware reuse and compute full-pol correlation matrices in one snapshot inside FPGA
16	Image capabilities	Dual-pol or full-pol (sequential)	Full-pol (non-sequential)	Necessary for GNSS-R applications
17	Integration time	1.2 s	Variable: 4 values 1s, 0.5, 100 ms , 10 ms	
18	Correlated Noise Injection	Distributed (Noise Source)	Centralized (Noise Source, PRNs)	Using PRNs independent number of receivers.

L-band radiometer share the same front-end and frequency band, minimizing the hardware requirements. Although sharing the same front-end provides a significant hardware reduction, this topology introduces some drawbacks. The first drawback concerns to the possible interference that GPS signals can introduce in the radiometric measurements. This non-optimal operation frequency for the radiometer instrument has an impact on the radiometric measurements, introducing some errors. For this reason, this point is analyzed in depth in Section 5.4. The second one concerns the bandwidth. In the case of MIRAS, the bandwidth is limited by the reserved band with a maximum value of 27 MHz and an effective bandwidth of 19 MHz. For the PAU-SA instrument the bandwidth is 2.2 MHz imposed by the IF frequency of the GP2015 chip used and by one of the commercial Surface Acoustic Wave (SAW) filters used for the implementation of the receiver chain. This reduction in the bandwidth has an impact on the radiometric resolution that can only be compensated by increasing the integration time.

Each arm of the MIRAS instrument is approximately three times longer than the PAU-SA ones: 4 m with 23 elements in front of 1.3 m with 8 elements. The total

number of antennas in MIRAS is 69, and in the case of PAU-SA is 25 (radiometer). This decision was taken for two reasons: The first one is due to the use of a part fix arms in order to simplify the mechanical complexity and the second one was pragmatic: were able to take the instrument out of the laboratory, where it was assembled. Since the bandwidth of PAU-SA is narrower than that used in MIRAS and the arm length is smaller, spatial decorrelation effects modeled by the FWF are negligible. This factor is quantified in Section 5.4. One of the innovations in PAU-SA is the incorporation of an additional dummy antenna at the end of each arm to improve the antenna pattern similarity (Section 7.1).

Concerning the antenna type and separation, they are quite similar in both instruments. For instance, both MIRAS and PAU-SA use patch antennas without dielectric substrate for the V- and H-polarizations. For hardware simplicity, MIRAS has non-sequential acquisitions sharing the receiver chain for both polarizations. In the case of PAU-SA, each polarization has its own receiver channel. Therefore, continuous acquisitions at both polarizations can be obtained simultaneously.

In order to increase the AF-FOV, the minimum distance between element spacing is kept to the minimum, only limited by the receiver's size. MIRAS has an antenna spacing of 18.75 cm, corresponding to 0.875 λ at 1,400 MHz. In the case of PAU-SA the antenna spacing is reduced to 15.5 cm = 0.816 λ at 1,575.42 MHz, the GPS L1 signal.

Moreover, the distribution of the LO used in the down-converter states is different in both instruments. MIRAS uses groups of 6 elements in order to feed all receivers, whereas PAU-SA uses a centralized reference clock of 10 MHz, and the LO is generated through the Phase Lock Loop (PLL) inside each receiver to minimize correlated offsets coming from common LO leakage through the down-converter.

The MIRAS'quantification scheme uses 1 bit IF sampling [26] depending upon the noise uptake level inside the Light Cost Effective Front-end (LICEF). PAU-SA uses 8 bits ADC using IF sub-sampling techniques to down-convert and demodulate simultaneously. Using 8 bits, it is possible to estimate inside the FPGA the In-phase and Quadrature components, and perform the power estimation, and using only 1 bit to obtain the three correlation matrices V, H, V/H (complex)

Due to the large number of elements in the instrument, it is advisable to obtain quasi-perfect matching, mass reduction and eliminate temperature and frequency drifts. For this reason, the most important contributions in PAU-SA are focused on the replacement of analog by digital subsystems being the most important:

- I/Q down-conversion, mass reduction, and elimination the quadrature errors.
- Digital filtering, replacing the narrow RF filter by a digital IF filter, to obtain a mass reduction, quasi perfect matching and no thermal and frequency drifts.
- Power estimation, eliminating the classical Schottky diodes, achieving a mass reduction, and eliminating temperature drifts and aging.

All these subsystems and the Digital Correlation Unit (DCU) to compute the full-matrix correlation (V, H and V/H) have been implemented in a FPGA. In this case, the clock frequency is much higher than the sampling one to allow hardware reuse techniques and compute full-polarization matrices in each snapshot.

The imaging capabilities can be dual-pol or full-pol, but sequential for the case of MIRAS, and full-pol non-sequential for PAU-SA. The use of both polarizations simultaneously is necessary to compose the reflected LHCP GPS signal.

The integration time is fixed for MIRAS with a value of 1.2 s and variable for PAU-SA with 4 values: 10 ms, 100 ms, 0.5 s and 1 s for tests purposes.

MIRAS uses a classical correlated noise injection method for calibration proposes. Due to the large number of receivers to feed, it is necessary to use several noise sources distributed along the instrument increasing the hardware complexity and introducing additional noise. This is not a problem if PRN signals are used instead of a centralized noise source for calibration purposes. PAU-SA has the possibility of use both the classical noise-injection method or use this new technique with PRNs. Moreover, since the PRN signals are deterministic and known, new applications are feasible through the correlation of the output signals with a local replica of the PRN signal, leading to the estimation of the receivers' frequency responses and the FWF [66, 67].

5.3 Calibration of correlation radiometers using PRN signals

One of the most important contributions in PAU-SA instrument is the use of pseudo-random signals for calibration purposes. The calibration of correlation radiometers, and particularly aperture synthesis interferometric radiometers, is a critical issue to ensure their performance. Current calibration techniques are based on the measurement of the cross-correlation of receivers' outputs when injecting noise from a common noise source requiring a very stable distribution network. For large interferometric radiometers this centralized noise injection approach is very complex from the point of view of mass, volume and phase/amplitude equalization. Distributed noise injection techniques have been proposed as a feasible alternative, but are unable to correct for the so-called "baseline errors" associated with the particular pair of receivers forming the baseline. In this section it is proposed the use of centralized PRN signals to calibrate correlation radiometers. PRNs are sequences of symbols with a long repetition period that have a flat spectrum over a bandwidth which is determined by the symbol rate. Since their spectrum resembles that of thermal noise, in principle they could be used to calibrate correlation radiometers. At the same time, since these sequences are deterministic, new calibration schemes can be envisaged, such as the correlation of each receiver's output with a baseband local replica of the PRN sequence, as well as new distribution schemes of calibration signals. This section analyzes the general requirements and performance of using PRN sequences for the calibration of microwave correlation radiometers, and chapter 8 particularizes this study with some results using the PAU-SA'receiver.

5.3.1 Background and instrument framework

Synthetic aperture interferometric radiometers have been successfully used in radio-astronomy and more recently, they have been used in Earth observation as well (ESA's SMOS mission). In radio-astronomy, due to the large antenna spacing, calibration is

usually performed taking advantage of mathematical properties of the observables (cross-correlations between pairs of receiver outputs) [68]. However, in Earth observation, due to the wide field of view, the antennas must be closely spaced and have a very wide pattern, which increases mutual coupling effects. In addition, the magnitude of the observables decreases much faster with the antenna spacing, and the signal-to-noise ratio rapidly degrades, preventing the application of Redundant Space Calibration (RSC) or other techniques used in radio-astronomy [68, 69]. MIRAS, the single payload of ESA's SMOS mission [1], is the first synthetic aperture radiometer devoted to Earth observation. Its calibration is based on the injection of distributed noise as an alternative solution to alleviate the mass, volume and phase/amplitude equalization technological problems associated with the injection of centralized noise from a single noise source [70]. A similar approach has been implemented in other instruments, such as the Geostationary Synthetic Thinned Aperture Radiometer (GeoSTAR) [71], and mixed approaches with two-level noise injection plus RSC have been proposed for Geostationary Earth Orbit Atmospheric Sounder (GAS) [72]. Although distributed noise injection overcomes the technical challenges of centralized noise injection, it has also several limitations:

1. only separable errors, those can be assigned to each particular receiver, can be calibrated [73], and

2. the thermal noise introduced by the equalized distribution network itself introduces an error [74, 75] that must be compensated by taking differential measurements acquired with two different noise levels.

Recently, arbitrary waveform generators have been used to generate controlled partially Correlated Noise Calibration Standards (CNCS) [76]. In this section, it is proposed the use of centralized PRN sequences for calibration purposes. PRN signals are periodic signals with very long repetition periods that are used in a variety of applications, such as Code Division Multiple Access (CDMA) communications or GNSS. They have a relatively flat spectrum, resembling that of thermal noise, over a bandwidth determined by the symbol rate. The calibration of microwave correlation radiometers (either aperture synthesis, interferometric, or polarimetric) can benefit from these properties by replacing the noise sources by PRN generators. This approach has several advantages:

- the signal amplitude is constant, which allows higher receivers input power levels than in the case of injecting noise, without the need to allow a margin to avoid signal clipping. This makes the calibration less sensitive to receivers' thermal noise,
- all receivers are driven with the same PRN signal, which allows the calibration of baseline errors as well (baseline calibration refers to all errors associated to the particular pair of receivers forming a baseline, and not just the "separable" error terms that can be associated to each particular receiver),
- 1 bit/2 level digital correlators can be used, the same ones typically used for the noise signals to be measured later on, the signal pattern is deterministic and known, which allows new calibration strategies different from the cross-correlation between receivers' outputs, such as the cross-correlation of receivers' output with an exact replica of the input sequence,
- new approaches to distribute the calibration signal such as:

  - electrical distribution at baseband,
  - optical distribution with a modulation at RF followed by an opto-electrical conversion at each receiver input, or even
  - the generation of the calibration signal at each receiver's input using a reference clock, and
- the PRN source can be turned ON for calibration and OFF during the measurements, without the thermal stabilization problems of noise sources. At the same time the isolation requirements of the input switch are fulfilled and Electro Magnetic Compatibility (EMC) problems minimized.

In principle, other signals covering the whole receivers' bandwidth could be used as well (chirp signals, etc.). However, in these cases the relationship between the measured correlation and the true one depends on the number of bits [77], and to increase the scale of integration of the correlators and reduce the power consumption, the number of bits is usually limited to 1 or 2 at most. This prevents using signals that do not behave as noise, unless the signal-to-noise ratio becomes too low. This section is organized as follows. First, the theoretical background and simulation description are introduced. Then, to validate the working principle, experimental results of the technique applied to PAU instrument [31, 35] are presented. Finally, a summary of the main conclusions of this work are discussed. This innovative technique for calibrating microwave correlation radiometers can be applied as well to other communication systems or phased-arrays where the receiver's frequency response needs to be measured with the system turned on.

5.3.2 Theoretical basis and simulator description

One of the most important phases of the measurement acquisition using a correlation radiometer is the calculation of the so-called FWF [78]. It provides an estimate of the spatial decorrelation of the signals measured by the instrument due to the different paths towards the different antennas. Its phase and amplitude at the origin ($\tau = 0$) are required to calibrate the correlation radiometer. In synthetic aperture interferometric radiometers, the shape of the FWF around $\tau = 0$ is also used in the image reconstruction algorithms to compensate for the spatial decorrelation effects out of boresight. If receivers' frequency responses are exactly the same, the FWF phase is equal to 0^{o}, and its amplitude is equal to 1.

Considering a signal $x(t)$ injected as input to the i-th receiver of a correlation radiometer, the output signal $y_i(t)$ will be a function of the frequency response of the entire receiver itself $H_i(f)$; if the input signal spectrum covers the receiver's bandwidth, it is then possible to retrieve $H_i(f)$ from $x(t)$ and $y_i(t)$.

To avoid error amplification, the spectrum of $x(t)$ must preferably be flat over the whole receiver's band, generally thermal Gaussian noise is used in this kind of applications, but another type of signals that exhibit a flat spectrum over a given bandwidth are the PRNs, widely used in CDMA and GNSS.

The FWF of the baseline formed by channels i and j can be estimated from the normalized cross-correlation ρ_{ij} [79] between the output signals $y_i(t)$ and $y_j(t)$). The correlation is calculated according to Eqn. 5.1, where N is the number of samples, and the result is normalized as shown in Eqn. 5.2:

$$r_{y_i y_j}(m) = \frac{1}{N}\sum_{n=1}^{N} y_i(n) y_j(n-m), \tag{5.1}$$

$$\rho_{ij} \triangleq \frac{r_{y_i y_j}(m)}{|r_{y_i y_j}(m)|_{MAX}}. \tag{5.2}$$

It has to be pointed out that in the usual definition, the FWF is normalized with respect to its value at the origin ($\mathrm{FWF_{ij}(n)} = \rho_{\mathrm{ij}}(\mathrm{n})/\rho_{\mathrm{ij}}(0)$), while in Eqn. 5.2, it is normalized with respect to its maximum value.

Two calibration methods are considered: injecting noise [FWF(noise)], as in Fig. 5.3 with the switch in position 1, and injecting the PRN sequence [FWF(Y1 · Y2)], as in Fig. 5.3 with the switch in position 2. In both cases, several noise sources affect the

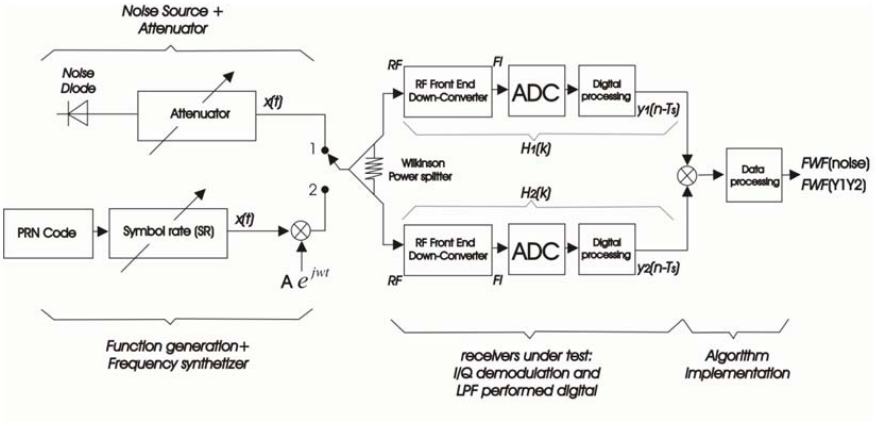

Figure 5.3. Block diagram of the calibration approach. FWF(noise) with the switch in position 1 and FWF(Y1 · Y2) with the switch in position 2.

result of Eqn. 5.1 such as the noise distribution network, the thermal noise present in PRN signal itself, leakages from the local oscillator noise through the mixer etc. All these contributions must be estimated and compensated for by taking differential measurements [75].

To overcome this problem PRN signals can be used to compute the receiver's frequency response before calculating the FWF. The receiver's frequency response is computed from the correlation between a baseband replica of the PRN signal injected [$x(n)$] and the sampled output signals (Fig. 5.4).

Recall that the output signals are represented in complex form by their in-phase and quadrature components as: $y(n) = i(n) + jq(n)$, where $j = \sqrt{-1}$. Being $y_i(n) = h_i(n) * x(n) + n(n)$, where $h_i(n)$ is the discrete impulse response of the i_{th} receiver and $n(n)$ is a random noise term, and expressing the correlation between $x(n)$ and $y_i(n)$ by Eqn. 5.3:

$$r_{xy_i}(m) = \frac{1}{N}\sum_{n=1}^{N} x(n) y_j(n-m). \tag{5.3}$$

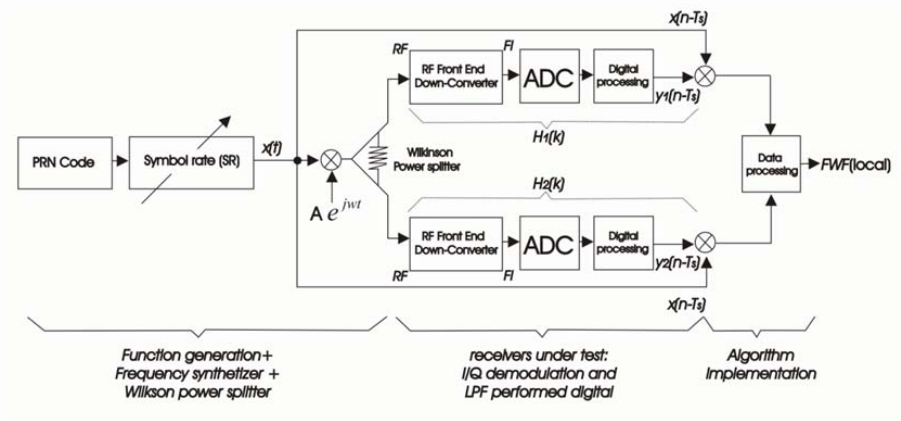

Figure 5.4. Block diagram of the calibration approach FWF(local).

The receiver's frequency response can be calculated computing the DFT of R_{xy_i} :

$$\begin{aligned} R_{xy_i}(k) &\triangleq DFT[r_{xy_i}(m)] = DFT[x(m)]DFT^*[y(m)] \\ &= DFT[PRN(n)]\{DFT^*[PRN(n)]DFT^*[h(n)] + DFT^*[x(n)]DFT^*[h(n)]\} \\ &\triangleq |DFT[PRN]|^2 H_i^*(k). \end{aligned} \tag{5.4}$$

Isolating H_i Eqn. 5.5 is obtained:

$$H_i(k) = \frac{R^*_{xy_i}(k)}{|DFT[PRN]|^2}. \tag{5.5}$$

It has to be noticed that in Eqn. 5.4 the correlation between $x(n)$ and $n(n)$ is zero.

Once the frequency response of the two channels involved $H_i(k)$ and $H_j(k)$ is determined, the FWF can be finally computed from:

$$\Gamma_{ij}(n) \triangleq IDFT[H_i(k)H_j^*(k)], \tag{5.6}$$

$$\rho_{ij} \triangleq \frac{\Gamma_{ij}(n)}{|\Gamma_{ij}(n)|_{MAX}}. \tag{5.7}$$

where IDFT stands for the inverse DFT.

5.4 PAU-SA's considerations

5.4.1 Impact of the frequency operation on the radiometer part

The receiver operating frequency is defined by the L1 signal of the GPS signal (1,575.42 MHz), which is also suitable for SSS estimation. On one hand the GNSS-R works with a spread spectrum signal that, due to the scattering on the sea surface, is at least 23 dB below the thermal noise. For this reason, thanks to the 30.1 dB correlation gain, GNSS-R can detect the GPS signal when the correct Coarse Acquisition (C/A) code is applied. On the other hand, from the radiometer point of view, the noise signal that we want to

detect is at least 23 dB above the GPS signal so the radiometric error induced is minimum, and it only occurs in the directions of specular reflection which are known in advance. Therefore, it is possible that both the radiometer and the reflectometer share the same receiver. Although the spread-spectrum of the GPS modulation is at least 23 dB below the noise level of the radiometric measurements, it has and impact on the radiometer behavior and has to be quantified. The GPS signal includes the P, C/A and M codes. Figure 5.5 shows the auto-correlation of these codes. The first one is the P code, it has

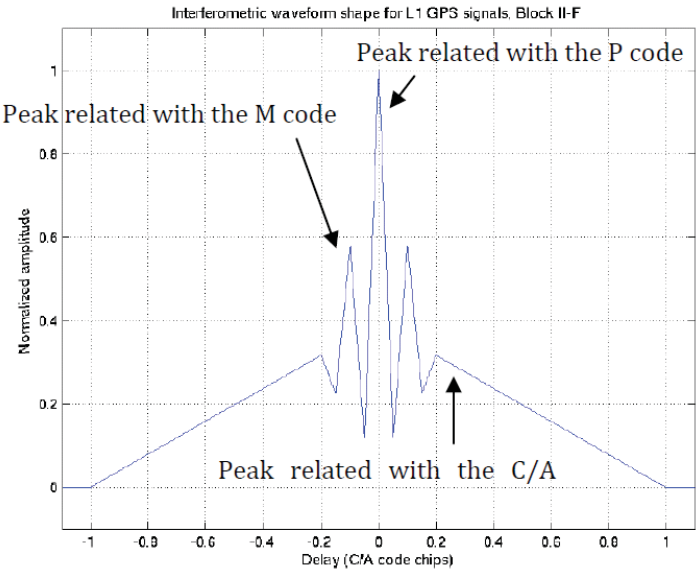

Figure 5.5. Auto-correlation of the P, M and C/A codes.

the largest repetition period of 6.1871×10^{12} bits long (6,187,100,000,000 bits, $\backsim$ 773.39 Gigabytes) it only repeats once a week, achieves a $\backsim$ 75 dB compression gain spread over 22 MHz band, and a power density of about -173 dBW/m^2 using linear polarization antenna). The C/A code has a period of 1023 bits every ms, -30 dB of compression gain spread 2.2 MHz and a density power of about -163 dBW/m^2. And the M code is still experimental and in addition to it distributes its power at the edges of the band, having less effect even than the P code. From the point of view of radiometric measurements, the correlation gain does not have any effect, only the power density associated at each code. For this reason the GPS signal to be into account is the C/A code, been 10 dB higher the P code. To measure the impact of the GPS signal in the PAU-SA's radiometric measurements, the PAU-SA's antenna pattern presented in the previous chapter has been analyzed in two extreme cases: The worst case is when the specular reflection point is at the antenna's boresight, (maximum directivity in the antenna diagram pattern of 46.5 dB), and the best situation comes from if the interference is in the edge of the AF-FOV (minimum directivity in the diagram antenna pattern of 45.5 dB), only 1 dB below the maximum. Figure 5.6 shows the contribution of the GPS signal (C/A code) to the radiometric measurements ΔT considering a sea surface reflection coefficient of $\Gamma = 0.7$ and the PAU-SA system parameters. As it can be noticed, independently of where the interference comes from, the GPS signal has a high contribution in the radiometric

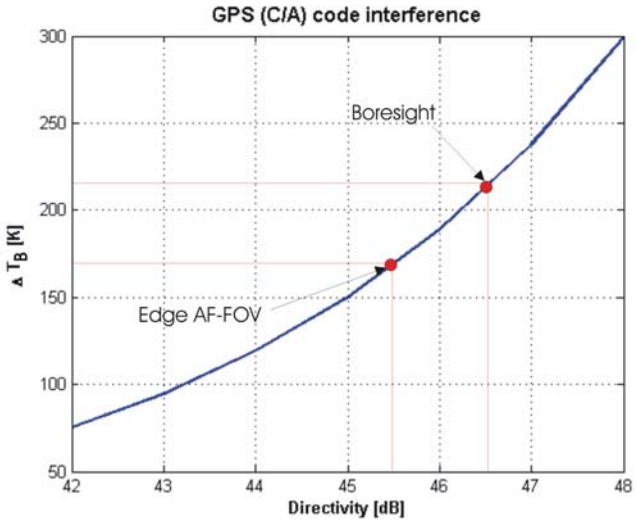

Figure 5.6. ΔT contribution due to GPS C/A code in the PAU-SA's radiometric part in function of the antenna pattern directivity or the GPS position.

measurements (between 220 K and 170 K respectively). However, in the PAU's real aperture version [38], this situation is favorable due to it has a Side Lobe Level (SLL) at least of 20-25 dB and can be electronically steered to avoid the interference. In the case of PAU-SA, to perform radiometric measurements it should be pointed to the North where there are no GPS satellites due to their orbital plane distribution. Moreover, if a GPS satellite is interfering in radiometric measurements, it will appear as a point source in the retrieved image, which could be subtracted by measuring at different time, locating the satellites interference and eliminating them.

5.4.2 Impact of the spatial decorrelation effects in the visibility function

The Fringe-Wash Function FWF indicates the spatial decorrelation of the signals coming from a given direction at a given baseline. Precisely, the FWF is related to the difference between the frequency responses of the receivers forming the baseline.

The amplitude of the FWF can be modeled around the origin by means of a sinc function as:

$$|G_{kj}(\tau)| \approx A \cdot sinc(B \cdot (\tau - C)). \tag{5.8}$$

where $A \cdot sinc(B \cdot C)$ is the amplitude at $\tau = 0$, B is the noise bandwidth, and C is the value of τ in which the fringe-washing function is maximum. The value of τ depends on the direction of the pixel in the scene (ξ, η), the baseline (u, v), and the center frequency (f_0), in our case $f_0 = 1{,}575.42$ MHz

$$\tau = -\frac{u\xi + v\eta}{f_0}. \tag{5.9}$$

The maximum value is found to the largest increment at the baseline level Δu_{max} and the distance between the boresight and the point farthest away in the AF-FOV, $|(\xi, \eta)|_{max}$

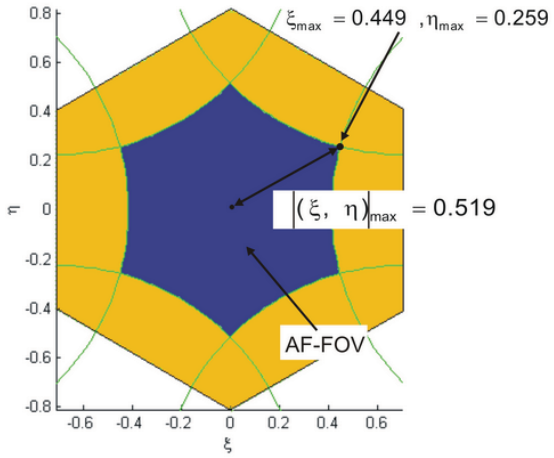

Figure 5.7. PAU-SA's AF-FOV showing the maximum distance in the plane (ξ, η).

= 0.519, (Fig. 5.7). The maximum antenna separation is given by

$$\Delta u_{max} = 2\sqrt{3} N_{EL} d. \tag{5.10}$$

where N_{EL} is the number of antennas in each arm and d is the distance between adjacent antennas. In the case of PAU-SA $N_{EL} = 8$, $d = 0.816\ \lambda$, and this value results in Δu_{max} = 22.61 λ.

The FWF is shown in, Fig. 5.8. As it can be noticed, the FWF in the evaluated range is very close to one, so that this parameter is negligible in the PAU-SA system. Figure 5.9 shows a comparison between the FWF of MIRAS and PAU-SA systems. In this case, since the bandwidth in MIRAS is about 10 times larger than PAU-SA, and the

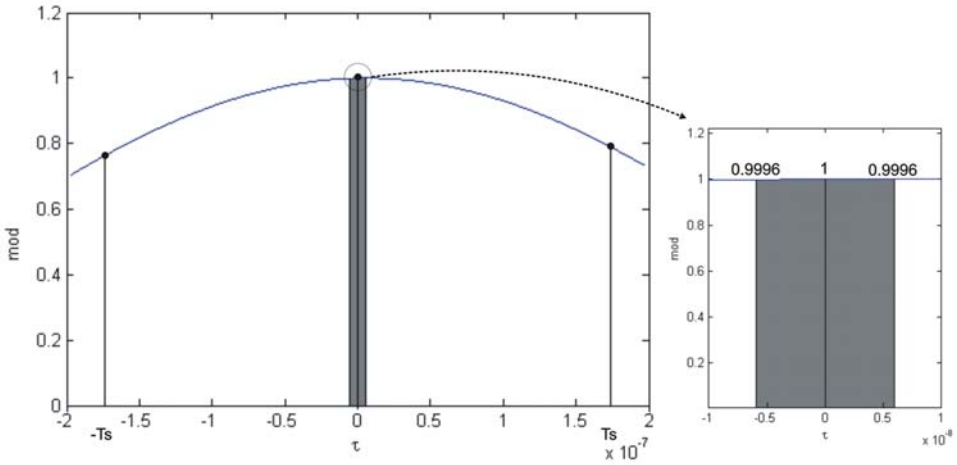

Figure 5.8. PAU-SA's FWF evaluated in the AF-FOV range showing that FWF effect are totally negligible.

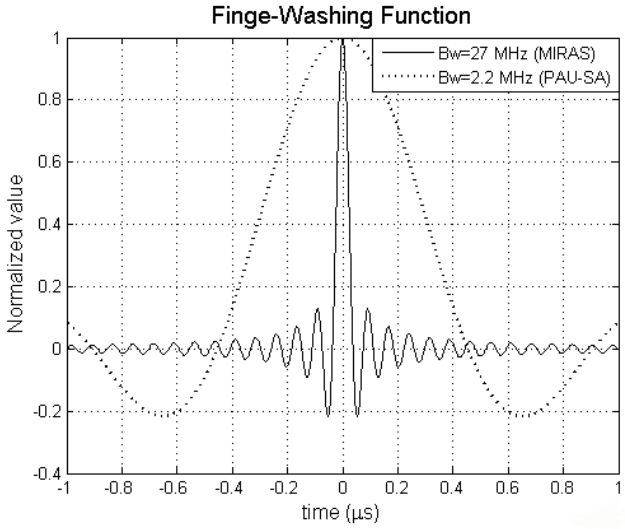

Figure 5.9. FWF comparison between MIRAS and PAU-SA instruments.

array size is approximately 3 times larger than PAU-SA, the FWF is ∼30 times narrower in MIRAS than in PAU-SA.

5.5 PAU-SA's processing implementation

As it explained in Section 5.1, when the electric fields arrive at each antenna, the induced signals are down-converted from RF to IF. Before the correlation matrices and the power measurements are calculated, the signals are digitalized using 8 bits with IF sub-sampling, and enter into the FPGA. Then, the I/Q components are extracted from the signal and low-pass filtered using 8 bits. Afterwards, the DCU computes all possible correlations between antennas pairs in each polarization by counting the number of samples with the same sign (1 bit), obtaining the so-called correlation counts matrices. Figure 5.10 shows a single polarization correlation count matrix structure: the upper triangular part of the matrix contains the I/I correlations between pairs of signals, the lower triangular part contains the I/Q correlations. The diagonal contains the correlations of I and Q components of the signals from the same antenna thus, because of the digital I/Q demodulation, there are no quadrature errors and the diagonal is always zero. This 25 × 25 matrix is then completed adding a right column containing the in-phase component correlated with 0's (I/0) and a bottom row with the quadrature component correlated with 0's (Q/0) (both for calibration purposes). These values are used to compensate for threshold errors in the comparators. The total number of samples $N_{c_{max}}$ is added in the right bottom element, which is used to normalize the whole N_c matrix. It can be observed that the number of correlation counts is an integer, with respect the equation : $0 < N_c < N_{c_{max}}$. Recalling that the sampling frequency (f_m) is 5.745 MHz, and that the maximum integration time (T_{int}) is 1 s, then the maximum number of counts or samples ($N_{c_{max}}$) is:

$$N_{c_{max}} = f_m \cdot T_{int} = 5.745 \quad \text{Ms.} \tag{5.11}$$

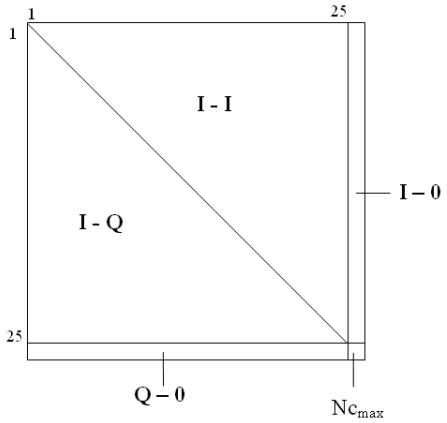

Figure 5.10. PAU-SA's correlation count matrix.

Finally, these matrices and the power measurements are sent to an external PC in real time, where calibration and the image reconstruction algorithms are implemented to retrieve the brightness temperature image.

The first step consists of computing the correlation (c) by normalizing the correlation count matrix to the maximum number of possible samples ($N_{c_{max}}$), at each polarization (V, H and V/H):

$$c_{m,n} = \frac{N_{c\,m,n}}{N_{c_{max}}}. \tag{5.12}$$

where the m and n indicate the corresponding receiver. Once c is computed, it is necessary to compensate the offset introduced in the measurements by the up-counters and apply a scaling factor to obtain the digital correlation (Z):

$$Z_{m,n} = A(c_{m,n} - \text{offset}_{m,n}). \tag{5.13}$$

The digital correlation is a real number, for which it can be assumed the following value $0 < Z < 1$. On one hand, when two signals are uncorrelated, the correlation $c = 0.5$ and $Z = 0$, and the other hand, when two signals are correlated, the correlation $c = 1$ and $Z = 1$, therefore, is

$$Z_{m,n} = 2\left(c_{m,n} - \frac{1}{2}\right). \tag{5.14}$$

The normalized correlation (μ) between two Gaussian signals sampled with 1bit (2 levels) is related to the digital correlation with the following expression :

$$\mu_{m,n} = \sin\left(\frac{\pi}{2} Z_{m,n}\right), \tag{5.15}$$

However, this relationship is only valid for ADCs having zero offset (ideal case). Taking into account the samples threshold, to correct the correlation offset, the normalized correlation μ is calculated with a non-linear relationship using an iterative method (fixed point iteration or Newton-Raphson) [80, 81] using Eqn. 5.15 as initial solution [81].

$$\mu_{m,n} = \sin\left(\frac{\pi}{2}\left(Z_{m,n} + \frac{2}{\sqrt{1-\mu_{m,n}^2}}\left(\mu_{m,n}X_{01}^2 + \mu_{m,n}Y_{01}^2 - 2X_{01}Y_{01}\right)\right)\right). \tag{5.16}$$

The objective of the method is to take into account the errors through the coefficient X_{01} and Y_{01}. Every element of the correlation matrix μ is iterated until the convergence condition is satisfied:

$$|\mu_{m,n}^{p+1} - \mu_{m,n}^{p}| \leq 10^{-6}, \tag{5.17}$$

where p and $p+1$ are the iteration numbers of the two compared values.

The correlation is computed between each antenna pair. In order to compute the errors, X_{01} is calculated from the first element of the pair, whilst Y_{01} is calculated from the second one. As the correlation matrix is divided into two parts: $I-I$ and $I-Q$ (above and below the diagonal), the matrix is correlated in a different way. For the upper diagonal part $(I-I)$ the last column (26^{th} column that is $I-0$) is taken into account in order to calculate the X_{01} and Y_{01}. For the lower diagonal part the last raw is considered (26^{th} raw that is $Q-0$).

The correlations with all "ones" are not necessary, because the number of counts is known. Therefore it is possible to express one of two variables as a function of the other one:

$$Z_0 = N_{c_{max}} - Z_1, \tag{5.18}$$
$$Z_1 = N_{c_{max}} - Z_0, \tag{5.19}$$

where $N_{c_{max}}$ is the total number of counts. The equation of X_{01} and Y_{01} can be represented in the same way as:

$$\begin{aligned} X_{01}, Y_{01} &= \frac{1}{4}(Z_0 - Z_1), \\ &= \frac{1}{4}(N_{c_{max}} - 2Z_1), \\ &= \frac{1}{4}(2Z_0 - N_{c_{max}}). \end{aligned} \tag{5.20}$$

After the fixed point iteration, the new normalized correlation matrices are reorganized to compute the 25×25 visibility matrices. The upper and bottom parts of the diagonal are filled up with respect to the equation:

$$\mu_{m,n} = \mu_{m,n}^{ii} + j\mu_{m,n}^{iq}\,, \tag{5.21}$$

where the subscripts stand for the correlation between two in-phase ii and quadrature - phase iq contributions. This relationship can be also be expressed as:

$$\mu_{m,n} = \frac{1}{\sqrt{T_{SYS_m} T_{SYS_n}}} \left(\Re e\left[\widetilde{r}_{m,n}^{ii}(0)\widehat{V}_{m,n}\right] + j\Im m\left[\widetilde{r}_{m,n}^{iq}(0)\widehat{V}_{m,n}\right] \right), \tag{5.22}$$

where $\Re e$ and $\Im m$ are the real and imaginary part respectively, and $\widetilde{r}_{m,n}^{ii}(0)$ and $\widetilde{r}_{m,n}^{iq}(0)$ are the Fringe washing functions at the origin for the corresponding pair of filters indicated by the sub-superscripts and the system temperatures of the denominator are given by Eqn. 3.40.

$\widehat{V}_{m,n}$ represents the corrected visibility: the m receiver at p-polarization and the n receiver at q-polarization which, assuming that both receivers are at the same physical

temperature T_{ph}, it is given by:

$$\begin{aligned}\widehat{V}_{m,n}^{pq} &= \iint_{\xi^2+\eta^2\leq 1} \frac{T_B^{pq}(\xi,\eta)}{\sqrt{1-\xi^2-\eta^2}} \cdot \frac{F_m(\xi,\eta)}{\sqrt{\Omega_m}} \frac{F_n(\xi,\eta)}{\sqrt{\Omega}_{\mathrm{n}}} \\ &\cdot \bar{\bar{r}}_{m,n}\left(-\frac{u_{m,n}\xi + v_{m,n}\eta}{f_0} \right) e^{-j2\pi(u_{m,n}\xi+v_{m,n}\eta)} d\xi d\eta \,, \end{aligned} \tag{5.23}$$

where the over bar in the FWF means a normalization to unity at the origin, that is:

$$\bar{\bar{r}}_{m,n}(t) = \frac{\widetilde{r}_{m,n}^{\alpha\beta}(t)}{\widetilde{r}_{m,n}^{\alpha\beta}(0)}, \tag{5.24}$$

which assumes to be the same for all superscript combinations. Once the normalized correlations μ have been calculated for every polarization, they are arranged into 25 $\times$ 25 visibilities matrices. Then thenormalized visibility function can be derived from Eqn. 5.25.

$$V_{m,n} = (\mu_{m,n} + j\mu_{m,n}) \cdot \sqrt{T_{SYS_m} T_{SYS_n}}, \tag{5.25}$$

and because the Hermitian property:

$$V_{m,n}^{*} = (\mu_{m,n} - j\mu_{m,n}) \cdot \sqrt{T_{SYS_m} T_{SYS_n}}. \tag{5.26}$$

Therefore, they keep the same antenna numbering/ordering of the correlation matrices. Finally, the visibility samples must be corrected with the phase and amplitude calibration:

$$\hat{V}_{mn} = (\mu_{mn} + j\mu_{nm}) \cdot \underbrace{\underbrace{\underbrace{\sqrt{T_{SYS_m} T_{SYS_n}}}_{\text{Denormalization}} \frac{1}{g_{mn}}}_{\text{Amplitude calibration}} \underbrace{e^{j\alpha_{mn}}}_{\text{Phase calibration}}}. \tag{5.27}$$

Afterwards these visibility samples must be ordered and assigned to the (u, v) points in order to apply the image reconstruction algorithms either an IFFT or the G-matrix (Section 4.3).

5.5.1 Instrument calibration

Periodic and accurate instrument calibration is crucial to obtain meaningful measurements. In systems as complex as an interferometric radiometer, this becomes even more important, since even small residual phase errors produce a noticeable image blurring. In this section it is explained how PAU-SA is calibrated. Despite many of the ideas are inherited from the core calibration of MIRAS on SMOS, new techniques have been implemented, and tested such as the injection of PRN signals, or new ways to perform the absolute amplitude calibration by imaging the GPS satellites, or new ways to measure the Flat Target Response, in the presence of the GPS satellites.

Before computing the visibility function, it is necessary to perform a denormalization and correction. To denormalize the visibility function (Eqn. 5.22), it is necessary to compute the system's temperature at the receivers input for both polarizations (H and V).

This temperature is calculated from the PMS in each receiver. Another parameter that affects the system temperature is the residual offset that must be corrected by means of the uncorrelated noise. The procedure consists of injecting uncorrelated noise, and computing the digital correlation, estimating directly the offset difference, and compensating the normalized correlation to obtain the corrected μ.

5.5.1.1 System temperature

Each PAU-SA element alone is itself of alone is a total power radiometer. A total power radiometer is structured as shown in Fig. 5.11. The power coming from the antenna is

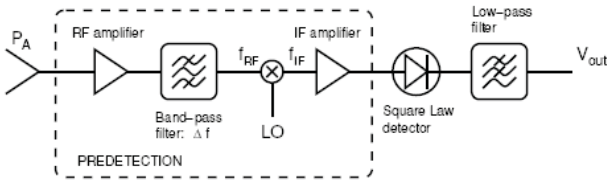

Figure 5.11. Block diagram of a total power radiometer.

calculated as:

$$P_A = k_B T_A B, \tag{5.28}$$

where k_B is the Boltzmann's constant, B the bandwidth, and T_A is the antenna temperature. Ideally the antenna ohmic efficiency $\eta_\Omega = 1$, but in the real case the power depends on η_Ω as well. Hence, the relationship becomes:

$$P_2 = k_B \Big[T_A \eta_\Omega + T_{ph}(1 - \eta_\Omega) \Big] B, \tag{5.29}$$

where T_{ph} is the physical temperature.

The gain factor (G) and the noise temperature (T_{REC}) of the receiver contributes to calculate the power:

$$P_3 = k_B G \Big[T_A \eta_\Omega + T_{ph}(1 - \eta_\Omega) + T_{REC} \Big] B, \tag{5.30}$$

where the power is estimated digitally by means of the FPGA using 8 bits. However in this case, it is obtained by the signal of each antenna as:

$$PMS = \frac{2}{N} \sum_{n=1}^{N} (I\_Squnat)^2. \tag{5.31}$$

where N is the total number of samples, I_Squnat is the in-phase quantified signal. Due to the in-phase and quadrature signals carry the same information, the power is evaluated as twice the power of the in-phase component only. To calibrate the PAU-SA instrument it is necessary to measure some known parameters, as the sky and an absorbent surface. The power expression to calculate the parameters must be expressed in the following way:

$$P = aT_A + b, \tag{5.32}$$

where a and b are two parameters. The a is assumed almost constant since it is computed numerically; and the b is the parameter that will be calibrated with the physical temperature variations. This method is used to calibrate a total power radiometer, beginning from two known values of temperature: the hot and the cold, as it is shown in the Figure 5.12.

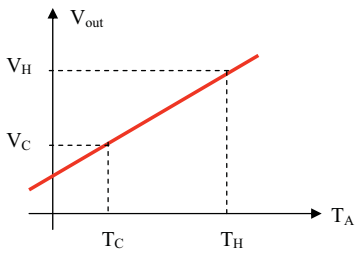

Figure 5.12. Calibration of a TPR, knowing two temperature of reference: hot and cold.

Equating the 5.30 with the Eqn. 5.32 two equations are obtained:

$$a = A \cdot \eta_\Omega, \tag{5.33}$$
$$b = A \cdot [T_{ph}(1-\eta_\Omega)] + A \cdot T_{REC} + offset. \tag{5.34}$$

where A is a constant equal to $A = k_B GB$. The a and b values are computed observing the sky (cold source) with a temperature of $T_{cold} \simeq 6$ K and an absorber surface (hot source), with temperature $T_{hot} = 293$ K. Measuring the two reference temperature (T_{hot} and T_{cold}), the two parameters a and b can be estimated. At the moment, many variables are unknown, as the A, the receiver noise temperature T_{REC}, and the ohmic efficiency η_Ω. To solve this problem correlated noise is injected, obtaining the following system:

$$\begin{cases} a = A \cdot \eta_\Omega, \\ b = A \cdot [T_{ph}(1-\eta_\Omega) + A \cdot T_{REC}] + offset, \\ P_{noise1} = A \cdot (T_{noise1} + T_{REC}) + offset, \\ P_{noise2} = A \cdot (T_{noise2} + T_{REC}) + offset. \end{cases} \tag{5.35}$$

This system of equations has three unknowns and four equations, been possible to resolved by means of the least squares method.

5.5.1.2 Phase calibration

Before explaining the PAU-SA's phase calibration method or Multiple Baseline Calibration MBC method, it is necessary to differentiate between two phase error terms:

1. Systematic phase error terms, originated by physical or constant paths such as cable length or the power splitter parameters. This term should be measured only the first time, and

2. Random phase error terms, generated at each receiver due to the initial phase to which the PLL has locked. This term changes with time since the system is turned on and depends of the physical temperature, so periodic calibration is required.

Internal reference signals are used to estimate the random phase errors. Internal calibration in PAU-SA can be performed either as in MIRAS/SMOS [82, 83] by injecting two levels of correlated noise, or in a novel way by injecting a Pseudo-Random Noise PRN signal to all receivers [67], which allows to correct for separable (can be assigned to each particular receiver) and non-separable errors (can only be assigned to the baseline formed by a pair of receivers) [73], is very robust in front of the noise introduced by the distribution network itself [74, 75], and allows to estimate and diagnose each receivers' frequency response individually.

The phase calibration in synthetic aperture radiometers is critical since it determines the blurring in the final reconstructed image, is therefore of vital importance to determine this parameter as accurately as possible.

The visibility matrix is composed by complex numbers. Each element is the cross-correlation between two receivers, and consequently the phase to be calibrated is the difference between the two the phases of the receivers involved. When the instrument is turned on, each receiver is initialized with a random phase and considering the other phase contributions constant (e.g. the path antenna-receiver or the path noise source-receiver), the main contribution is given by the receiver.

To estimate the receiver's phase, the internal noise injection method allows to calculate the phase difference between the correlated from the noise source to the end of the chains. Once the two noise levels are injected, in order to eliminate the contribution to the correlation of the noise distribution network, mismatches etc, the phase is calculated as the difference of the correlations at the two levels. As the injected noise and the S-parameters attenuation are known, it is in principle possible to estimate the phase error that affects the network and the receiver, and calibrate the visibility function as shown in Eqn. 5.38. The receivers' phases are then calculated taking as a reference the first receiver, that for simplicity is assumed to have a 0º phase. Figure 5.13 shows an example

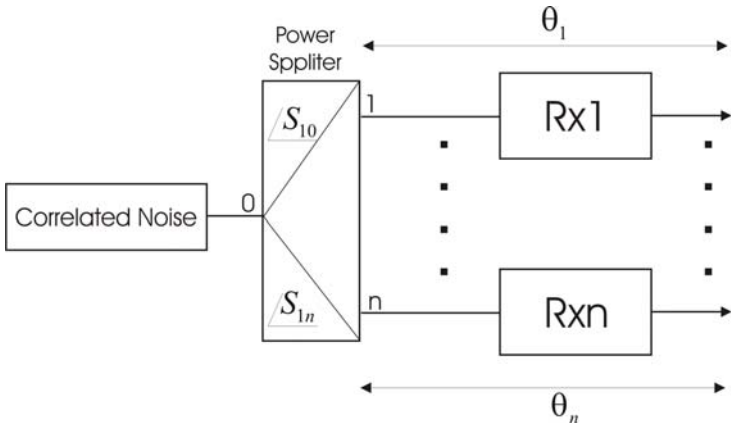

Figure 5.13. Phase calibration between two receivers.

of correlation between two receivers. The phase of the first chain and the n^{th} chain are done respectively by:

$$\angle\varphi_{chain_1} = \angle S_{10} + \theta_1, \tag{5.36}$$

$$\angle\varphi_{chain_n} = \angle S_{n0} + \theta_n. \tag{5.37}$$

The visibility phase, calculated between these two elements when correlated noise is injected, is equal to:

$$\angle V_{1n} = \angle S_{10} + \theta_1 - (\angle S_{n0} + \theta_n) = (\angle S_{10} - \angle S_{n0}) + (\theta_1 - \theta_n), \tag{5.38}$$

since the phase of the first receiver is taken as a reference (0^o), and the other parameters are known, it is been possible to compute the phase of any receiver. Each element of the visibility matrix, computed with the signal coming from the antenna, is compensated with the difference of the two phase receivers of the antenna taking into account, as it is explained in Eqn. 5.39. Hence, the visibility phase at the antenna reference plane, can be corrected as:

$$\angle V_{1n}^{cal} = \angle V_{1n}^{ant} + \theta_1 - \theta_n. \tag{5.39}$$

With this procedure only the contribution of the receiver phase is bear in mind, in addition to assuming the same antenna-receiver paths for all chains. Moreover it is necessary to have a well-characterized the noise distribution network. In practice, inaccuracies in the measurements of the S parameters of the distribute network are made, been this method very complex in the real instrument. For this reason another method has been devised. It consists of injecting two known signals the first time. The first one is an external signal transmitted ideally in the far field of the array, arriving thus in phase to all antennas. The second one, is the internal correlated noise previously used. With this method the physical phases can be accurately estimated and all baselines can be calibrated simultaneously. For this reason, the name of the method is called Multiple Baseline Calibration. The phase calibration process is shown for the V-polarization, the same process holds at H-polarization. Figure 5.14, shows the receiver block diagram, where it is possible to distinguish two signal paths. External point source signal with the same phase injected to all antennas ϕ_{1V} (Eqn. 5.40), and internal correlation noise injected to all receivers ϕ_{2V} (Eqn. 5.41). As it can be noticed, each signal path has different contributions of physical phase ($\phi_{physical\,1V}$ and $\phi_{physical\,2V}$), being invariable in the time, and a common term of the phase of the receiver ($\phi_{Rx\,V}$), changing every time that the instrument is turned on. Subtracting Eqns. 5.40 and 5.41 the common term $\phi_{Rx\,V}$ disappears, (Eqn. 5.44) remaining only the two physical contributions $\phi_{physical\,1V}$ and $\phi_{physical\,2V}$. Once these physical terms are determined and stored for future calibrations, it is possible to retrieve the phase of the future target (Eqn. 5.46). The external signal or target measured by the antennas is subtracted both the physical paths, estimated previously Eqn. 5.44, and the correlated term, Eqn. 5.41. Substituting ϕ_{1V} by Eqn. 5.40 and ϕ_{2V} by Eqn. 5.41 in Eqn. 5.46 and after some straightforward algebraic manipulation, remain only the phase of the target, (Eqn. 5.46).

$$\phi_{1V} = \phi_{physical\,1V} + \phi_{Rx\,V}, \tag{5.40}$$

$$\phi_{2V} = \phi_{physical\,2V} + \phi_{Rx\,V}, \tag{5.41}$$

$$\phi_{1H} = \phi_{physical\,1H} + \phi_{Rx\,H}, \tag{5.42}$$

$$\phi_{2H} = \phi_{physical\,2H} + \phi_{Rx\,H}. \tag{5.43}$$

$$\phi_{1V} - \phi_{2V} = (\phi_{physical\,1V} + \cancel{\phi_{Rx\,V}}) - (\phi_{physical\,2V} + \cancel{\phi_{Rx\,V}}) = \phi_{physical\,1V} - \phi_{physical\,2V}, \tag{5.44}$$

$$\phi_{1H} - \phi_{2H} = (\phi_{physical\,1H} + \cancel{\phi_{Rx\,H}}) - (\phi_{physical\,2H} + \cancel{\phi_{Rx\,H}}) = \phi_{physical\,1H} - \phi_{physical\,2H}. \tag{5.45}$$

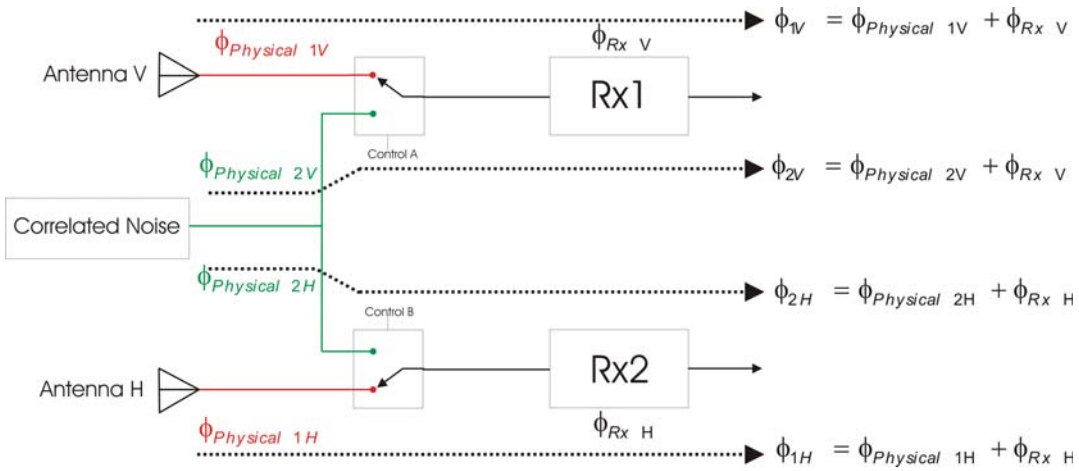

Figure 5.14. Phase calibration with the Multiple Baseline Calibration MBC method.

$$\underbrace{\phi_{target} + \phi_{1V}}_{\text{External signal}} - \underbrace{(\phi_{physical\,1V} - \phi_{physical\,2V})}_{\text{Physical Path}} - \underbrace{\phi_{2V}}_{\text{Correlated signal}} = \phi_{target} \tag{5.46}$$

$$\underbrace{\phi_{target} + \phi_{1H}}_{\text{External signal}} - \underbrace{(\phi_{physical\,1H} - \phi_{physical\,2H})}_{\text{Physical Path}} - \underbrace{\phi_{2H}}_{\text{Correlated signal}} = \phi_{target} \tag{5.47}$$

With the Multiple Baseline Calibration (MBC) method physical phase terms can be estimated. This information will be used in future measurements. To carry out the the calibration it is necessary lo locate an antenna pointing to the center of the array in the far-field. Since it is not practical a near-field to far-field correction is necessary to compensate for the spherical wavefront phase error [84], (Eqn. 5.48):

$$V_{m,n}^{far-field}(u,v) = V_{m,n}^{near-field}(u,v) \cdot e^{+jk(r_m - r_n)}. \tag{5.48}$$

where k is the electromagnetic wavenumber ($k = 2\pi/\lambda$)· and $r_{m,n}$ are the distances from the beacon antenna phase center to the phase center of antenna elements m and n. Figure 5.15 shows the measurement setup with a transmitting antenna and the PAU-SA instrument in the back.

5.5.1.3 Amplitude calibration

Amplitude calibration requires the knowledge of the system temperatures of each channel ($T_{SYS_{m,n}} = T'_{A_{m,n}} + T_{REC_{m,n}}$ in Eqn. 5.27), which requires a knowledge of the antenna temperatures and the receivers' noise temperature (including all losses in the antenna, switch ...), been necessary to characterize the instrument in an anechoic chamber. In the case of PAU-SA this has not been possible. Alternatively, the amplitude calibration is performed in three steps:

- The first step, the normalized visibility samples $\mu_{m,n}(u,v)$ are multiplied by $\sqrt{P_m \cdot P_n}$, where $P_{m,n}$ is the power (in counts) detected by the digital power detectors implemented in each channel using the 8 bits samples of the received signal, Eqn. 6.3. To do so, it was first checked that the offsets in the digital detector were negligible so that $P_{m,n} \propto T_{SYS_{m,n}}$ (b = 0, Eqn. 5.32).

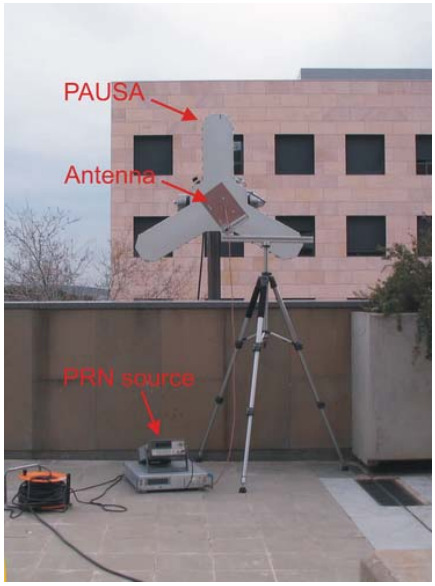

Figure 5.15. PAU-SA instrument pointing to the beacon antenna for phase calibration.

- In the second step, a relative calibration is performed by forcing all the different visibility amplitudes to be equal when an antenna was transmitting a strong PRN (or noise) signal in the boresight (Fig. 5.15). Since the transmitting antenna is in the near-field, an amplitude correction of the spherical wavefront is also required:

$$V_{m,n}^{far-field}(u,v) = V_{m,n}^{near-field}(u,v) \cdot (r_m/r_0) \cdot (r_n/r_0), \tag{5.49}$$

  where $r_{m,n}$ is the distance from the beacon antenna phase center to the antennas m and n phase centers, and r_0 is the distance from the transmitting antenna phase center to the central antenna.

- Finally, in the third step, a known signal in the far field of the antenna is used as a beacon for amplitude calibration, as a scaling factor for all the visibilities. Since our instrument was conceived as a technology demonstrator and commercial GPS chips operating at L1 band were used, it was found that the instrument was capable of nicely imaging the position of the satellites of the GPS constellation when looking to the zenith (Fig. 5.16), and therefore these signals have been used as calibration signals of opportunity. Knowing the GPS Equivalent Radiated Isotropic Power (ERIP), the satellite's distance ($r(\xi_0, \eta_0)$) at a given direction (ξ_0, η_0) (preferably around the antenna boresight), and the radiation pattern of the elementary antenna $t(\xi_0, \eta_0)$, the amplitude of the point source (in Kelvin, Fig. 5.17) can be estimated from Eqn. 5.50:

$$T = ERIP \cdot \lambda^2 \cdot t(\xi_0, \eta_0)/(4 \cdot \pi k_B \cdot B \cdot r^2(\xi_0, \eta_0) \cdot \Omega). \tag{5.50}$$

  where $k_B = 1.38 \cdot 10^{-23}$ J/K is the Boltzmann's constant, B the receivers' noise bandwidth (which can be estimated from [67]), λ the electromagnetic wavelength, and Ω the solid angle of the synthetic beam created by the array that can be

Figure 5.16. PAU-SA instrument pointing to the zenith for absolute amplitude calibration and GPS satellites imaging.

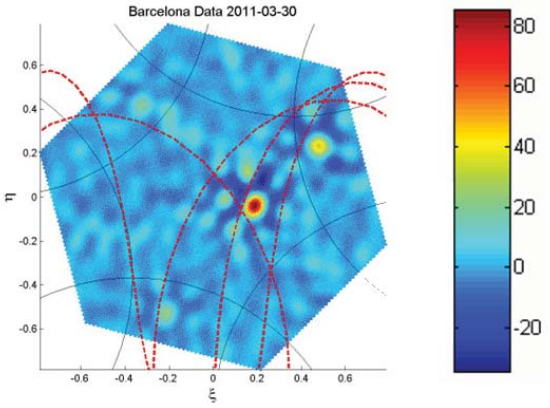

Figure 5.17. PRN 10 GPS satellite sample measurement for amplitude calibration and imaging tests. Hexagon: fundamental period where the T_B images are formed by a hexagonal Fourier transform. Note: the hexagon is rotated so that the upper part corresponds to the North. Solid lines represent the replicas of the unit circle that define the borders of the alias-free field-of-view of the instrument. Dashed lines represent the GPS satellites paths.

estimated as $\Omega = 4 \cdot \pi/\Delta\xi^2$, where $\Delta\xi$ is the half-power beamwidth, that can be computed from Eqn. 4.77 [22] (chapter 4) or from Eqn. 4.79 The last step in the amplitude calibration is equalization of the amplitude response in different directions. The approach follows the ideas of [85] of using a multiplicative Flat Target Response or FTR [85], instead of an additive one [86] to compensate for the (ξ, η) spatial patterns induced by an imperfect characterization of the antenna patterns and other residual calibration errors. Note that in the case of PAU-SA it is not possible to enter the instrument in the Universitat Politècnica de Catalunya (UPC) anechoic chamber [87] and therefore the antenna patterns used are the ones

of the insolated individual element. The Flat Target Response (FTR) is obtained by measuring the instrument's response to a flat and relatively constant scene over a long period of time. However, in our case this is not possible, due to the passage of the GPS satellites through the field of view. A proposed solution to alleviate this problem consists of computing the *mode* (most probable value in a data set) for each image pixel, instead of the *mean*. Results computed from 80 different snap-shots acquired on April 1st, 2011 in intervals of 11 minutes are shown in Figs. 5.18a and 5.18b at vertical and horizontal polarizations. Note the strips at horizontal polarization due to the failure of some elements. This issue will be treated in more detail in chapter 8. The calibrated average antenna temperatures in the series of 80 snap-shots are 5.90 K and 5.03 K at vertical and horizontal polarizations, respectively. The multiplicative mask to flatten these images is then computed from the average antenna temperature at each polarization (5.90 or 5.03 K), divided by the image at that polarization (Figs. 5.18a or 5.18b). These masks are then be applied to all the snap-shots.

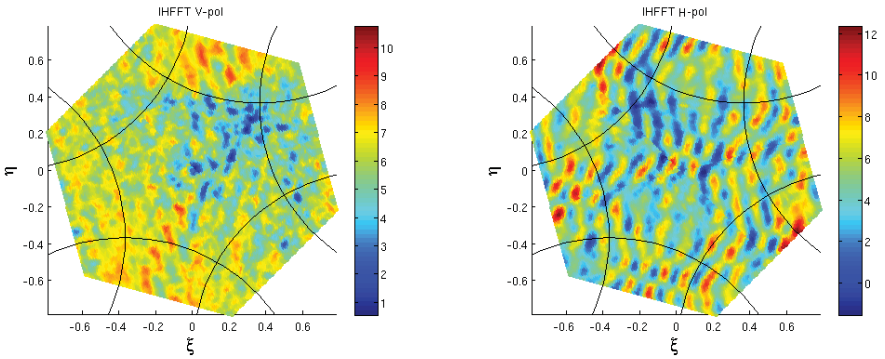

Figure 5.18. Estimated Flat Target Response (units Kelvin) obtained by computing the mode instead of the mean of the brightness temperature values of each pixel for a temporal series of snap-shots to eliminate the effect of the passing GPS satellites.

5.5.2 Implementation of the inversion algorithm

In order to have a complete knowledge of the image reconstruction process, this section reviews the basic steps. Once the visibility matrices have been calculated in Eqn. 5.27, it is necessary to first determine the (u, v) fundamental period for reordering the indices of the visibility matrices, and finally apply the image reconstruction. The number of non-redundant (u, v) points and of zero padded samples in a period are given by Eqns. 4.45 and 4.46. The last one is usually chosen greater than N_V– in order to stabilize the inversion by G-matrix; on the other hand, it is usually a power of two, in order to make the algorithm quicker when the inversion is made by means of an IFFT.

The variable NT determines the grid of the final map temperature. The larger NT, the finer the grid. The minimum value of NT is the one that allows to fill a complete hexagonal period (in the case of PAU-SA correspond with the number of antennas, 25).

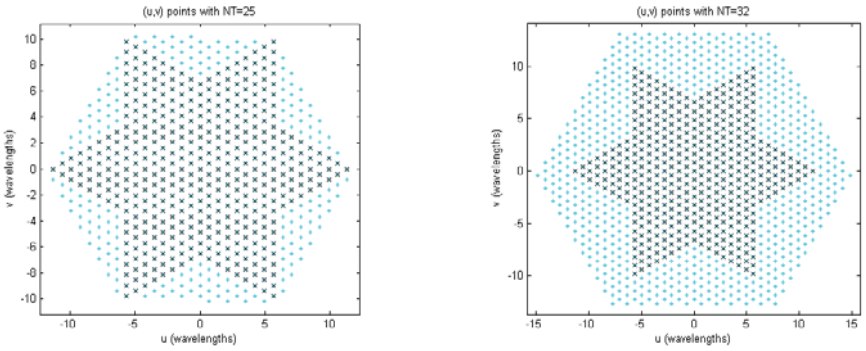

(a) **(b)**

Figure 5.19. Fundamental period with (a) NT = 25, and (b) NT = 32.

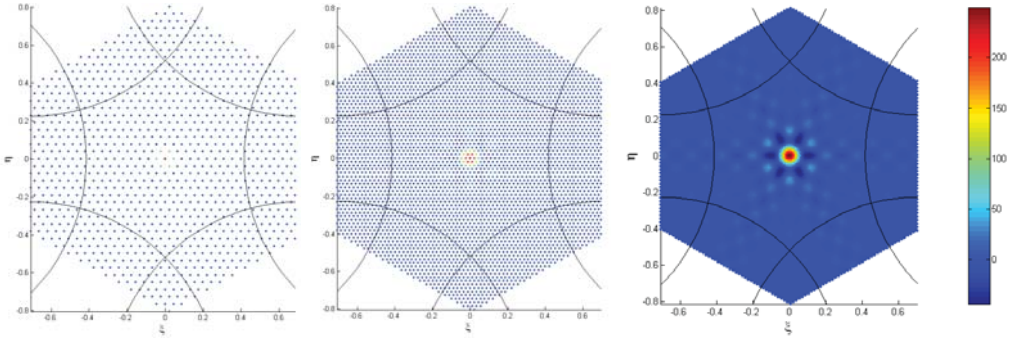

(a) **(b)** **(c)**

Figure 5.20. Image reconstruction representation of a source point for different grid a) NT = 32, b) NT = 64, and c) NT = 128.

Figure 5.19 compares the resulting fundamental period with NT = 25 and another one with NT = 32. Note that the black points are the visibilities samples to be used as input for the 2D FFT, the grey points are extra samples to fill fundamental period (zero-padding). The shape of the rectangularized period directly comes from the choice of the periodicity that can be seen in Fig. 4.5, considering the k_1 and k_2 axes.

Once the (u, v) hexagon fundamental period has been calculated, the calibrated visibilities calculated in Eqn. 5.27, ordered by antennas, can be associated to the (u, v) point. With this operation, redundant visibilities corresponding to the same (u, v) point are also accounted for and averaged. Finally the inversion method is applied with an IFFT or G matrix, retrieving the corresponding brightness temperature image. Figure 5.20 shows the same image reconstructions of a point source at the origin using the IFFT method for different grid NT values. As it can be noticed in Fig. 5.20, for a better view of the brightness temperature image it is necessary to use at least NT = 128, with the drawback of increasing the computational requirements.

5.6 PAU-SA's features

Once the theory of synthetic aperture interferometric radiometry has been reviewed in chapter 4, and the overview of the PAU-SA'instrument has been presented, it is now possible to determine PAU-SA's features and performances. This section presents the main features of the system.

5.6.1 PAU-SA's AF-FOV

One of the main parameters to determine in a synthetic aperture interferometric radiometry is the AF-FOV. As it can be noticed in Eqn. 4.66 it is inversely proportional to the antenna spacing in terms of the wavelength. Table 5.2 shows the AF-FOV comparison of MIRAS and PAU-SA. It is important to emphasize the operational frequency, different for both instruments: 1,400 MHz for MIRAS, and 1,575.42 MHz in the case of PAU-SA. As determined in Fig. 4.6a, to avoid aliasing, the maximum antenna spacing should be at most $d \leq \frac{\lambda}{\sqrt{3}}$. Despite it has not possible to achieve this requirement, in the case of PAU-SA, it separation has been determined by the antenna/receiver size, placing them as close as possible.

Table 5.2. AF-FOV determination of the MIRAS and PAU-SA instruments in the ξ plane.

Instrument	**Antenna spacing (d)**	AF-FOV(º)
MIRAS	0.875λ	37.3º
PAU-SA	0.816λ	49.0º

5.6.2 Angular resolution

The angular resolution depends on the dimension of the array size, and the antenna spacing in terms of the wavelength. For a determined antenna spacing, the larger the array size, the better the spatial resolution. At present, due a problem with some receivers, the number of receivers per arm has been reduced from 8 to 7 elements. So, the angular resolution has been determined in both cases. As it can be noticed in Table 5.3, the best angular resolution is achieved for $N_{EL} = 8$ and rectangular window with a value of approximately 4º (with method 1, Eqn. 4.77) and 4.6º (with method 2, Eqn. 4.79). Nowadays, with 7 elements per arm these parameters degrade to 4.6º(with method 1) and 5.25º (with the method 2).

5.6.3 Number of pixels in the AF-FOV

The number of independent pixels inside the AF-FOV in 1-D determines the accuracy of the image. This parameter depends on the AF-FOV width, and the angular resolution, as shown in Eqn. 4.82. In PAU-SA, the best results correspond with rectangular window and 8 elements per arm with approximately 12 x 12 independent pixels with the method

Table 5.3. PAU-SA's angular resolution function of the number of elements per arm (N_{EL}).

N_{EL}	Window	$\Delta\theta$ (°) (Method 1)	$\Delta\theta$ (°) (Method 2)
8	$\Delta\xi^{rec}_{-3dB}$	3.99	4.60
	$\Delta\xi^{triag}_{-3dB}$	4.94	5.70
	$\Delta\xi^{Hamming}_{-3dB}$	5.01	5.80
	$\Delta\xi^{Hanning}_{-3dB}$	5.30	6.11
	$\Delta\xi^{Blackman}_{-3dB}$	5.90	6.80
7	$\Delta\xi^{rec}_{-3dB}$	4.60	5.25
	$\Delta\xi^{triag}_{-3dB}$	5.67	6.50
	$\Delta\xi^{Hamming}_{-3dB}$	5.74	6.60
	$\Delta\xi^{Hanning}_{-3dB}$	6.05	7.00
	$\Delta\xi^{Blackman}_{-3dB}$	6.73	7.77

1, (Eqn. 4.77) and 10 x 10 with the method 2, Eqn. 4.79. In the case of use 7 elements per arm it parameter degrade to 10 x 10 and 9 x 9 using method 1 and 2 respectively.

Table 5.4. Number of independent point sources in the PAU-SA's AF-FOV.

N_{EL}	Window	# sources in AF-FOV ($\Delta\xi^{rec}_{-3dB}$ Method 1)	# sources in AF-FOV ($\Delta\xi^{rec}_{-3dB}$ Method 2)
8	$\Delta\xi^{rec}_{-3dB}$	12.32	10.67
	$\Delta\xi^{triag}_{-3dB}$	9.93	8.60
	$\Delta\xi^{Hamming}_{-3dB}$	9.78	8.47
	$\Delta\xi^{Hanning}_{-3dB}$	9.26	8.02
	$\Delta\xi^{Blackman}_{-3dB}$	8.32	7.21
7	$\Delta\xi^{rec}_{-3dB}$	10.78	9.33
	$\Delta\xi^{triag}_{-3dB}$	8.69	7.53
	$\Delta\xi^{Hamming}_{-3dB}$	8.55	7.14
	$\Delta\xi^{Hanning}_{-3dB}$	8.10	7.02
	$\Delta\xi^{Blackman}_{-3dB}$	7.28	6.31

5.7 Conclusions

In this chapter an overview of the PAU-SA instrument has been presented. Despite this thesis has been developed under the framework of the PAU concept (common receiver front-end for radiometric and GNSS-R applications), this part has been simplified due the added complexity of the synthetic aperture radiometer hardware. The reduction consists of the replacement of the 7 central elements for GNSS-R applications by a single commercial receiver. A comparative table between MIRAS and PAU-SA has been pre-

sented in order to show the potential improvements that we want to evaluate. The most remarkable contributions have been the migration of some parts from analog to digital to eliminate temperature and frequency drifts such as: digital I/Q down-conversion, digital filtering, and power estimation. Moreover, a dummy antenna at the end of each arm has been considered to improve the antenna pattern inter-similarity.

Correlation radiometers require the injection of known calibration signals. Currently these signals are generated by one or several noise sources and are distributed by a network of power splitters, which is bulky, difficult to equalize, and introduces additional noise. Aiming at alleviating these problems a new technique is presented. It consists of the centralized injection to all receivers of a deterministic PRN signal, providing a complete baseline calibration. PRN signals exhibit a flat spectrum over the receivers' bandwidth, which makes possible to use them for calibration purposes instead of the usual thermal noise. Since the PRN signals are deterministic and known, new calibration approaches are feasible: 1) through the correlation of the output signals at different time lags, as it is usually done when noise is injected, but allowing a much easier distribution of the signal to all the receivers simultaneously, or 2) through the correlation of the output signals with a local replica of the PRN signal being injected, leading to the estimation of the receivers' frequency responses, and of the FWF. In this last case the distribution network has no influence on the correlation.

The impact of the frequency operation in the radiometric part and the contribution of the FWF term have been discussed. Concerning the operational frequency (L1 of the GPS), in the real aperture version PAU-RA, it is not an inconvenient since it is possible electronically to steer the main beam and avoid direct GPS signals. However, in the case of the synthetic aperture version (PAU-SA), since the array pattern is the antenna pattern pondered by the AF, it has a high level of GPS contribution, been mandatory pointing to the north where there are absence of GPS satellites to perform radiometric measurements. In relation to the impact of the term FWF in PAU-SA, since the dimension is 3 times smaller respect to MIRAS and the bandwidth is a factor of 10 smaller, the FWF is totally negligible.

Once the basic processing steps from the cross-correlations coming from the FPGA to the visibility function have been discussed, the instrument calibration has been proposed. Due to some critical parameters of the instrument to be characterized such as: antenna efficiency, several physical paths, or the S parameters of the correlated power splitter, the estimation of the T_{SYS} among other have been impossible to estimate directly, an alternative calibrations have been proposed. Concerning the phase calibration the MBC method is applied. It consists of transmitting a signal with an antenna pointing to the central array element and with combination of internal correlation signals, the physical path is estimated and stored for future calibrations. In the case of the amplitude calibration, it requires the knowledge of the system temperatures including all losses of the antennas switch etc, been necessary to characterize the instrument in an anechoic chamber. For this reason an alternative amplitude calibration has been performed. Basically it consists of denormalized the visibility samples with the power in counts and the use of individual GPS satellite as a beacon signal in the far field as a scaling factor for all the visibilities.

Finally the main PAU-SA features have been presented.

Chapter 6

PAU-SA's Physical Modeling Simulator

The PAU-SA's physical modeling simulator has been implemented in MATLAB language and runs on the external PC. It is an end-to-end simulation (from the noise generation and instrument behavior, to the image reconstruction and calibration procedures) modeling of all the system as faithfully as possible. The signals collected by the antennas, as well as the FPGA operations are simulated when the "Simulation Mode" is active. The same software has also been conceived to process the data acquired by the PAU-SA instrument ("Processing Mode"). In this process, the signals are not generated, but really collected by the real instrument: antennas, down-converter, ADC board and the correlation matrices come directly from the FPGA, where the signals are already demodulated, filtered and correlated. From this point, the signal processing is common to the two modes of operation.

6.1 Simulation mode

This section briefly explains how the simulation works. The goal of this part is to develop a tool to better understand the instrument. In this mode of operation it is possible to introduce a variety of parameters such as: integration time, number of bits, processing window, inversion mode etc., and also to model a number of imperfections such as: phase, gain, receiver's noise etc in order to determine the contribution of each one in the system. To our knowledge this is the first physically-based end-to-end 2-D synthesis aperture radiometer simulator. Other contributions of physical-based end-to-end 1-D synthetic aperture radiometer [88] and in [89]. In the PAU-SA's simulation mode, the signals are simulated at the antenna reference plane, and the external interferences RFI are not taken into account.

6.1.1 PAU-SA's simulator graphical interface

Figure 6.1 shows the PAU-SA's simulator graphical interface. It allows to select the parameters, procedures and characteristics for the simulation in a simple and quick manner. It has been developed with MATLAB 7 using the Graphical User Interface Design Environment (GUIDE). This subsection briefly describes the main features of the interface. In the simulator it is possible to select different hardware errors independently or a combination of them, been the most representatives:

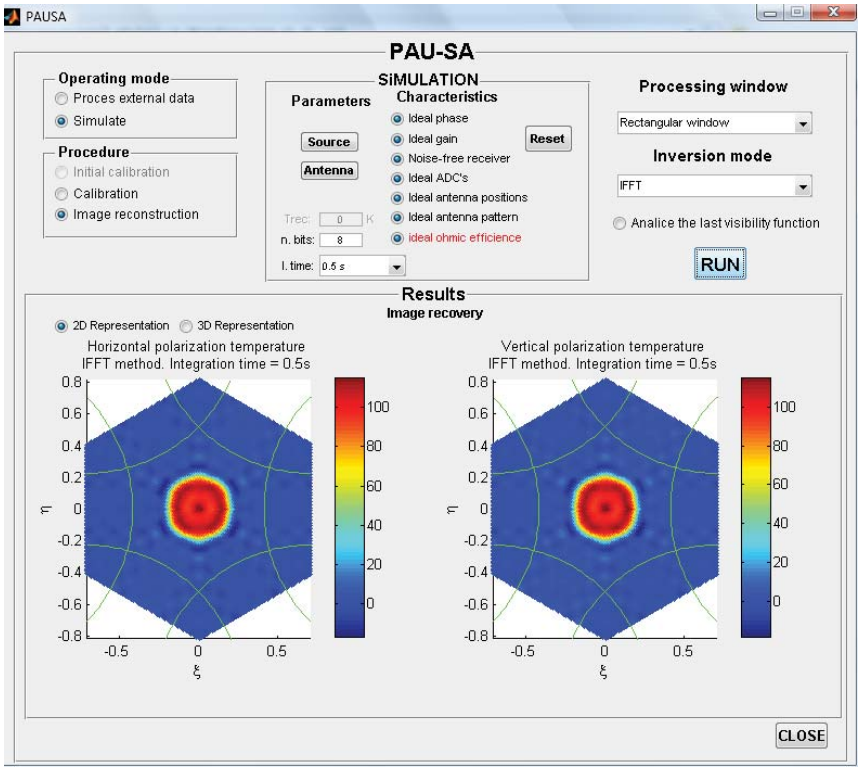

Figure 6.1. Front panel of the PAU-SA's simulator interface.

- **Ideal phase** allows to the user add uniformly distributed phase errors in $[0, 2\pi)$ or consider ideal receivers,
- **Ideal gain** allows the user to add amplitude errors or consider ideal receivers. The gain of the receivers follows a Gaussian distribution with nominal value of 110 dB and standard deviation of, for example, 1 dB,
- **Noise-free receiver** is used to take into account the receiver thermal noise or to consider noise-free receivers. The receiver thermal noise follows a Gaussian distribution with nominal value of 250 K, and a standard deviation of, for example, 5 K,
- **Ideal ADCs** allows to consider a threshold voltage in the ADCs or to consider ideal ADCs. The threshold voltage variations follow a Gaussian distribution with nominal value of 0 V and standard deviation of, for example, 0.5 mV,
- **Ideal antenna positions** introduces random displacements of the antennas due to oscillations of the arms, thermal effects, mechanical tolerances, etc; or consider this term ideal. Each antenna position has a Gaussian distribution with standard deviation of 2 mm around the ideal place,
- **Ideal antenna patterns** incorporates the distortion of the ideal antenna pattern due to antenna coupling or considers, it ideal,
- **ideal Ohmic efficiency** introduces a tolerance in the Ohmic efficiency or considers it ideal. The Ohmic efficiency follows a uniformly distribution between 0.6 and 1.

Moreover, it is possible select different parameters such as:

- **Integration time** selects the integration time between 1 s, 0.5 s, 100 ms, 10 ms, or enters the number of simulated signals samples,
- **n.bits** is the number of bits of the analog/digital conversion (maximum 8 bits),
- **Antenna** selects the antenna diagram radiation voltage between two possible: the first one is $cos^n\theta$ for academic purposes and the second one is the patch antenna implemented PAU-SA (Section 7.1). Nowadays all antenna patterns are considered identical, as in Fig. 6.2a,
- **Source** allows to the user select the number of sources in the brightness temperature image. It is possible to choose between point sources with a maximum of 9 or extended source, Fig. 6.2b.

6.1.2 Signal generation

In the configuration interface, to perform an image reconstruction, it offers the possibility to select between two types of sources to be analyzed: point sources and extended sources. Since the simulator works with finite signals, it is necessary define a grid in the plane

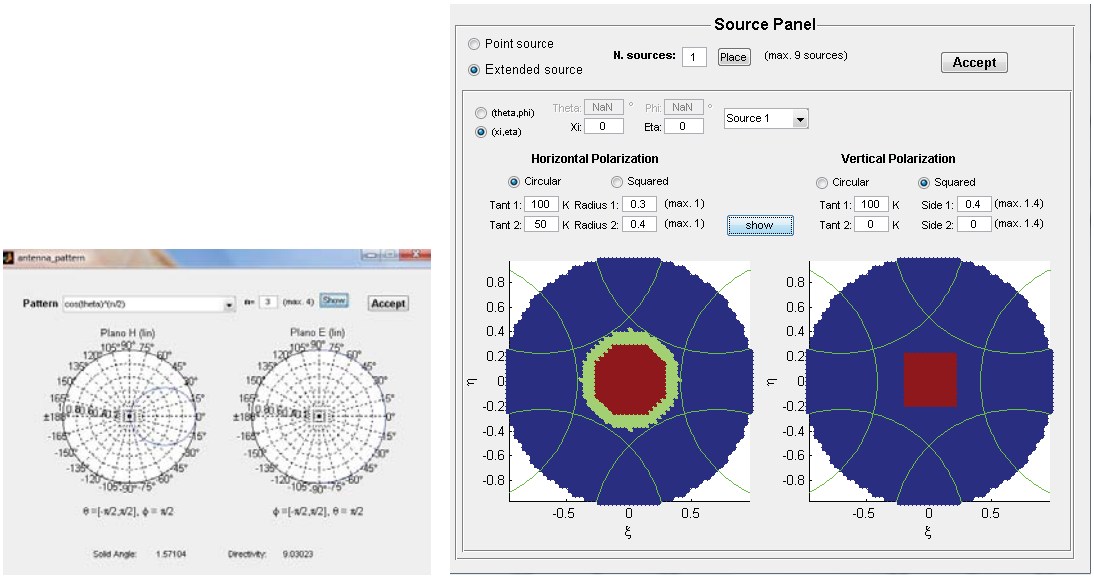

(a) **(b)**

Figure 6.2. PAU-SA's GUI parameter panels. a) Antenna pattern selection, and b) source panel viewer with extended source selection.

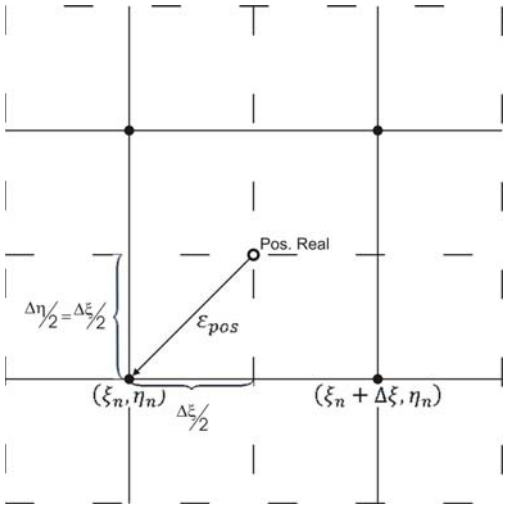

(a)

Figure 6.3. (ξ, η) plane and the discretization error .

(ξ, η) where place these point sources. Since $\Delta\xi = \Delta\eta$, Figure 6.3 shows the (ξ, η) plane where the maximum error is given by Eqn. 6.1.

$$\varepsilon_{pos}|_{max} = \sqrt{\left(\frac{\Delta\xi}{2}\right)^2 + \left(\frac{\Delta\xi}{2}\right)^2} = \frac{\sqrt{2}}{2}\Delta\xi. \tag{6.1}$$

In the case of working with extended sources, a superposition of point sources very close to each other are used, which result in an image that is not noticed the separation between

them. So, all signals are also generated with point sources. The optimum grid is one in which the maximum point source separation is the angular resolution of the system with a rectangular windowing and the minimum separation is limited by the computational cost and the memory of the PC.

The signal generated depend on the input selected (antenna, correlated or uncorrelated noise injection), each with its equivalent temperature $T'_A, T_{corr}, T_{uncorr}$ respectively. In the case of uncorrelated signals, it generates 50 random processes (25 receivers x 2 polarizations) with variances $\sigma^2 = k_B T_{Uncorr} BG$, being k_B the Boltzmann's constant, B the bandwidth, and G the overall gain. Since the simulator works with finite sequences, the power of the random process can be different of one. For this reason, all signals are normalized with the same expression to ensure the desired power, Eqn. 6.2:

$$S(r,n) = \sqrt{k_B T B G}\left(\frac{n_i(r,n)}{\sqrt{2}\sigma(n_i(r,n))} + j\frac{n_q(r,n)}{\sqrt{2}\sigma(n_q(r,n))}\right). \tag{6.2}$$

where $S(r,n)$ is the input signal at each receiver, n_i is a Gaussian random function, r is the number of receiver, and n is the sample number that depends on the integration time. For the correlated noise injection the equivalent noise temperature is the same for all receivers. In the case of antenna signals, once these noises have been generated, each term is arranged for every antenna, taking into account the observation angles, the propagation terms e^{-jkr} and $e^{j\omega t}$ and the antenna positions. At this point the receiver thermal noise is generated for each one knowing its variance in the same way it was done for the input signals. The noise is then added to the complex signal and both are band-pass filtered with a fifth order Butterworth filter, setting the system bandwidth of 2.2 MHz. The 25 different output signals for each polarization (V, H, VH), which can still be affected by phase and amplitude errors, are then arranged in a 25 × n matrices. Before the correlation matrices are calculated as it is done in the FPGA, the signals are then low-pass filtered and quantized on 1 bit/2 levels (Section 7.4). Finally, the I and Q components are extracted from the signal and the correlation matrices are calculated and arranged as shown in Fig. 6.4. The power estimation for denormalization procedures

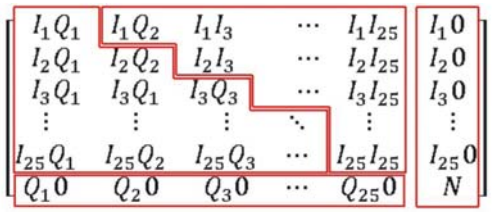

Figure 6.4. PAU-SA's correlation matrix structure.

are calculated from the quantized signal *Squant*, with a determined number of bits as:

$$\overline{P_s}(a) = \frac{2}{N}\sum_{n=1}^{N}(I\_Squant(r,n))^2. \tag{6.3}$$

where N is the total number of samples, $I\_Squant(r,n)$ is the in-phase quantified signal. Since the in-phase and quadrature signals carry the same information, the power is evaluated as twice the power of the in-phase component only. Once the signals have been

generated, the correlation matrices and the power estimation are performed as explained in section 5.5.

6.2 Simulation results

6.2.1 Results with a point source

This section shows some results of the simulations performed with a point source inside and outside the boresight, in addition to two point sources. All images are obtained for an ideal instrument, with a two-dimensional IFFT as inversion algorithm, a brightness temperature of 100 K and 5,700,000 samples, that corresponds to an integration time of 1 s (sampling frequency = 5.7 MHz).

6.2.1.1 Point source at the origin

Figure 6.5 shows a point source at $\theta = \phi = 0^{o}$ obtained with a rectangular and Blackman windowing. As it can be noticed, there is a trade-off between the beamwidth and the side lobes level. In the case of a rectangular window, the six side lobes of the impulse response of the system are visible around the maximum, spaced by 60º. With this window is possible to achieve the narrowest beamwidth. On the contrary, a Blackman window minimizes the side lobes level but, the beamwidth is the widest. Table 6.1 presents the parameters of a point source at the boresight imaged with different windows.

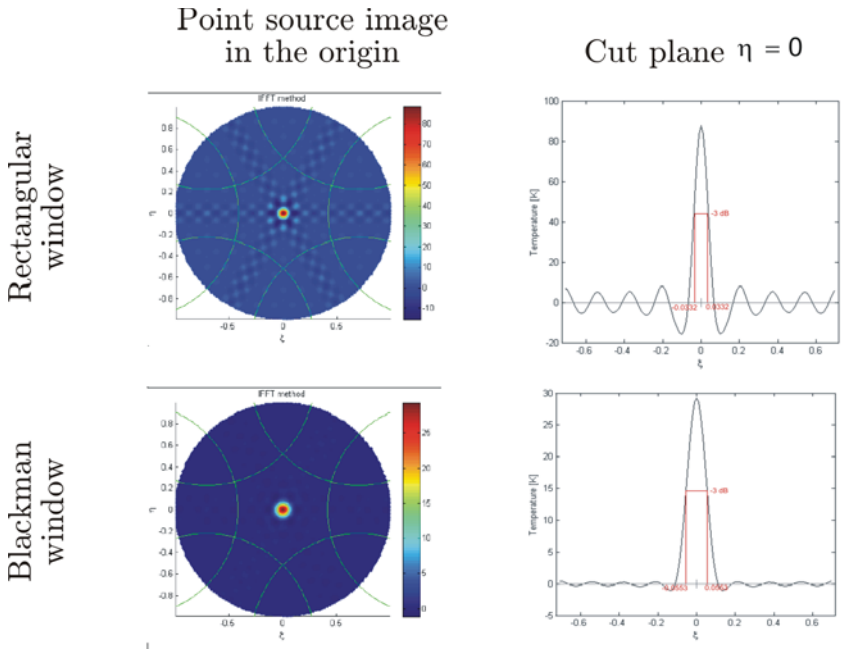

Figure 6.5. Representation of the point source at the origin obtained with a) rectangular window, and b) a Blackman window.

Table 6.1. Inter-comparison table of the point source at the origin with different windows. Beamwidth at -3 dB calculated with two theoretical methods (1 using Eqn. 4.77 and 2 using Eqn. 4.79).

	Windowing				
Parameter	Rectangular	Triangular	Hamming	Hanning	Blackman
Maximum	88.02 K	39.94 K	42.66 K	38.71 K	29.24 K
Mean	0.11 K	0.12 K	0.11 K	0.11 K	0.11 K
RMS	3.33 K	1.60 K	1.74 K	1.65 K	1.35 K
RMS in FOV	6.97 K	3.48 K	3.82 K	3.63 K	2.98 K
Half-power beamwidth (theoretical method 1)	0.0695	0.0862	0.0876	0.0924	0.1029
Half-power beamwidth (theoretical method 2)	0.0802	0.0995	0.1011	0.1067	0.1187
Half-power beamwidth (simulated)	0.0756	0.0922	0.0950	0.0900	0.1166

6.2.1.2 Point source outside the origin

Several simulations have been performed to test the correct operation of the simulation algorithm varying the observation angles θ and ϕ. Considerations about integration time and windows are still valid in this subsection. Figure 6.6a shows a point source observed

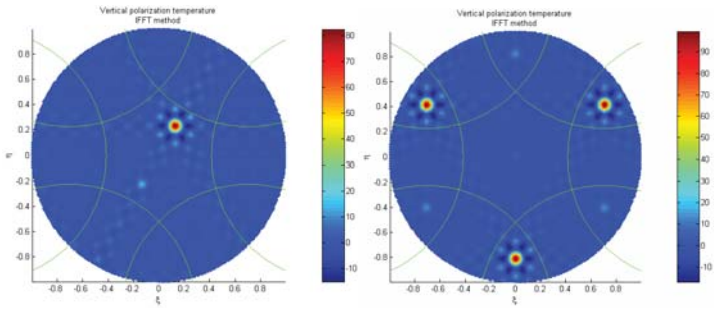

(a) **(b)**

Figure 6.6. Point source at different observation angles a) $\theta = 15^{o}$,$\phi = 60^{o}$, and b) $\theta = 55^{o}$, $\phi = 30^{o}$.

at $\theta = 15^{o}$ and $\phi = 60^{o}$. The source still appears inside the FOV, thus no aliasing effects appear. Figure 6.6b shows the point source observed at $\theta = 55^{o}$ and $\phi = 30^{o}$, going out of the top right hand corner of the hexagonal sampling grid and reappearing at the opposite corners of the hexagon for periodicity.

Once the effect with a point source at the origin using different windows has been analyzed, the effect of a point source outside the boresight at ($\xi = \eta = 0.1$), but inside the AF-FOV also has been simulated. Figure 6.7 shows two simulations with this configuration obtained with rectangular and Blackman windowing, and Table 6.2 compares the effect of using different windows.
In this case the maximum amplitude is smaller than in the boresight case due to the attenuation of the elementary antenna radiation pattern.

6.2.1.3 Angular resolution

To determine the angular resolution it is necessary to define a criterion to distinguish two point close spaced sources. To determine the angular resolution using different windows, a set of simulations with two separations has been performed. The first one determines

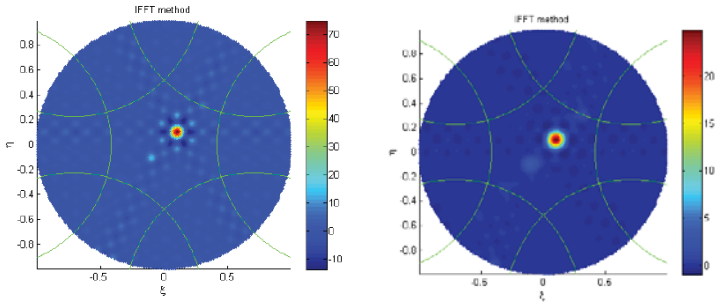

(a) **(b)**

Figure 6.7. Point source outside the boresight at ($\xi = \eta = 0.1$) with a) rectangular window, and b) Blackman window.

Table 6.2. Inter-comparison table for a point source outside the origin ($\xi = \eta = 0.1$) for different windows.

	Windowing				
Parameter	Rectangular	Triangular	Hamming	Hanning	Blackman
Maximum	74.97 K	33.40 K	36.31 K	32.95 K	24.89 K
Mean	0.12 K	0.13 K	0.12 K	0.12 K	0.12 K
RMS	2.90 K	1.34 K	1.50 K	1.42 K	1.17 K
RMS in FOV	6.03 K	3.00	3.28 K	3.11 K	2.55 K
$\frac{Max(0,0)}{Max(0.1,0.1)}$	1.1741	1.1749	1.1750	1.1751	0.1749

the best angular resolution, is one that can be discern two point sources with rectangular window. The second one is, the same, but with a Blackman window instead. Figure 6.8 shows all possible combinations where is possible to appreciate the contribution of the windowing. As expected, the rectangular window has the best angular resolution for N_{EL} = 8 and $d = 0.816\ \lambda$ it is approximately $\Delta\xi = 0.106$, and in the case of Blackman window this has been reduces till $\Delta\xi = 0.152$.

6.2.2 Results with extended sources

6.2.2.1 Generation of extended sources

It is also possible to simulate up to nine different point sources or extended sources. Point sources are defined by the brightness temperature (in Kelvin) and the position in degrees or in director cosines (ξ, η). In the case of extended sources, it has been implemented placing several point sources as close as possible, been the angular resolution the maximum separation. The optimum separation has been determined empirically by the desire shape and the computational time in the CPU to implement the extended source as shown in Fig. 6.9. As it can be noticed in Fig. 6.9a, if $\Delta\xi$ is of the order of the beamwidth at -3 dB with rectangular window, two point sources appear as a single one, but it is possible to distingued. This effect is due to the superposition of two point sources in the same way as it can be seen in Fig. 6.8 with $\Delta\xi = 0.106$ and Blackman window. For this reason it is necessary a $\Delta\xi$ of at least 0.033 to process extended sources. Below this value changes are not noticeable in the image, only the computational time

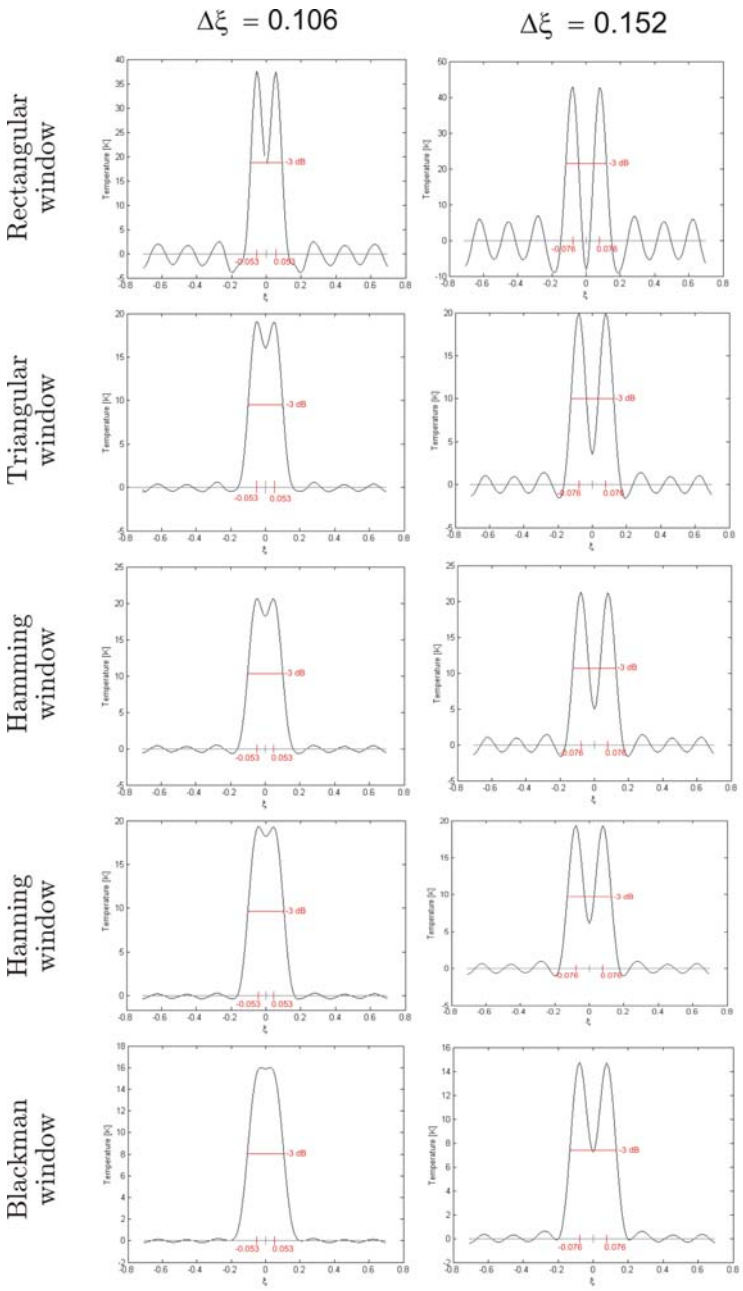

Figure 6.8. Representation of the angular resolution at ($\Delta\xi = 0.106$ and $\Delta\xi = 0.152$) and different windowing.

increases.

6.2.2.2 Measurements of extended sources

Once the grid of the (ξ, η) plane has been determined, a test with extended sources has been performed. It consist of a simulation with two different extended sources, circular and rectangular, as shown in Fig. 6.10.

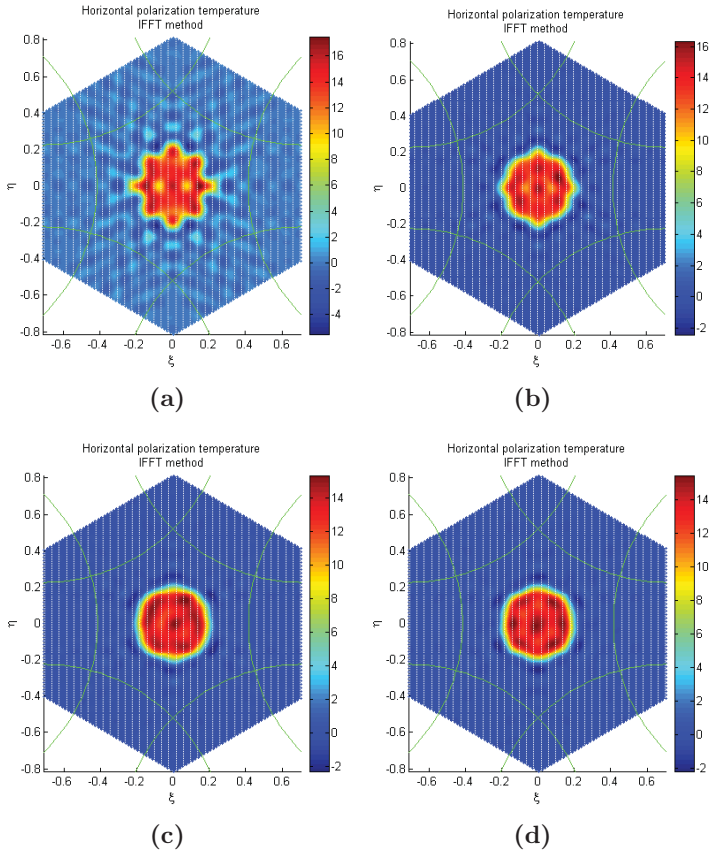

Figure 6.9. Determination of the distance of point sources to implement a extended source. Conditions: No instrumental errors, IFFT inversion method, $\tau = 0.1$ s, Rectangular window, T = 100 K, circular extended source with a radio of 0.2 located in the origin ($\theta = 0^o, \quad \phi = 0^o$). Separation in the director cosines of a) $\Delta\xi = 0.0667$, CPU = 98.34 s b) $\Delta\xi = 0.0500$, CPU = 107.45 c) $\Delta\xi = 0.033$, CPU = 132.08 s, and d) $\Delta\xi = 0.0250$, CPU = 180.07 s.

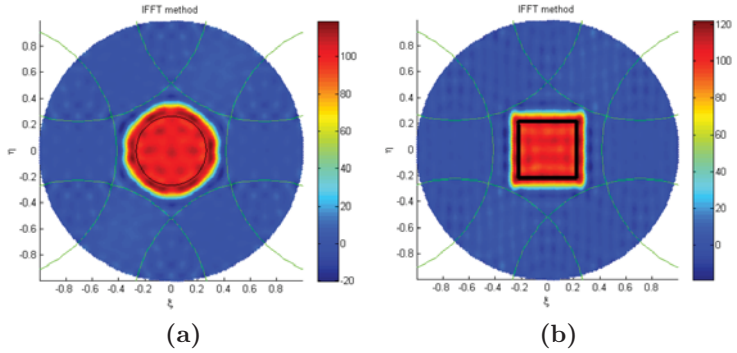

Figure 6.10. Simulation of the extended sources. Conditions: No instrumental errors, IFFT inversion method, $\tau = 0.1$ s, Rectangular window, T = 100 K, location in the origin ($\theta = 0^o, \quad \phi = 0^o$) a) circular extended source with a radio of 0.35, and b) square extended source with a size of 0.55.

It is important that the parameters of interest are estimated on the Gibbs free area as

shown in Fig. 6.11.

Table 6.3 shows the results of the simulation for different windowing.

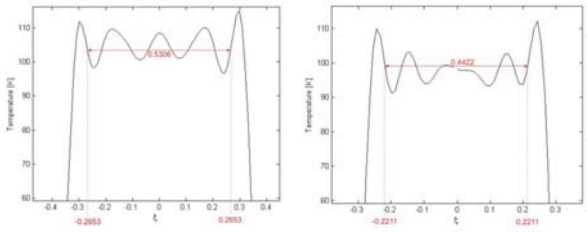

(a) **(b)**

Figure 6.11. Representation of Fig. 6.10 with a cut in the plane $\eta = 0$, a) circular, and b) square.

Table 6.3. Inter-comparison table of an extended source in the origin for different windows.

Windowing	Circular source		Square source	
	Mean value	RMS	Mean value	RMS
Rectangular	101.43 K	3.76 K	102.58 K	5.78 K
Triangular	96.58 K	1.41 K	96.08 K	1.87 K
Hamming	101.93 K	1.20 K	102.21 K	1.67 K
Hanning	101.98 K	1.08 K	102.18 K	1.47 K
Blackmann	101.69 K	0.60 K	101.15 K	1.56 K

6.2.2.3 Impact of individual errors in the image reconstruction

All tests presented previously have been done without instrumental errors in order to determine the impact of the windowing. The real instrument combines at the same time all hardware errors presented in (Section 6.1.1). In order to determine the impact of these imperfections independently, a set of simulations introducing these errors one by one have been performed. In order to compare the different tests, all simulations have been done with the same parameters, in addition has been used the same seed to generate the random sequences that form the signal recorded by the antennas. As it can be noticed in Fig. 6.12, at first glance each of the errors has a different contribution in the image reconstruction. Some of them have a higher impact in the image recovery such as: the introduction of the noise receiver, (Fig. 6.12c), even totally blurring the image as in the case of the phase error, Fig. 6.12a. Other contributions have an estrange behavior for instance the antenna coupling, Fig. 6.12f, deforming the recovered image asymmetrically or the introduction of the Ohmic losses of the antennas, Fig. 6.12g. In this case, the antenna input is attenuated, the lower the efficiency, the higher noise power, and the less will be the useful signal. On the other hand, there are other error contribution with a little impact or almost negligible for example: the error gain, Fig. 6.12b, ADCs error, Fig. 6.12d, or the antenna positioning, (Fig. 6.12e). Finally, Fig. 6.12h shows the impact of a combination of several errors at the same time. The PAU-SA's physical modeling simulator it is possible determine which errors have a greater contribution to the recovery of the image and act accordingly.

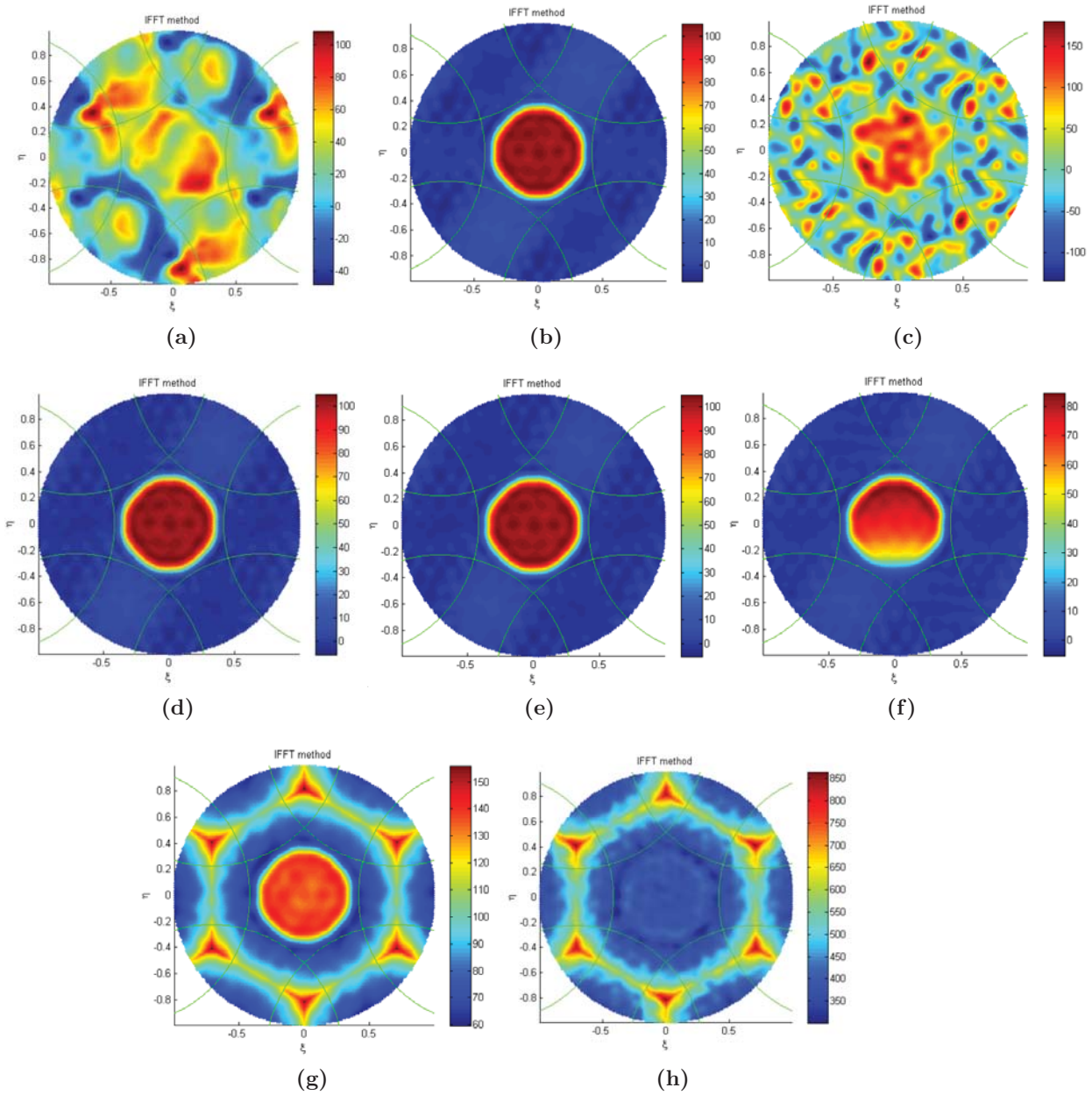

Figure 6.12. Impact of the individual errors in the image reconstruction. Conditions: circular extended source with a radius of 0.35 and location in the origin ($\theta = 0^o$, $\phi = 0^o$), IFFT inversion method, τ = 0.1 s, Blackman window, T = 100 K. a) uniform phase error, b) gain error, c) noise receiver with a T_{REC} = 250 K, d) ADCs, e) antenna position with a standard deviation of 2 mm around the ideal place , f) antenna coupling, g) Ohmic efficiency (all antennas with $\eta = 0.9$), and h) combination of a, b, c, g errors.

6.2.2.4 Calibration results

Once the impact of the individual errors in the recovered image has been presented previously, this section presents the results of applying the calibration. To work with the calibration algorithms as mentioned in (Section 5.5), several signals with known statistics are needed. In order to test the effectiveness in the recovering of these errors, several simulations have been performed with an initial calibration (taking into account the errors of antenna), and compared in Table 6.4 the values obtained with the generated in the simulation and the retrieved. In the case of phase error, to compare more clearly the

Table 6.4. Results of a calibration to estimate the phase receiver, noise receiver, and the Ohmic efficiency with a integration time of 1 s.

Receiver / antenna	Phase error [rad]			Receiver noise [K]			Ohmic efficiency		
	Theoretical	Retrieved	Error	Theoretical	Retrieved	Error	Theoretical	Retrieved	Error
1	0	0	0	250	249.673	0.326	0.9	0.899	6.21e-4
2	-0.045	-0.044	-0.001	250	250.298	-0.298	0.9	0.899	0.0013
3	-1.148	-1.158	0.01	250	241.058	8.942	0.9	0.904	-0.004
4	-0.321	-0.321	-1.2e-4	250	245.808	4.192	0.9	0.902	-0.0017
5	-1.842	-1.839	-0.003	250	244.693	5.307	0.9	0.901	-0.0013
6	-0.162	-0.161	-8.1e-4	250	246.404	3.596	0.9	0.901	-0.0012
7	-2.280	-2.297	0.016	250	248.549	1.451	0.9	0.898	0.002
8	-1.510	-1.507	-0.003	250	242.454	7.546	0.9	0.902	-0.0022
9	-2.235	-2.248	0.013	250	248.535	1.465	0.9	0.899	6.42e-4
10	-2.075	-2.081	0.006	250	248.571	1.429	0.9	0.899	8.51e-4
11	0.206	0.200	0.006	250	271.078	-21.078	0.9	0.889	0.0108
12	-0.197	-0.195	-0.002	250	268.743	-18.743	0.9	0.889	0.0102
13	-1.384	-1.389	0.005	250	263.474	-13.474	0.9	0.893	0.0073
14	0.604	0.587	0.017	250	271.768	-21.768	0.9	0.888	0.0118
15	-2.272	-2.287	0.015	250	270.525	-20.525	0.9	0.890	0.0096
16	-1.002	-1.017	0.015	250	262.579	-12.579	0.9	0.892	0.0078
17	-1.182	-1.195	0.013	250	262.459	-12.459	0.9	0.893	0.0066
18	0.024	0.026	-0.002	250	250.799	-0.799	0.9	0.897	0.0027
19	0.117	0.114	0.003	250	249.123	0.877	0.9	0.898	0.0018
20	-1.793	-1.787	-0.006	250	244.965	5.034	0.9	0.902	-0.0021
21	-0.842	-0.855	0.013	250	242.732	7.268	0.9	0.904	-0.0045
22	-0.981	-0.996	0.016	250	241.748	8.252	0.9	0.903	-0.0035
23	-0.350	-0.350	8.5e-4	250	246.121	3.879	0.9	0.901	-0.0011
24	-0.152	-0.150	-0.001	250	248.579	1.421	0.9	0.899	0.0014
25	-0.009	-0.008	-8.5e-4	250	248.779	1.221	0.9	0.898	0.0021

difference between the error applied to the simulation, and the error in the calibration recovered, the phase calibrated has been determined as the difference between the phase of each receiver and the first element (receiver 1). Finally, once the calibrated parameters have been retrieved, they have been applied to the image reconstruction. Figure 6.13 shows the result obtained after calibration of Fig. 6.12h. As it can be noticed the improvement is considerable, although it is possible to appreciate the effect of thermal noise around the surface under observation. This noise effect can be reduced by increasing the integration time.

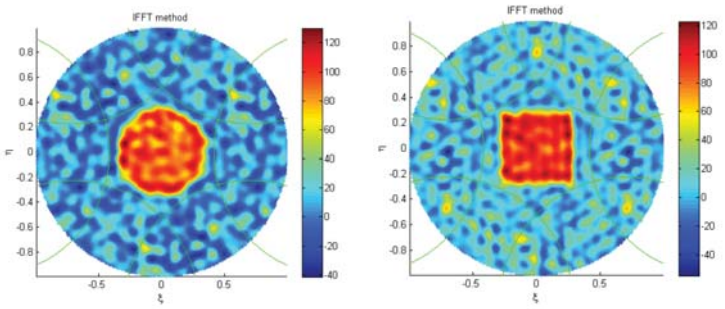

(a) (b)

Figure 6.13. Image recovered after calibration procedures.

6.2.3 Error budget of the system

In order to summarize the errors of the system, Table 6.5 shows the effect of some of the most important errors in the interface. These have been obtained simulating an

Table 6.5. Error budget of the system with a integration time of 1 s.

		Error source	$(\delta T/T)\delta\sigma_\Delta$	Accuracy "Budget"	Sensitivity "Budget"	Bias
Concept Limitations		Finite (u, v) coverage		3.76 K		
		Noise receiver T_R = 250 K , T_A = 100 K			13.29 K	
System limitations	Antenna errors	Crosstalk ($\lvert S_{12} \rvert_{max}$ = 25 dB)		5.31 K		
		In-plane osc. (2 mm)	0.025/mm		0.05 K	
		Off-plane osc. (2 mm)	0.8/mm		1.60 K	
	Receiver errors	In-phase (σ_ϕ=1º)	2.06/º	2.06 K		
		Amplitude errors (TPRad)				1.43 K
Total (quadratic summation)				6.82 K	13.39 K	1.43 K

extended source, using a rectangular window to the visibility function before retrieving the brightness temperature. It should be noted that the rectangular window has largest errors, been the worst case, with a sensitivity of approximately 15 K, while for the Blackman window could be reduced to 6 K. Others results have been obtained because the simulator works with discrete signals, grid plane (u, v), with a residual error of 0.24 K.

6.3 Acquisition mode

In spite of the PAU-SA's Physical Modeling Simulator has been implemented to perform the function of the simulator of the instrument and also to process external data in the same environment. This last part is under development to have a centralized control of the PAU-SA instrument. In "Acquisition Mode", external data are processed being the hardware parameters defined by the real instrument. In this case, the user can choose between the next integration times: 10 ms, 100 ms, 0.5 s and 1 s for calibration and image recovery procedures and the selected the processing window and select the inversion method for the image recovery mode. This information is sent to the FPGA to control the input selection switches of the receivers. A screenshot of the Graphical Interface is shown in Fig. 6.14.

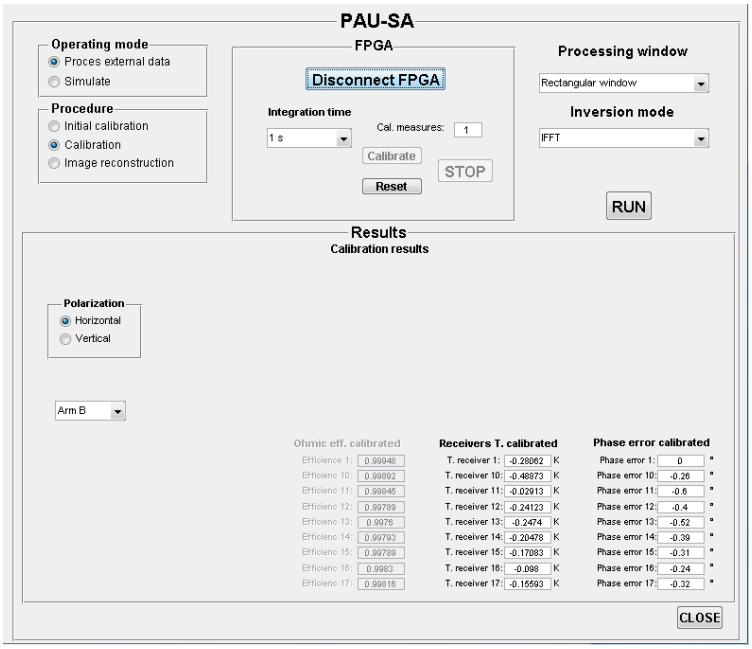

Figure 6.14. Front panel of the PAU-SA's acquisition mode.

6.4 Discussion and considerations

The PAU-SA's physical modeling simulator has been presented as well as the results of several tests with point and extended sources. The goal of this environment is to validate and understand better the PAU-SA instrument modeling all the system as faithfully as be possible with $N_{EL} = 8$ and $d = 0.816\ \lambda$. This has the peculiarity to introduce a set of error independently, in order to determine which error, degrade the image reconstruction with the objective to improve the system continuously. Concerning the tests carried out in the simulator, the first part has been focused in the point sources. The beamwidth at -3 dB has been determined theoretically with the two methods (Eqn. 4.77 and Eqn. 4.79) obtaining better results with the last one especially in the rectangular

Chapter 7

PAU-SA: instrument description

The purpose of this chapter is the description of the PAU-SA instrument completely designed and implemented in the frame of this Ph.D. thesis. In the sections of this chapter, an overall vision of the different subsystems is given. Due to the complexity to explain in detail the instrument, a summary will be presented to provide a global understanding of the system.

PAU-SA implementation overview

This chapter presents in the next sections the individual modules in which the system has been divided, (Fig. 7.1). This has been separated in two main blocks: the PAU-SA instrument and the mobile unit, been organized in three parts. The first part presents the main modules of the instrument and how they are interconnected. The second part presents the onboard computer, and the external computer and also the commands to control the PAU-SA instrument. Finally, the mobile unit is presented. Due to the large number of modules and interconnections in the block diagram, each individual module or group of these have been numbered in brackets according to its functionality. The next sections present these modules according to the established order. For a better understanding of the global system, a brief operational description was presented in chapter 5.

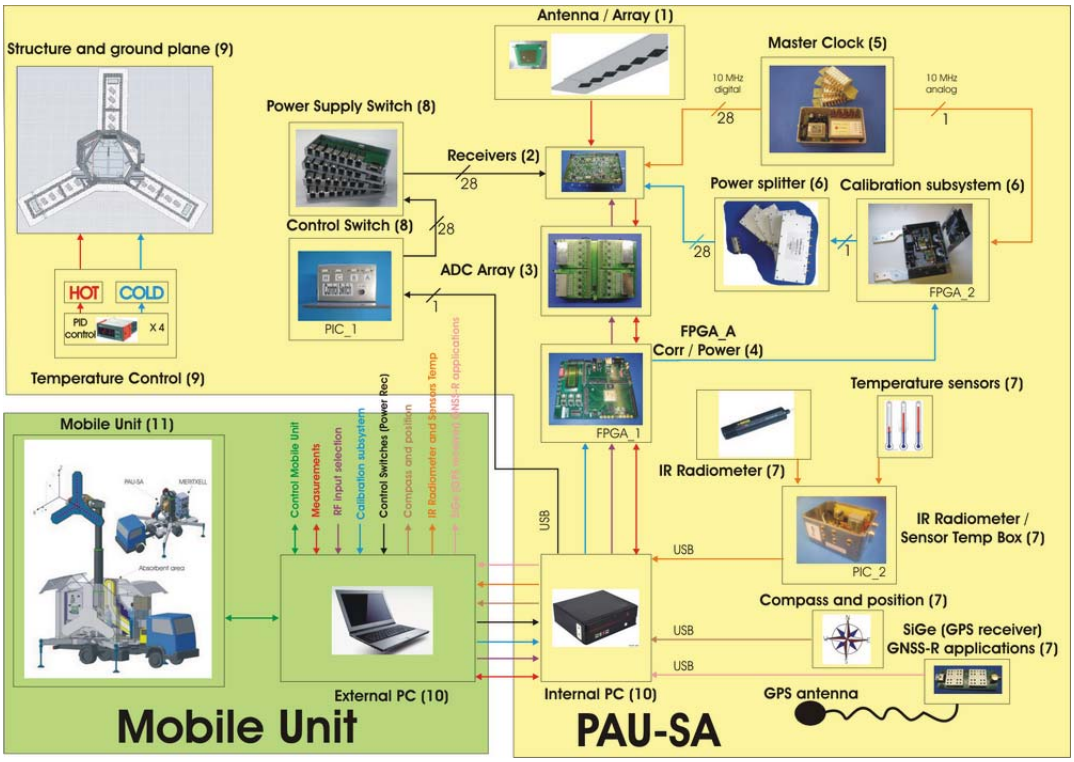

Figure 7.1. PAU-SA's system block diagram indicating the interface connections between different modules.

7.1 PAU-SA's antenna array

The goal of this section is to analyze the different elements of the PAU-SA's antenna array. The first part is devoted to present a brief description of the elementary antenna and its main characteristics. The following part shows the antenna distribution that constitutes the antenna array. Figure 7.2a, shows in a red box the PAU-SA's elementary antenna / array located in the PAU-SA's system block diagram, Fig. 7.1. As expected, the antenna is only connected to the receiver module (Section 7.2). Figure 7.2b shows a picture of the global array distribution.

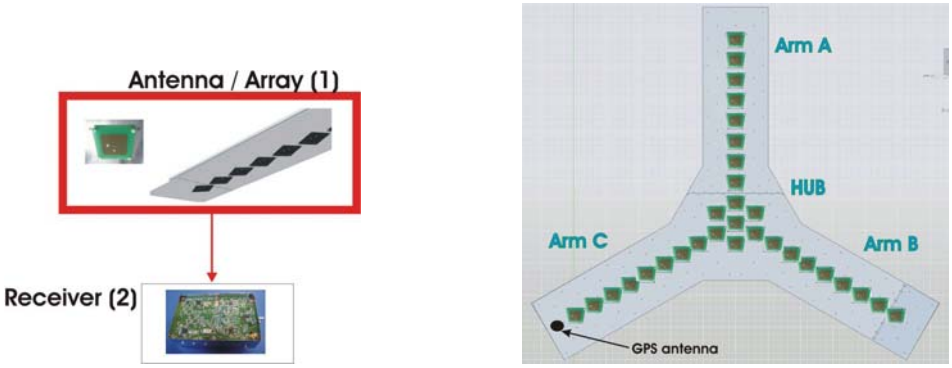

(a) (b)

Figure 7.2. a) PAU-SA's antenna identification in the PAU-SA's system block diagram. b) Antenna distribution in the PAU-SA' array.

7.1.1 Elementary antenna

The first element of the instrument is the antenna. The antennas used in PAU-SA are the same ones designed for PAU-RA [38]. These are square patch antennas [90] with dielectric air to resonate at 1,575.42 MHz (GPS L1 frequency). The patch side is 7.9 cm and the external dimensions of 11.75 cm; and it is printed on 0.6 mm FR4 substrate offering simplicity and low production costs. These types of antennas have high antenna efficiency (low ohmic losses, measured $\eta_\Omega = 0.98$). The antenna patch is located at 9 mm of the ground plane, setting the half-power beamwidth of 60º. It is supported by four nylon screws at the corners and a metallic one in the center used to connect the patch to ground plane. Figures 7.3a and 7.3b show the elementary antenna where is possible to distinguish two little square capacitive pads used to feed the vertical and horizontal polarizations. The position and the dimensions of these pads with respect to the center determine the antenna matching. Figures 7.3c and 7.3d show the matching of the vertical and horizontal polarizations respectively. As it can be noticed, both polarizations have a matching better than -22 dB.

In order to determine the antenna pattern, it has been measured in the UPC anechoic chamber [87] at E-plane and H-plane respectively. As it can be observed in Figs. 7.4a and 7.4b, the antenna pattern over the beam can be reasonable well approximated by a cardioid. Both of them have a good agreement, except at large off-boresight angles,

where the antenna pattern is much attenuated in both cases, and the disagreement has no relevance. Table 7.1 summarizes the main parameters of the PAU-SA'patch antenna.

7.1.2 PAU-SA's structure array

Figure 7.5a shows the structure of PAU-SA and the corresponding antenna numbering. The array consists of 25 antennas distributed over a Y-shaped array, with 8 antennas

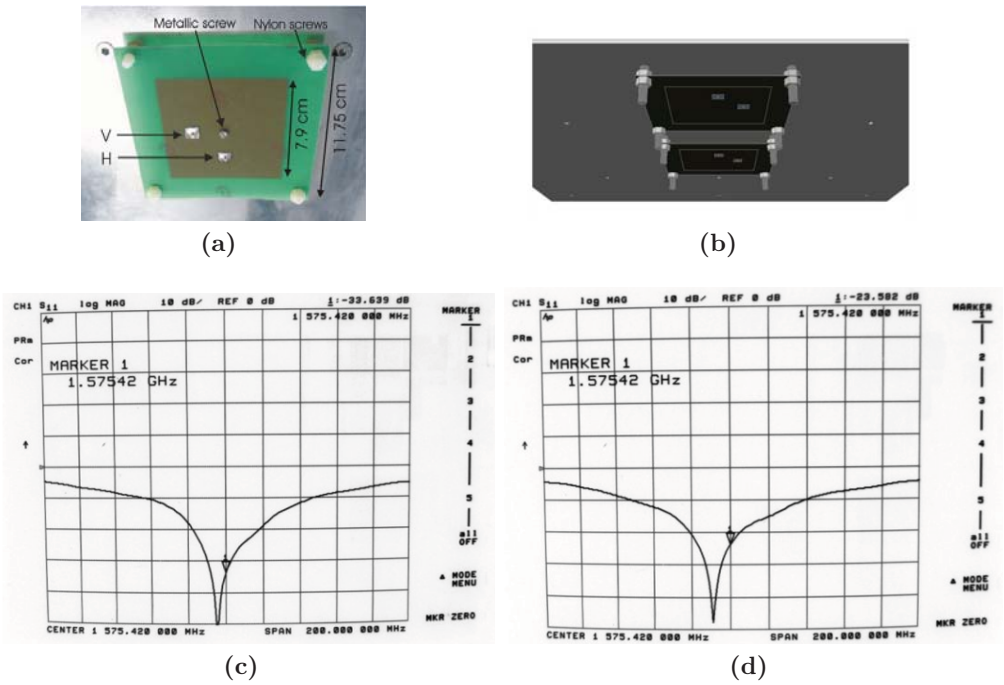

(a) (b) (c) (d)

Figure 7.3. a) Picture of the elementary patch antenna, b) Virtual image of the PAU-SA's elementary antennas located in the ground plane, c) Matching at Vertical (V) polarization $|S_{11}|$ = -33.64 dB, and d) Matching at Horizontal (H) polarization $|S_{11}|$ = -23.58 dB.

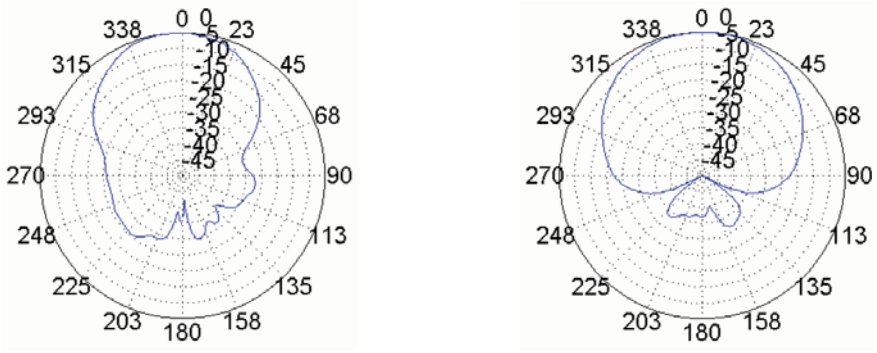

(a) (b)

Figure 7.4. Normalized cut of the power pattern [dB] at V-polarization a) E-plane, and b) H-plane.

Table 7.1. Nominal parameters of the PAU-SA's patch antenna.

Parameter	Value
Antenna type	Patch
Material	FR4 /0.6 mm
External dimensions	11.75 x 11.75 cm
Central frequency	1,575.42 MHz
Half-power beamwidth	60 °
Polarization	V/H
Directivity	7.08 dB
Gain	7 dB
Cross-pol	-30 dB
Antenna efficiency	0.98
Matching $\lvert S_{11} \rvert$ V/H	≤-22 dB

per arm and a central one for radiometry applications. Three extra dummy antennas (with no receiver connected) are placed at the end of each arm to avoid antenna voltage patterns distortion. Moreover, three antennas are placed around the central one for future GNSS-R applications [32]. Nowadays this part has been substituted by a ceramic patch GPS antenna and a GPS L1 receiver (SiGe GN3S Sampler v.2) [91] connected to the internal PC for acquisition of the raw GPS data. The choice of the distance between the antennas was part of this work. As shown in chapter 4, a maximum distance of $\lambda/\sqrt{3}$ (d = 0.577 λ) is required to avoid aliasing in the image reconstruction. However, PAU-SA, due to the physical side of the receivers and antennas, a minimum distance of 15.5 cm (d = 0.816 λ) is feasible, thus a certain amount of aliasing will affect the borders

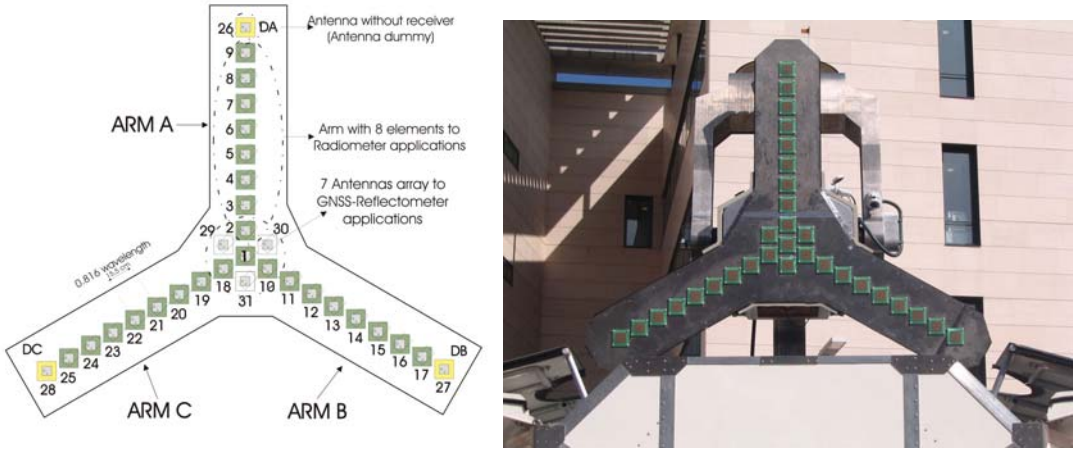

(a) **(b)**

Figure 7.5. a) Scheme of the antenna distribution in the PAU-SA' array. b) Mechanical layout of PAU-SA consists of three arms forming a Y-shape.

of the recovered image. However, less than in MIRAS, where d = 0.875 λ. As it can be seen in Fig. 7.5a, all antennas have the same orientation to maintain the phase of the array. Figure 7.5b shows a picture of the PAU-SA'array without the radome. The array size has been chosen as large as been possible to improve the angular resolution. At the beginning, it was selected to have 10 antennas per arm, but finally it was reduced to 8 elements in order to be able to take the instrument out the laboratory. Although the strong similarity between the real system and the scheme, it can be noticed that the corners of the arms have been cut due to space limitations in the truck location.

7.1.3 Antenna coupling effects in PAU-SA

The proximity of the antennas and their wide beamwidth, while reducing the aliasing effects and enlarging the AF-FOV, lead to antenna coupling effects. Although the chosen antennas have low mutual impedance, this effect is still considerable and it mainly affects the last antenna radiation pattern of each arm. In [92] and [93], this phenomenon was analyzed in depth. It can be demonstrated that the antenna voltage pattern measured under mutual coupling, is a linear combination of the free-space antenna voltage patterns and other terms, that are proportional to the mutual coupling, and are weighted by an exponential term at the same spatial frequency as the baseline formed by the antennas being coupled:

$$F_{n1}^{L}(\theta,\phi) \approx \frac{Z_L}{Z_L + Z_{in}}\{F_{n1}^{0}(\theta,\phi) - \sum_{\forall m \neq 1} \frac{Z_{1m}}{Z_L + Z_{in}} F_{nm}^{0}(\theta,\phi) e^{jk(m-1)d\sin(\theta)}\}, \tag{7.1}$$

where $F_{nm}^{0}(\theta,\phi)$ is the free-space antenna voltage pattern, Z_L and Z_{in} are the load and input impedances as shown in Fig. 7.6. In order to obtain realistic values, mutual impedance

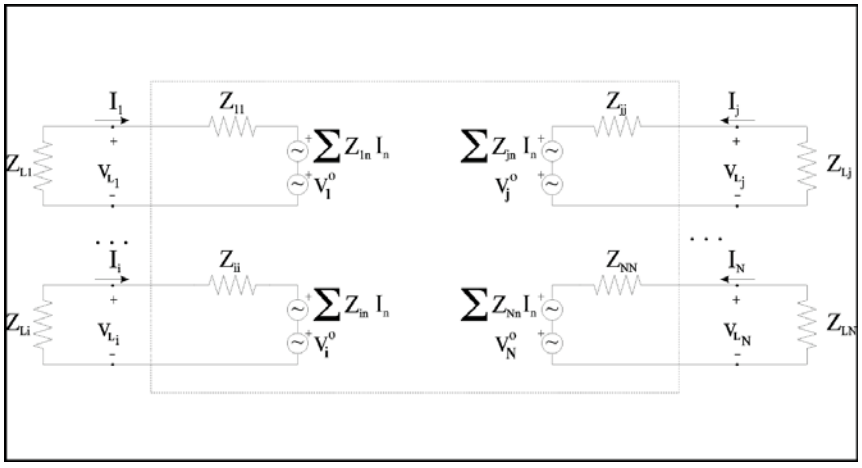

Figure 7.6. Multiport representation of interferometer antenna array [93].

between adjacent antennas have been measured, extrapolating to the rest of antennas. Taking into account that coupling between two antennas of the same arm is slightly different from that between antennas located on different arms. For instance, coupling between antennas 1 and 2 of Fig. 7.5a is different from coupling between antennas 1 and 10 as

polarizations are aligned differently. Thus, in order to have values for all the possible baselines, S parameters between antenna pairs 1-2, 1-18 and 2-18 have been measured (Table 7.2) and the mutual impedance has been calculated is given by Eqn. 7.2.

Table 7.2. Adjacent antennas S-matrix (dB/degrees).

Antenna	1	2	18
1	$-25.8\ \angle 126.7^o$	$-23.16\ \angle 19.34^o$	$-35.4\ \angle 124^o$
2	$-23.16\ \angle 19.34^o$	$-37.7\ \angle -134.1^o$	$-27.8\ \angle -4^o$
18	$-35.4\ \angle 124^o$	$-27.8\ \angle -4^o$	$-15.6\ \angle 86^o$

$$\overline{\overline{Z}} = (\overline{\overline{I}} + \overline{\overline{S}})(\overline{\overline{I}} - \overline{\overline{S}})^{-1}. \tag{7.2}$$

Then, this value can be extended to antenna pairs m, n with distance r taking into account the expression:

$$Z_{m,n} = Z' \frac{e^{-jkr}}{r}. \tag{7.3}$$

Figure 7.7a shows the normalized antenna voltage pattern for antenna number 9, at the

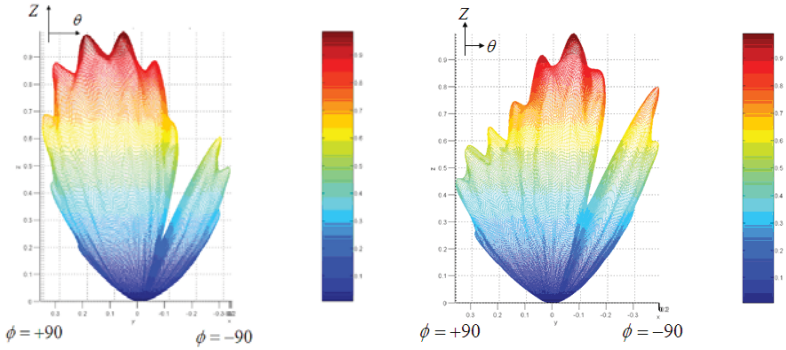

(a) **(b)**

Figure 7.7. Theoretical normalized antenna voltage pattern at the end of each arm a) without dummy antenna and, b) with dummy antenna.

end of the A-arm of Fig. 7.5a, with or without the use of the dummy antenna. To avoid antenna pattern distortion towards the end of the arm a dummy antenna is used, producing the pattern of Fig. 7.7b, where the maximum has been centered and is better pointed toward the boresight. Finally Fig. 7.8 shows the complete set of antenna patterns.

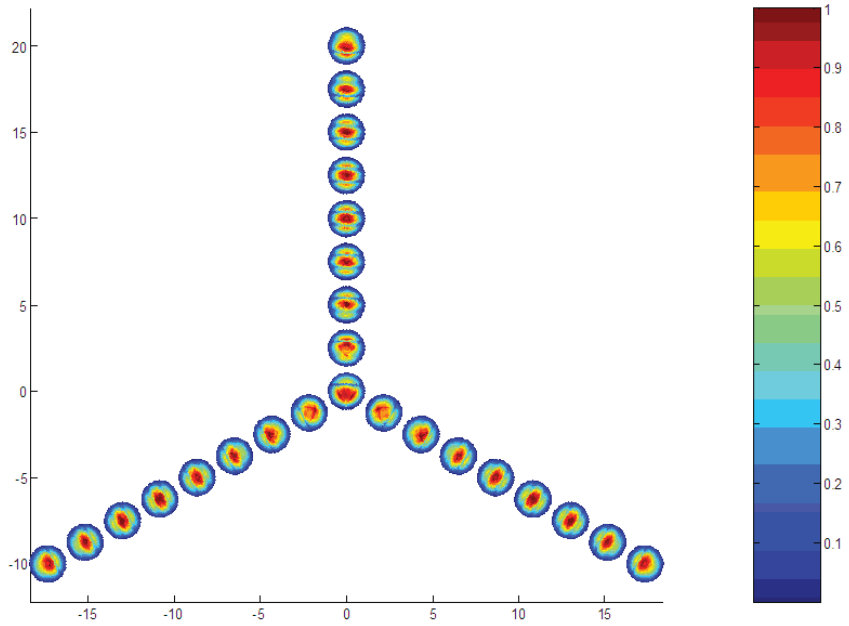

Figure 7.8. Normalized antenna voltage pattern in PAU-SA (using dummy antennas).

7.1.4 Conclusions

In this section, the description of the PAU-SA's element antenna has been presented. A patch antenna type has been selected for simplicity and low costs. Measurements of antenna matching at both polarizations and the antenna pattern has been measured with very satisfactory results. Once introduced the elemental antenna, the PAU-SA's array has been presented. Antennas are spaced 0.816 λ to achieved an AF-FOV of $\sim 50^{o}$. A dummy antenna has been placed at the end of each arm to improve the antenna pattern similarity. For simplicity, the ground plane has not articulated moving parts, determining the size of the instrument. The array size has been selected as large as possible to obtain the best angular resolution and have the possibility to take the instrument out of the laboratory. Nowadays, for simplicity the central elements that would be used to GNSS-R applications have been replaced by a single ceramic patch antenna connected to a GPS receiver an data logger.

At present the free-space voltage radiation patterns and the mutual coupling between them are simulated, while in the near future they should be replaced with the anechoic chamber measured ones to improve the quality of the image reconstruction.

7.2 The receiver

This section presents the receiver's design. A full explanation of the receiver design with layouts, list of components etc. can be found in [94]. Since this Ph.D. thesis started during the M.Sc which the design of the PAU-RA's receiver [94], witch has then been re-used and adapted for the PAU-SA's receiver, as well as the other instruments of the PAU family (including PAU-RA, griPAU etc. presented in chapter 2), a trade-off between both instruments specifications is necessary. Figure 7.9a shows in red the PAU-SA's receiver location and interconnection in the PAU-SA's system block diagram. As it can be noticed, the receiver is one of the modules with more interconnections, being a critical part of the project. Moreover, the receiver is one of most sensitive elements of the analog part, been specially designed to have a linear and stable behavior, avoid EMC, and channel cross-talk etc. Figure 7.9b shows the receiver distribution in the PAU-SA's array. Since each receiver has its own antenna, the receives and antennas have the same distribution.

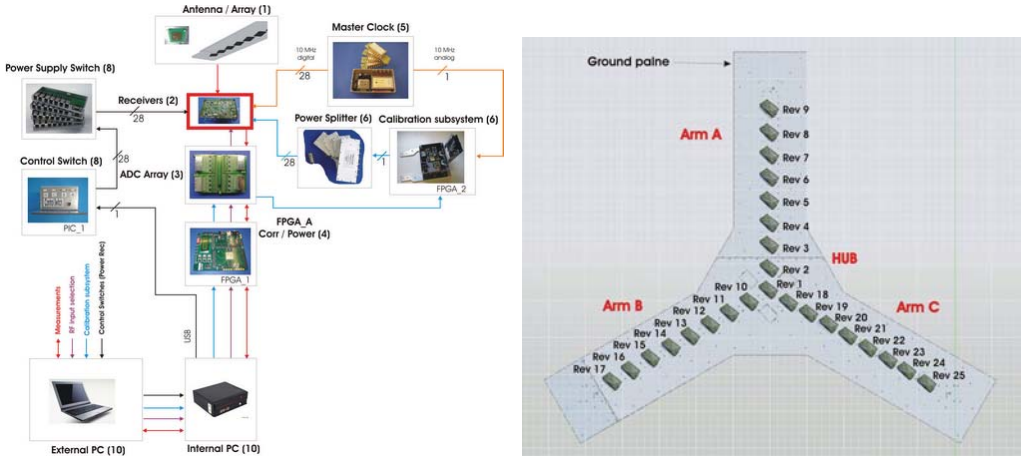

(a) (b)

Figure 7.9. a) PAU-SA's receiver location showing the interface connections between modules, and b) receiver distribution in the PAU-SA' array.

7.2.1 Design of PAU-RA and PAU-SA receivers

Since PAU-RA and PAU-SA have different topology requirements it is necessary to accomplish a trade-off between the specifications in order to share the same receiver. Moreover, each one merges two different sub-systems: an L-band radiometer (PAU-RAD) and a GNSS Reflectrometer PAU-GNSS-R. Before entering in the design details of the front-end, it is necessary to set the specifications for each instrument, and thus determine how a single receiver could be designed to satisfy the following objectives, as shown in Table 7.3. Apparently, both instruments have a high number of channels, but the FPGA used to process has limited resource such as: number of available I/O pins in each FPGA. Accordingly, the topology of the ADC output (parallel or serial) has been set for the same reason.

Table 7.3. Comparative table between PAU-RA [38] and PAU-SA (Section 5) with their respective instruments: Radiometer (RAD) and Reflectometer (GNSS-R).

	PAU-RA		PAU-SA		
Parameter	RAD	GNSS-R	RAD	GNSS-R	Limited
Operating frequency	L-band (1-2 GHz)	**1575.42 MHz**	L-band (1-2 GHz)	**1575.42 MHz**	1575.42 MHz
Data acquisition	non-continuous	**continuous**	non-continuous	**continuous**	continuous
Input signal level	- 110 dBm	-133 dBm	- 110 dBm	-133 dBm	
Polarization	**V & H** to obtain the four Stokes parameters	RHCP	**V & H** to obtain the full Matrix correlation (V, H and cross-pol)	RHCP	Right hand circular implemented as combination of V & H
Number of antennas or receivers	**4 x 4 array**	central 2 x 2 array	**25 Y-shape**	7 central Y-shape	set receiver's size
Number chains per receiver	**4 TPRs**		**2 TPRs**		
Total chains	**64 TPRs**		**50 TPRs**		
Signal quantization	**(8 bits)** for SLL > 20 dB and MBE > 94 %	(1 bit) for C/A code	**(1 bit)** matrix correlation and **8 (bits)** power measurements	(1 bit) for C/A code	(8 bits) for radiometry application
ADC topology	8 bits /parallel	1 bit	8 bits /serial	1 bit	Limited number of I/O pins in FPGA
I/O FPGA	Altera (High)		Xilinx (Low)		
Calibration	**Gain & phase**	Phase	**Gain & phase**	Phase	Gain & phase

7.2.2 PAU-RA's receiver topology

Since this Ph.D. thesis began with the receiver design for PAU-RA, we will start explaining which factors were taken into account in its design, and who has been modified to implement the PAU-SA's receiver. As previously mentioned, the number of I/O pins in the selected FPGA has been an important factor to determine the receiver design. Focusing on the PAU-RA's receiver structure, the radiometer stability requirements lead to a Dicke or noise injection topology to compensate for gain fluctuations, as much as possible. However, the reflectometer requires continuous data acquisition, and the input cannot be chopped. Therefore, a new pseudo-correlation topology, see Fig. 7.10 was devised. The receiver has two radiometers, one for each polarization vertical and horizontal (V/H), and each one has two TPR chains: one with the antenna and the reference noise signals in phase (branch 1, Eqn.7.4), and the other one with the noise signal 180º out of phase (branch 2, Eqn.7.5). The reference noise signal is generated by the 100 Ohm resistor of a Wilkinson power splitter used to divide the input signal [35]. Afterwards each chain is individually amplified in a TPR topology, down-converted and amplified again to allow an 8-bit quantification for later digital processing (cross-correlation, calibration, and beamforming). Since the noise introduced by the amplifiers is uncorrelated (not considering the cross-talk), it vanishes when the output signals are cross-correlated (branch 3, Eqn.7.6). Therefore, the output is proportional to the difference between the antenna temperature and the physical temperature of the Wilkinson power splitter resistor. That is, the system output is the same as that of the Dicke radiometer, but the input signal is

not chopped, so that it can be used to track the GPS-Reflected signal.

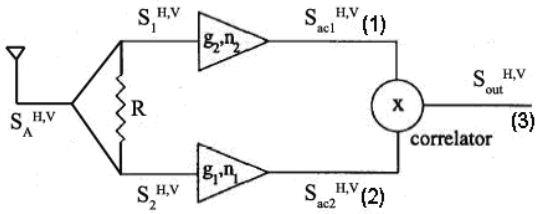

Figure 7.10. Pseudo-correlation's topology block diagram composed of Wilkinson power splitter, two TPR chains and a correlator.

$$S_{ac1}^{H,V} = \left(\frac{S_A^{H,V} + S_R}{\sqrt{2}} + n_1 \right) \cdot g_1^{1/2}, \tag{7.4}$$

$$S_{ac2}^{H,V} = \left(\frac{S_A^{H,V} - S_R}{\sqrt{2}} + n_2 \right) \cdot g_2^{1/2}, \tag{7.5}$$

$$S_{out}^{H,V} = \left(\frac{(S_A^{H,V})^2 - (S_R)^2}{2} \right) \cdot \sqrt{g_1 g_2}. \tag{7.6}$$

As described in the next sections, the receiver has been designed in two separated boards, one for the RF stage using microstrip technology. The RF board implements: switches for input signal selection (calibration or antenna acquisition), the Wilkinson power splitter, Low Noise Amplifiers (LNAs), and Band Pass Filters (BPFs). The second board performs the IF stage implementing the down-converter modules, video preamplifiers, and matching network. For space reasons, the cross-correlation module has been implemented externally in a FPGA.

7.2.3 Receiver requirements

Before beginning with the hardware design, it is necessary to know the maximum dimensions for the implementation, delimiting the receiver size. The inter-element spacing determines the maximum size of the receiver to which the antenna is connected. In this case PAU-RA is more restrictive than PAU-SA. As shown the Fig. 7.11 the antenna spacing in PAU-RA is found to be 0.63 λ at L1 of GPS signal with 12 cm to achieve a MBE larger than 94% in PAU-RAD [38]. At this point of the design, the problem of receiver dimension was found. In this case, it was limited to (11 cm x 7 cm x 3 cm), corresponding to a standard metallic box. As it can be seen in Fig. 7.11 this disposition leaves enough space even for wiring purposes.

To implement the receiver in the reduced space, it has been necessary to use commercial components. Taking into account that the operating frequency is the L1 GPS band, and that many components were already designed for its commercial applications, some of them have been used for the implementation of this receiver. One that helped to fulfil the size requirements has been the use of a Zarlink GP2015 GPS front-end as down-converter. The second key point in terms of surface availability is the implementation

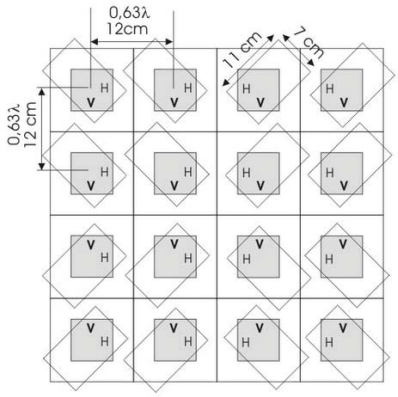

Figure 7.11. PAU-RA's array distribution.

of the Wilkinson power splitter. At the operating frequency (1,575.42 MHz) and using transmission lines the area required would have been unacceptably large approximately 5 cm (corresponding to $\lambda/4$). Therefore, an implementation with lumped elements has been selected to minimize the occupied area. Others components for GPS applications such as Low Noise Amplifier (LNA)s and SAW filters have also been used.

7.2.4 PAU-RA's receiver implementation

In this section, the structure of the PAU-RA's receiver is defined, and each is explained: receiver's topology, calibration purpose, isolation among desired signals, signal conditioning stages, wire's type etc. The block diagram corresponding to the receiver design is presented in Fig. 7.12. As it can be noticed, this is composed of two pseudo-correlation topologies, one for each polarization. The correlator module has been implemented externally for space reasons. The receiver was carefully designed to preserve symmetry, minimize cross-talk, and interconnection routes, while maintaining equal delays for all paths, being divided in two parts: RF and IF stages. Due to space reasons the two stages have been implemented one over the other one, using different substrates according to the frequency of each stage.

7.2.5 RF stage

In order to ensure a constant impedance of the transmission lines, the RF stage has been implemented with ROGERS 4003 (H = 0.8 mm) substrate. Its structure consists of two parts as shown in Fig. 7.13. First, the switching stage and then an amplification stage. The receiver requirements are summarized in Table 7.4. The main objective of the RF stage is to achieve a gain of at least 30 dB over the input signals, keeping the NF as low as possible. This is necessary to work in the linear region of the down-converter module located in the IF stage. The matching of each input/outputs ports have to be at least -10 dB. The required isolation between antenna signal and calibration (correlated and uncorrelated) signals has been determined being better than -80 dB. Finally, the cross-talk between adjacent chains (ports 2-3) has to be better than -40 dB. This parameter

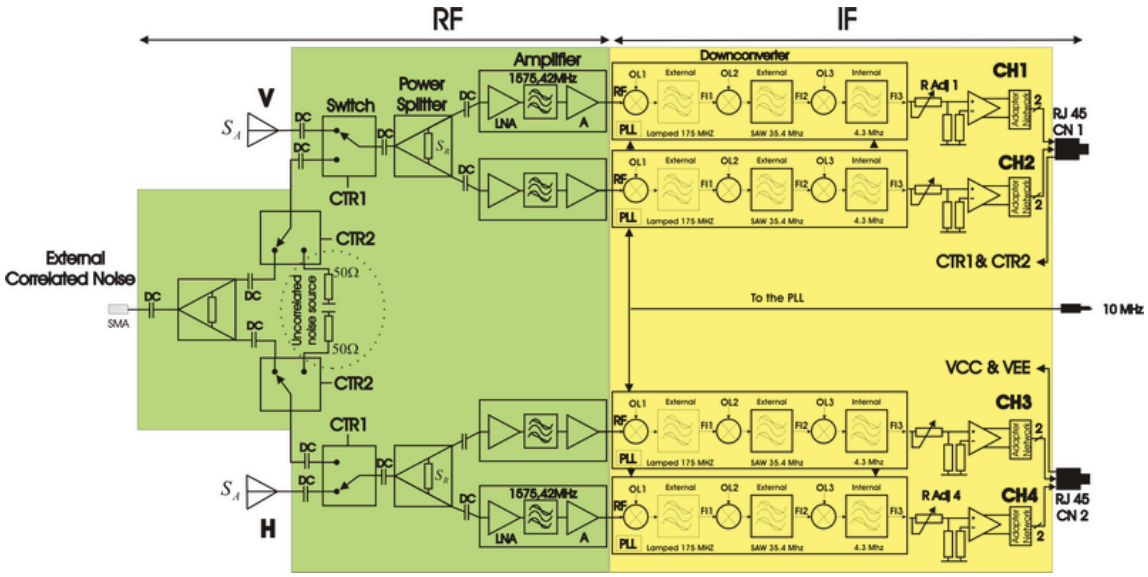

Figure 7.12. PAU-RA's receiver uses two pseudo-correlation topologies one per polarization (V & H).

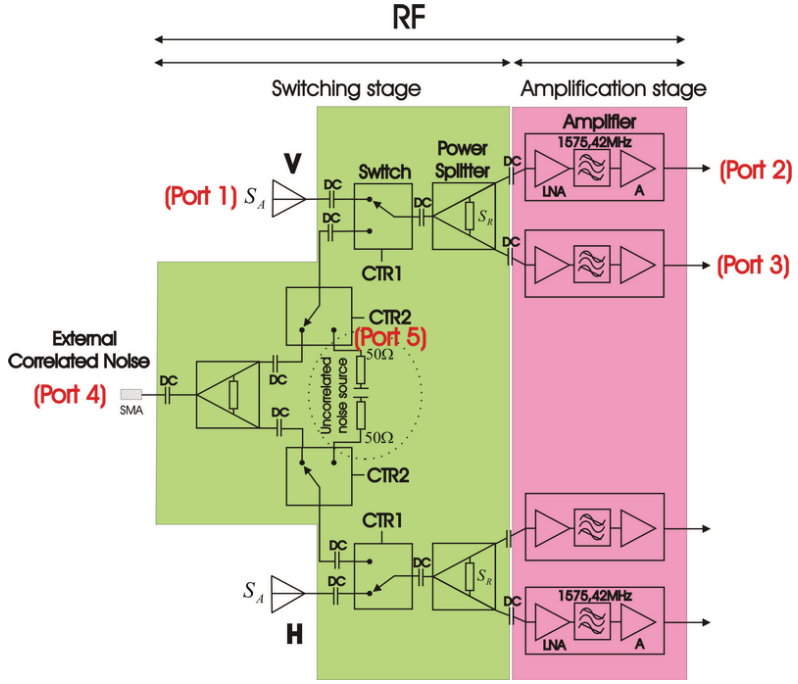

Figure 7.13. PAU-RA RF stage.

is very important in the pseudo-correlator topology, since a poor insulation between channels imply poor results. Fig. 7.14 shows the outline of the isolation between channels conditioning.

where

- T'_A is the antenna temperature with losses,

Table 7.4. PAU-RA'receiver requirements.

Parameter	Definition	Nominal Requirement
$\boldsymbol{Z_0}$	Impedance	50 Ω
$\lvert\boldsymbol{S_{21}}\rvert$	RF gain	≥ 30 dB
$\lvert\boldsymbol{S_{XX}}\rvert$	Port matching	≪-10dB
$\lvert\boldsymbol{S_{14}}\rvert$	Isolation ports 1-4	< -80 dB
$\lvert\boldsymbol{S_{32}}\rvert$	Cross-talk ports 3-2	< -40 dB

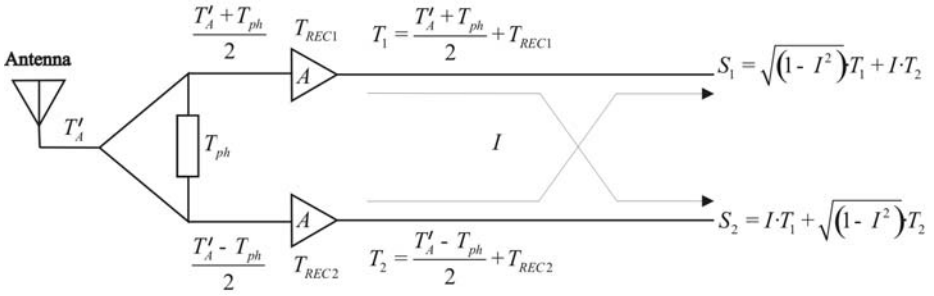

Figure 7.14. Isolation between two adjacent channels of a pseudo-correlation receiver.

- T_{ph} is the physical temperature introduced by the Wilkinson power splitter,
- $T_{REC\,1,2}$ is the receiver temperature introduced by in each channel,
- $T_{1,2}$ is the equivalent temperature in each channel,
- I is the isolation between channels ports ($I = 40$ dB or 10^{-2} in linear),
- $S_{1,2}$ is the equivalent temperature in each output,

Correlating the two outputs, the resultant is obtained in Eqn. 7.7.

$$\big(I\sqrt{1-I^2}\big)\langle T_1T_1^*\rangle + \big(1-I^2\big)\langle T_1T_2^*\rangle + I^2\langle T_2T_1^*\rangle + \big(I\sqrt{1-I^2}\big)\langle T_2T_2^*\rangle, \tag{7.7}$$

After some straightforward algebraic manipulations, it is possible to obtain Eqn. 7.8 and substituting these values in Eqn. 7.9.

$$\approx 10^{-2}\big(\frac{T'_A+T_{ph}}{2}+T_{REC1}\big)+\frac{T'_A-T_{ph}}{2}+10^{-2}\big(\frac{T'_A+T_{ph}}{2}+T_{REC2}\big), \tag{7.8}$$

$$\approx \underbrace{0.51}_{\text{linearity error}}\cdot T'_A - \underbrace{0.49}_{\text{linearity error}}\cdot T_{ph} + \underbrace{0.01\cdot T_{REC1}+0.01\cdot T_{REC2}}_{\text{Bias}}. \tag{7.9}$$

As it can be appreciate in Eqn. 7.8, the output should be proportional to $(T'_A - T_{ph})$ being possible increasing the isolation between channels.

Concerning the switching stage is controlled externally by the Control Unit (CU) implemented in the FPGA and switches between three different states: the antenna acquisition and two calibration purposes. Table 7.5 shows the selected RF signal in

Table 7.5. RF signal selection.

CTR2	CTR1	RF signal
0	0	Correlated Noise (external)
0	1	Antenna acquisition
1	0	Uncorrelated Noise (internal)
1	1	Antenna acquisition

function of CTR1 and CTR2 external control signals. Usually this stage is connected to antenna acquisition, necessary for GNSS-R applications. The input antenna is connected directly to the patch antenna through a 50 Ω cable. To carry out the calibration process two signals are selected by means of CTR2 control signal: uncorrelated noise, generated internally by a matched load of 50 Ω, to compensate instrumental biases, and a two level correlated noise, same for all receivers, generated externally from a common noise source. It is necessary to compensate different phases and amplitudes among channels. To implement this structure two switches model RSW-2-25P by MiniCircuits have been used, one for each radiometer, increasing the isolation between correlated noise and antenna signal. Once selected, the signal is input into a Wilkinson power splitter model DS52-0004 by MACON, which divides the signal in two. These signals are amplified to adjust the antenna input power (aprox -110 dBm), to the down-converter linear behaviour power margin. According to Friis formula, to achieve the best NF factor, the first element of the chain should be the LNA. In this case the first elements have an attenuator behavior being: a switch to select between different signals with a insertion loss of 1.1 dB, and the Wilkinson power splitter for topology requirements, with a insertion loss of 0.4 above 3 dB. In order to minimize the NF of the receiver, the immediate next element is a LNA, followed by a band-pass filter centered to 1,575.42 MHz, and next, a second amplifier to obtain the necessary gain, (Fig. 7.12). The total RF gain is aprox 33.3 dB, obtaining an input power level for down-converter of aprox -76.7 dBm, within the linear behaviour, and a total NF of 5.3 dB, including the noise generated by the Wilkinson power splitter, adding 3 dB. Another point to be taken into account is the high isolation among signal conditioning stages necessary to obtain a proportional output to $T'_A - T_{ph}$, being T'_A the antenna temperature with losses, and T_{ph} the physical temperature of the Wilkinson power splitter resistor. For this reason, these stages are highly isolated using ground drills and a metallic structure to electrically isolate the channels and minimize the cross-talk better than -40 dB.

7.2.6 Noise Figure estimation

According to the Friis formula, the NF depends mainly on the first elements of the chain. Figure 7.15 shows the elements involved in the calculation of this parameter and Eqn. 7.10 shows the resulting expression.

$$F_{eq} \simeq L_1 + L_1(F_2 - 1) + L_1L_2(F_3 - 1) + \frac{L_1L_2}{A_3}(F_4 - 1) + \frac{L_1L_2L_4}{A_3}(F_5 - 1). \qquad (7.10)$$

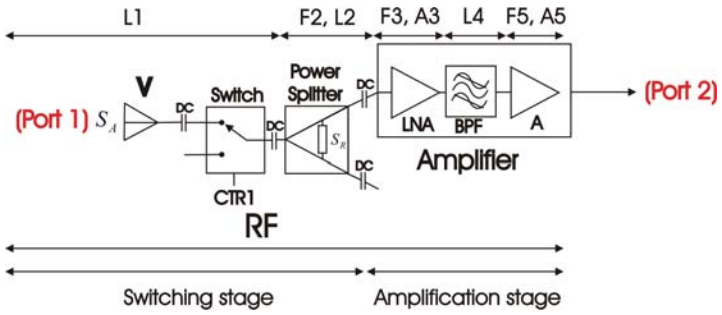

Figure 7.15. Block diagram for the PAU-RA RF stage to calculate the NF of the system.

Since the gain of the LNA is high, therefore, it is possible to neglect the terms divided by the LNA gain, simplify Eqn. 7.10 to:

$$F_{eq} = L_1 + L_1(F_2 - 1) + L_1L_2(F_3 - 1). \tag{7.11}$$

To obtain an estimated value of the equivalent NF, Table 7.6 shows in detail a description of each element and its NF contribution. Finally substituting these values in Eqn. 7.11

Table 7.6. NF elements contribution in the PAU-RA RF chain.

Element	Description	Nominal value (dB)	lineal
L_1	Insertion losses of antenna connector + switch + 2 DC blocks	0.1+1.1+2*0.05=1.2	1.318
L_2	Insertion loss of Wilkinson + 3dB + DC block	0.4+3+0.05=3.45	2.213
F_2	NF of Wilkinson power splitter	3	1.995
F_3	NF of the LNA	1	1.258
A_3	Gain of the LNA	26	398.107

the equivalent NF results:

$$NF = 10\log(\mathrm{F_{eq}}) = 10\log(3.4) = 5.3\,\mathrm{dB}. \tag{7.12}$$

and therefore the equivalent T_{REC} considering a physical temperature of 290 K is:

$$T_{REC} = (F_{eq} - 1)T_{ph} = (3.4 - 1)290\mathrm{K} = 696\,\mathrm{K}. \tag{7.13}$$

7.2.7 IF stage

The main goal of the IF stage is to shift the RF signal to the IF signal using a super-heterodyne receiver or down-converter. Moreover this stage pre-amplifiers the IF signal to send it to the ADC module through an Ethernet cable (IF stage of the Fig. 7.12). This stage has been implemented with a FR4 substrate. The output of each RF chain is interconnected by means of semi-flexible cable to the input of each down-converter located in this stage (Fig. 7.21a). It mainly consist of the translation from 1,575.42 MHz to 4.309 MHz with a bandwidth of 2.2 MHz amplifying the RF signal by approximately 52 dB. To put the down-converter into operation, a common external Transistor–Transistor Logic (TTL) signal of 10 MHz is necessary. This signal is distributed by a coaxial cable and it is used to internally synthesize the different local oscillators through the PLL. The most innovative fact of the IF stage is the use of a commercial GPS receiver is used for

radiometric applications. Usually these devices provide the output at IF digitized to 2 bits (sign and magnitude) enough to recover the C/A code, used in GPS applications. Originally, it was intended to determine the signal's power using just 1 bit as in [95] using the Nemerix GPS device model NM1100, but with this coarse sampling the array pattern exhibited side lobes at a level of only 5 dB below the main one PAU-RAD, witch was totally unacceptable for radiometric applications. For this reason it was determined that a minimum quantification of 8 bits was necessary to obtain at least 20 dB of side lobe level [38]. Therefore, the Zarlink GP2015 GPS down-converter was used instead, since it has an analog output test that can be sampled (pin 1, Fig. 7.16). To use a commercial

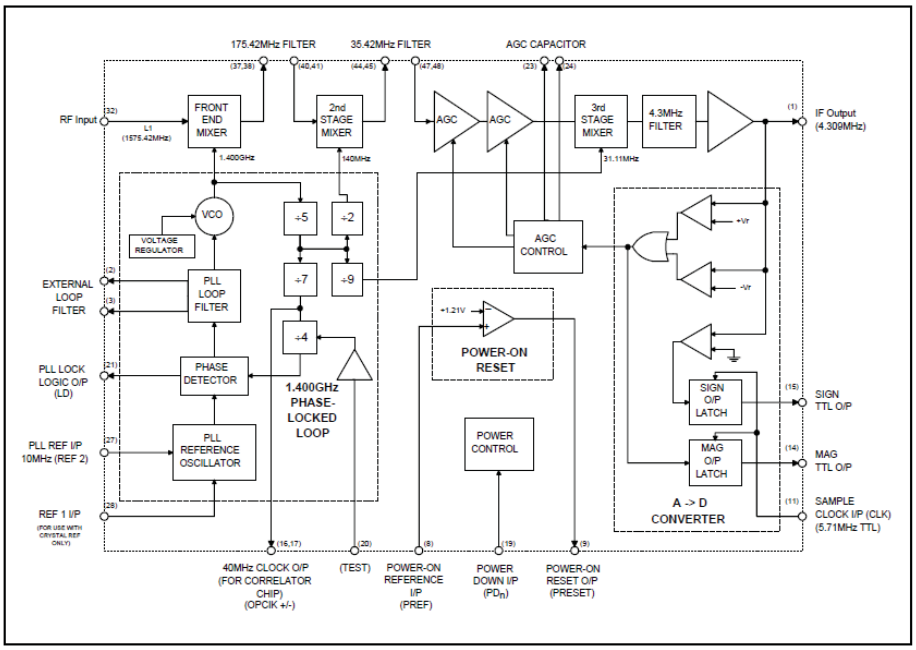

Figure 7.16. GP2015 block diagram, showing the LO generations through the PLL module, the three mixers, and the analog output (pin 1) [96].

GPS down-converter for radiometric applications it must have a linear behavior, however, all commercial GPS receivers have an Automatic Gain Control (AGC) circuitry which modulates the gain depending on the input signal remain constant the power level at its output. Fortunately, the GP2015 has accessible the AGC control (pins 23 and 24) which has been tuned forcing a differential voltage between the AGC pins. Fig. 7.17 shows the linear behavior of the GPS down-converter for radiometric applications. For input levels from -85 dBm to -60 dBm there is a linear behavior, with a gain of 52 dB, and with a maximum linearity error of 0.25 dB. At the receiver output the signals are centered around $f_{IF} = 4.309$ MHz with a $B = 2.2$ MHz bandwidth, to ease the ADC conversion. The output of each down-converter is amplified by a NE592D video amplifier, with fix gain and differential output in order to cancel the common mode errors in the transmission to the ADC array. Due to component tolerances is necessary to carry out manually a relative independent calibration to each channel by means of the voltage divider, (R_{adj}), which is located between the down-converter and the video amplifier (Fig. 7.12). The goal of the voltage divider is to adjust the gain to obtain a 110 mV rms signal at the

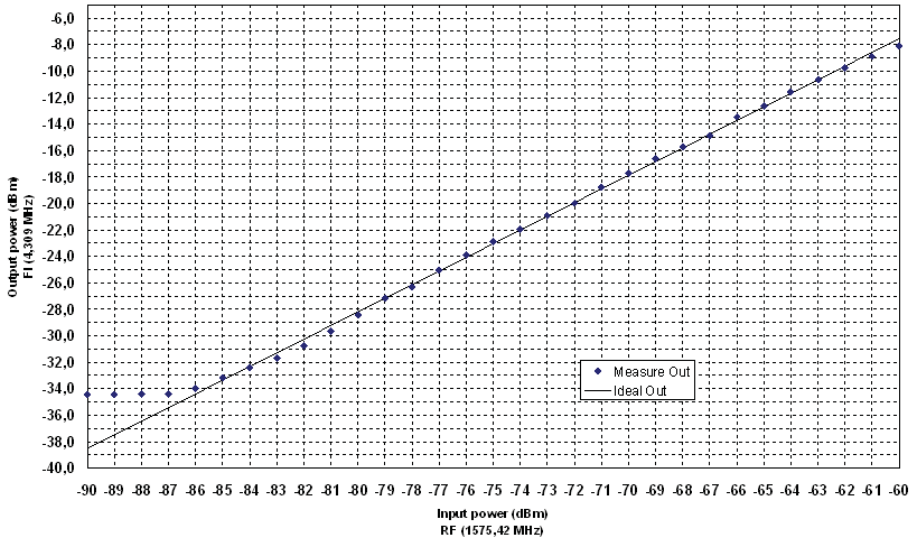

Figure 7.17. Output power versus input power for front-end GP2015 with manually set AGC for obtaining a linear behavior at 25°C.

receiver's output, to match the ADC input range. The gain of each stage should have a maximum error of ±1 dB to make possible the correction in the digital process part. Due to the space limitations the correlation function is implemented digitally outside the receiver, inside a FPGA. The analog signals are sent to an external ADC array to be digitalized. To do this, the output of each video amplifier is connected to a matching network to match its output impedance to the twisted pair (RJ45 grade 5 cable) one. This connector is shared by four differential outputs at 4.309 MHz, two RF switch control inputs, and two power supplies. Due to the amount of pairs, two RJ45 connectors are needed. This method minimizes considerably the total number of cables connected to the receiver, and at the same time provides a high isolation against possible interferences.

7.2.8 PAU-SA's receiver implementation

Both PAU-RA and PAU-SA should have the same receiver design. However, due to the large number of receivers needed in PAU-SA instrument and the limited number of I/O pins in the FPGA, this was not possible. For these reasons a limited version of the receiver design was implemented, moving from a pseudo-correlation topology to the TPR one. In this case to avoid gain fluctuations PAU-SA needs a good control temperature. This change reduces by half the number of pins needed in the FPGA. For the PAU-SA's receiver, the Wilkinson power splitter and one TPR chain have been eliminated in each polarization, as shown the Fig. 7.18, presenting a simplify Friis Formula given by Eqn. 7.14.

$$F_{eq} = L_1 + L_1(F_2 - 1). \tag{7.14}$$

Fig. 7.19 and Table. 7.7 shows in detail a description of each element and its NF contribution. Finally substituting these values in Eqn. 7.14 the equivalent NF of PAU-SA is given in Eqn. 7.15, and the T_{REC} in Eqn. 7.16.

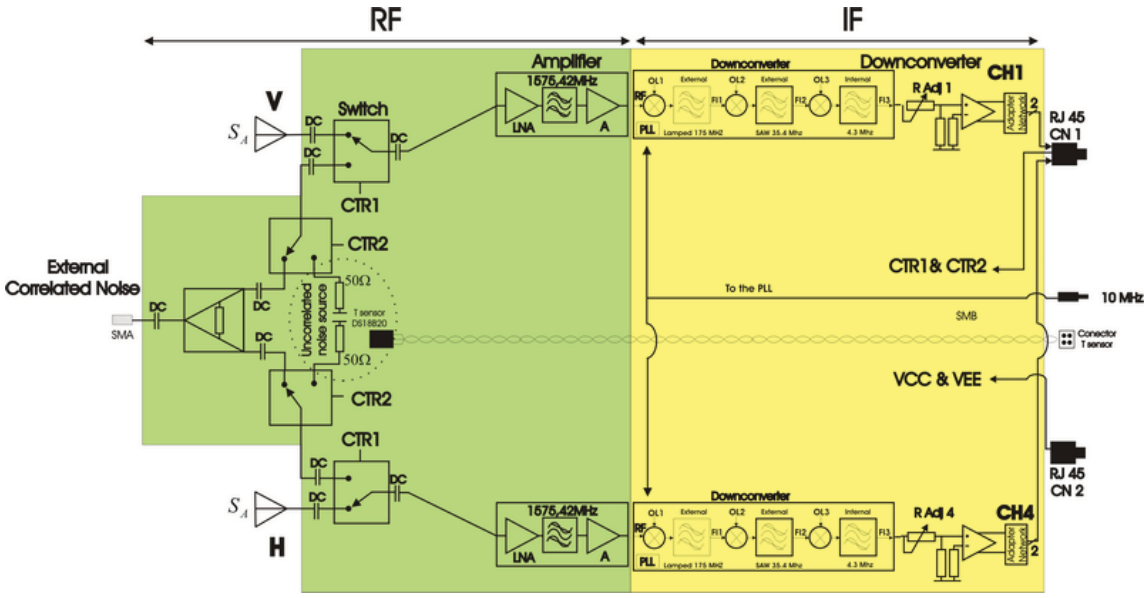

Figure 7.18. PAU-SA's receiver uses two TPR topologies one per polarization (V & H).

Table 7.7. NF elements contribution in the PAU-SA RF chain.

Element	Description	Nominal value (dB)	lineal
L_1	Insertion losses of antenna connector + switch + 2 DC blocks	0.1+1.1+2*0.05=1.2	1.318
A_2	Gain of the LNA	26	398.107
F_2	NF of the LNA	1	1.258

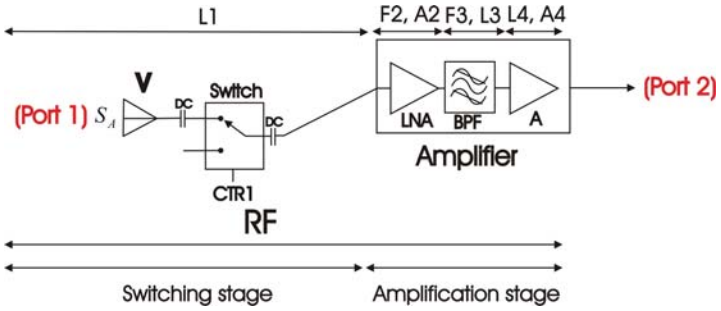

Figure 7.19. Block diagram for the PAU-SA RF stage to calculate the NF of the system.

$$NF = 10\log(\mathrm{F_{eq}}) = 10\log(1.66) = 2.2\,\mathrm{dB}. \tag{7.15}$$

$$T_{REC} = (F_{eq} - 1)T_{ph} = (1.66 - 1)290\mathrm{K} = 191\,\mathrm{K}. \tag{7.16}$$

A temperature sensor (model DS18B20, resolution of 0.125ºC) has been placed above of one of the matched loads at the input of the radiometer to measure its physical temperature.

7.2.9 PAU-RA and PAU-SA's receivers comparison

Table 7.8 compares the main characteristics between PAU-RA and PAU-SA's receivers. The main difference between both receivers is the topology. In this case it has been

Table 7.8. Comparative between PAU-RA and PAU-SA receivers main characteristics.

Parameter	**PAU-RA's receiver**	**PAU-SA's receiver**
Receiver topology	Pseudo-correlation radiometer	Total power radiometer (TPR)
Components mounted	All components	Half components: Wilkinson power splitter, two TPR chains, one per polarization has been eliminated
Gain	110 $\pm$ 1 dB	113 $\pm$ 1 dB
Noise factor	5.3 dB	2.2 dB
T_{REC}	696 K	191 K
BW	2.2 MHz	2.2 MHz
Crosstalk between chains	< - 40 dB	<< - 40 dB
Dimensions	11 x 7 x 3 cm	11 x 7 x 3 cm
weight	250 g	250 g
VCC	+ 7 V, 0.5 ± 10%	+7 V, 0.5 ± 10%
VEE	- 7 V, 0.07 ± 10%	- 7 V, 0.07 ± 10%
Clock 10 MHz	TTL, 5 V_{pp}	TTL, 5 V_{pp}
Switching time (CTRX)	17 ns	17 ns

implemented a single design for the IF and RF stages and the components have been mounted according to the receiver's requirements. As it can be seen in Figs. 7.20a and 7.20b, PAU-SA's receiver has only half of the components in the IF stage mounted and Figs. 7.20c, and 7.20d show the RF stages. Concerning the gain, PAU-SA has 3 dB more of gain due to the lack of Wilkinson power splitter necessary to implement pseudo-correlation topology as can be compared in schemes 7.12 and 7.18 and Figs. 7.20c and 7.20d. With respect to the NF, PAU-SA has improved the NF from 5.3 dB to 2.2 dB for the same reason and therefore the T_{REC}. Related to the channel isolation, PAU-RA has crosstalk between chains around -40 dB. In this case, due to PAU-SA use the most separated channels, its value has been significantly improved and can not be measured with the Vector Network Analyzer (VNA). Figure 7.20a and 7.20b show the interconnection between the RF and IF stage of the PAU-RA, and PAU-SA's receivers.

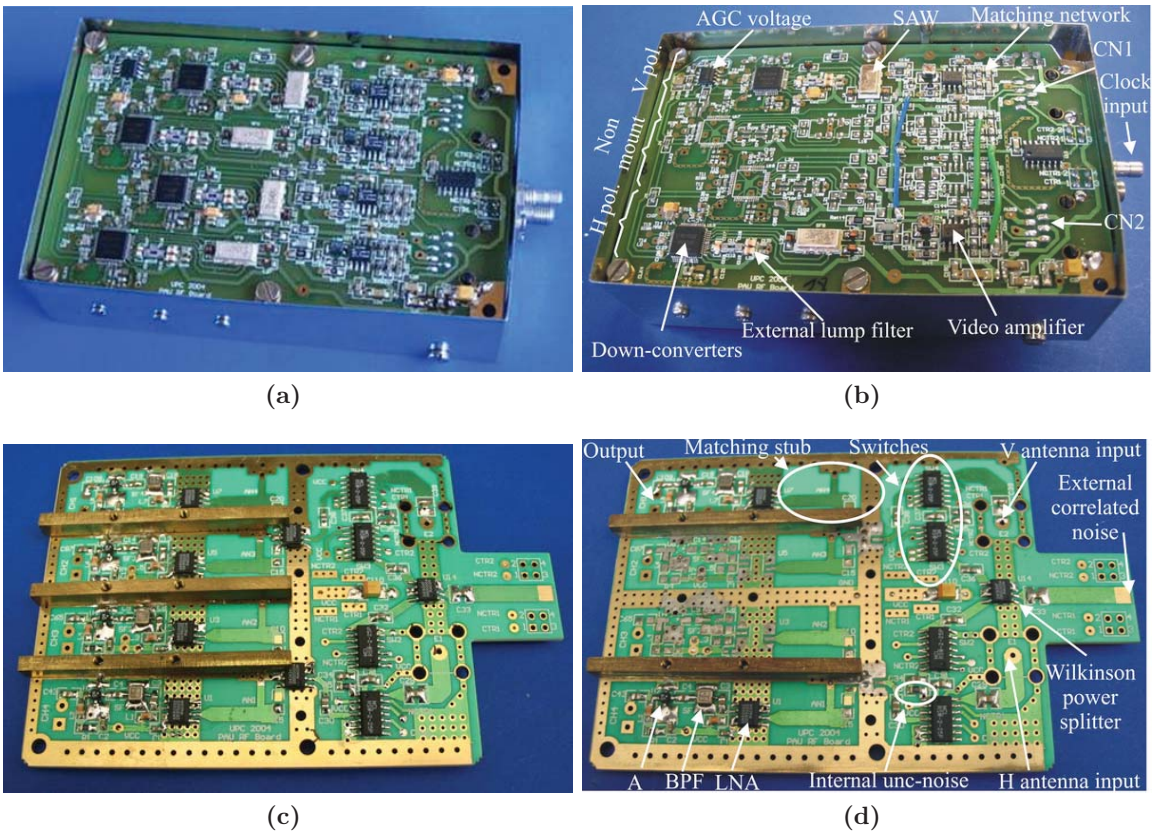

Figure 7.20. a) PAU-RA's receiver IF stage view with box, b) PAU-SA's receiver IF stage view with box, c) PAU-RA's receiver RF stage view without box, d) PAU-SA's receiver RF stage view without box.

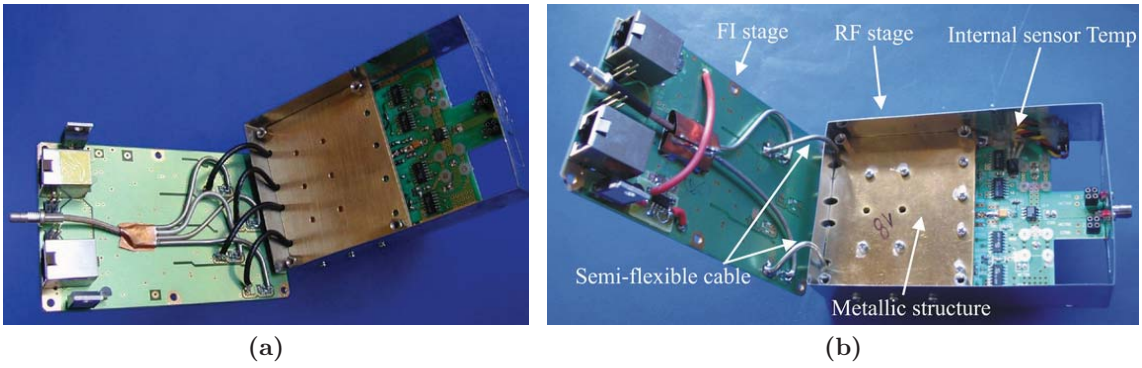

Figure 7.21. Picture of the RF-IF interconnection stages of a) PAU-RA'receiver, and b) PAU-SA'receiver.

A picture of the receiver assembled without box is shown in Fig. 7.22a. Both stages are assembled to minimize the required area: (top) IF stage and (bottom) RF stage. The receiver is introduced into a metallic box of (11 x 7 x 3 cm) to protect it against undesired signals, and it has also been added a Band Pass Filter (BPF) eliminating spurious out of

band to improve the frequency response of the receiver as shown in Fig. 7.22b.

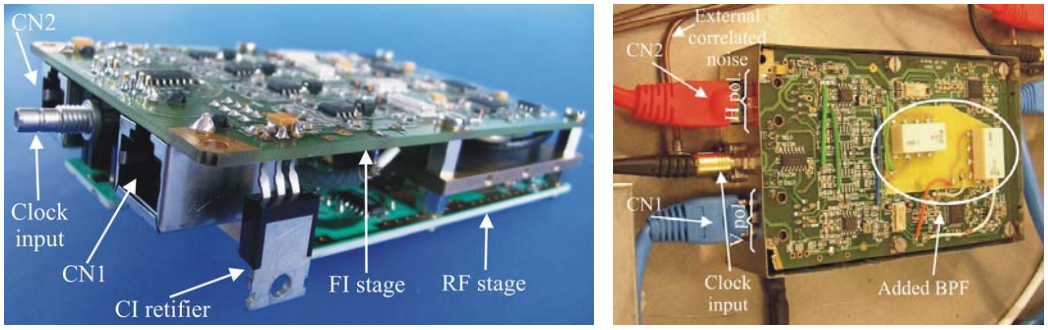

(a) **(b)**

Figure 7.22. Picture of the RF-IF ensambled stages of a) PAU-RA'receiver, and b) PAU-SA'receiver.

Figure. 7.23 show the frequency response of two complete RF-IF receivers. This test has been performed injecting a carrier signal centered at 1,575.42 MHz with a power of -131.52 dBm at the antenna port. The output signal is centered exactly at 4.309 MHz, the down-conversion is properly working, and the output power is -19.52 dBm, the whole receiver gain, is about 112 dB (distributed along different down-conversion stages to avoid input output coupling). Furthermore, it shows that the frequency response has a bandwidth of 2.2 MHz and a 40 dB of attenuation between the pass-band and the rejected band. One thing to consider is the signal distribution in the RJ45 PAU-RA and

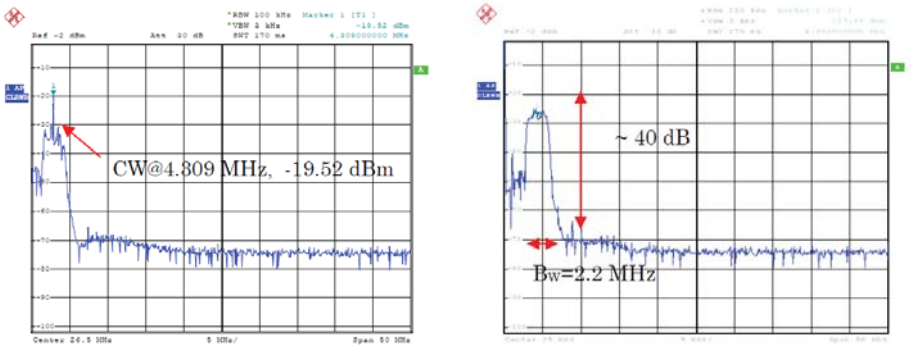

(a) **(b)**

Figure 7.23. PAU-SA'receiver frequency response. a) Test performed with CW centered at 1,575.42 MHz with a an input power of -112 dBm at the RF front-end input, and b) System response without input.

PAU-SA connectors. Figure 7.24 shows these signal assignments. PAU-RA's connectors mix different signals such as: analog signals, control switch and power supply into the two connectors. However, PAU-SA uses the CN1 connector for analog signals and control switch and the CN2 only for the power supply.

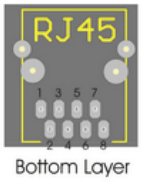

PAU-RA

CN1	CN2
1=V1+	1=V3+
2=V1-	2=V3-
3=NC	3=VCCNR
4=V2+	4=NC
5=V2-	5=VDDNR
6=NC	6=GND
7=CTR1	7=V4+
8=CTR2	8=V4-

PAU-SA

CN1	CN2
1=V1+	1=NC
2=V1-	2=NC
3=NC	3=VCCNR
4=V2+	4=NC
5=V2-	5=VDDNR
6=NC	6=GND
7=CTR1	7=NC
8=CTR2	8=NC

Figure 7.24. PAU-RA and PAU-SA'signal assignment in the CN1 and CN2 connectors.

7.2.10 Discussion and considerations

This section has presented an overview of the PAU's receiver design. In order to have a unique design for both PAU-RA and PAU-SA receivers a trade-off between both receivers specifications has been presented. This has been the most difficult task and the part in which I have spent more time in the project due to large number of receivers to assemble and calibrate: 16 for PAU-RA and 25 for PAU-SA. The design started with the design of the PAU-RA's receiver with has determined the receiver size and the receiver topology (pseudo-correlation). The high integration level has been possible thanks to the use of commercial components such as: amplifiers, filters and front-end. Especially, a GPS front-end has been selected as down-converter manipulating the AGC in order to obtain a linear response. The implementation of the RF and IF stages in the case of PAU-RA was critical due to crosstalk between stages, having to shield from neighboring stages. In the case of PAU-SA's topology a TPR chain for each polarization has been chosen due to the limitations in I/O pin in the FPGA 1. An external LPF has been added to improve the frequency response. The bandwidth of the PAU instrument of 2.2 MHz is determined by a SAW filter located in the down-converter stage. At present there are disparities with the gains of different channels, so it is advisable to substitute the manual gain potenciometer, by a programable video amplifier to equalize the channels when necessary. At the beginning, the 5 V power supply at the down-converter stage led to overheating, and it was necessary to change the voltage down to 3.3 V. Concerning the theoretical NF of the PAU-SA'receiver with 2.2 dB corresponding with a T_{REC} of 191 K, the measurement mean value has been 2.69 dB with a T_{REC} of 250 K. For this reason, this last value will be use to be more realistic.

7.3 PAU-SA's ADCs board array

Before start explaining the design of the whole analog to digital converter subsystem, is necessary to analyze the specifications and the limitations that the ADCs need to fulfill in order to be interconnected with the other parts of the instrument: the receivers and the FPGA. Figure 7.25a shows the PAU-SA's ADC array location and the interconnection in the PAU-SA's system block diagram. Figure 7.25b shows the ADC array location in the PAU-SA's structure scheme. The block diagram of the ADC array interconnections is presented. The second part of this section is devoted to select the individual ADC device. Then, a proposed platform to interconnect all devices is presented and finally the final implementation and test are shown. Due to the complexity of the design, it is presented in a synthesized form in order to have a global view of the design.

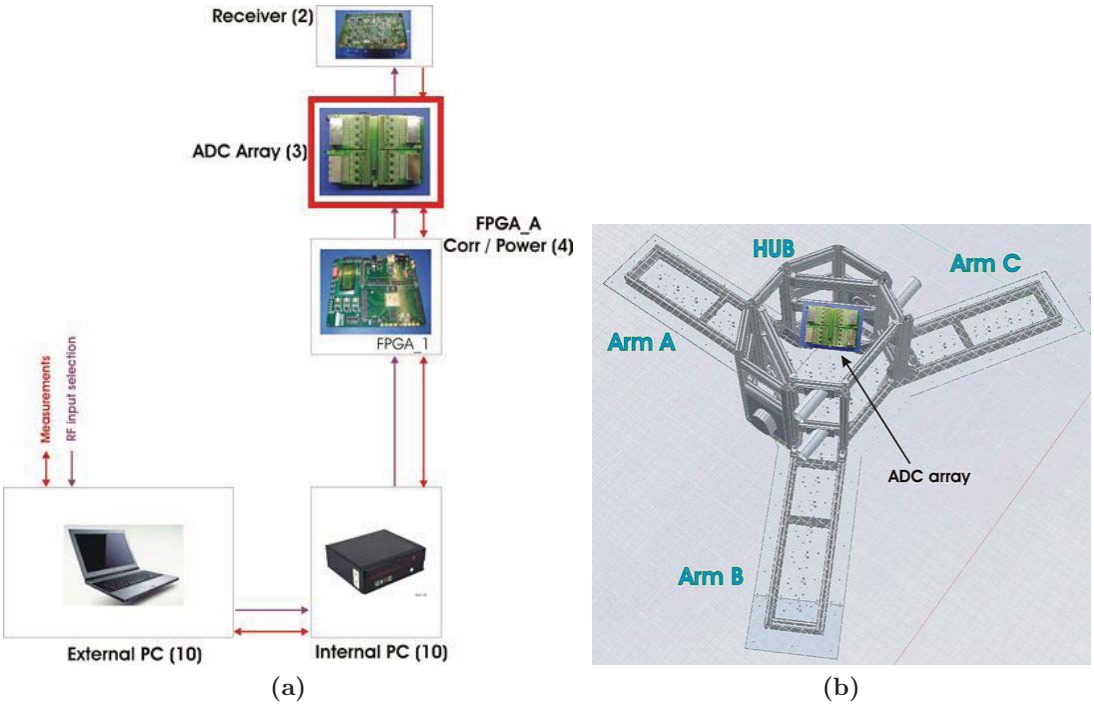

Figure 7.25. a) PAU-SA's ADC array location and interconnection in the PAU-SA's system block diagram, and b) ADC array location in the PAU-SA's structure scheme.

7.3.1 Receiver requirements

The PAU-SA instrument includes an array of 31 antennas from which only 25 are operational for the synthetic aperture radiometer. Each dual polarization antenna is connected to a dual channel receiver (one per polarization). As each channel has a differential output, a total of 50 analog differential channels are connected to the ADC array. Moreover the receivers need two unipolar common control signals (CTR1 and CTR2) to select the different RF inputs. These two control signals are sent by the external PC to the receivers through the FPGA first, and then via the ADC array. These signals have a frequency smaller than 1 Hz, and they are buffered in the ADC array interface by a 74VHC244

buffer chip (Fig. 7.26). The IF output signals are transmitted at a central frequency of 4.309 MHz with a bandwidth of 2.2 MHz and a dynamic range of the output voltage of 1 V_{rms}. Another point to take into account is the impedance of the cable used to inter-connect the receivers and the ADC array. This implementation has been performed using a RJ-45 grade five cable to minimize the number of cables in the instrument. The cable impedance of each differential pair is about 150 Ohms, as seen from the FPGA.

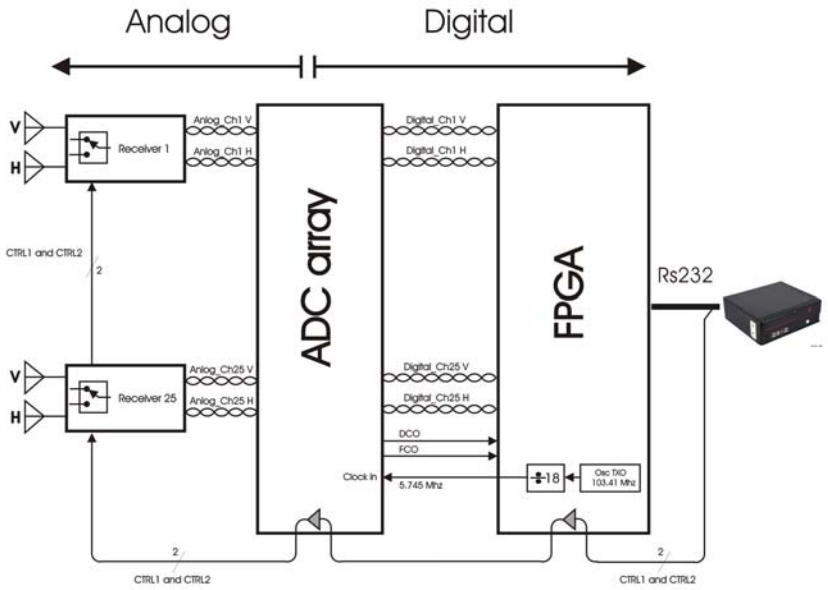

Figure 7.26. Block diagram of the ADC array interconnectivity.

7.3.2 FPGA requirements

The FPGA used for PAU-SA in the radiometric sensor is a Virtex-4 LX 60 in a Memec Virtex-4 MB Development Kit (Fig. 7.27). This evaluation board has available 52 differential input signals distributed in a special socket connector and 10 unipolar input signals distributed in a standard connector. Since the radiometric part needs 50 differential input channels, close to the total number of differential inputs in the FPGA, a serial topology for the ADC output was selected. Moreover, two common unipolar input control signals are required for synchronization procedures and a unipolar output clock for the sampling clock.

7.3.3 ADC selection

Taking into account all the previous requirements it is now possible to select a dedicated integrated circuit for this application. There are many integrated circuits able to be used in this particular application. However, the selected IC was the AD9287 from Analog Devices, based on the strict specifications concerning the area occupation, power consumption, cost requirements, and serial output. The AD9287 is available in a 48-lead LFCSP package; it has 4 differential input channels with a conversion at 8 bits,

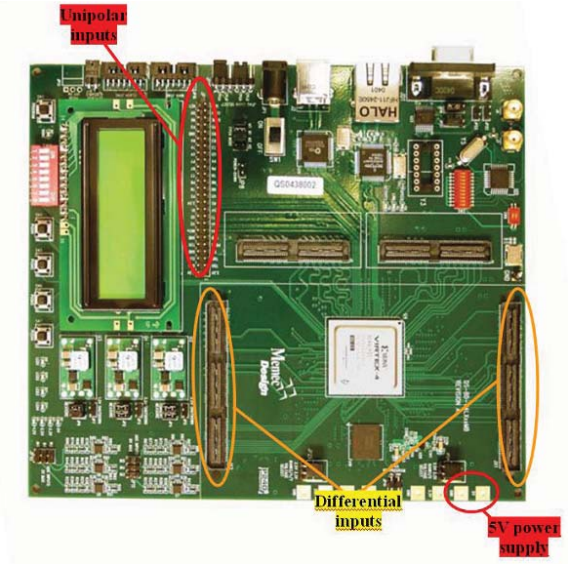

Figure 7.27. FPGA Virtex-4 LX 60 with a Memec Virtex-4 MB Development Kit used for PAU-SA's radiometric sensor.

and individual differential serial output. Figure 7.28 shows a picture taken from the oscilloscope with the ADC working in test mode. The sampling frequency common for all ADCs comes from the FPGA. Internally each ADC generate automatically multiplies the sampling clock to the appropriate LVDS serial data rate, through the control signals: (DCO) and (FCO). The data clock FCO indicates the capture data on the output. It is used to signal the start of a new output byte at every rising edge. The DCO signal on the rising and falling edges clocked out the single bit of data byte.

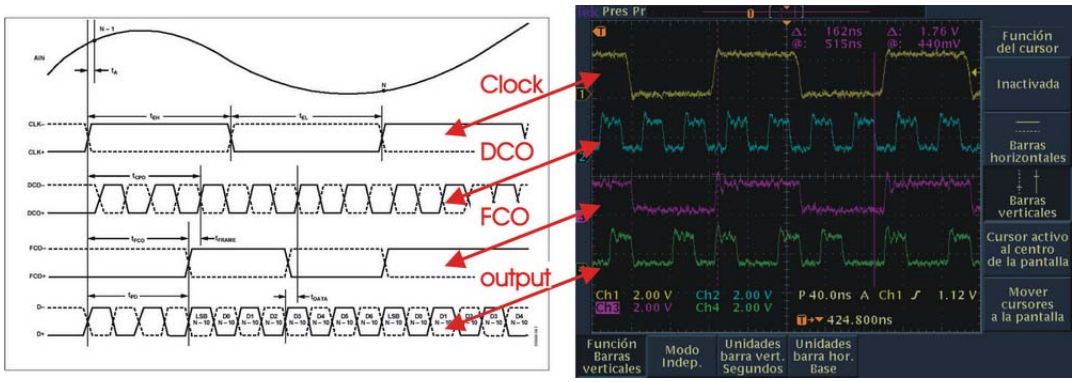

(a)

Figure 7.28. ADC internal control signals.

7.3.4 Sampling frequency

The fundamental requirement of a sequential electronic block is the frequency of operation. In the case of the ADC, the frequency of operation determines the sampling

frequency. In the PAU radiometer the receiver has a 4.309 MHz central frequency, and then it is digitized to translate the frequency to baseband with the Digital Down Converter (DDC). The Nyquist sampling theorem states that the sampling frequency should be at least twice the highest frequency components in the signal. This means that, to sample a 4.309 MHz signal a minimum 8.618 MHz sampling frequency is required. Higher sampling frequency implies a higher data rate, and the DDC function will be very complex to implement in the FPGA because the input signal of DDC should be multiplied by a cosine function using all the 8 bits. Another option is the so called "band-pass sampling". With this technique a smaller sampling frequency can be used, thus reducing the data rate, and simplifying the implementation of the DDC. The "band-pass sampling" technique is described in the following paragraphs. Considering the sampling frequency of ADC (F_S) and the frequency of output signal from receiver (F_{IF}), the central frequency of the digitalized signal is:

$$F_{FINAL} = F_S - F_{IF}. \tag{7.17}$$

Then, the input signal of DDC should be multiplied by $\cos(2\pi F_{FINAL} n)$.

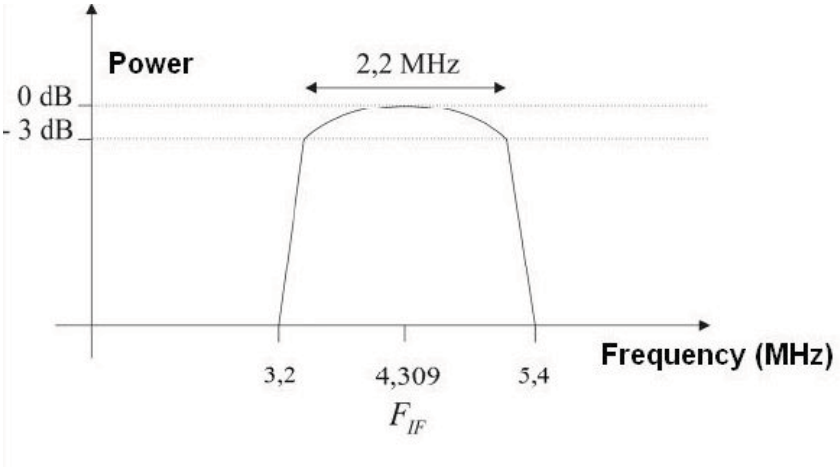

Figure 7.29. Frequency domain of input signal.

If F_{FINAL} is represented in the frequency domain (Fig. 7.29), the selected value F_{FINAL} = 0.25. Thus the previous expression is now:

$$\cos(\frac{\pi}{2} \cdot n) = 1, 0, -1, 0... \qquad with\ n = 0, 1, 2, 3... \tag{7.18}$$

This means that now, the input signal has to be multiplied by the sequence 1,0,-1,0... thus reducing the cost of operation. Now it is possible to compute the frequency of sampling of the ADC in the following way:

$$F_{FINAL} = \frac{F_S}{4}. \tag{7.19}$$

$$F_S = 4 \cdot F_{FINAL} = 4 \cdot (F_S - F_{IF}) \Rightarrow F_S = \frac{4}{3} F_{IF}. \tag{7.20}$$

$$F_{IF} = 4.309 \text{ MHz} \Rightarrow \mathrm{F_S} = 5.745 \text{ MHz}.$$

Thus, the output signal of the ADC is centered at the frequency F_{FINAL} = 1.436 MHz as shown in Fig. 7.30:

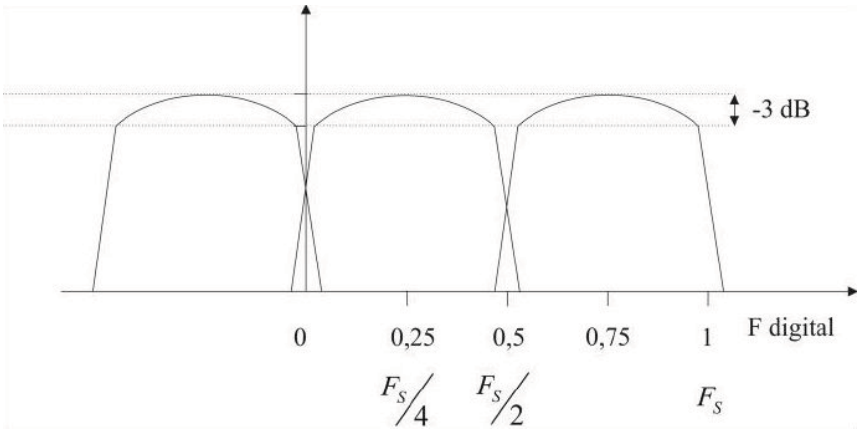

Figure 7.30. Frequency domain of input signal digitalized.

7.3.5 FPGA's interface

The object of this part is to design a simple interface able to convert the complex pinout of FPGA in to a simpler connector available for the ADC array. In order to minimize the wiring between the ADCs and the FPGA, the ADCs array should be located as close as possible to the FPGA. For this reason it has been designed to be just above, as shown in Fig. 7.31. To do this, it has been necessary to implement the following interface. In order

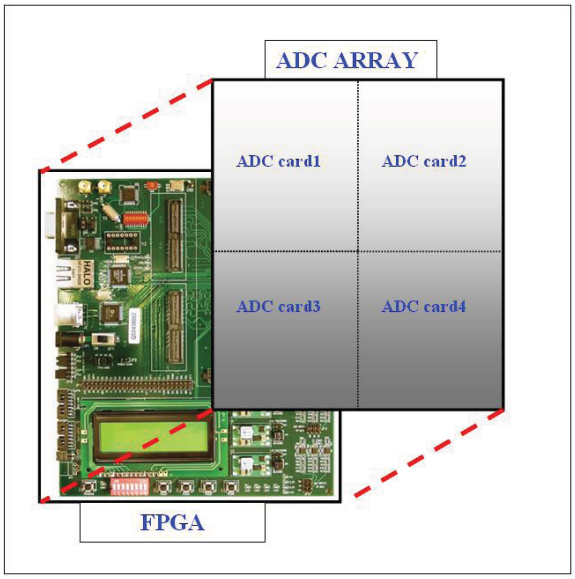

Figure 7.31. ADC's array scheme with FPGA.

to simplify the design of the ADC array, this part has been divided in several ADC cards. Thus, it is only necessary to design a single ADC card and then repeat it four times, taking into account the symmetry of the system. The maximum area available for each ADC card is a quarter of the size of the FPGA, as shown in Fig. 7.31. Figure 7.32 shows a basic diagram of how the FPGA's Interface has to be implemented. Since the FPGA has a lot of peripherals, it was impossible to design a single interface. In this case it was

decided to implement two interfaces T1 and T2. The first one T1 is needed to convert the socket pinout of the FPGA to a simpler used to interface T2. The interface T2 is larger than interface T1, and simplifies the routing of the very large number of wires between the FPGA and the ADC cards. The first step of the design was the implementation of

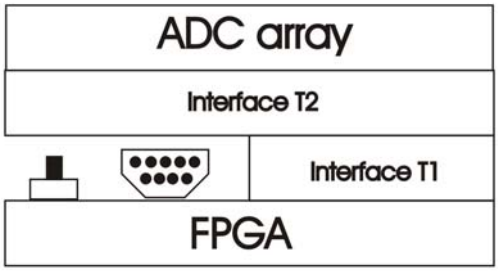

Figure 7.32. FPGA's Interface hierarchy.

the interface T1. The FPGA board uses the 0.80 mm high QSE series speed differential socket from Samtec Corporation. Figure 7.27 shows a picture of the FPGA platform, and it possible to distinguish the differential input pins from the unipolar ones. The differential pinout connected to the socket connectors to the FPGA board are converted by the interface T1 in a "turned pole connectors" males in order to allow board-to-board mounting with a low insertion force. Figure 7.33 shows the T1 interface mounted upon the FPGA structure; the axial fan was included to help heat dissipation of the components under the interface. The axial fan works at 5 V, and it is supplied directly from the FPGA. Once the differential inputs of the FPGA are accessible through the T1 interface,

Figure 7.33. FPGA with the T1 interface in order to adapt the QSE differential socket to a standard differential socket.

the T2 interface is presented. This interface performs different tasks such as: distributing of the sampling clock to each device, routing of the differential signals to the T1 interface, distributing the common unipolar control signals CTR1 and CTR2 to all receivers and reading the unipolar signals DCO and FCO by an ADC device for synchronization and

acquisition purposes. The FPGA 100 MHz global clock is a dedicated network specifically designed to reach all clock inputs to the various resources in an FPGA. The clock buffer can be programmed to divide the incoming clock frequency by any integer number. As described in the previous section, PAU-SA instrument works with a 5.745 MHz frequency. Using VHDL program is very difficult to obtain a frequency of 5.745 MHz from an initial value of 100 MHz. Fortunately with FPGA Virtex-4 MB is possible to drive the system with an external clock signal using a particular pinout of the FPGA. For this reason,

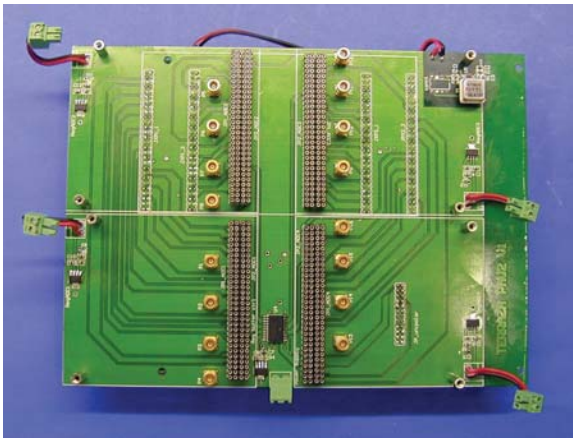

Figure 7.34. T2 interface, implemented to easily connect the elementary ADC cards with the T1 .

an external clock of 103.41 MHz was used. It can be seen in the top right corner of the Fig. 7.34. This clock reference is divided by 18 times inside the FPGA to obtain the 5.745 MHz. The resulting signal is transmitted through the unipolar connector, directly to the T2 interface (Fig. 7.27), and finally, it is buffered to feed each ADC device through the SMB connectors (Fig. 7.34).

7.3.6 Elementary ADC card

As mentioned in the previous section, PAU-SA is composed by a Y-shaped array of 8 antennas per arm plus the one in the center: 25 antennas for radiometry applications. Each dual-polarization antenna is connected to a dual channel/dual polarization receiver; two channels per receiver. The outputs of each receiving unit are the input of each ADC channel, as a total: 25 receivers x 2 channels/receiver equal 50 channels. Taking into account that the ADC array is formed by 4 ADC cards, (Fig. 7.31), and that each single ADC IC has 4 channels, 4 ADC ICs are required per ADC card. The throughput of each ADC card is: 4 channels x 8 bits x 5.745 MHz = 183.84 Mb/s, and the total input rate at the FPGA is thus 13 times higher, approximately 2.4 Gb/s.

The ADC card can be divided in different blocks such as the input stage (input connectors and filter block), conversion stage (ADC converters), power supply stages (analog and digital), buffer and output stage. The new component in this implementation is the buffer block circuit used to control the two receiver's switches, CTR1 and CTR2. All the stages are already explained in the previous sections and these are been implemented according with the requirements. Figures 7.35a and 7.35b show the final ADC card with

all components soldered. It is possible to distinguish the various subsystems such as filter block, single ADC, I/O connectors, power supply etc. Finally Fig. 7.36a shows the final

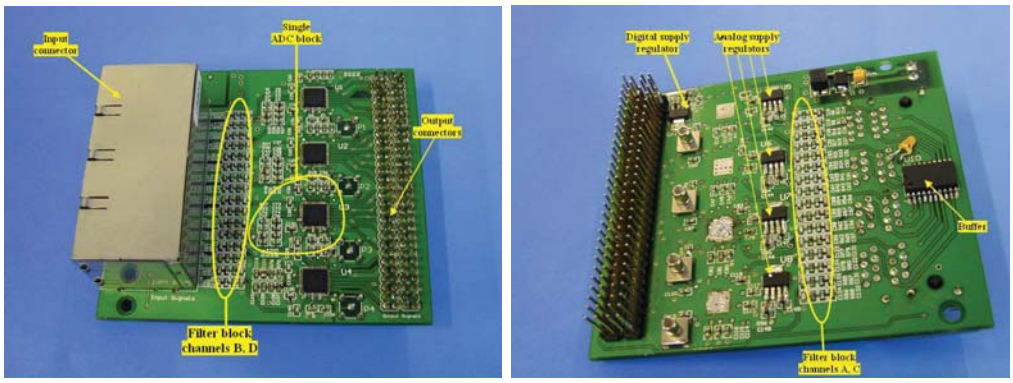

(a) **(b)**

Figure 7.35. a) Top layer of the ADC card, b) Bottom layer of the ADC card.

implementation of the ADC array subsystem. As it can be seen, this is composed by 4 ADC cards. Figure 7.36b shows a side view, being possible to distinguish the FPGA, interfaces T1 and T2, and the ADC cards.

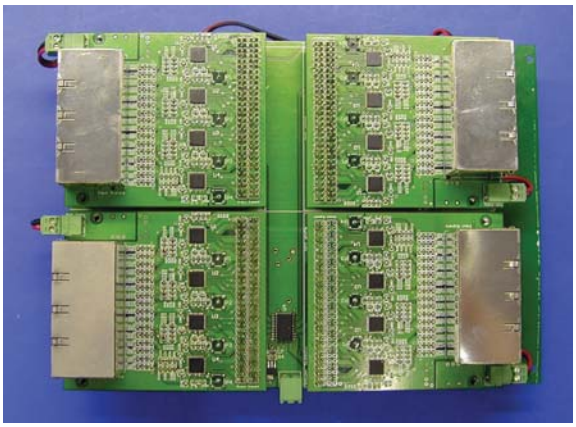

(a)

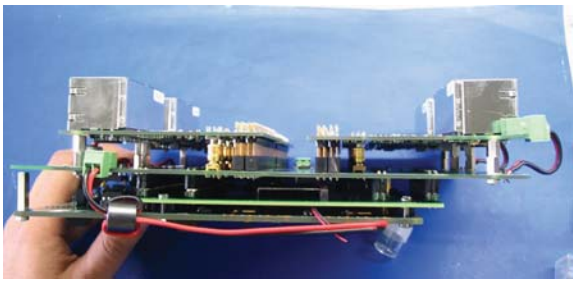

(b)

Figure 7.36. a) Frontal view of the FPGA and ADC array, b) Side view of the FPGA and ADC array.

7.3.7 Test results

In this section some results obtained with the ADC card are presented. The method used to test the ADC system has been to inject in inputs a sinusoidal signals and analyze the digitized output. Figure 7.37 shows the "testbench components":

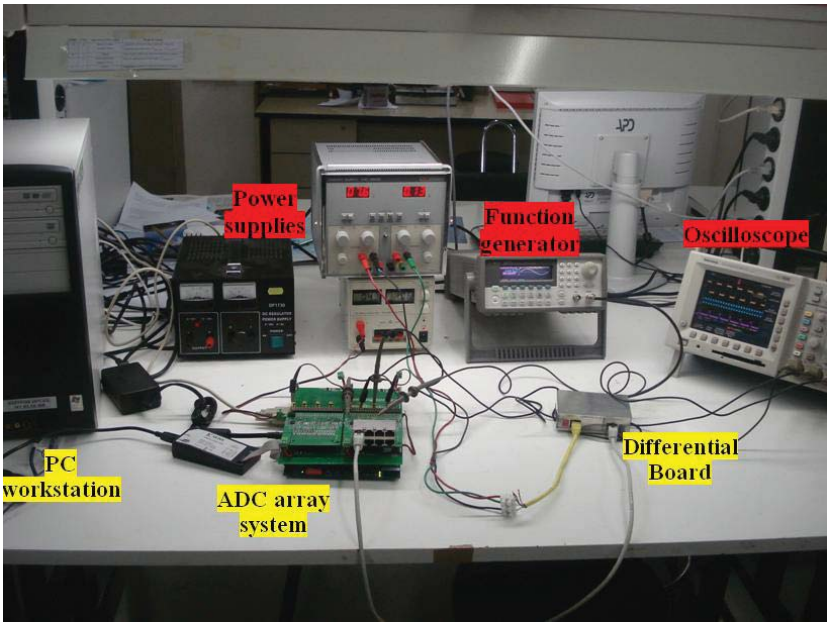

Figure 7.37. Testbench of a single ADC card.

- Power supply sources of 3.3 V.
- Power supply sources $\pm 10\ V$.
- Function generator *Agilent 33250*.
- Oscilloscope *Tektronix 3054 - 4channels*.
- Differential Board.
- FPGA *Virtex-4 LX 60* (Xilinx family).
- ADC card.
- PC with MATLAB simulator / Processor.

The input signals are generated by a chain composed by a function generator and a differential board. Function generator produces a unipolar signal transformed in differential one by the differential board emulating a receiver. Then, once the ADC has digitalized the data, the outputs are analyzed by the MATLAB simulator / processor. The acquired ADC data outputs have been reconstructed in the frequency and time domains. In order to check the ADC behavior several test has been done.

7.3.7.1 Receiver test varying the input level

The first test are done with input signal at $F_{IF} = 4.309$ MHz in order to model the receiver system. These tests were performed changing the input voltage magnitude in order to see the range where the system works properly (until ADC goes in saturation mode), remembering that input voltage span of ADC is 1 Vpp. Simulation results are

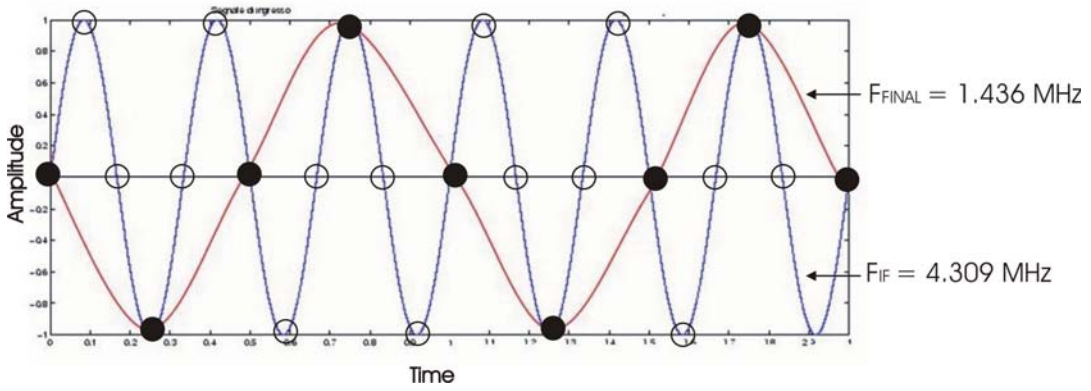

Figure 7.38. Time evolution of the input signal F_{IF}, and the digitalized signal F_{FINAL}.

done in both frequency and time domains. It is possible to note that in the frequency domain two "delta" functions are shown at a particular frequency value. To explain this result it is possible to refer to 4.309 MHz input signal:

$$4.309\,\text{MHz} \approx \frac{3}{4} 5.745\,\text{MHz}, \tag{7.21}$$

it means that input signal at $F_{IF} = 4.309$ MHz is sampled every $\frac{3}{4}$ of it.

Regarding Fig. 7.38 is more easy understand what it means; in fact in blue is the input signal at $F_{IF} = 4.309$ MHz. If this signal is divided by four parts, and every three parts we take a sampling of it, we will have the F_{FINAL} signal of 1.436 MHz in red, Eqn. 7.17. Applying the Fourier transform it will be obtain, two delta spikes will be obtained as a digital representation of a sinusoidal signal (Fig. 7.39). Each pair of figures

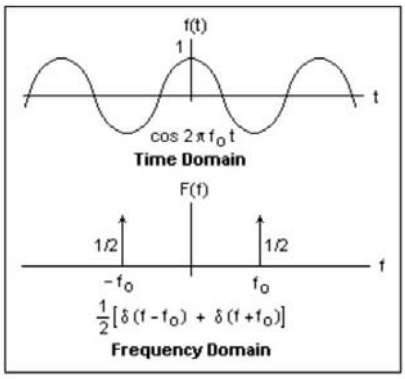

Figure 7.39. Sinusoidal signal: representation in time and frequency domain.

consist of a time and frequency representation. In time domain the X-axis represents the number of samples that the FPGA use to reconstruct the signal. In this case the maximum number of samples is 1000. Y-axis of the time domain plots the amplitude of the signal, not in voltage, but in digital levels. As the sampling is carried out at 8 bits, the maximum resolution is 256 levels. In frequency domain the X-axis represents the frequency domain, and the Y-axis represents the dB/level. The input signal is produced by a function generator in order to vary the average voltage between 400 mVpp and 1.5 V and confirming the proper operation of the device. Fig. 7.40 is done applying an input signal of 400 mVpp and Fig. 7.41 with an input signal of 800 mVpp. It is possible to note that regarding time domains the amplitude of signal of 800 mVpp is not the double of the signal of 400 mVpp because they are represented in digital levels. In Fig. 7.42, the input signal has now an amplitude of 1 Vpp. As the ADC input voltage span is 1 Vpp the time domain representation requires all the 256 digital levels to reconstruct the input signal. An important consideration can be done regarding Fig. 7.43; where the input signal voltage is now 1.5 Vpp. The ADC is no longer able to reconstruct the part of signal larger than 1 Vpp. The converter is pushed to create a signal with more power than it can support; the signal simply "cuts" at the maximum amplitude of the converter (1 Vpp). The extra signal which is beyond the capability of the converter is simply cut off, resulting in a distorted waveform.

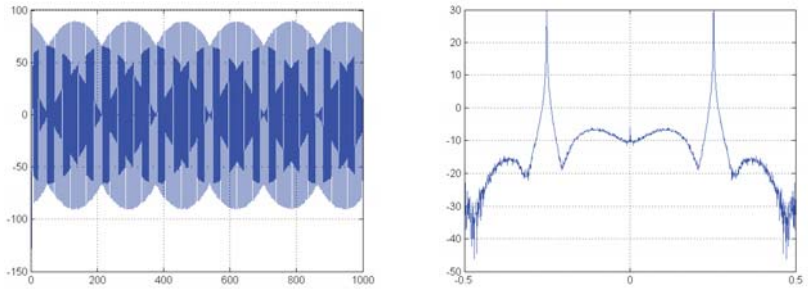

(a) Time domain **(b)** Frequency domain

Figure 7.40. 4.309 MHz - 400 mVpp.

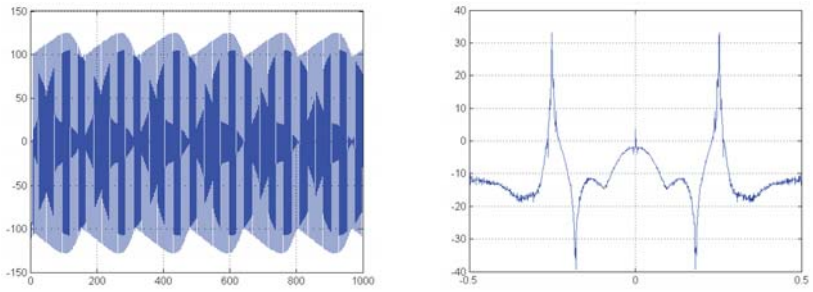

(a) Time domain **(b)** Frequency domain

Figure 7.41. 4.309 MHz - 800 mVpp.

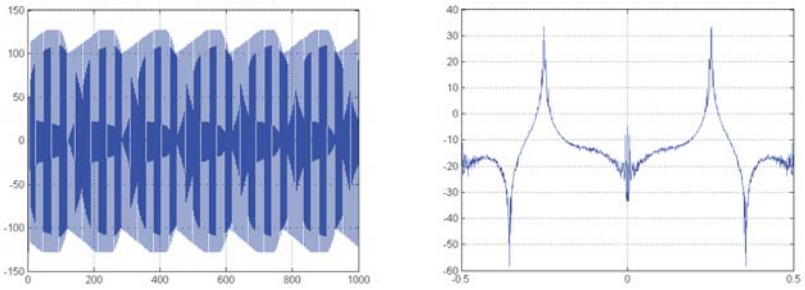

(a) Time domain **(b)** Frequency domain

Figure 7.42. 4.309 MHz - 1 Vpp.

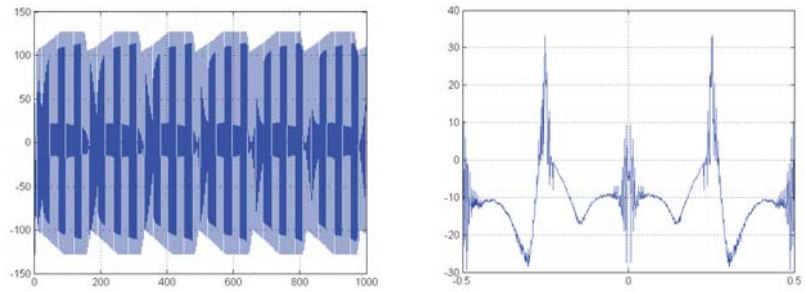

(a) Time domain **(b)** Frequency domain

Figure 7.43. 4.309 MHz - 1.5 Vpp.

7.3.7.2 Receiver test varying the frequency

An important test is done connecting an input signal of exactly 5.745 MHz. In this case, the frequency of input signal is the same as the sampling. Figure 7.44b shows the frequency domain of the signal recostructed; now the two delta are overlapped in the center. This is the limit in frequency of the converter. Over this frequency the converter saturates in frequency and is not able to reconstruct the input signal properly (as shown in the Fig. 7.44). Concerning the ADC cards will not report all the measures of all channels of each ADC stage due to the large number of channels, but the verification was

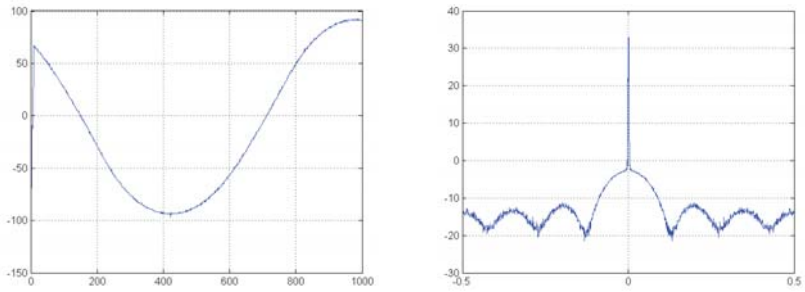

(a) Time domain **(b)** Frequency domain

Figure 7.44. 5.745 MHz - 400 mVpp.

performed separately for each one with respect to the signal distribution signals through the T1 and T2 interfaces, being the test satisfactory.

7.3.8 Conclusions

This section has presented the implementation of the ADC array for the interferometric radiometer part. Taking into account the spectra of the receiver, it has been possible use the "band-pass sampling" technique using a smaller sampling frequency to reduce the data rate and simplifying the implementation in the DDC. Due to the large number of receivers and the limitation inputs pins in the FPGA 1, it has been necessary to use a serial output converter structure instead of a parallel one to reduce the number of wires. The entire ADC converter system has been designed to avoid EMC interferences. It has been divided in 4 independent ADC cards in order to have a flexible structure that can be easily repaired if an ADC card does not work properly. Moreover, an implementation and design of a structure able to connect the ADC array to the FPGA. Two interfaces have been designed: interface T1 being able to convert the special socket connectors of the FPGA in a "turned pole connectors" males in order to allow board-to-board mounting with a low insertion force, and interface T2 being able to connect all the signals from FPGA to the ADC cards and vice versa.

To synchronize the digitized signals coming from the ADCs (data and control) it has been necessary to share the sampling clock signal in all ADC chips. This is located at the interface T2, generating the pattern clock signal by an external oscillator. The requirements for this clock frequency were: as high as possible to use hardware reuse techniques and also to be a multiple of the sampling frequency. For this reason the value of fs x 18 was chosen = 18 x 5.745 MHz = 103.41 MHz.

Nowadays a de-synchronization problem exits in the FPGA in 3 of the data acquisition inputs. For this reason the arm size has had to be reduced to 7 elements per arm instead of the initial 8 elements. The problem is due to a limitation of the number of pins in the FPGA. With these requirements it was necessary assume that the control outputs (DCO and FCO) of all ADCs were synchronized due to the synchronous architecture. For this reason, one of the ADC control has been taken as a reference. The best way to solve this problem implies wire individually each ADC (data and its control) with the FPGA, eliminating the problems of synchronization. This method implies an increase in the number of pins and force to replace the FPGA. Another possible solution has been proposed in the section of the FPGA.

In the design of interface T2 it was needed to implement a simple circuit to generate the clock signal by an external oscillator.

7.4 Design of the hardware processor unit

As mentioned in the description of the PAU-SA instrument, the main goal of PAU-SA is to test some improvements over the current MIRAS design, especially migrate from analog to digital. Due to the large number of receiving elements in synthetic aperture radiometers, the use of today's digital technology is strongly recommended. In PAU-SA, all analog technology from the IF has been replaced by digital technology. For this reason, digital design takes a relevant part in this design, and digital techniques have been implemented in many sub-systems. The objective of this section is to present the design and implementation of the digital sub-systems related to the radiometric part implemented in a FPGA. Figure 7.45a shows the FPGA 1 interconnection in the PAU-SA's system block diagram and Fig. 7.45b shows the FPGA 1 location in the PAU-SA's structure scheme.

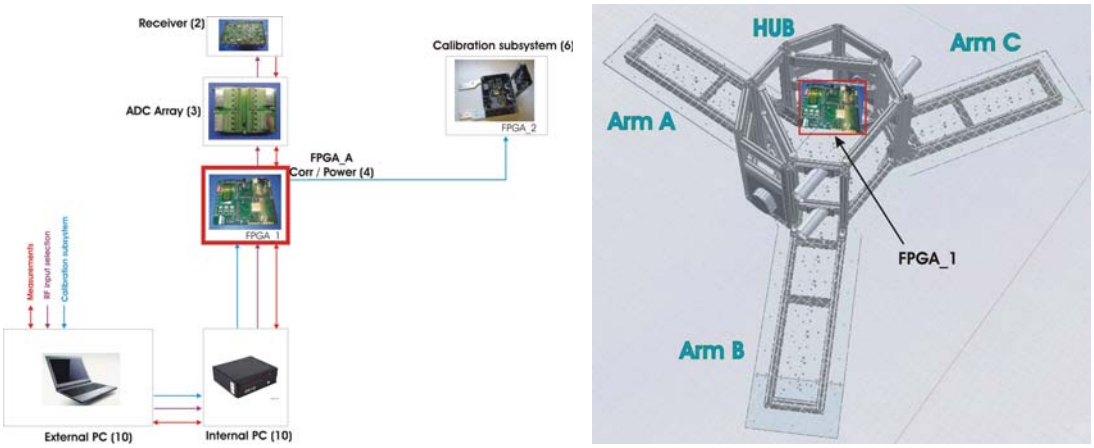

(a) (b)

Figure 7.45. a) PAU-SA's FPGA 1 interconnection in the PAU-SA's system block diagram, and b) FPGA 1 location in the PAU-SA's structure scheme.

The VHDL sub-systems that are implemented in the FPGA:

- In-phase (I) and quadrature (Q) demodulation of the receivers' output digital signals coming from the array ADC of (8 bits),
- Digital LPF (8 bits),
- Power estimation system of the 50 signals receivers'output (25 receivers x 2 polarizations at 8 bits),
- Correlation unit of the three correlation matrices (V, H, VH), at 1 bit, and
- Communication protocol and control with a PC, and data collection.

In order to implement the digital design a programmable hardware was used, and more specifically a FPGA. It has been chosen over a full-custom design because it is reconfigurable and it can be tested internally. Moreover, it is an easy and affordable option

to implement a prototype. The FPGA device used in the design is the Virtex-4 LX 60 distributed by Xilinx. It has been selected since it has the largest variety of resources available in its commercial development board (Menec Virtex-4 Development Kit). Table. 7.9 summarizes the main resources available in this FPGA. A slice is the basic unit of

Table 7.9. Resources available in Virtex-4 LX 60 FPGA device.

Resource type	Total
Slices	26,624
RAMB16s	160
DSP48s	64
GCLKs	32

the Xilinx FPGAs architecture. This model has 26624 slices. It has also 160 Random Access Memory (RAM) blocks (RAMB16s) and 64 XtremeDSP slices (DSP48s), resources devoted to applications for digital signal processing. Moreover, in this FPGA it is possible to distribute up to 32 clock networks (GCLKs). One of the reasons to choose this FPGA was the required number of inputs and outputs to communicate with the ADC array. Figure 7.46 shows the block diagram of the main sub-systems previously discussed and their implementation in the FPGA. Other peripherals connected to the FPGA, such as an external PC, and an array of ADCs are also shown for clarity.

7.4.1 I/Q demodulation unit

Before calculating the correlation matrices, it is necessary to down-converter the digital signals of the receivers to baseband and obtain their in phase (I) and quadrature (Q) components. This section briefly presents the theoretical formulation and then explains the main blocks. The I/Q demodulation unit is composed of four blocks as shown in Fig 7.47: serial to parallel converter, two's complement, I/Q demodulation, and a selective LPF. The serial to parallel block is necessary to convert serial output of the ADCs forced by the limited number of pins in the FPGA to parallel for easier internal operations. Therefore the ADC device has been chosen with serial output and a sampling frequency of 5.745 MHz. Since the raw data that comes from the ADC is not suitable for data processing due its offset (128), this offset has to be subtracted. This offset is related with the fact that the ADC output gives a binary quantification of the analog signal between 0 and 255 (8 bits). So that, it is necessary to subtract this offset to have symmetrical positive and negative values at the same time, convert the data into 2's complement for to make easier the signal processing. The two main blocks: I/Q demodulation and the LPF are explained in detail in this section. Once the receiver's signal has been digitized the output has the following expression:

$$S(n) = \mathbb{R}\{(i(n) + jq(n)) \cdot e^{j\Omega n}\}, \tag{7.22}$$

where $\Omega = 2\pi F_{digital}$ is the carrier frequency. The above given expression can be rewritten as:

$$S(n) = i(n)cos(\Omega n) - q(n)sin(\Omega n), \tag{7.23}$$

Taking into a count the previous equation, it is possible obtain the $I(n)$ and $Q(n)$ components multiplying $S(n)$ by a cosine and a sine respectively, and low-pass filtering them:

$$I(n) = S(n)cos(\Omega n) = \frac{1}{2}i(n) + \frac{1}{2}(i(n)cos(2\Omega n) - q(n)sin(2\Omega n)), \tag{7.24}$$

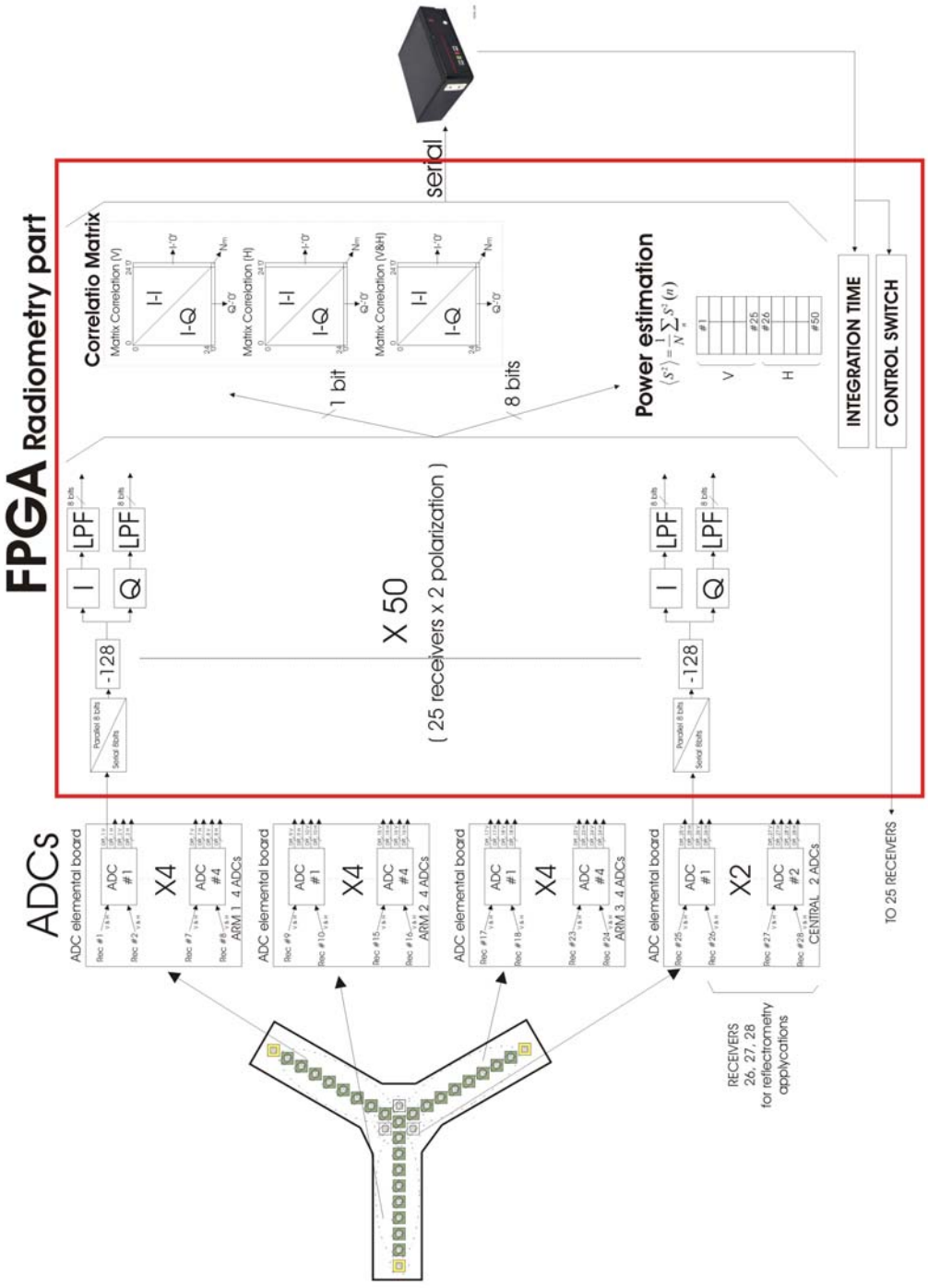

Figure 7.46. Global vision of the sub-systems implemented in the FPGA (radiometer part) and peripherals in PAU-SA.

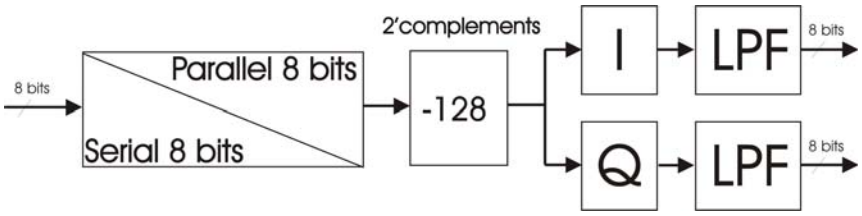

Figure 7.47. Block I/Q demodulation unit.

$$Q(n) = S(n)(-sin(\Omega n)) = \frac{1}{2}q(n) - \frac{1}{2}(i(n)sin(2\Omega n) + q(n)cos(2\Omega n)), \tag{7.25}$$

If these expressions are particularized to the digital frequency signal of $F_{digital} = 0.25$, the product of $S(n)$ by a cosine and a sine is equivalent to multiply $S(n)$ by a periodical sequence with period four:

$$cos(2\pi F_{digital}n) = cos(\frac{\pi}{2}n) = 1, 0, -1, 0... \quad with \quad n = 0, 1, 2, 3... \tag{7.26}$$

$$-sin(2\pi F_{digital}n) = -sin(\frac{\pi}{2}n) = 0, -1, 0, 1... \quad with \quad n = 0, 1, 2, 3... \tag{7.27}$$

Working with the ADCs, and using band-pass sampling it is possible to work with a specific digital frequency that minimizes the required hardware resources. In this particular case it is not necessary to implement a multiplier stage that requires lots of resources, but only to take either or not, a sample with the corresponding signs. These modules are implemented with a multiplexer block and an inverter function. Table. 7.10 shows true table with the different states to implement the in-phase and quadrature modules. Figure 7.48 shows the block diagram of the demodulation I/Q and filtering. Figure 7.49

Table 7.10. True table of the in-phase and quadrature modules.

state(2:0)	*MUX cos*	*MUX sin*
"111" (initial state)	"0"	"0"
"000"	sample	"0"
"001"	"0"	- sample
"010"	- sample	"0"
"011"	"0"	sample

presents a simple simulation to test the 2'complement and demodulation I/Q blocks without filtering. For a given input "s" of 130 equivalent to 2 in 2'complement, it is possible to check the expected values at the outputs of the demodulation I/Q blocks "si" and" sq" outputs in-phase and quadrature respectively. Every 8 clock periods "clk" or a clock period "n_m" the input signal is converted from serial to parallel 8 bits and then is 2'complement. The outputs "si" and "sq" match with expected values in Table. 7.10, equivalent to multiply the input signal by the sequence cosines and - sinus respectively

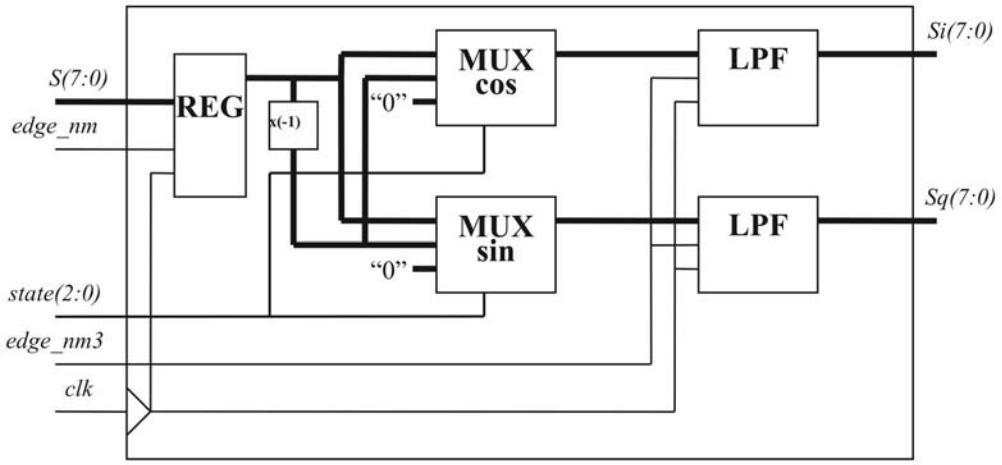

Figure 7.48. I/Q Demodulation block and low-pass filtering.

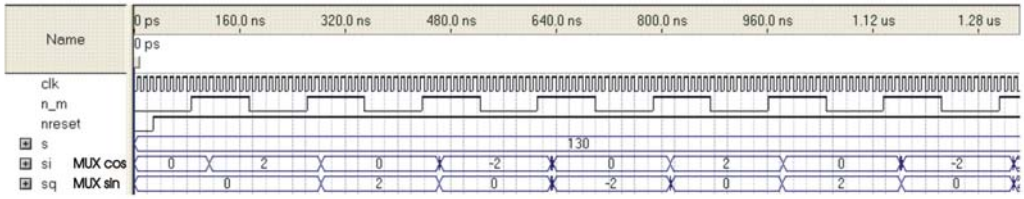

Figure 7.49. Time diagram to test the 2'complement and demodulation I/Q blocks without filtering output.

in 2'complement format. In the Eqns. 7.24 and 7.25 is it possible to observe a low frequency in-phase and quadrature terms plus a high frequency contribution that must be eliminated by a low-pass filter. In this case the digital LPF to use is the same as in PAU-RA. The filter implements an Infinite Impulse Response (IIR) LPF with a cut-off frequency of 0.25 in the digital domain with an attenuation of 20 dB at the frequency of interest, as shown in Fig. 7.50a. The filter behavior has 6 dB of gain that compensates the 0.5 factor in the phase and quadrature Eqns. 7.24 and 7.25. The disadvantage is that the phase does not have a perfectly linear behavior (Fig. 7.50b), and the group delay changes with frequency. This is not relevant, since all filters have exactly the same behavior and uniformity is guaranteed between receivers, unlike with analog filters. These filters have been implemented with elementary functions: delay blocks, adders and shift registers using the minimum FPGA resources Fig. 7.51a. To test the filter behavior, a pseudo-random sequence has been generated internally by means of a Linear Feedback Shift Register (LFSR) and introduced in the input of the filter. The Fourier Transform of the input and output response is plotted in Fig. 7.51b. As it can be noticed, the output response (in green) has a decrease of 3 dB at, similar behavior that in the theoretical case, Fig. 7.50a.

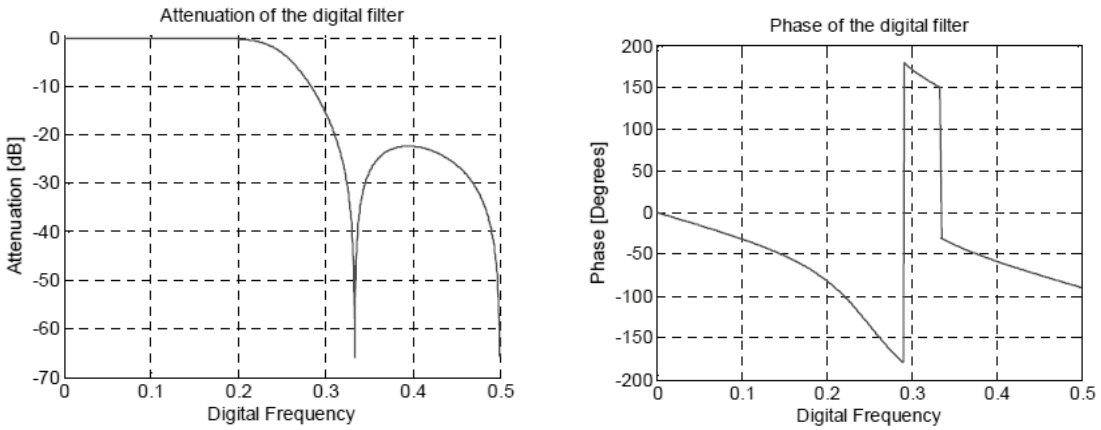

(a) (b)

Figure 7.50. a) Gain response IIR filter b) Phase response IIR filter.

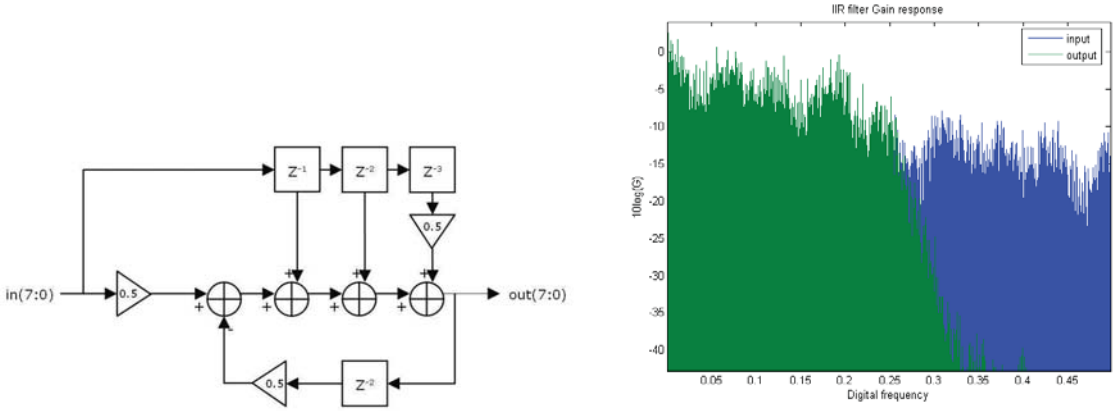

(a) (b)

Figure 7.51. a) IIR filter block diagram b) IIR filter gain response, in blue (input), green (output).

7.4.2 Power measurements

To recover the visibility function provided to the matrix correlation it is necessary an estimation of the system temperature for both polarizations. This means 25 (receivers) x 2 (polarizations) = 100 different power measures. To obtain this, each channel is considered as a total power radiometer with the following expression, Eqn. 7.28. Since it is not possible to work with infinite-bit samples, it is necessary to use a finite number of samples as show in Eqn. 7.29.

$$< S^2 >= \lim_{N \to +\infty} \frac{1}{N} \sum_n S^2(n), \tag{7.28}$$

$$< \widehat{S}^2 >= \frac{1}{N} \sum_n S^2(n), \tag{7.29}$$

$$< n^2 >=< n_i^2 >=< n_q^2 > . \tag{7.30}$$

To obtain this goal three components are going to be used: the IF signal, and the I/Q modulated components. Recalling that the nature of the signal is white noise is it possible to use any of the power measurements shown in Eqn. 7.30. On the other hand, the correlation matrix and the power measures must have the same number of samples. To simplify the synchronizing controls it is preferable to use the I/Q modulated components. To implement a power measurer it is necessary a multiplier and an adder. For this application it is preferable to use the internally implemented functions.

7.4.3 Digital Correlation Unit (DCU)

The digital correlations along with the power measures are the pre-processing signals implemented in the FPGA that allow applying in the image reconstruction algorithm and recovering the brightness temperature images. The Digital Correlation Unit DCU measures using 1 bit (sign bit) the equality between both signals. Basically it consists of counting the number of samples (N_c) with the same sign between all possible baseline combinations. Moreover, it is necessary obtain the maximum number of samples ($N_{c_{max}}$) proportional to integration time to normalize and obtain the (correlation, c) in the post-processing. Recalling that the sampling frequency (f_m) is 5.745 MHz and that the maximum integration time (T_{int}) is 1 s, then the maximum number of counts ($N_{c_{max}}$) is given by Eqn. 7.31, been necessary a counter of 23 bits $2^{23} \simeq 8.388$ Ms enough to count up to 5.745 Ms.

$$N_{c_{max}} = f_m \cdot T_{int} = 5.745 \quad \text{Ms}, \tag{7.31}$$

In this case, with 25 receivers and the I and Q demodulated components, the matrix correlation results (Fig. 7.52).

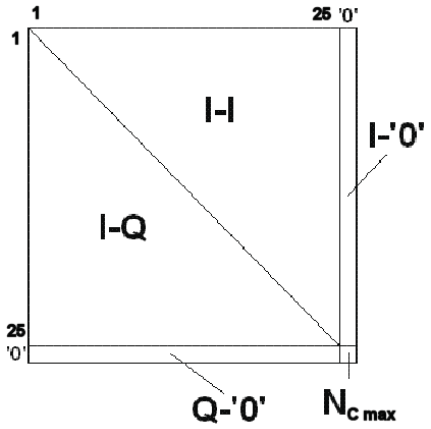

Figure 7.52. PAU-SA's correlation matrix.

where the correlations to calculate are:

$$\begin{gathered} R_{I_m,I_n}(0) \quad \forall n > m \\ R_{I_m,Q_n}(0) \quad \forall n \leq m \\ R_{I_m,'0'}(0) \quad \forall m \\ R_{'0',Q_m}(0) \quad \forall n \\ R_{'0','0'}(0) \quad N_{c_{max}} \end{gathered} \tag{7.32}$$

where $R_{X,Y}(0)$ are the correlations between the signals in-phase or quadrature X and Y, and the subindexes m, n are the receivers numbering. Therefore, the correlations between phase components (I-I) are the real part of the normalized visibility μ_r, and the correlations between in-phase and quadrature components (I-Q) correspond with the imaginary part of the normalized visibility μ_i. In the diagonal, are implement the the in-phase and quadrature components (I-Q) of the same signal, so it is expected a 0 value. Basically, to implement the correlator block two elementary components are required: a logic equality detector or XNOR gate (Table 7.11), and a 23 bits counter, as shown in Fig. 7.53. To implement only one polarization matrix, 676 results of 23 bits each one

Table 7.11. XNOR truth table.

S1	S2	OUT
0	0	1
0	1	0
1	0	0
1	1	1

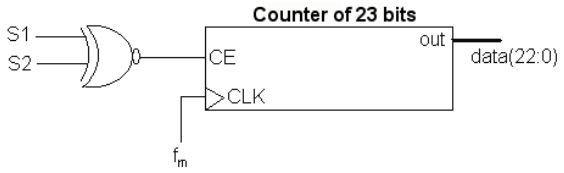

Figure 7.53. Elemental correlator block.

are necessary, this means that the design needs 15,548 slices. This is a problem since the FPGA used has only 26,624 slices; therefore, with this topology it is only possible to implement one of the three matrixes: both polarization and the cross-polarization. In this moment arises a new strategy to overcome this problem. From one hand, the use of the internal RAM memory to implement the counters (Fig. 7.54a), in total 676 x 3 = 2,026 counters, so it is possible to use the slices for other applications. On the other hand, when the working frequency is higher than the sampling frequency as it is the case here ($f_{clk} = 103.41\,\text{MHz} \gg f_m = 5.5745\,\text{MHz}$), it is possible to divide the sampling time

in different slots (Fig. 7.54b), and reused the hardware. The RAM memory used, can be read and written at the same time, therefore the maximum hardware reuse factor is:

$$r = \frac{T_m}{T_{clock}} = 18. \tag{7.33}$$

This value means that it is possible to do 18 internal operations until the next sample arrive. In our case the FPGA used has 160 independent RAM blocks for implementing 3 correlation matrices, this means 53 blocks for each block. In this case the hardware reuse factor necessary is:

$$r = \frac{676\, counters\, each\, matrix}{53\, RAM\, blocks\, each\, matrix} = 12.7. \tag{7.34}$$

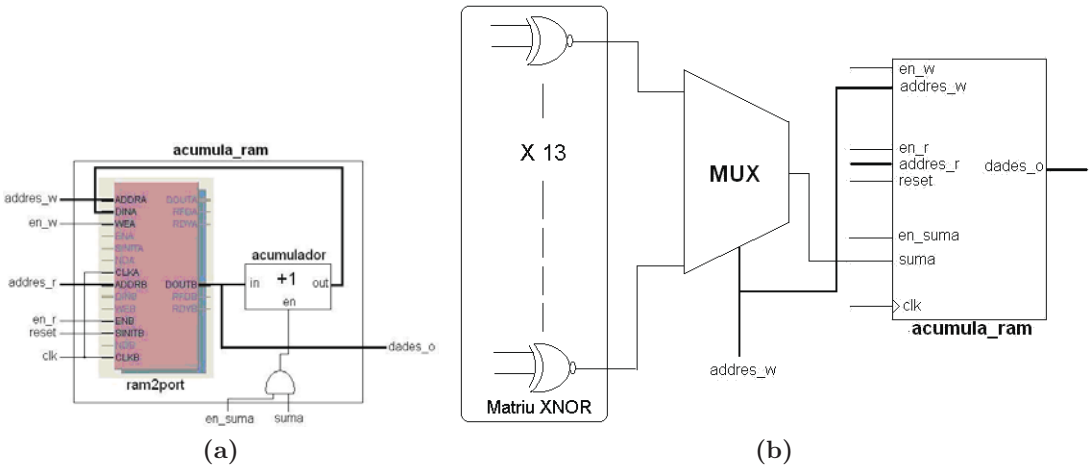

Figure 7.54. a) Memory counter architecture, and b) block reuse architecture.

7.4.4 Occupation of the FPGA resources

Once implemented the complete design in the FPGA, three correlations matrices (V, H, and VH) and the power estimations of each channel, in total 25 receiver x 2 polarization, 100 power estimations. The occupation level in the FPGA has been presented in Table 7.12. As it can be noticed, thanks to the hardware reuse, the implementation of the initial requirements has been possible. To avoid internal delays it is recommended not to exceed the 60% of use slides, in this case the 67%.

Table 7.12. Final report of the FPGA resources.

Resource type	Total	Used	Occupation
Slices	26,624	17,973	67 %
RAMB16s	160	160	100 %
DSP48s	64	50	78 %
GCLKs	32	1	3 %

7.4.5 Conclusions

This section has presented one of the most important parts in the PAU-SA instrument, the hardware processor unit implemented in a FPGA. With this unit it is possible to process in real time two important parameters for the later post-processing: the correlation matrices using 1 bit and the power estimation estimated with 8 bits. One of the factors to select the development board has been the number of Input/Output (I/O) pins; due to the high number the receivers in PAU-SA. The calculation of the three correlation matrices (V, H, and VH) and the power estimations has been possible, thanks to the minimization of the required internal data processing using the "band-pass sampling frequency" used in the ADC stage in addition the hardware reuse technique increasing the clock frequency.

Currently in the FPGA there are problems of de-synchronization presented in section ADC's board array (Section 7.3). These are caused by internal delays in the connections due to the high occupation rate and that can not be controlled during the design process. Three solutions with different levels of complexity are proposed to solve the problem. The first one leads to a study / simulate the entire system to compensate for possible delays. Although this part has already been implemented, and the design was designed with pipeline architecture (architecture to achieve synchronization) to avoid delays, in practice has not been possible. Several variants of the architecture were tested getting worse results. The second option involves the reduction of requirements eliminating some correlation matrices. The latest solution is presented in (Section 7.3), it consist of make independent the (data and control) of each ADC.

7.5 Master clock

The basic operation in a synthetic aperture radiometer is the correlation of signals coming from each pair of antennas (baseline) in the same time slot. Therefore keeping a synchronous system is fundamental. For this reason all receivers are fed with the same clock reference (Master clock) to synthesize their internal local oscillators. This section presents the master block module and its respective buffers to distribute the clock signal. Figure 7.55a shows the Master clock location and interconnection in the PAU-SA's system block diagram and Fig. 7.55b shows, the Master clock distribution in the PAU-SA's structure scheme.

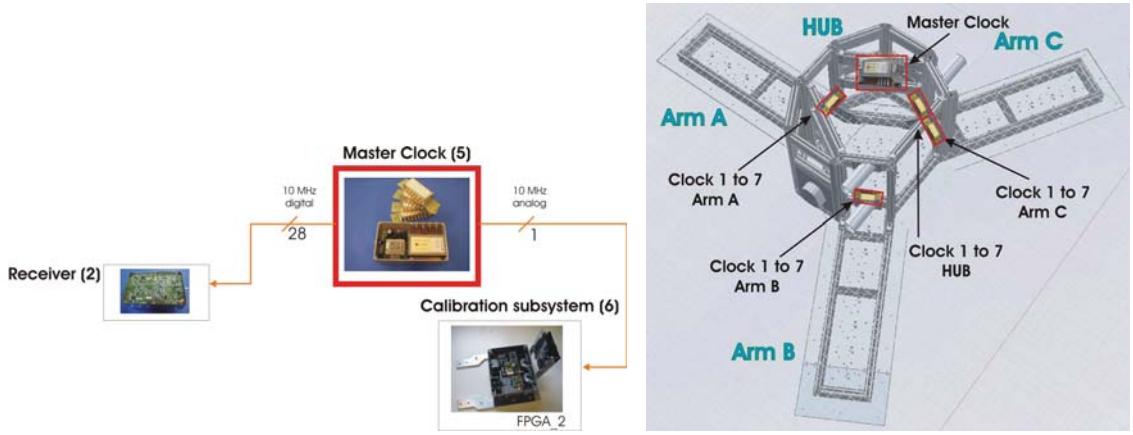

(a) (b)

Figure 7.55. a) PAU-SA's Master clock location and interconnection in the PAU-SA's system block diagram, and b) Master clock distribution in the PAU-SA's structure scheme.

7.5.1 Master clock unit

Figure 7.55a shows the modules connected to the Master clock unit. As it can be appreciated, there are 28 digital clock references to feed each receiver. Moreover, an independent analog clock reference is necessary in the calibration subsystem. The core of the Master clock is the low noise Oven Controlled Crystal Oscillator (OCXO) model OX6749A-LZ-1 from RALTRON (Fig. 7.56a). It is a 10.00000 MHz analog clock with an excellent frequency stability of 0.01 ppm, and an output amplitude of +7 dBm. Since it is not feasible to feed all receivers directly; it is necessary to add several intermediate buffers. The module of the Master clock core converts the single Master clock in four digital references, one for each of the three arms and the hub, a one analog for the calibration subsystem as shown in Fig. 7.56b. The analog clock is used in the correlation noise unit to generate a local oscillator through the internal signal synthesizer necessary to up-convert the PRN base-band signal in a RF signal at the work frequency. Each of these four digital references feed an external 1 to 7 buffer box as shown in Fig. 7.56c. Since the distance between the Master clock unit and each receiver is considerable, to avoid Electro Magnetic Interference (EMI) problems, the ground connection in the clock distribution

network is especially critical. For this reason a star-shape distribution connection has been chosen for this purpose. Figure 7.56c shows the Master clock unit opened. It is

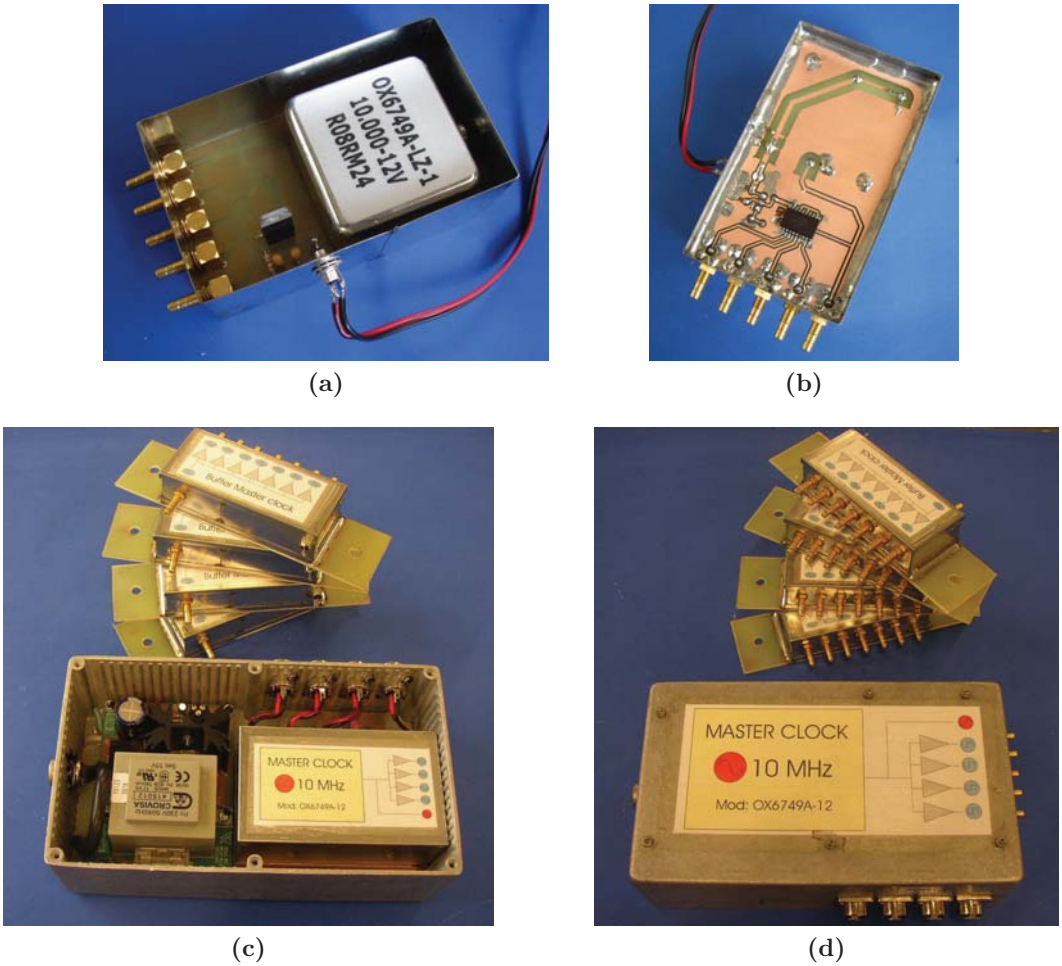

(a) **(b)** **(c)** **(d)**

Figure 7.56. a) Picture of the module Master clock core (top view), b) picture of the module Master clock core (bottom view), c) picture of the Master clock unit opened and 1 to 7 buffer distribution, d) picture of the Master clock unit closed and 1 to 7 buffer distribution.

possible to observe the Master clock core, Figs. 7.56a and 7.56b and the clock distribution power supply. Moreover, there are four connectors to lead the power supply to the external buffers in a star-shape configuration. Figure 7.56d shows the Master clock unit closed.

7.5.2 Conclusions

This section has presented the Master clock unit. This is the module that generates the common oscillator necessary to feed the PLL of the local oscillators of all receivers. The Master clock is the low noise OCXO from RALTRON model OX6749A-LZ-1. Since it is not possible to feed with a single clock all receivers, a clock power splitter has been implemented. Moreover, this frequency is used in the correlated noise unit to generate

a local oscillator to up-convert the PRN signals from baseband up to the frequency of operation.

To distribute the master clock to all receivers, semi-flexible cable with SMB connectors has been used. In the first version, Ethernet cable with RJ45 connector was proposed to reduce the wiring, but it was discarded due to degradation of the analog signal, having to use shielded cable. Another important part is the clock distribution topology, choosing a star topology (all ground cables in a common place) to avoid RFI.

7.6 Calibration subsystems

The calibration of correlation radiometers, and particularly aperture synthesis interferometric radiometers, is a critical issue to warrant their performance. Current calibration techniques are based on the measurement of the cross-correlation of receivers' outputs when injecting noise from a common noise source requiring a very stable distribution network. For large interferometric radiometers this centralized noise injection approach is very complex from the point of view of mass, volume and phase/amplitude equalization. Distributed noise injection techniques have been proposed as a feasible alternative, but are unable to correct for the so-called "baseline errors" associated to the particular pair of receivers forming a baseline. Moreover, the thermal noise introduced by the equalized distribution network itself introduces an error that must be compensated by taking differential measurements acquired with two different noise levels. In order to feed all receivers with a centralized noise topology, this section presents the correlated noise unit in witch is possible to select between the injection of two different noise signals: the classical noise source, and a new technique using PRN sequences. Figure 7.57a shows the correlated noise unit location and the interconnection in the PAU-SA's system block diagram, Fig. 7.57b shows the correlated noise unit distribution in the PAU-SA's structure scheme.

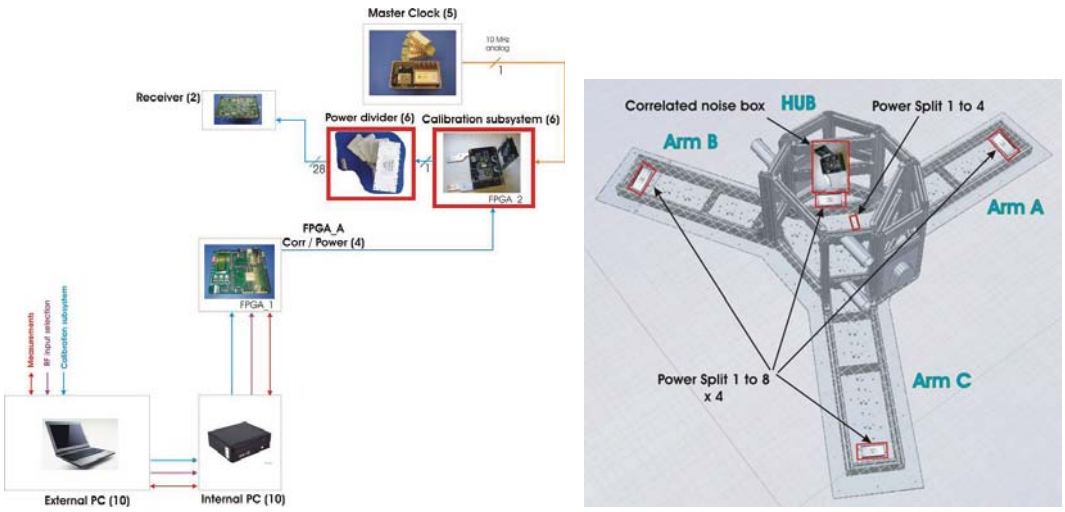

(a) (b)

Figure 7.57. a) PAU-SA's correlated noise unit location and intercommunion in the PAU-SA's system block diagram, and b) correlated noise unit distribution in the PAU-SA's structure scheme.

7.6.1 Correlated noise unit

Figure 7.58 shows the correlated noise diagram. It consist of three main blocks: two block for the signal generation (on the left), composed of thermal and pseudo-random noise and a selection circuitry (on the right). Regarding the noise signals there are two different: a classical noise source, and a new technique using Pseudo-Random Noise PRN sequences. Any of these signals can be selected using the selector block.

7.6.1.1 Thermal noise

The Classical noise source has been implemented with a NoiseCom noise source model NC346D with an Excess Noise Ratio (ENR) of 21.31 dB. The ENR can be related with an equivalent temperature T_n at the output of the noise source as:

$$ENR_{dB} = 10 \log \left(\frac{T_n}{T_0} \right) - 1 \quad [\text{dB}], \tag{7.35}$$

where T_0 is the reference temperature of the noise considering it of 290 K. In this case the T_n resulting:

$$T_n = T_0 \cdot \left(10^{\frac{ENR_{dB}}{10}} + 1 \right) = 39.5 \cdot 10^3 \quad [\text{K}]. \tag{7.36}$$

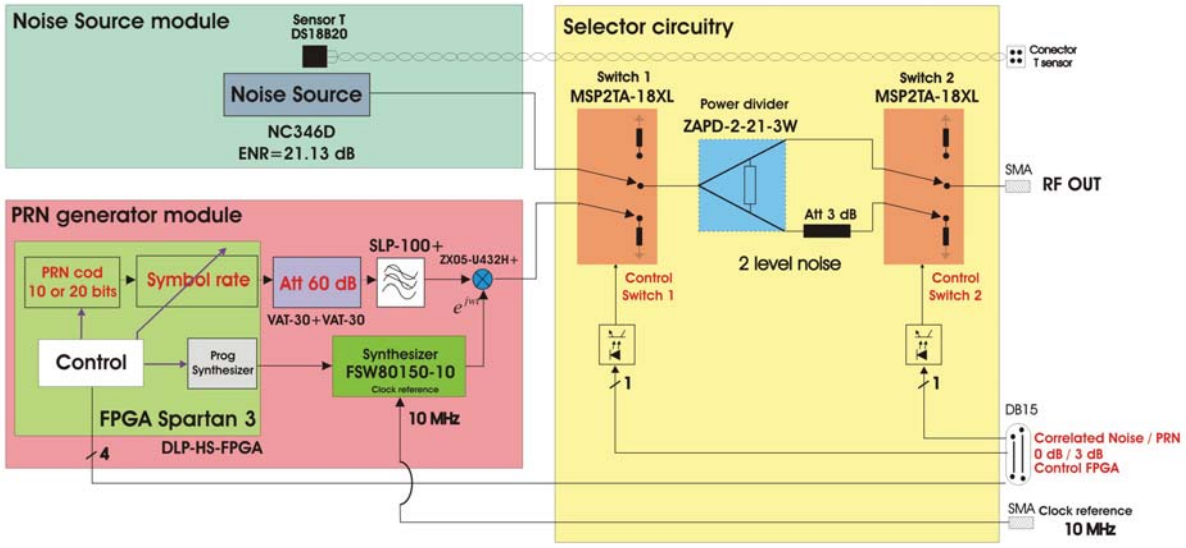

Figure 7.58. Correlated noise unit block diagram.

7.6.1.2 Pseudo-Random Noise (PRN)

Pseudo-Random Noise (PRN) sequences are signals with very long repetition periods that are used in a variety of applications, such as CDMA communications or positioning systems. They have a relatively flat spectrum over a bandwidth determined by the length of the sequence and the speed of the code or SR. Their spectra looks like the noise spectrum, and the calibration of a microwave correlation radiometer (either interferometric or polarimetric) can benefit from these properties (Fig. 7.59). The SR parameter is used to determine the speed of the PRN code in order to control the bandwidth of the spectrum. The symbol rate is defined as the ratio of the bandwidth of the PRN signal (B_{PRN}) and the receiver's lowpass equivalent bandwidth (B), Eqn. 7.37. B_{PRN} is related

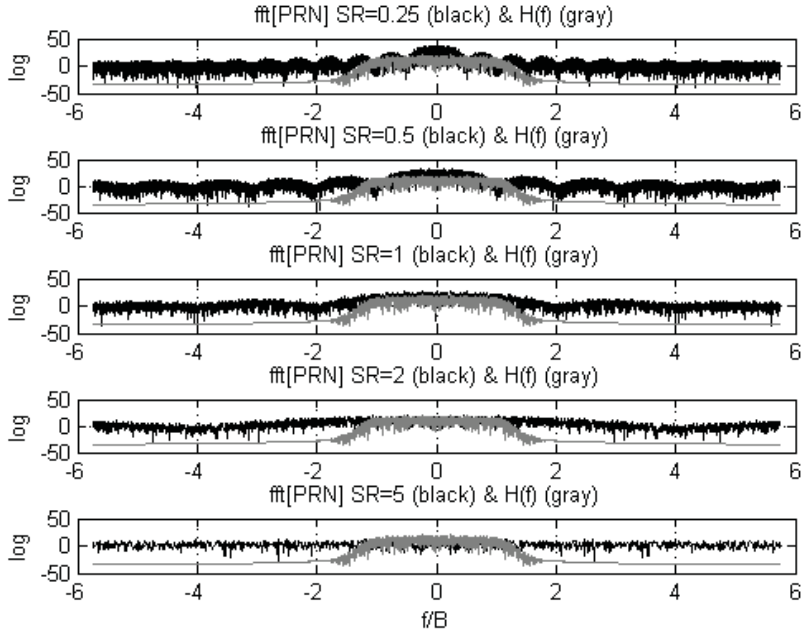

Figure 7.59. Equivalent lowpass spectrum of PRN sequence (black) with different SR and H(f) (gray). Positive and negative frequencies plotted.

to the sequence duration (τ_{PRN}) and the number of chips (a chip is like a bit, but it does not carry any information) N_{chips} as shown in Eqn. 7.38.

$$SR = \frac{B_{PRN}}{B}, \tag{7.37}$$

$$B_{PRN} = \frac{N_{chips}}{\tau_{PRN}}. \tag{7.38}$$

The equivalent noise temperature of the PRN signal (T_{PRN}) at the PRN generator module output is defined in terms of the PRN signal's amplitude (A) : $P_{PRN} = A^2/2 \triangleq k_B \cdot T_{PRN} \cdot B_{PRN}$, where P_{PRN} is the PRN signal power and k_B is the Boltzmann constant ($1.3806503 \cdot 10^{-23}$ J/ K).

The PRN is generated with a LFSR [97] as used for example in GPS applications. This part has been implemented in the FPGA model Spartan 3 of Xilinx using the module HLP-HS-FPGA of DLP Design shown in Fig. 7.60. The system has been designed to have the possibility to select between 10 or 20 order primitive polynomials which maximum-length to generate two pseudo-random sequences of length $2^{nbits} - 1$, respectively. The LFSR can produce output at different speeds by selecting the SR parameter. Internally the reference clock of 1.023 MHz is multiplied by the SR parameter to change the speed of the sequence. Taking as a reference the polynomial of order 10 with a length sequence of 1023 chips, with SR = 1, the complete sequence is generated in 1023 chips / 1.023 MHz = 1 ms, with SR = 2, there are two complete sequences generated in the same time and so on. With the 20 order polynomial with a length sequence of 1,048,575 chips, the sequence looks like more random, that is to say, with SR = 1, needs 1,048,575 chips /

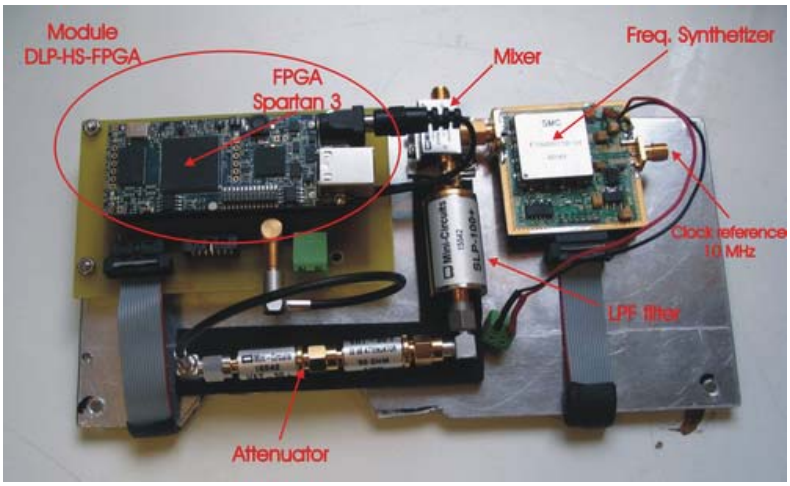

Figure 7.60. PRN module circuitry.

1.023 MHz = 1,025 ms to repeat the sequence, and with SR = 2 needs half the time and so on. The output of the LFSR is baseband and it is internally modulated up to 80 MHz to be up converted with the external mixer up to 1,575.42 MHz. Since the output of the digital signal is around 3.3 V, it has been necessary to put some attenuators in order not to saturate the receivers. In this case a 60 dB attenuator has been achieved cascading two attenuators of 30 dB model VAT-30 from MiniCircuits. Then, this signal is low-pass filtered at 100 MHz with the filter model SLP-100+ from MiniCircuits to eliminate possible spurious out of the band of interest. Finally the baseband signal is up-converted to the frequency of interest (L1) using the ZX05-U432H+ mixer from MiniCircuits. To do this, the mixer needs a local oscillator of 1,575.42 MHz - 80 MHz = 1,495.42 MHz, which has been implemented using a surface mount frequency synthesizer model FSW80150-10 from Synergy Microwave Corporation. This device is programmed at the beginning through the Spartan 3 FPGA. An analog reference clock of 10 MHz and 1 Vpp generated in the module Master clock (Section 7.5) is necessary in the synthesizer to feed the internal PLL. Figure 7.61 shows an acquisition with the spectrum analyzer where it is possible appreciate the PRN bandwidth in function of the SR parameter. The higher the SR the higher the PRN bandwidth.

7.6.1.3 Selection circuitry

Once the two different noise sources (thermal and PRN) have been independently generated, these are injected into a selector circuitry (Fig. 7.58). The function of this part is to select between the Noise Source or the PRN generator, and provide two power levels so as to perform differential measurements. Figure. 7.62 shows the hardware implementation. The first element (switch 1) is an absorptive mechanic switch model MSP2TA-18XL from MiniCircuits to select between the two sources. It has an isolation of 100 dB at the frequency of operation. The selected source is divided into two branches through a power combiner model ZAPD-2-21-3W from MiniCircuits. One of the branches is attenuated 0 dB and the other is 3 dB. Finally a second absorptive mechanic switch (switch 2), selects the required attenuated output. It is recommended be absorptive in order to not modify

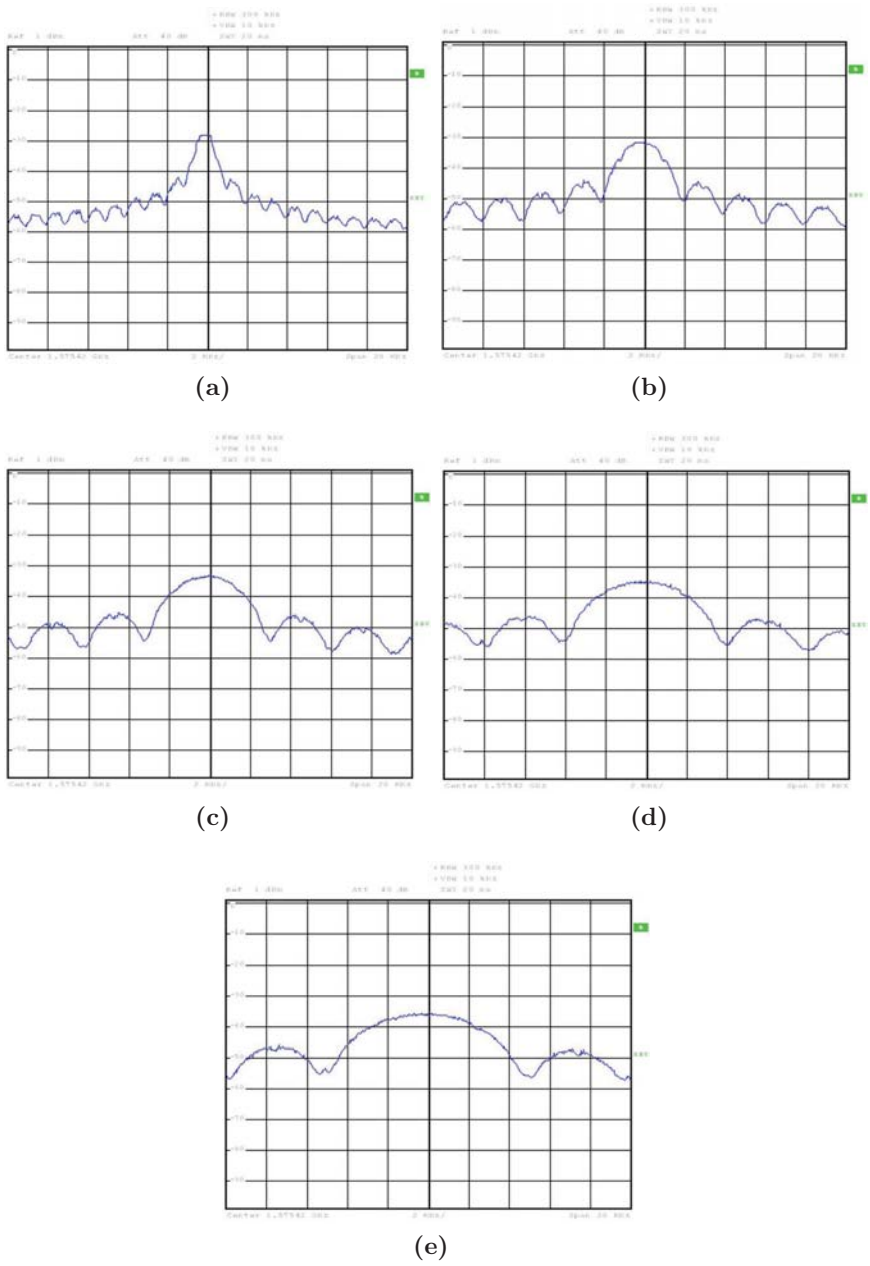

Figure 7.61. Spectrum analyzer acquisitions of different PRNs generated with different SRs. Central frequency of 1,575.42 MHz, 2 MHz/div, span = 20 MHz and 10 dB/div. a) SR = 1, b)SR = 2, c) SR = 3, d) SR = 4 ,and e) SR = 5.

the power level of the sources.

7.6.1.4 Correlated noise unit integration

Figure 7.63 shows the metallic box where the correlated noise sources and the selection circuitry have been integrated. In order to minimize the area these modules have been

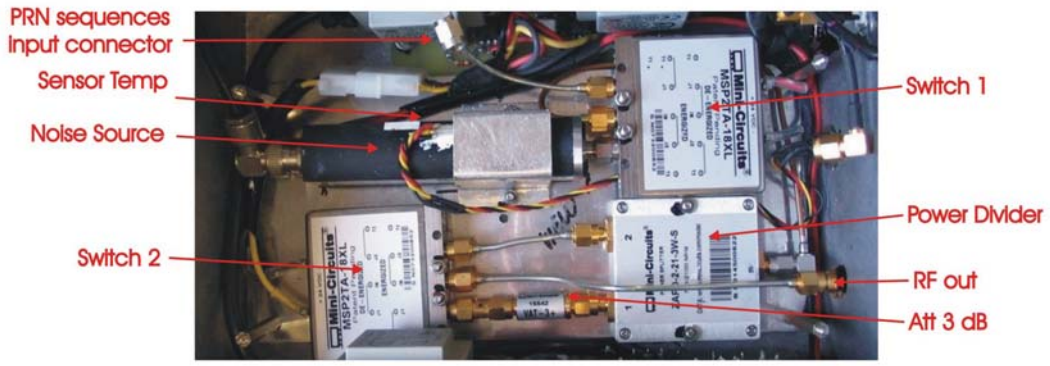

Figure 7.62. Hardware implementation of the selection circuitry.

integrated in different layers. In the bottom layer the Noise Source module and the selection circuitry have been implemented and the PRN sequences module in the top layer. The FPGA 2 synthesizes the PRN sequences. It is controlled with a DB15 connector through the internal PC as shown in Fig. 7.63. Three commands are required to fully control the correlated noise unit, one to select the attenuation, 0 or 3 dB (Table 7.19), another to select the correlated noise (Table 7.20), and the last one to select the SR of the PRN (Table 7.21).

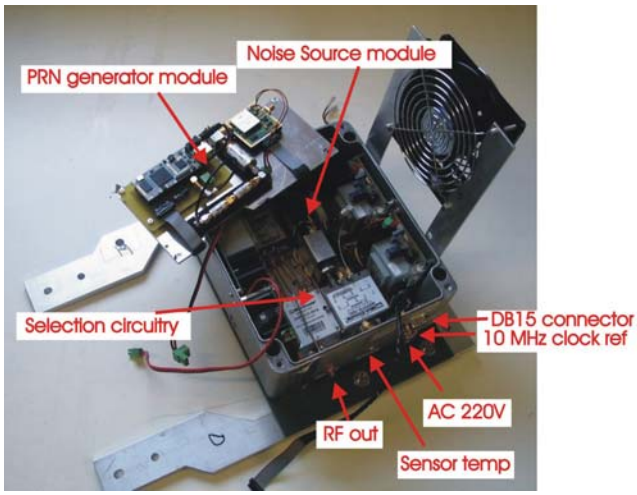

Figure 7.63. Hardware implementation of the correlated noise unit.

7.6.2 Correlated noise network distribution

For the standard calibration process it is necessary to know some parameters that affect the instrument. Hence, it is necessary to measure or characterize them (ancillary data). The scattering parameters of the noise injection network and the noise source are essential parameters for the calibration. The network is composed by:

- Noise source selected,

- Attenuator (0 / 3 dB),
- Power splitter, and
- Cables and connectors.

The noise injection network is composed by five power splitters. As the injection is centralized, the noise source selected (RF out of the correlated noise unit) is connected directly to the first 4-way power splitter (model ZX10-4-19). Each output is connected to the other four 8-way power splitter (model ZB8PD-2), and it to the receivers. The last output of the 8-way power splitter or not used is adapted, as it is not connected to any receiver. The scattering parameters of each power splitter are measured in the laboratory and then combined to obtain the resulting matrix of S-parameters of the noise injection network. To construct the resulting matrix, it has been assumed that all ports are perfectly matched, the cables attenuation and phase are taken into account.

7.6.3 Cables and connectors

The cables used to distribute the correlated noise source through the power splitter and the receivers is a EZ-86-TP-M17 model. To compute the attenuation the following equation must be solved:

$$attenuation = a \cdot f^{0.5} + b \cdot f \qquad \text{[dB/m]}, \tag{7.39}$$

where the constant a and b depend on the frequency. For the PAU-SA operating frequency, the following values are assumed:

$$\begin{aligned} a &= 0.58454, \\ b &= 0.03967. \end{aligned} \tag{7.40}$$

The resulting attenuation depends on the length of the cables, where all path are the same length (2.5 m). The obtained attenuation is 2 dB. The cable also affects the phase, which depends as well on the cable length:

$$phase = e^{-j\beta l} \qquad \text{[rad]}, \tag{7.41}$$

where l is the cable length and β is:

$$\begin{aligned} \beta &= k\sqrt{\varepsilon_r}, \\ k &= 2\pi/\lambda, \\ \varepsilon_r &= 2.2. \end{aligned} \tag{7.42}$$

Between the input and any output there are 11 connectors, each one with an attenuation of approximately 0.1 dB. Figure 7.64 shows the complete network distribution been composed of the elements numerated as:

1. Noise source model NC346 Series by NoiseCom with a ENR of 21.32 dB at 1.5 GHz or the PRN sequences,

2. Power divider 1 to 2 model ZAPD-2-21-3W by Minicircuits,
3. Switch 1 to 2 model MSP2TA-18XL by Minicircuits,
4. Attenuator 3 dB VAT-3 by Minicircuits,
5. Power splitter 1 to 4 model ZX10-4-19 by Minicircuits,
6. Power splitter 1 to 8 model ZB8PD-2 by Minicircuits, and
7. Semi-rigid microwave cable model EZ-86-TP-M17 by Huber & Suhner.

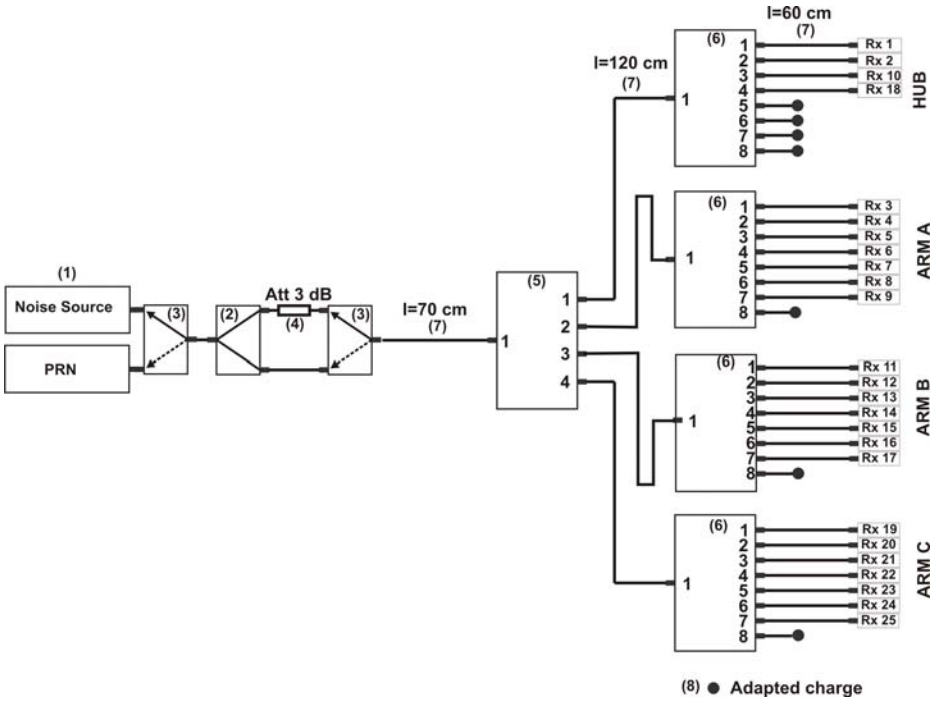

Figure 7.64. Correlated noise source network distribution.

Table 7.13 shows the attenuation of both of the possible paths (T_{hot} with 0 dB and T_{warm} with 3 dB).
At each receiver input two level temperatures are obtained given by Eqn 7.43.

$$T_{hot} = \frac{T_n}{L_{hot}} + T_{ph}\left(1 - \frac{1}{L_{hot}}\right) = 452.3\,\mathrm{K} \tag{7.43}$$

$$T_{warm} = \frac{T_n}{L_{warm}} + T_{ph}\left(1 - \frac{1}{L_{warm}}\right) = 371.3\,\mathrm{K}$$

where T_n is the equivalent temperature in the select circuitry input, Fig. 7.58, L_{hot} and L_{warm} are the selected attenuation calculated in Table 7.13, and T_{ph} is the physical temperature (290 K).

Table 7.13. Attenuation of the noise distribution network.

Device	Units	Att / unit	Total Att	
			L_{hot}	L_{warm}
SMA Connectors	11	0.1 dB	1.1 dB	1.1 dB
Cable EZ-86-TP-M17	2.5 m	0.78 dB/m	2 dB	2 dB
Switch 1 to 2 MSP2TA-18XL	2	0.15 dB	0.30 dB	0.30 dB
Attenuator 3 dB	1	3 dB	0 dB	3 dB
Power splitter 1-2 ZAPD-2-21-3W	1	3.4 dB	3.4 dB	3.4 dB
Power splitter 1-4 ZX10-4-19	1	6.75 dB	6.75 dB	6.75 dB
Power splitter 1-8 ZB8PD-2	1	9.8 dB	9.8 dB	9.8 dB
Total			23.35 dB	26.35 dB

7.6.4 Discussion and consideration

Correlation radiometers require the injection of known calibration signals. Currently these signals are generated by one or several noise sources and are distributed by a network of power splitters, which is bulky, difficult to equalize, and introduces additional noise. In this section a correlated noise unit has been presented that has the possibility to inject different noise signals: a noise source and PRN sequences. Due to the reduced number of receivers in PAU-SA is possible the use of a centralized noise injection using a single noise source. Moreover, a new technique to feed a number of independent of receivers is presented. It consists of the centralized injection of a deterministic PRN signal to all receivers, providing a complete baseline calibration. The PRN signal exhibits a flat spectrum over the receivers' bandwidth, which allows its use for calibration purposes instead of the usual thermal noise. Moreover, its signal amplitude is constant and therefore the power can be much higher than in the case of injecting noise (no need to have margin to avoid signal clipping) making the calibration less sensitive to the receivers' thermal noise. Once determined by measuring the power level of the receivers using the noise source, was preceded to adjust the PRN signal. In this case has been necessary attenuate 60 dB the output of the FPGA to achieve the same levels as in the previous case. Nowadays in the case of the PRN signal exist a maladjustment being necessary a readjustment of value. For this reason it is recommended replacing the fixed attenuator by a programmable one in order to modify the power level of the PRN with the noise source when necessary.

7.7 Other sensors

This section is devoted to present the rest of sensors located in PAU-SA instrument. To retrieve the SSS and the SM, in addition to the brightness temperature collected by the antennas are necessary additional information such as: receivers's physical temperature by means of temperature sensors to denormalize the visibility function, measurement of the target physical temperature pointed with the antennas through a IR as input parameter, sea state roughness by means of the GPS receiver as input parameter, and positioning parameters through a compass to georeference the measurements. Figure 7.65 shows the location, and interconnection in the PAU-SA's system block diagram.

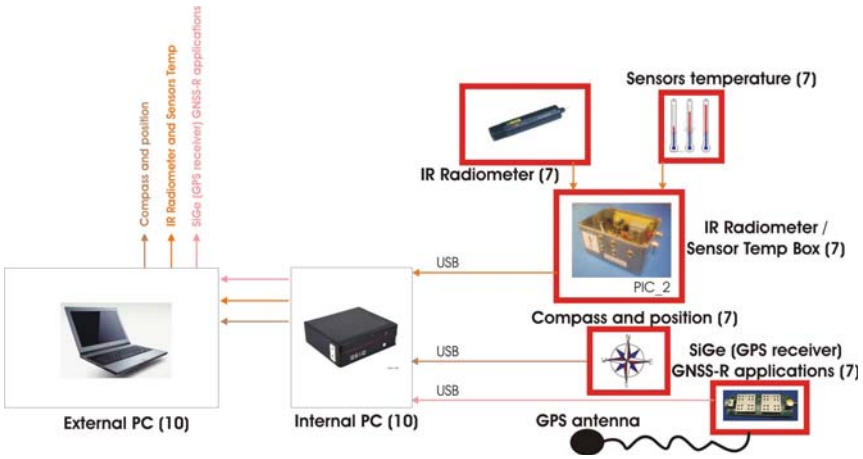

Figure 7.65. Other sensors location and interconnection in the PAU-SA's system block diagram.

7.7.1 IR / temperature sensor unit

Both the Infrared Radiometer (IR) and the temperature sensor located in the receivers and the structure are controlled with Programmable Interrupt Controller (PIC) 2. For this reason the IR and sensor temperature have been implemented in the same box as show Fig. 7.66. The next sections present each one of these parts.

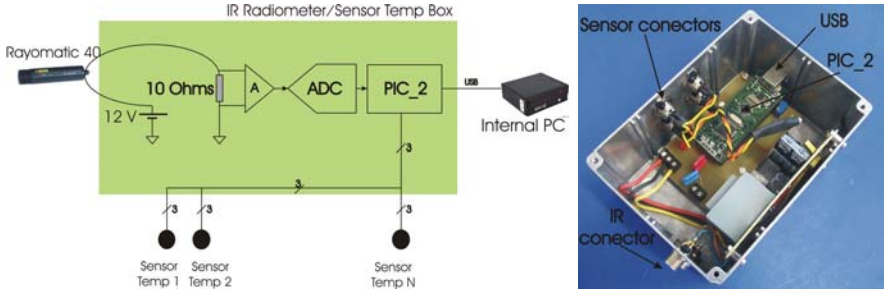

(a) (b)

Figure 7.66. a) Block diagram of the IR and temperature sensors unit connections, and b) Picture of the IR and temperature sensors unit.

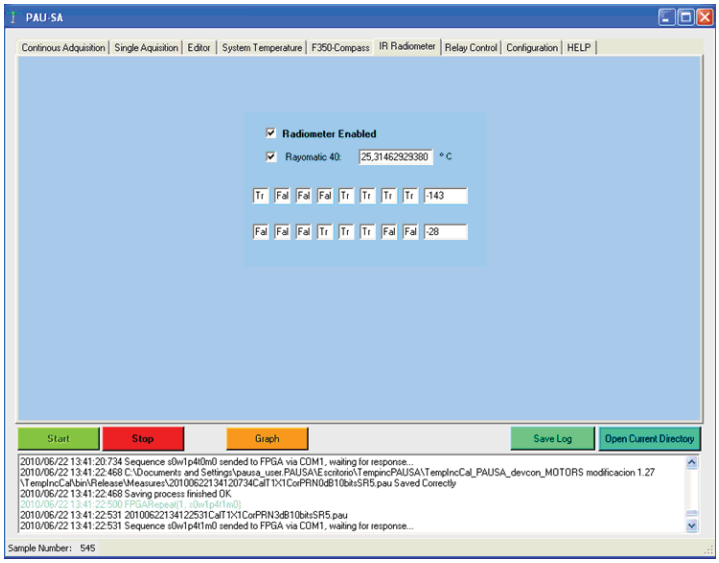

Figure 7.67. PAU-SA's main program showing the IR window.

7.7.1.1 IR radiometer

One of the three sensors necessary to retrieve the SSS is the IR. To measure the physical temperature of the target a commercial infrared thermometer model Rayomatic 40 from Eurotron has been used. It is an analog current loop device that has been digitalized for easy manipulation. The IR needs a 12 V power supply and its current power consumption is proportional to the measured temperature as:

$$I = 4\,\text{mA} + \frac{16\,\text{mA}}{60^{\text{o}}\text{C}} \cdot \text{T} \quad [^{\text{o}}\text{C}]. \tag{7.44}$$

Table. 7.14 shows the range current to temperature conversion. To manipulate this

Table 7.14. Rayomatic 40 current to temperature conversion.

Current	Temperature
4 mA	0 ° C
20 mA	60 ° C

information a current to voltage conversion has been implemented inserting in the current loop a low tolerance load resistor of 10 $\Omega \pm 0.1\%$ as shown in Fig. 7.66a. Now the range of obtained voltages is from 40 mV to 200 mV. This information is sent to an instrumentation amplifier INA101KU from Texas Instruments to adjust the voltage dynamic range of the ADC model LTC2451 from Linear Technology. Finally, the digital information is send to the PIC 2 via the I^2C protocol, and it sends the digital measurement via the USB to the internal PC. Figure 7.66b shows the IR/ temperature sensor unit. In it, it is possible to appreciate the IR connector, the PIC, and the USB to connect with the internal PC. Figure 7.80b in Section 7.9 shows the IR location, pointing to the target. Figure 7.67 shows the main program in the IR window showing the resultant measurement in decimal and in binary for test purposes.

7.7.1.2 Temperature sensors

In order to measure a large number of temperatures sensors grouped according: 25 sensors located inside each receiver in order to measure the physical temperature of the internal matched load, Fig. 7.68a, other 12 sensors distributed over the ground plane every two antennas to sense the antenna physical temperature (Fig. 7.68b), other in the noise source to monitor its temperature drifts (Fig. 7.62), and another sensor for future GNSS applications. In total 39 temperature sensors have been placed inside the PAU-SA instrument been possible to select every single sensor independently to plot and register in a file the thermal drifts evolution (Fig. 7.69). For this application the temperature sensor model DS18B20 from Maxim in case TO92 has been chosen. This is a temperature digital sensor which only requires three wires, one for the serial communication, and two more for power supply. To connect several sensors they must be connected in parallel,

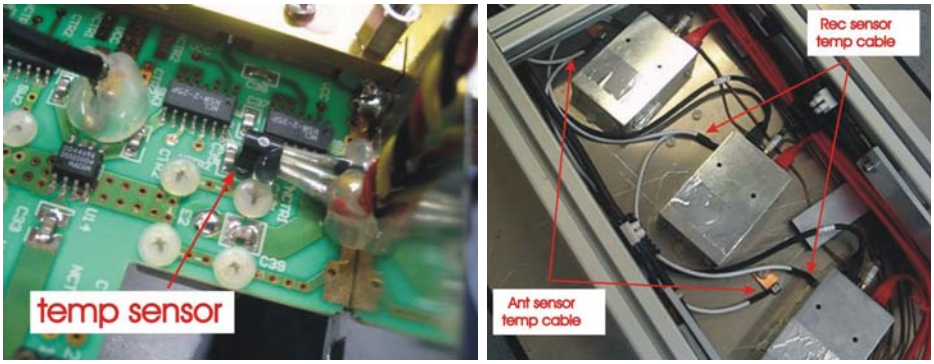

(a) **(b)**

Figure 7.68. a) Block diagram of the IR and temperature sensors unit connections, and b) Picture of the IR and temperature sensors unit.

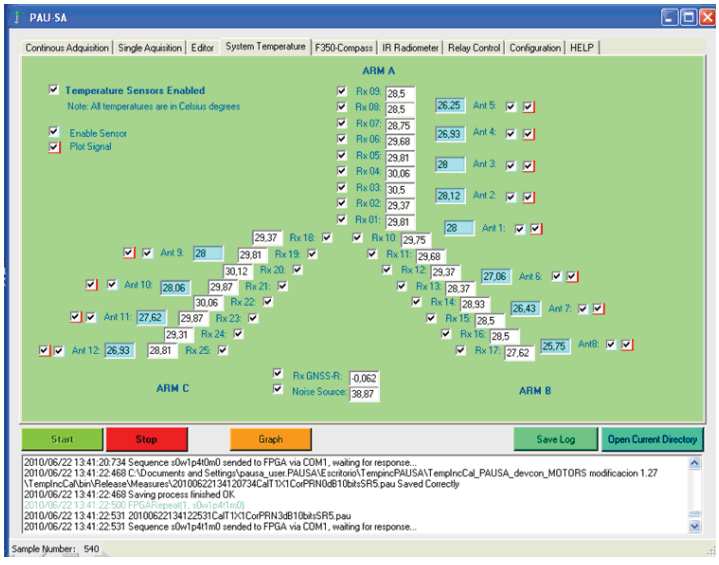

Figure 7.69. PAU-SA's main program showing the system temperature window.

minimizing the wiring, and not requiring external components. Since each device has a unique code of 64 bits stored in its on-board Read Only Memory (ROM), they can be identified uniquely. The measured temperatures are from -55 ºC to 125 ºC with ±0.5 °C of accuracy. Temperature resolution is selectable by the user from 9 to 12 bits.

7.7.2 Compass and position

In addition of the two position sensors located on the elevator tower for movements purposes, a digital compass has been placed inside the instrument to record the attitude of each measurement (Fig. 7.70). The digital compass is a fully functional tilt compensated compass, and combines magnetic and tilt measurement sensors. It consists of a magnetized pointer, free to align itself accurately with Earth's magnetic field providing three angles:

- azimuth angle: angle between magnetic North and the heading direction in sexagesimal, and
- inclination angles of tilt on both X and Y axis measured correctly up to 70º on both axes in degrees.

For proper operation the compass has to be calibrated the first time. It is connected via Universal Serial Port (USB) (no battery required) with the internal PC, and controlled with the PAU-SA'main program (Fig. 7.71).

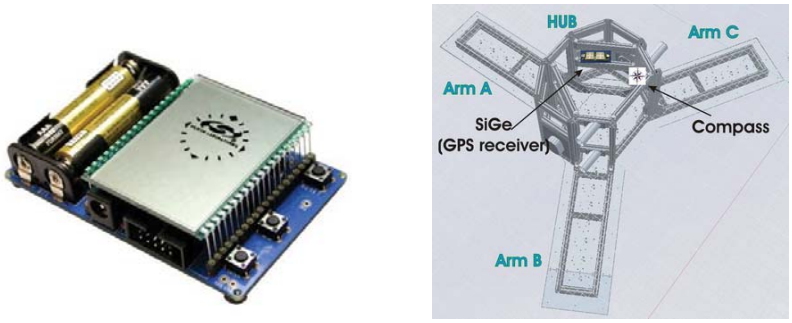

(a) **(b)**

Figure 7.70. a) Digital compass used in PAU-SA model F350 from Silicon Laboratories, and b) compass location in the instrument.

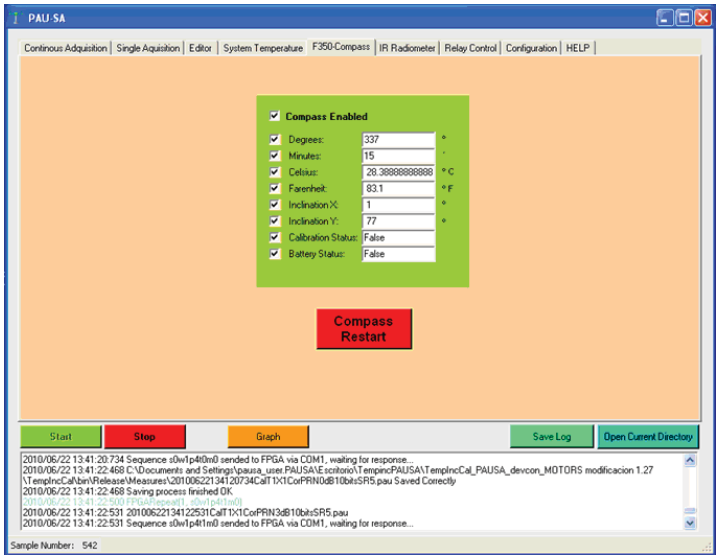

Figure 7.71. PAU-SA's main program showing the F-350 Compass window.

7.7.3 GNSS-R aplications

To determinate the sea state roughness PAU-SA will use GNSS-R techniques. At the beginning of the project, this part used the 7 central elements for this application, but for timing and simplification reasons it will be implemented in a near future. Nowadays this part has been substituted by a commercial GPS receiver .The antenna has been placed at the end of the arm C as shown in Fig. 7.2b, and the receiver located as shown in Fig. 7.70b. In the same way of the other sensors, it is connect via USB to the internal PC.

7.7.4 Discussion and consideration

This section has presented the auxiliary sensors located in PAU-SA to provide ancillary data. Nowadays some of these sensors are placed for future SSS processing such as: the IR to retrieve the physical temperature of the target and the a commercial GPS receiver for GNSS-R applications. In order to simplify the hardware complexity, the original PAU concept (radiometer and GNSS-R combined in the same receiver) has been discarded focusing in the synthetic aperture radiometer part. The GNSS-R part has been replaced by a commercial GPS receiver, leaving the initial requirements (use the seven central elements to create a steerable array to be able to point to the GNSS signal specular reflection point) for a future incorporation in the instrument.

7.8 Control switch

One of the most critical operations in PAU-SA instrument is the moment in which it is turned on. The receivers have high gain and the power supply has to be stable to have its expected behavior. For this reason the receivers are the last elements to be turned on in a controlled manner. PAU-SA is sequentially turned on to avoid problems with the power supply such as demanding too much current that will cause a voltage fall. To do this two modules have been designed: the control switch and the power supply switch modules. Figure 7.72a shows the Control switch location and interconnection in the PAU-SA's system block diagram. Figure 7.72b shows the control switch distribution in the PAU-SA's structure scheme.

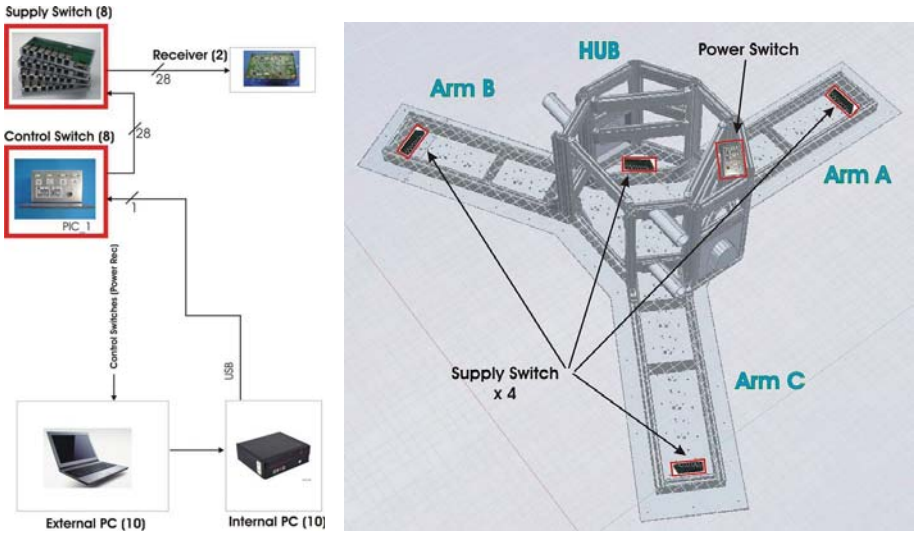

(a) (b)

Figure 7.72. a) PAU-SA's control switch location and interconnection in the PAU-SA's system block diagram, and b) control switch distribution in the PAU-SA's structure scheme.

7.8.1 Control switch unit

The goal of this module is to wait until the rest of the instrument has been turned on and is stable, and then, turn on the receivers sequentially. Moreover in the case of detect a malfunction receiver it can be isolate. This module controls the receivers' power supply remotely, and individually. The receivers are controlled by an external PC through the PAU-SA's main program (Section 7.10) in the top (Relay Control) Fig. 7.73, sending the commands of the receivers selected to the internal PC, and this last controlling the register C (Table 7.22) and register A (Table 7.23) with the PIC 1 in the control switch module (Figs. 7.74 and 7.75a). In this module PIC 1 (Fig. 7.74a) controls four octal D flip-flops with tri-state outputs (model 74LS574), one for each arm and the HUB, as it can be seen in Fig. 7.74c. The output of each flip-flop drives a phototransistor opto-isolator model TIL111 in order to isolate the control module to the power supply module (Figs. 7.74b and 7.74d). Finally, these photo-transistors are connected to the standard

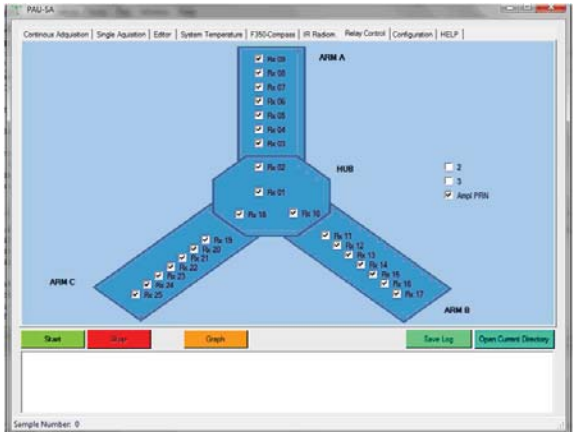

Figure 7.73. PAU-SA's main program interface (Section 7.10) in the (Relay Control) screen showing the selected receivers to be turned on.

serial DB9 connectors in a metallic box, Fig. 7.75a in order to control the external supply switch modules located near of its respective receivers, Figs. 7.75b and 7.75d. These modules are composed of relays normally on, this means that in a normal situation is not necessary to energize the coil of the relay. The input of each module has a ±7.8 V power

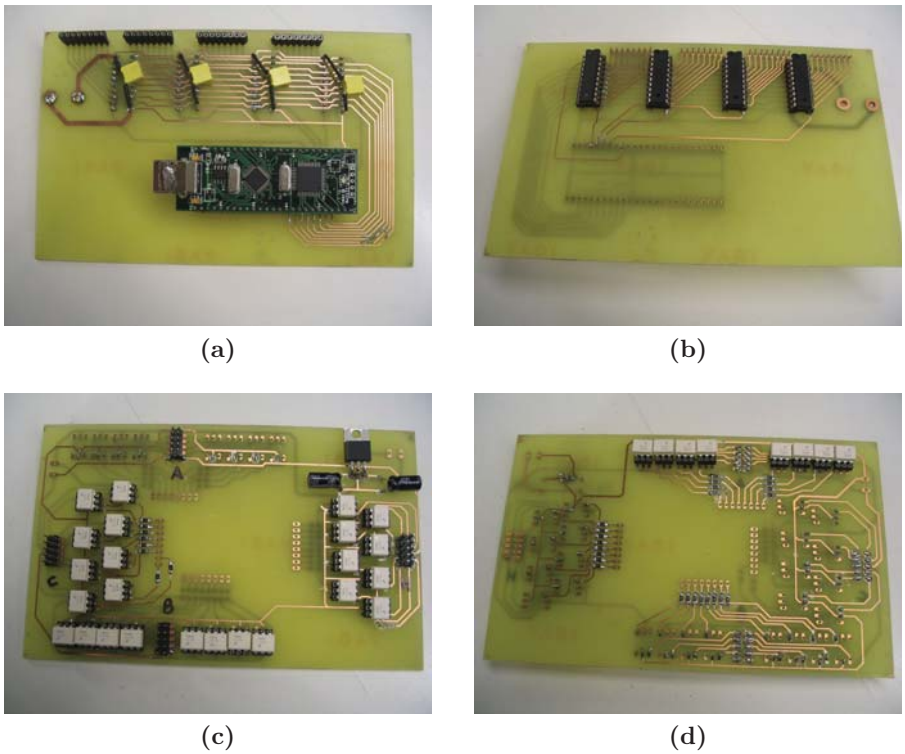

(a) **(b)**

(c) **(d)**

Figure 7.74. Control switch board a) PIC 1 module (top layer), and b) D flip-flops on (bottom layer), c) and d) phototransistor module (top layer) and (bottom layer) respectively.

supply for the receivers as a function of the relay. Finally the outputs of these relays

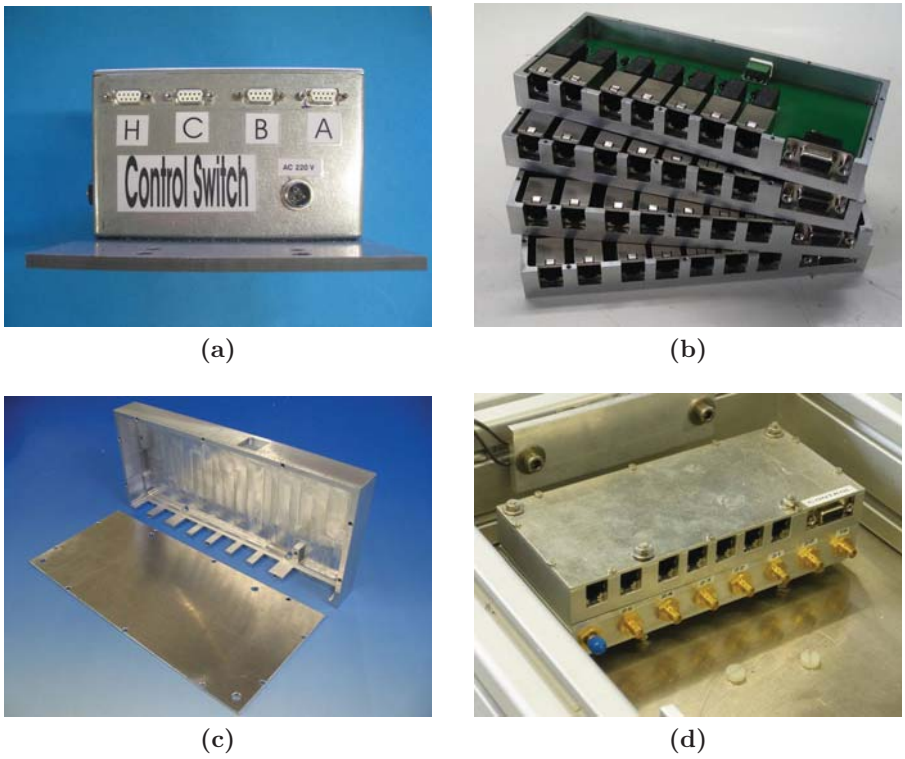

Figure 7.75. a) Control switch unit, b) metallic box and board of the power supply switch showing the relays , c) metallic box of the power supply switch), and d) power supply switch located at the end of a arm near its required receivers.

are connected to the Ethernet RJ45 connectors. The outputs of the power supply switch modules are connected to the receivers using red Ethernet cat-5 cables (Section 7.2).

7.8.2 Discussion and considerations

In this section the control switch module has been presented. The goal of this part is to control the receiver power supplies individually from the external PC. Due to the low power consumption, Ethernet cat-5 cables have been used for this purpose. Since the receivers have a very high gain; they are very sensitive devices, and must be turned on sequentially in a smooth and stable manner. In this manner, it is possible to isolate an unstable receiver from the others in case of a system malfunction in order to find the source of the problem. Moreover, for experimental results, selected receivers can be turned off in order to simulate future receivers malfunction. The power supply switch boxes (array of relays) are controlled with the control switch unit trough the PIC1 (control and memory) and the commands send via the internal PC. Since the PIC1 has not enough outputs to control all receivers, a memory array of 1 bit (flip-flop type D), one for each receiver has been implemented. The first version of this board was designed with a Port Input Output (PIO) model 8255, but it was discarded for loss of data.

7.9 PAU-SA's structure, ground plane, radome and temperature control system

This section is devoted to present the PAU-SA's structure, the ground plane, the radome and finally the temperature control system. Due to the complexity of some of these parts, these have been outsourced to specialized companies. Moreover, due to the large dimensions of the metallic structure, a special temperature control has been implemented. Figure 7.76 shows the location and interconnection of these parts in the PAU-SA's system block diagram.

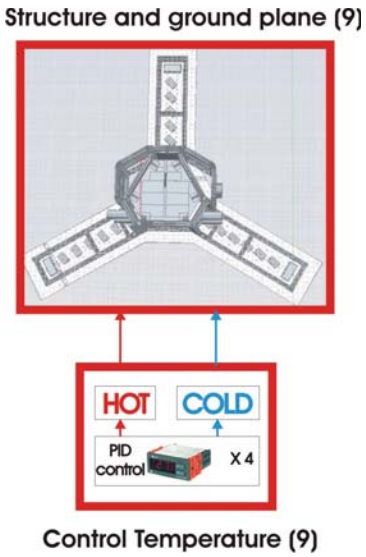

Figure 7.76. PAU-SA's structure, ground plane and control temperature system location in the PAU-SA's system block diagram.

7.9.1 PAU-SA's structure

Due to the mechanical complexity of the project, this part has been designed, simulated and implemented by Gutmar S.A. Along the project two versions of the mechanical structure have existed, being this last one a reinforced version of the first one (Figs. 7.77a and 7.77b). To do this, the 3D CATIA software has been used in the design to place the elements, calculate of strengths, center of gravity etc. The design conditions have been the following: to have the same antenna distribution shape in order to minimize area, weight and surface of opposition to the wind to support a velocity of 100 km/h. The chassis has been made with high-tensible anodized aluminium profiles, being easy and rapidly to assemble by means of T-slot nuts as shown in Fig. 7.78b. The dimensions of the structure are shown in Figs. 7.78a and 7.78b.

7.9.2 PAU-SA's ground plane

In the bottom part of PAU-SA's structure the ground plane is placed, been necessary to place the antennas and guarantee a solid structure of the instrument. It has been

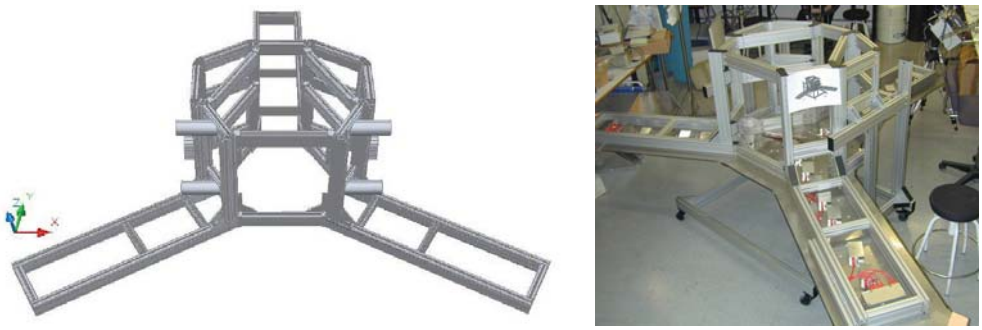

(a) (b)

Figure 7.77. a) 3D scheme of PAU-SA's chassis (reinforced version), and b) Picture of PAU-SA's chassis (reinforced version) located in the D3-213 laboratory.

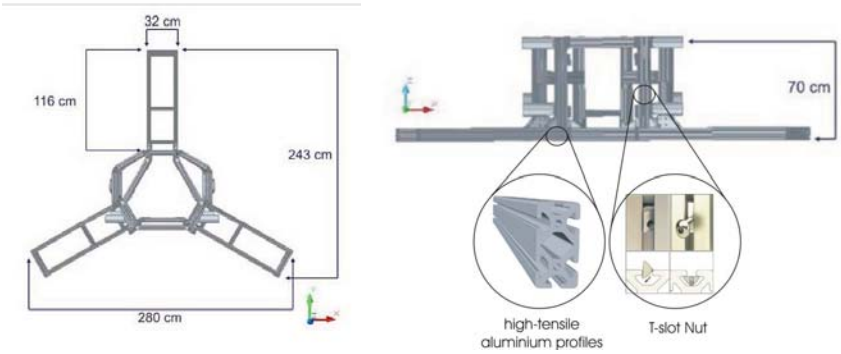

(a) (b)

Figure 7.78. a) Scheme of PAU-SA's chassis (reinforced version) with dimensions, and b) 3D scheme of PAU-SA's chassis (reinforced version) with dimensions and basic material.

designed using AutoCAD software. The ground plane has the same Y-shape in order to minimize the area and the weight, as it can be seen in Fig. 7.79a. This has been made of aluminum material with 3 mm thickness. Since the large number of holes in it, these are not represented (Fig. 7.79a), but they can be appreciated in the metallic structure, Fig. 7.79b. These holes are for attaching the ground plane with the structure and place the antennas and receivers in their respective positions. In order to minimize these position errors, this part has been cut using laser with a maximum error of 0.1 mm.

7.9.3 PAU-SA's radome

This part has been designed by Gutmar S.A and implemented by Fuhta S.A. Once the chassis and the ground plane have been assembled, it has been possible to place the radome. Its function is to thermally insulate the instrument in addition to protect from adverse weather conditions. The radome is made up of five pieces forming together a single one. These pieces are: a fix part in the hub as shown in Fig. 7.80a, three arms (receiver part) and the antennas removable part. This latter is formed in one piece, being

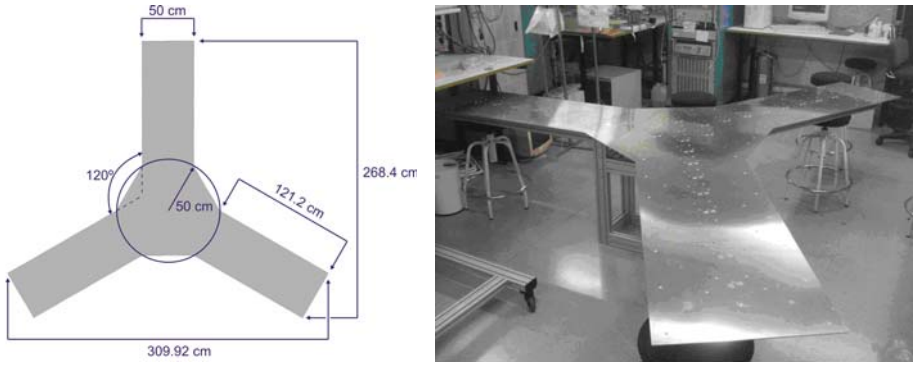

(a) **(b)**

Figure 7.79. a) Basic PAU-SA's scheme ground plane, and b) Picture of PAU-SA's ground plane metallic structure.

made of a material transparent to the electromagnetic waves. Figure 7.80b shows the instrument with all the parts of the radome.

(a) **(b)**

Figure 7.80. a) Picture of PAU-SA instrument in the radome assembling process, and b) Picture of PAU-SA instrument with radome in measurement procedures pointing to a target.

7.9.4 PAU-SA's temperature control system

Once of the most difficult parts of this part of the project has been the design of the temperature control. This is due to the difficult to control thermally a large amount of metallic material such as in this case. In this design, alternating current (AC) heaters throughout the structure location according Fig. 7.81a, have been chosen to heat the structure using control pulse modulation technique and cool by Peltier devices and air distribution system located in Fig. 7.81b. As temperature controlling elements, commercial PID controllers (model EUROTHERM 2132) have been used. The temperature control system has been divided into 4 areas: each of the 3 arms and the hub. Every PID has

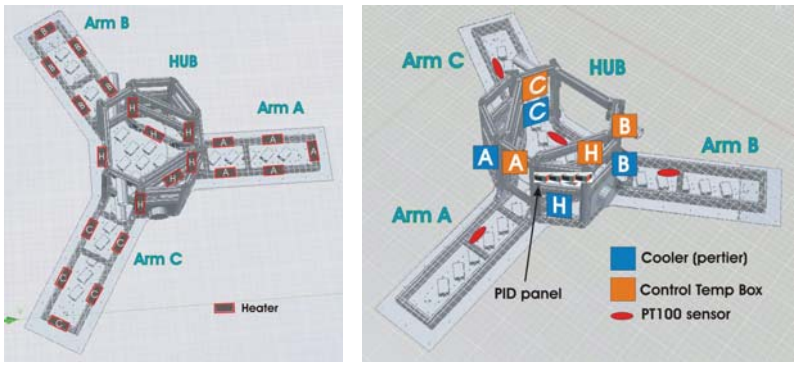

(a) (b)

Figure 7.81. a) AC heater devices distribution in the PAU-SA's structure scheme, and b) PIDs, coolers control temp units and other sensors distribution in the PAU-SA's structure scheme.

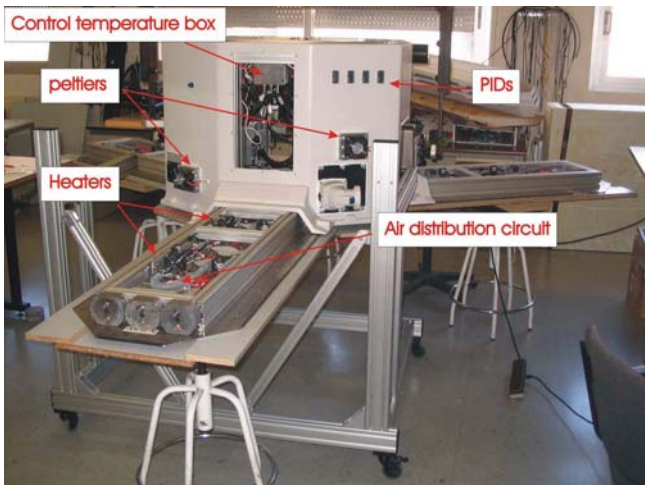

Figure 7.82. PAU-SA instrument picture showing some of the control temperatures elements.

a PT100 sensor to control each area independently located as shown in Fig. 7.81b. The control signals of each PID are sent to its control temperature unit, located as shown in Fig. 7.81b. This has been the function of heat the structure through the heaters elements or cool through the Peltier devices and the air distribution circuit. Figure 7.82 shows a picture of the PAU-SA instrument in which is possible to observe some elements of the temperature control system. Moreover, there is air circulation by means of different fans located in the instrument.

7.9.5 Discussion and considerations

This section has presented some of the mechanical parts of the instrument, besides the thermal control system. Although each one of the three mechanical parts: structure, ground plane, and radome are implemented individually, these are designed to be assembled to form a single piece. The structure has been one of the most controversial parts having two versions. The second is an extended version of the first one having to be

reinforced to pass the force and vibrations requirements. Regarding the ground plane, it had to cut corners at the ends of the arms to make easier the positioning inside the trailer. Due to the large volume of metal in the structure and the ground plane, one of the most difficult parts of this project has been the temperature control system. Commercial PIDs in combination with the control temperature have been used for this propose. During the temperature tests have been detected an uncontrolled behavior with an unexpected increasing of the temperature. For this reason, it is recommended to limit the upper temperature with a thermostat in each section.

7.10 PAU-SA's computers and communication protocols

This section is devoted to present both the external and internal computers in order to control the movements of the instrument and perform measurements procedures. Moreover, protocols and commands used are presented. Figure 7.83 shows the PCs and the interconnection in the PAU-SA's system block diagram. Figure 7.84 shows the internal PC location in the PAU-SA's structure scheme.

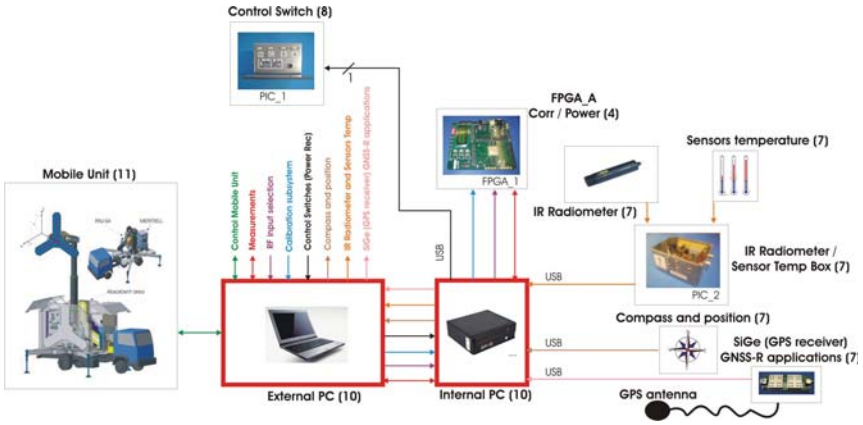

Figure 7.83. PAU-SA's PCs and interconnection location in the PAU-SA's system block diagram.

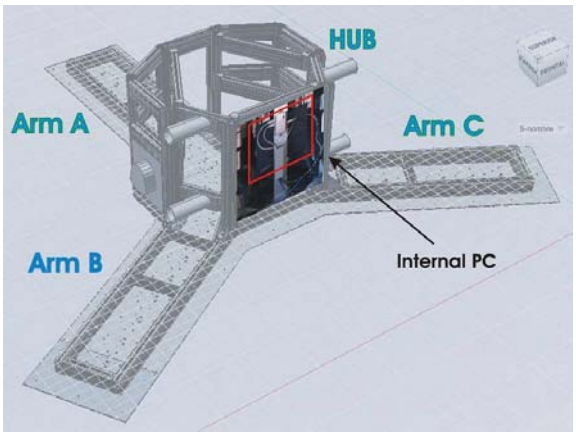

Figure 7.84. Internal PC location in the PAU-SA's structure scheme.

7.10.1 External PC

PAU-SA instrument has adopted a centralized control through the external computer, in our case is an industrial laptop model Dell LATITUDE E6400 ATG. This basically makes two control tasks: to control the motion of the articulated arm, and to control the devices located inside the PAU-SA instrument. On one hand, using a RS232 serial protocol to communicate with the Programmable Logic Controller (PLC) located into the truck, it

controls the actuators and sensors to perform the movements of the articulated arm. On the other hand, communication through an Ethernet category 6 connection with the computer located inside the instrument so in its turn it controls the PAU-SA instrument. The control software has been implemented in Visual Basic been possible to work in two operation modes: basic and advanced. The first one is used to work automatically (Fig. 7.85a). In this case, it is possible to perform three tasks: on the top left hand, to establish the communication with the PLC through a serial port, on the top right hand, first to wake up the internal computer, and second to establish the configuration of the Virtual Network Computing (VNC) software to control remotely the internal computer, and finally on the bottom, to show the communication messages with the PLC. The second one is the advanced operation mode (Fig. 7.85b). This mode has in addition to the previous functions, on the blue screen, the possibility to set manually the commands to control the movements of the elevation tower for calibration and measurement proposes of both instruments. Moreover, on the right framework, is possible to visualize and modify the internal PLC variables, which is only be recommended for advanced users.

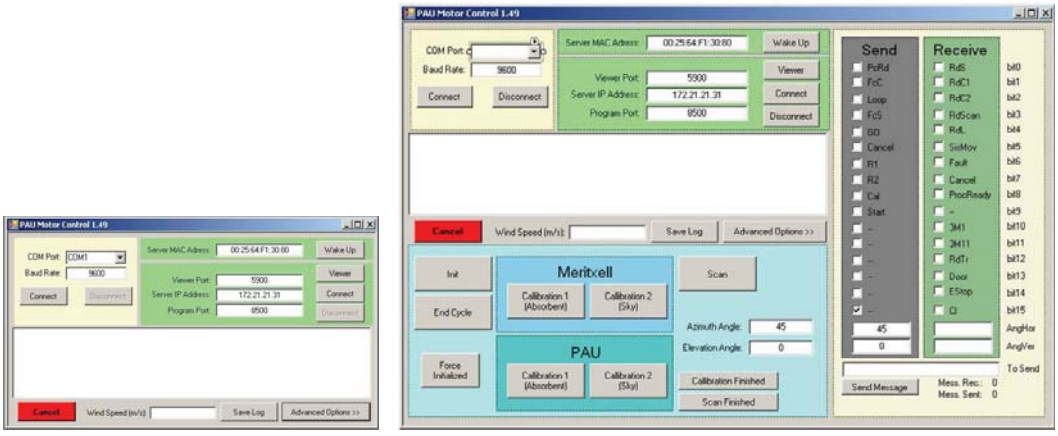

(a) **(b)**

Figure 7.85. Software to control the system in a) the basic mode window, and b) the advanced mode window.

7.10.2 Internal PC

The internal PC is located inside the PAU-SA instrument (Fig. 7.84). It is controlled externally, not requiring the screen or the keyboard. Since PAU-SA instrument has movements in the elevation and azimuth angles, is recommended the used of Solid-State Drive (SSD) in the PC instead of the traditional Hard Disk (HD). For this reason the PC used onboard is the model Dell OptiPlex 780USFF with SSD technology. As mentioned previously, it is controlled by means of the external computer via the VNC software. In the internal computer the main program is executed. The PAU-SA's software is a user-friendly Graphical User Interface (GUI) from where the system (instrument and truck) is totally controlled. It has been written in Visual Studio, been possible to execute command lists, mixing commands to control the instrument for calibration and

measurements purposes and send commands to the external computer to control the elevator tower trough the PLC. Figure 7.86 shows the appearance of the PAU-SA's main program, which is divided in 9 tabs enumerated as:

1. Continuous Acquisition,
2. Single Acquisition,
3. Editor,
4. System Temperature,
5. F350-Compass,
6. IR Radiometer,
7. Relay Control,
8. Configuration,
9. HELP.

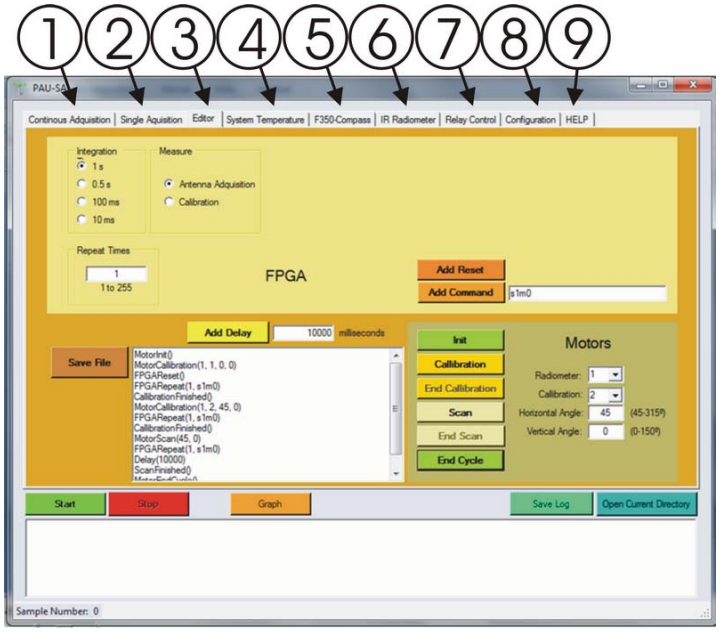

Figure 7.86. PAU-SA's main program interface in the editor mode.

The acquisition modes work in two main modes: "continuous acquisition" and "single acquisition". In continuous acquisition it is possible to control: the robotic mast of the mobile unit in azimuth and elevation angles for calibration and antenna acquisition proposes (Section 7.11), the (V, H, VH) matrix correlations, and the power acquisition with a set of possibilities and other sensors measurements numbered from 4 to 7 (Fig. 7.86) such as: system temperature monitoring, pointing angle, physical temperature estimation of the target using an external IR, and the power receiver control by means of relays. This is the usual mode of operation, getting the system fully autonomous been only necessary to run the desired sequence of commands previously saved in a file. These sequences of operations can be programmed in the Editor panel (Fig. 7.86), in the same interface. The acquired data are recorded in separate files according to the type of measurements. This data is saved in the internal computer for later post-processing. The single acquisition is normally used only for testing purposes. In this mode, it is only possible acquire data

selecting one operation each time. Moreover, in the configuration panel is possible to configure the other sensors in addition to set the sample rate acquisition and select the data recorded folder among others. In the help mode a tutorial shows how to use the program.

7.10.3 Protocols and commands

This section is focused to present the different protocols and commands of the main devices. The FPGA 1 (Section 7.4) in addition to calculate the correlation and power estimation matrices, is the interface to control several devices such as: the receiver input selection (measurement/ calibration section 7.2), control the correlated noise unit (Section 7.6), to control the FPGA 2, and the relay control to turn on the receivers. Table 7.15 shows the configuration settings of the FPGA 1. Each command is constituted by two characters, a letter and a number. The next sections shows the main commands implemented in the FPGA 1.

Table 7.15. Configuration settings of the FPGA 1.

Protocol	**RS-232**
Transmission velocity	115,200 bits/s
Data Bits	8
Stop Bits	1
Parity	None
Flow control	None

7.10.3.1 Measurements commands

These commands are used for data acquisition of the instrument.

- **r0:** This command make a **reset** in all FPGA 1 internal peripherals: correlations and power estimators.
- **s#:** This command selects the receiver input source, changing the **s**witch positions (CTR1 and CTR2) located in the receiver RF stage. This is a decimal number between 0 and 2 given by the parameter #, as shown in Table 7.16.

Table 7.16. Selection of receiver input source.

Value of the parameter #	**Measurement selected**
0	Correlated noise
1	Antenna signal
2	Uncorrelated noise

- **m#:** This command select the integration time. In first instance, the FPGA 1. reset all peripherals **r0** and launches a measure with the integration time given by the parameter # according to the Table 7.17.

Table 7.17. Selection of integration time.

Value of the parameter #	Integration time selected
0	1 s
1	0.5 s
2	100 ms
3	10 ms

- **n0:** This command allows to interrogate the FPGA if it has data from a new measurement. The FPGA returns a "0" either the integration time has not finished or the data has been transferred to the temporary SDRAM memory, and returns a "d" when both the measurements has finished and the data has not been transferred to the temporary SDRAM memory.
- **c0:** This command reads the matrix correlations and power estimation measurements and transfers them to the internal temporary SDRAM memory.
- **l#:** This command request to the FPGA to send the data packet identifier by the parameter #, as shown in Table 7.18.

Table 7.18. Identifier data to request.

Value of the parameter #	Data to request
0	Correlation matrix (V pol)
1	Correlation matrix (H pol)
2	Correlation matrix (V / H pols).
3	Power estimation

7.10.3.2 Correlated noise commands

These commands control the correlated noise unit (Section 7.6).

- **t#:** This command changes the attenuation in the calibration subsystem by the parameter #, as shown in Table 7.19.
- **w#:** This command changes the source selected in the calibration subsystem by the parameter #, as shown in Table 7.20.
- **p#:** This command changes the symbol rate and number of bits selected in the calibration subsystem by the parameter #, as shown in Table 7.21.

Table 7.19. Attenuation selection in the calibration subsystem.

Value of the parameter #	Attenuator selected
0	0 dB
1	3 dB

Table 7.20. Source selection in the calibration subsystem.

Value of the parameter #	Correlated source selected
0	Noise Source
1	PRN sequence

Table 7.21. Symbol rate and number of bits selection in the calibration subsystem.

Value of the parameter #	Symbol rate and number of bits selected	
0	SR1	10 bits
1	SR2	
2	SR3	
3	SR4	
4	SR5	
5	SR1	20 bits
6	SR2	
7	SR3	
8	SR4	
9	SR5	

7.10.3.3 Relay control commands

The receiver power supply is controlled through the control switch unit (Section 7.8). It is controlled with the PIC 1, being necessary two registers. Register C is used to select the RJ45 connector in the power splitter unit Table 7.22, and the register A is used to choose the selected power splitter unit Table 7.23. Once the receivers have been selected with the register C, it necessary to select its power splitter unit.

Table 7.22. Register C to control the power receiver in each of the power splitter unit.

RJ45 connector	Pin 8	Pin 7	Pin 6	Pin 5	Pin 4	Pin 3	Pin 2	Pin 1
Register position	C7	C6	C5	C4	C3	C2	C1	C0
Decimal value	**128**	**64**	**32**	**16**	**8**	**4**	**2**	**1**
RXs Arm A		9	8	7	6	5	4	3
RXs Arm B		11	12	13	14	15	16	17
RXs Arm C		25	25	23	22	21	20	19
RXs HUB		10	1	18	2			

Table 7.23. Register A to select the power splitter unit.

Power supply unit	/Enable	None	RXs HUB	RXs Arm C	RXs Arm B	RXs Arm A
Register position	A6	A5	A4	A3	A2	A1
Decimal value	32	16	8	4	2	1

7.10.4 Discussion and considerations

This section has presented the external and internal computers and their respective programs to control the system. Through the external computer the user can control all the system. It has the control motor program to control the articulated arm motion with two different modes: basic and advanced. Furthermore, it is possible to control the internal computer remotely in order to work with the main program for the instrument control. Moreover, a set of commands to control the FPGA 1 for measurements purposes and the PIC 1 to control the receiver power supply have been presented.

7.11 PAU-SA's mobile unit

The goal of this section is to present PAU-SA's mobile unit made ad-hoc for its transport and measurements purposes, sharing place with another radiometer called MERITXELL [49]. The mobile unit has only one robotic arm, so only one of the two radiometers is able to operate at each time. Due to the mechanical complexity of the mobile unit, this part the design and implementation has been outsourced to an external company. Figure 7.87 shows the PAU-SA's mobile unit location and interconnection to the PAU-SA's system block diagram.

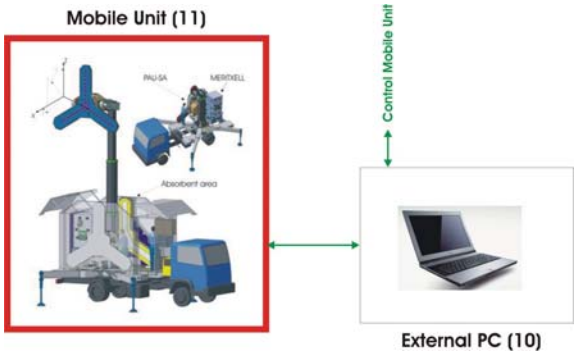

Figure 7.87. PAU-SA's mobile unit interconnection in the PAU-SA's system block diagram.

7.11.1 Mobile unit construction

This part of the project started in 2007 with internal brainstorming sessions. At the beginning the idea was the use of a commercial mechanism, such as used in moving in order to elevate the PAU-SA instrument for measurement purposes and use of a truck to transport it. However, because of different drawbacks such as stability this idea was rejected. The idea was matured eventually till in the middle of 2007, the decision was made to combine these two objectives in the truck. Due the mechanical complexity and effort that represent this part of the project, it was assigned to an external company called Gutmar S.A., responsible of the design and simulation in 3D CATIA software of the mechanic part, outsorced other companies for the implementation and assembly process. One of the most important outsourced companies has been the Fundació Eduard Soler Corporation, who has implemented and assembled the mechanical parts. Although this part of the project has been done by external companies, we have had to work exhaustively to define the specifications and then checking the different implementation states, becoming one of the most ambitious and complex parts, in addition to the design of the PAU-SA instrument itself.

7.11.2 General description of the mobile unit

Before starting with the design of the mobile unit it has been necessary to define a set of specifications in order to establish the necessary requirements. Despite the large number of specifications, these have been classified in four groups:

- The mobile unit or truck (Fig. 7.88a and 7.89a),
- The elevator tower (Fig. 7.88b and 7.89b),
- The enclosure (Fig. 7.88c and 7.89c), and
- The absorber material (Fig. 7.88d and 7.89d).

In order to transport the instruments, it has been necessary to choose the mobile unit. Since the two instruments have a considerable mass and volume a NISSAN ATLEON 8.19.3 truck with a maximum weight of eight tons was selected, Fig. 7.88a and 7.89a. The elevator tower for measurement purposes is eight meters height and it has azimuth and elevation movements $0^{\text{o}} \leqslant \theta \leqslant 150^{\text{o}}$ and $-180^{\text{o}} \leqslant \phi \leqslant +135$, Figs. 7.88b, 7.88e and 7.89b. It is compatible to work with both instruments, but only one is able to be operated meanwhile the other one is parked. The elevator tower has four positions: up or measuring, down or parked, calibration or looking to the internal absorber and change the radiometer. All these movements are sent through the external computer, and finally controlled via a PLC located in the control panel located in the truck. Moreover, the mobile unit has four stabilization legs controlled manually covering the maximum surface allowing to work with an instrument at eight meters high supporting wind velocity of 100 km/h. Both the elevator tower and the stabilization legs work with an hydraulic unit. In addition to providing the truck with an elevator tower for measurement purposes, it has an enclosure to storage and transport the instruments (Figs. 7.88c and 7.89c). A microwave absorber area has been placed inside the mobile unit for calibrations purposes one for each instrument Figs. 7.88d and 7.89d). In addition to these main four groups there is a diesel electricity generator set of 10 kVA in order to power the electronic parts of the mobile unit.

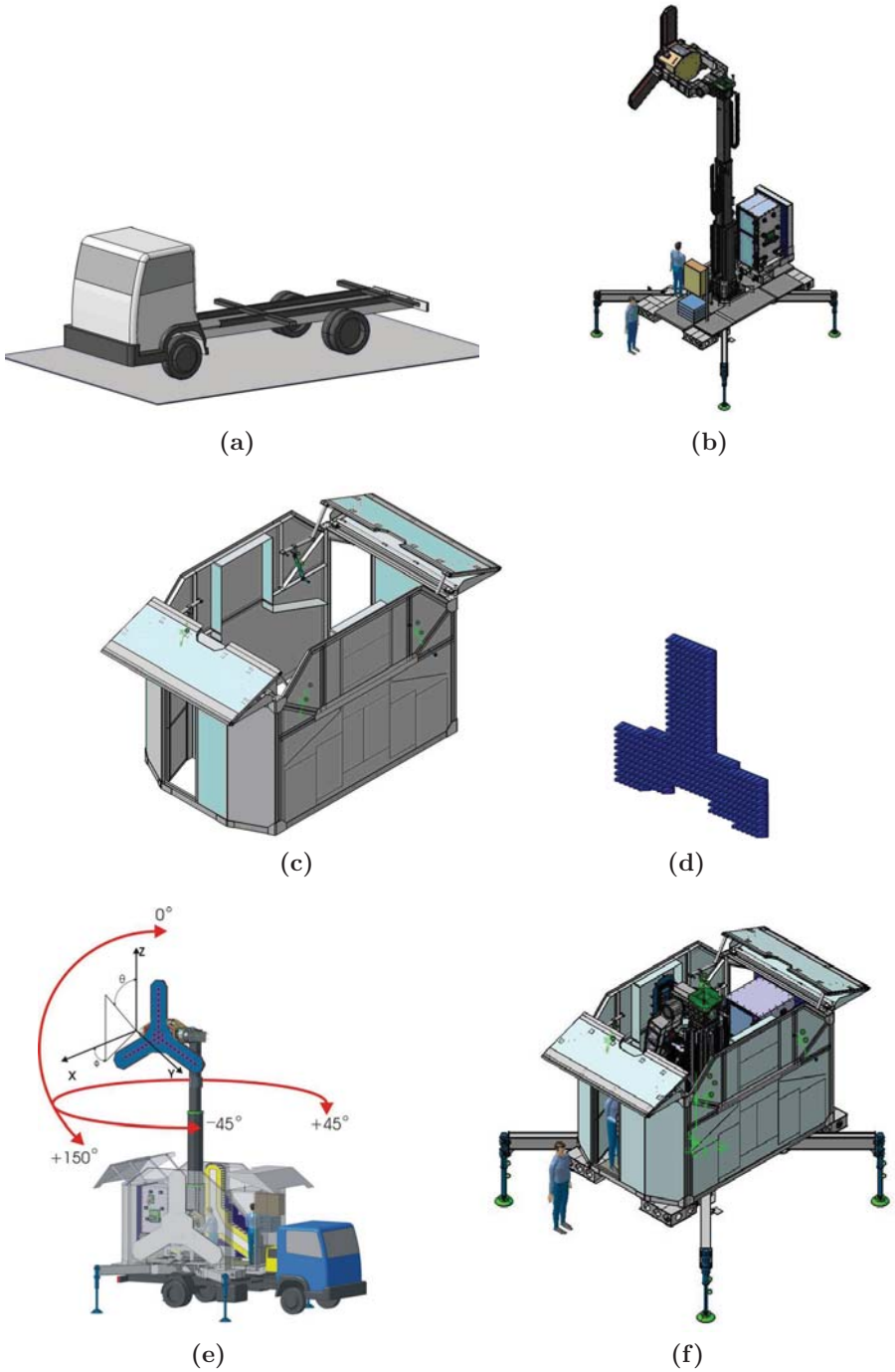

Figure 7.88. 3-D design of a) the truck model NISSAN ATLEON 8.19.3, b)the elevator tower with PAU-SA instrument to work, c) the enclosure, d) the PAU-SA's absorber, e) the mobile unit with the enclosure and elevator tower showing all possible movements and f) the self-sufficient measurement station, independent of the truck.

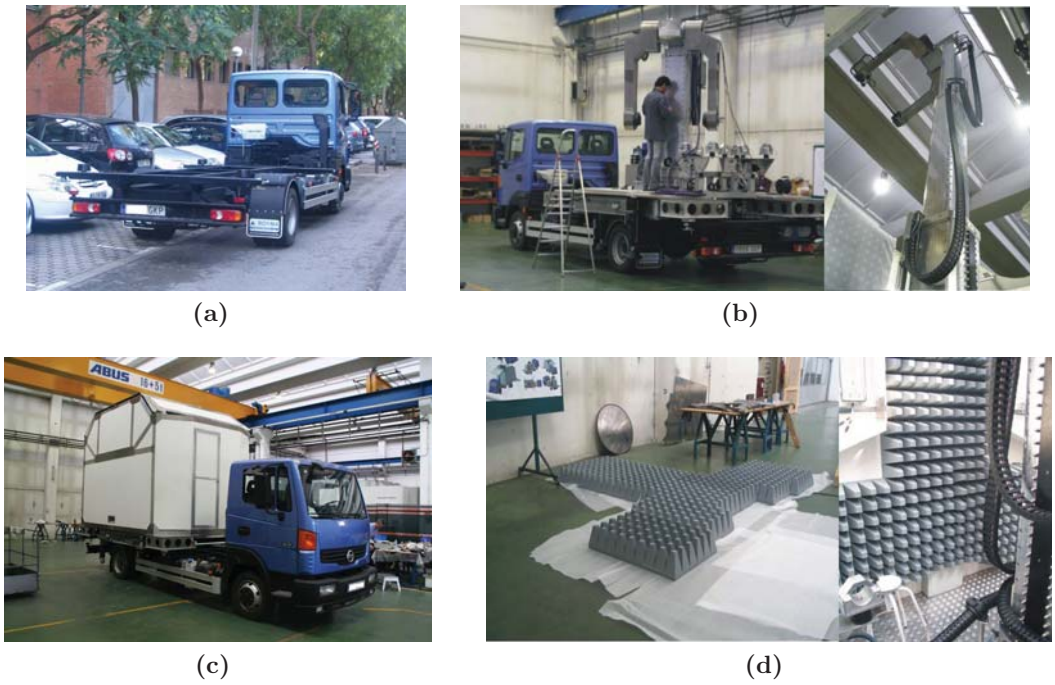

(a) (b)

(c) (d)

Figure 7.89. Picture of a) the truck, b) the truck and elevator tower in the factory on the left and elevator tower deployed on the right, c) the truck with the enclosure before leaving the factory, and d) PAUSA's absorber in the factory on the left and located in the enclosure on the right.

7.11.3 Conclusions

In this section the PAU-SA's mobile unit has been presented. It has been presented from the beginning to the present state, being one of the most ambitious project implemented in our department. The mobile unit has been divided in four parts: the truck, the elevator mast, the enclosure, and the absorber material. Finally, the PAU-SA's mobile unit has been implemented successfully for transporting and measurements purposes of both PAU-SA and MERITXELL instruments. This part, from the beginning till now has been one of the most complicated parts, having to solve many problems such as: definition of requirements, check and detection irregularities, etc. The most remarkable have been two of these. The first one, once assemble the instrument in the laboratory placed on the second floor of the Theory of Signal and Communications (TSC) D3 building at the UPC Campus Nord, it was took out through the window and assembled in the measurement station. The second one was a mechanical accident being damaged the elevator tower early 2011. Although the mobile unit has sensors to prevent human mistakes, some of these sensors were not consider in the control software. Specifically the sensors that indicate when the instrument is parked were not taken into account in the PLC with disastrous consequences. Nowadays, the mobile unit is under repairing waiting to finish the experimental measurements and calibration results.

Chapter 8

Instrument characterization

Once the instrument has been presented in previous chapters, this chapter is devoted to present the functionality tests. The first part presents the instrument thermal control performance. The second part presents the results at baseline level. Measurement were carried out in the anechoic chamber of the UPC [87]. The third part applies the proposed calibration method of correlated radiometers using pseudo-random noise signals. Finally, the instrument characterization and the experimental images recovered are presented.

8.1 Thermal control performance

As discussed in previous chapters, thermal control is very important from the point of view of the radiometric performance. Since receivers have phase and amplitude drifts due to temperature changes, it is necessary to stabilize and control the temperature of the instrument. Figure 8.1 shows the typical power and phase drifts, in this case the receiver 21 at H-pol. As it can be notied, the power has a quasi-linear dependence with the temperature, whereas the phase has a random trend with a σ of $\pm$ 5º in the stable temperature range. The better the control temperature, the longer the inter-calibration

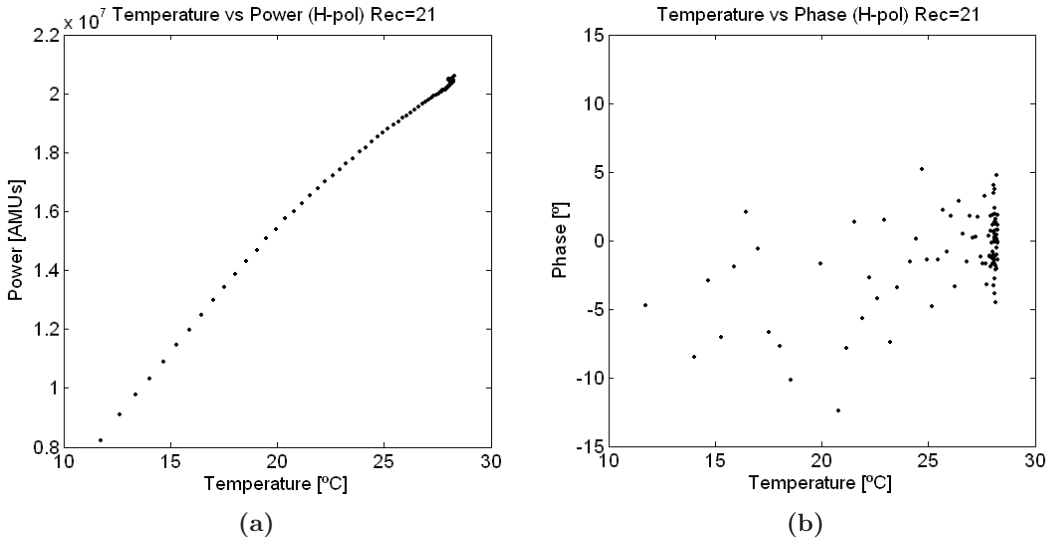

Figure 8.1. Typical power and phase dependence with the temperature in PAU-SA instrument (Receiver 21 at H-pol).

period. That is, with a good control temperature the instrument can devote more time to measurement acquisitions, instead of calibration. Figure 8.2 shows a plot of the control temperature during one day long in a measurement campaign using the graph mode of the system temperature monitor (Fig. 7.86). In order to control the temperature of the instrument, in addition to the internal temperature sensor in each receiver, other twelve sensors are located on the ground plane to plot the temperature of the metallic structure, and estimate the antenna physical temperature required to estimate the system's temperature for denormalization purposes. It is important to know the evolution of this parameter, since the actuators (heaters and coolers) are placed over this metallic structure, and there is a great thermal inertia. Although each PID has been set to stabilize at 25º C, each temperature sensor stabilizes at different temperatures, as it can noticed in Fig. 8.2. It is a well-know problem in temperature control when the air circulation is not sufficient. PAU-SA's control temperature has an air control by means of fans to distribute the air along the instrument and forcing the air circulation as much as possible, but in the case of the HUB it is not sufficient. As expected, the receivers' temperature, (Fig. 8.3) has similar transitory that the metallic plane temperature (Fig. 8.2). Figure 8.3 shows the receiver behavior with the temperature along the time, being the receivers located

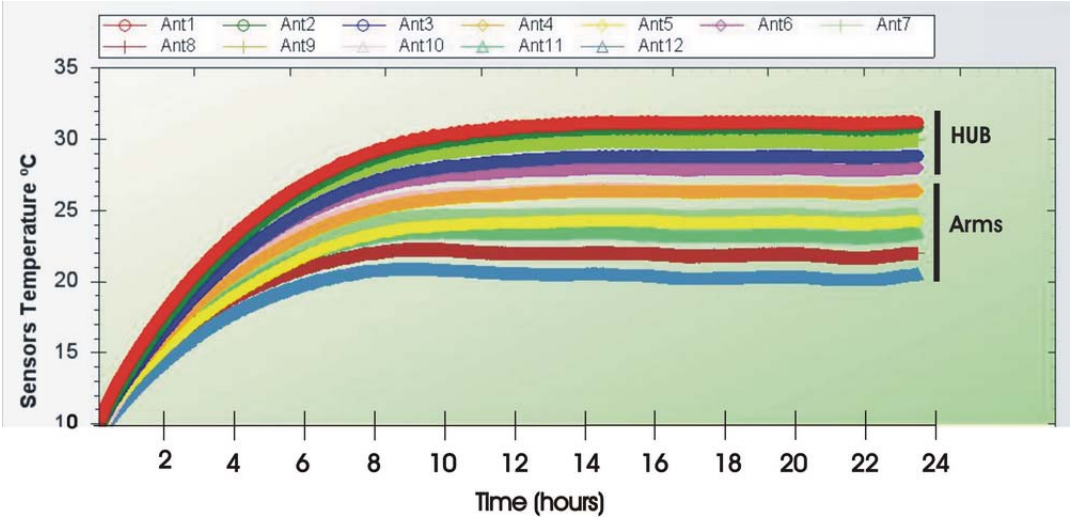

Figure 8.2. Time evolution of the PAU-SA's metallic structure acquired during the day (2011-02-15).

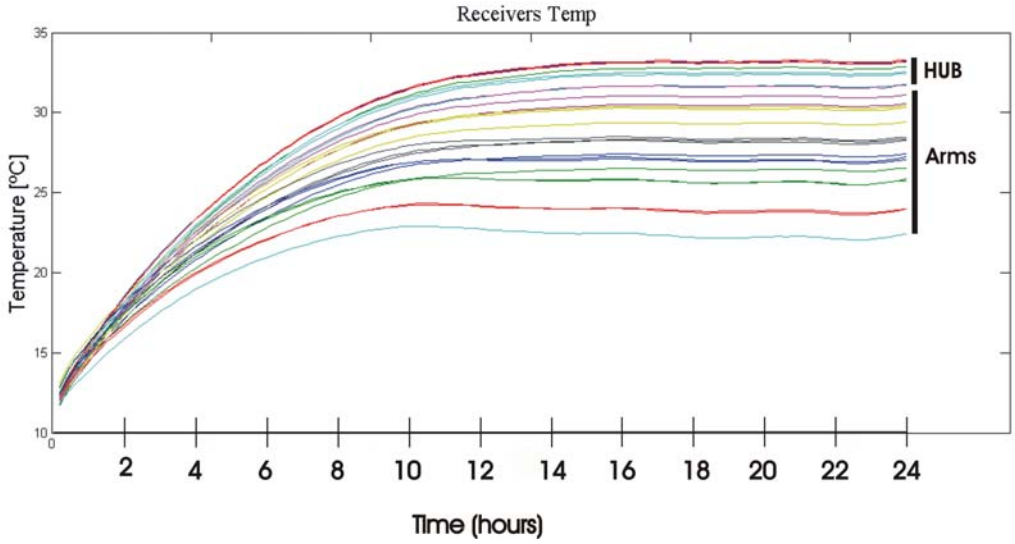

Figure 8.3. Time evolution of the PAU-SA's receivers acquired during the day (2011-02-15).

in the HUB the warmest elements. Relating to the necessary to stabilize the metallic structure or the receivers, in this case has been stabilized in half a day before starting the calibration and the measurement process. This time depends on the PID configuration and training, initial conditions, outside temperature, etc. In this application an over-dumped transitory has been selected preferring a slow, but stable transitory. Table 8.1 shows the mean and variance statistics in a stabilized transition of the PAU-SA'receivers and Fig. 8.4 shows a graphical representation of the temperatures.

Table 8.1. Statistics of the receiver´s temperature when thermally stabilized (10 last hours).

Receiver	Location	Mean value [° C]	Std value [° C]
1	HUB	33.00	0.27
2	HUB	32.62	0.28
3	A	33.96	0.27
4	A	31.51	0.24
5	A	30.35	0.20
6	A	30.27	0.17
7	A	28.18	0.13
8	A	27.29	0.11
9	A	26.38	0.09
10	HUB	33.05	0.27
11	B	32.34	0.25
12	B	30.91	0.20
13	B	29.26	0.14
14	B	28.35	0.07
15	B	26.99	0.07
16	B	25.72	0.10
17	B	23.96	0.13
18	HUB	32.21	0.26
19	C	31.49	0.22
20	C	30.13	0.16
21	C	28.11	0.09
22	C	27.07	0.08
23	C	25.73	0.12
24	C	23.89	0.16
25	C	22.37	0.19

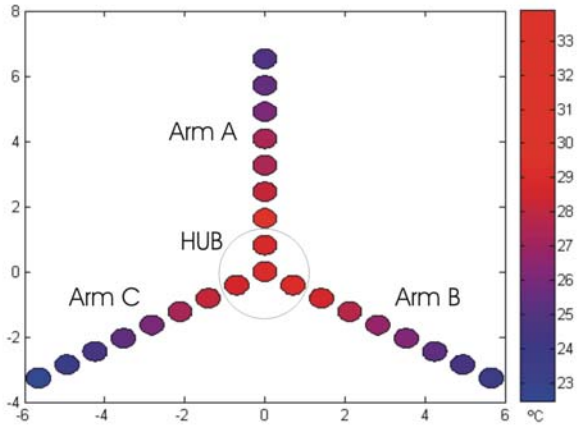

Figure 8.4. Temperature distribution of the PAU-SA's receivers in in the stabilized transition.

8.2 Measurements at baseline level

This section presents the tests results at baseline level of the PAU-SA instrument. These are the first steps in the characterization of whole instrument. The tests performed are:

- characterization of the radiometer noise and its stability through "Allan's variance" [98], and
- baseline response to a point source at different angles and polarizations.

8.2.1 Baseline measurement setup

Figure 8.5 shows the block diagram of a baseline tested. It is composed of two antennas, two receiving chains, two ADCs, and a FPGA to implement the correlations and the power estimation. This information is sent to the PC to perform the calibration and plot of the measured visibility sample. For the experiment setup the worst case at baseline level has

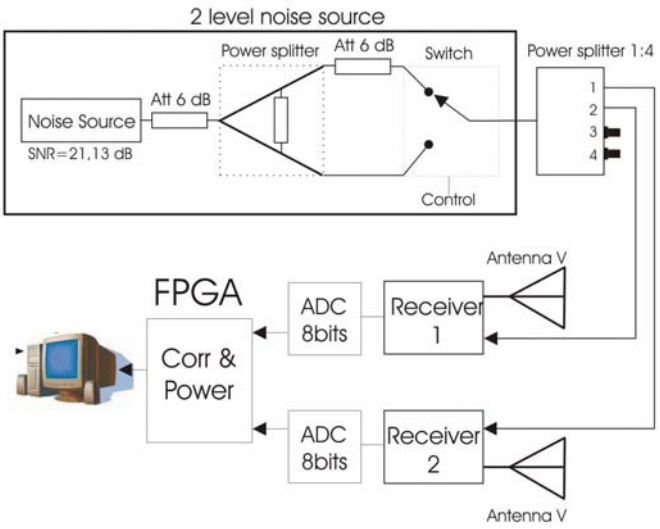

Figure 8.5. Global diagram of the baseline level configuration.

been considered, maximum distance between antennas. This implies the maximum cable length for: the correlated noise source, the IF signal to the ADC board, and the master clock to the down-conversion, etc.

For the FPGA digital signal processing, two tests have been performed: the computation of the normalized visibilities with correlated and uncorrelated noise, and the digital I/Q down-conversion. Once the normalized visibility and the power estimation have been computed, they are sent to the computer, where the calibration algorithms are applied. Since correlations are computed using 1 bit/2 level digital correlators, amplitude errors must be corrected from the estimated power measurements.

The calibration procedures have to take into account three types of errors:

- the offsets introduced by the ADC, that are estimated using uncorrelated noise (μ^{uncorr}),
- the relative phase error between receivers that is estimated using two levels of correlated noise (μ^{corr}), and

- the correlation offsets when the array is pointing to the microwave absorbers μ^{ECCO}.

With antenna measurements, the obtained correlations include contributions from: the target to retrieve, the uncorrelated offsets, and the Empty Chamber Correlation Offset (ECCO)s, Fig. 8.6b. This last error is measured in the anechoic chamber [87] Fig. 8.6a. It accounts for many different contributions: the receiver's backward noise waves emitted by the antennas and coupled to others (including mismatches and multiple reflections). Let $\mu^{0^o raw}$ be the uncalibrated normalized correlation with the antenna pointing at boresight, the calibrated normalized correlation μ^{0^o} is then given by:

$$\mu^{0^o} = (\mu^{0^o raw} - \mu^{ECCO} - \mu^{uncorr}) \cdot e^{-jphase(\mu^{corr})}, \tag{8.1}$$

and the general normalized correlation can be computed as:

$$\mu = (\mu^{0^o raw} - \mu^{ECCO} - \mu^{uncorr}) \cdot e^{-jphase(\mu^{corr})} \cdot e^{-jphase(\mu^{0^o})}. \tag{8.2}$$

Finally,the visibility function is derived as:

$$V = \mu \cdot \sqrt{T_{SYS_1} \cdot T_{SYS_2}}. \tag{8.3}$$

Figure 8.6b shows the ECCO contribution. To retrieve this term it is necessary to subtract to the anechoic chamber measurement the uncorrelated offset. As it can be noticed, in this baseline a cloud of points exits in which the main contribution is centered at (0.015,0.055), therefore, it indicates an offset from the origin being to subtract in the measurement data.

8.2.2 Radiometer stability

In order to determine the optimum range of integration times for best use of the system, the characterization of the radiometer noise and stability has been perform measuring

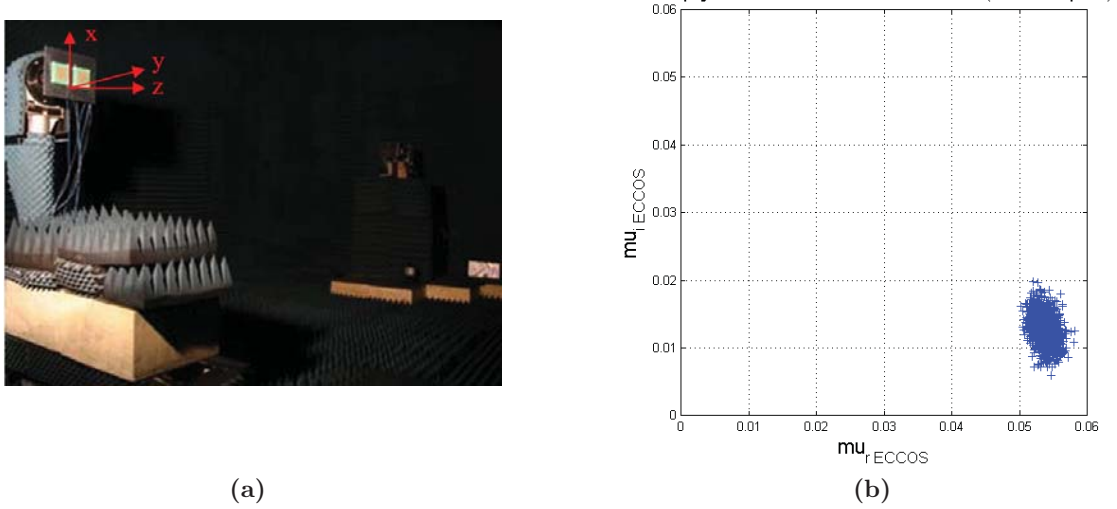

(a) **(b)**

Figure 8.6. a) Picture of baseline level measurements during anechoic chamber tests [87], and b) ECCO measurement at baseline level inside the anechoic chamber.

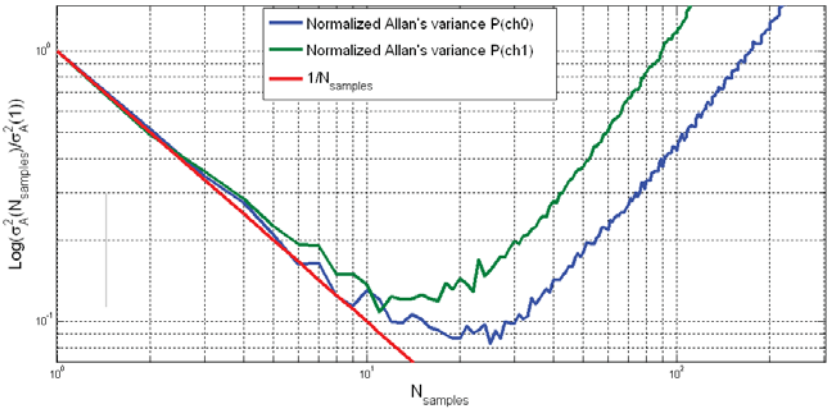

(a)

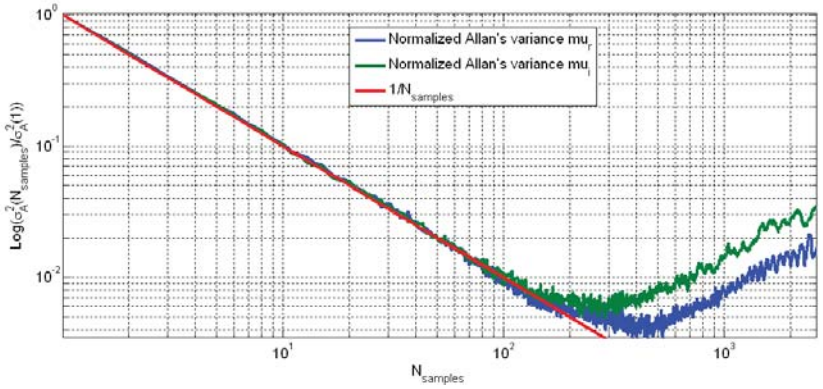

(b)

Figure 8.7. a) Normalized power variance versus number of samples, and b) normalized correlation (real and imaginary parts) vs. number of samples.

the Allan's variance [98] given by:

$$\sigma_A^2(\tau) = \frac{1}{2}\langle(\overline{\mu}_{n+1} - \overline{\mu}_n)^2\rangle. \tag{8.4}$$

where τ is the integration time, and $\overline{\mu}_n$ is the n^{th} fractional frequency average over the observation period. This method consists of the determination of the Allan's variance versus integration time allowing to determine the different types of fluctuations of the radiometer output signal. In particular, the range of integration times for the optimum setup of the calibration and measurement is shown in Fig. 8.7. It shows the evolution of the variance of both channels versus the number of samples. The ideal case (thermal Gaussian noise) must decrease monotonically decreasing function as:

$$\sigma_A^2 = \frac{1}{N_{samples}}. \tag{8.5}$$

However, due to system instabilities, after a given N value, the variance σ_A^2 increases again. Taking into account that a sample represents a measurement of 1 s, the optimum number of samples is the value of minimum variance and determines the maximum

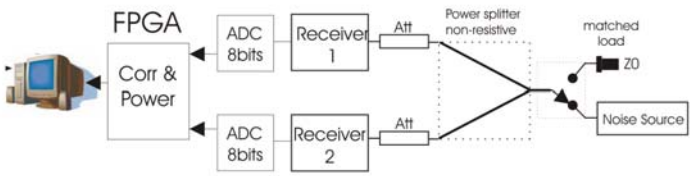

Figure 8.8. Sensitibility measurement test set-up.

integration time that may be used, without degradation due to radiometer drifts. On one hand, Fig. 8.7a plots the power variance vs. the number of samples. The maximum integration time to calibration with correlated noise and measure the visibilities desnormalization procedures is 15 s. One the other hand, Fig. 8.7b shows the normalized correlation versus the number of samples to determine for phase and the ADC offset calibration. This time is $\sim$ 200 s. Therefore, amplitude fluctuations are dominant, and are ones that limit the maximum integration time.

8.2.3 Radiometer resolution validation

The characterization of the radiometric resolution has been performed with the set up shown in Fig. 8.8. A noise source or a matched load are connected to the input of a non-resistive power splitter producing correlated noise. Two adjustable attenuators are connected to the power splitter's outputs producing uncorrelated noise and attenuating the correlated noise generated by the matched load. The complex correlation is then measured for different values of the attenuation and for different phases, as shown in Fig. 8.9. The phase has been obtained randomly by disconnecting and connecting again the master clock, so each receiver's PLL locks to a different phase. Note that in all measurements are not appreciable offset contribution, in contrast with the ECCO measurements, Fig. 8.6b. It is possible if the ECCOs and the uncorrelated noise have the same amplitude and thus counteracts. Concerning the shape of the circle is clearly distinguished up to 2 x 20 dB attenuators and since the I/Q demodulation is performed digitally, there are neither quadrature errors, nor amplitude unbalances between branches that need to be corrected [22]. The radio of the circles can be determined estimating the correlation μ of two digital signals, Eqn. 8.6.

$$\mu = \frac{T_c}{T_{SYS}} = \frac{T_c}{T'_A + T_{REC}}. \tag{8.6}$$

where μ is equal to the corresponding analog signal T_c normalized to the system temperature T_{SYS}, T_{REC} is the receiver temperature, and T'_A is the antenna temperature including losses. The T_{SYS} can be estimated through Eqn. 8.7.

$$T_{SYS} = T_c + T_{ph}\left(1 - \frac{1}{L}\right) + T_{REC}. \tag{8.7}$$

where L is the introduced attenuator, T_{ph} is the physical temperature, and $T_c = \frac{397\,K}{L}$. Evaluating the previous equations with L = 20 dB, T_{ph} = 290 K, and $T_{REC} \approx$ 250 K

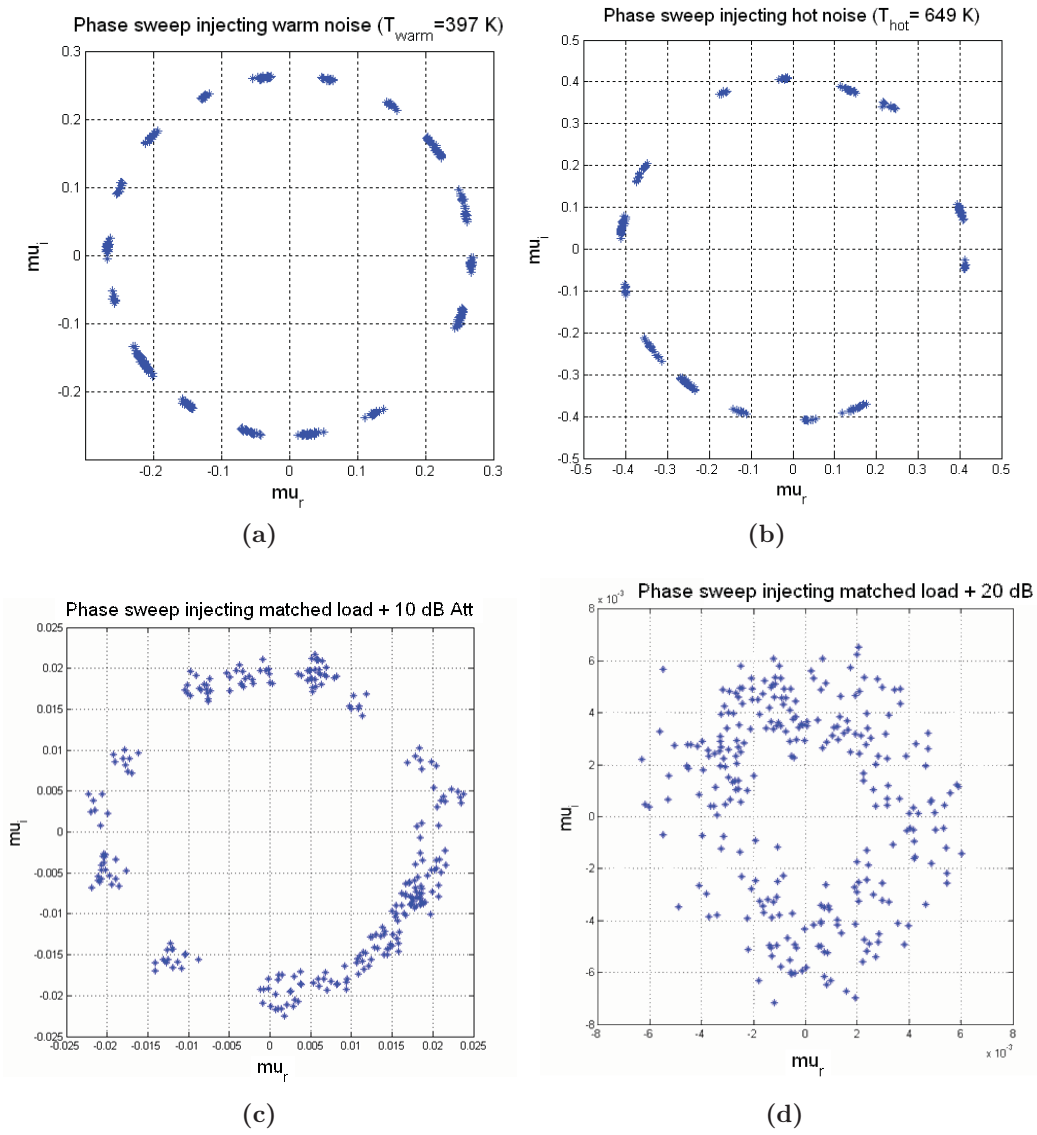

Figure 8.9. Measured sensibility circles with a) warm noise source, b) hot noise source c) load matched + 10 dB attenuator, and d) load matched + 20 dB attenuator.

we obtain, $T_{SYS} = 541.07$ K, and the correspondent $\mu = 7.3 \cdot 10^{-3}$. Comparing the estimated value with the measurement one (Fig. 8.9d) results are smaller, probably due to an increment in the estimated T_{REC}.

8.2.4 Measurement of the baseline response

This test has been performed in the anechoic chamber [87] to measure the normalized visibility by scanning the pairs of receivers from -90º to 90º, at the polarization from V to H as show in Fig. 8.6a. Results are contrast with theoretical results trough Eqn. 4.25. Considering that the fringe-wash function is negligible (1/B $\ll$ maximum transit time) [99]

and that both antenna patterns can be considered to be equal, the normalized visibility can be determined by:

$$V(\theta) = \frac{P_T G_T(\theta)}{4\pi r^2} \frac{\lambda^2}{4\pi} D_R t(\theta) e^{-j2\pi \frac{d}{\lambda} sin\theta}. \tag{8.8}$$

In this situation, the theoretical real and imaginary normalized correlations should vary according to: real part in Eqn. 8.9 and the imaginary part in Eqn. 8.10 as shown in Fig. 8.10.

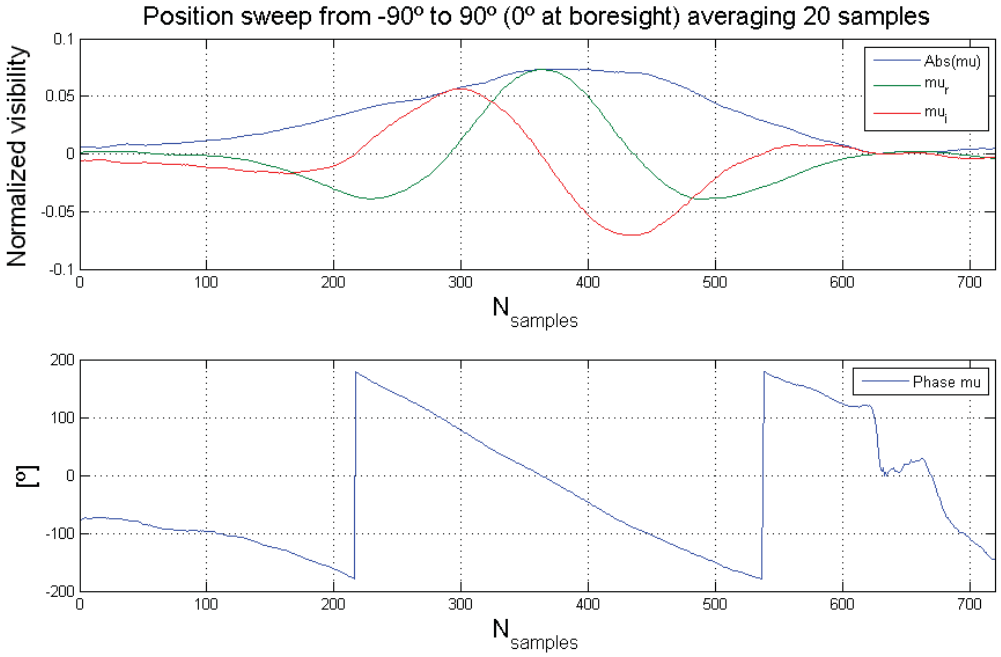

Figure 8.10. Correlated measurement with baseline rotate X-axis. a) normalized correlations (real and imaginary parts), and b) phase correlation.

$$\mu_r = -sin\Big(\frac{2\pi d}{\lambda} sin\theta_0\Big), \tag{8.9}$$

$$\mu_i = cos\Big(\frac{2\pi d}{\lambda} sin\theta_0\Big). \tag{8.10}$$

Due to the previous considerations, in Eqn. 8.8 the absolute value of the normalized visibility is the antenna radiation voltage pattern $t(\theta)$ when transmitting antenna has an orthogonal polarization. In Fig. 8.11 it is observed that the behavior of the normalized correlation to sweep the emitter with different polarization, in the center with opposite polarization.

8.2.5 Conclusions

A representative baseline of the PAU-SA instrument has successfully been tested in controlled conditions in an anechoic chamber. The optimum integration times for the power

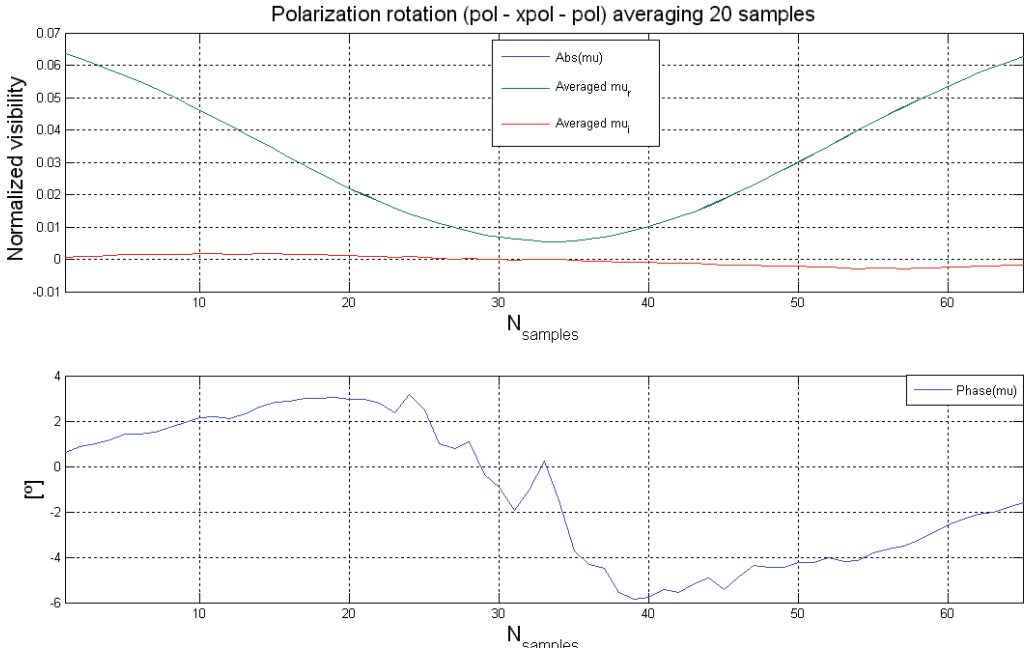

Figure 8.11. Correlated measurement with baseline rotate Z-axis. a) Normalized correlations (real and imaginary parts), and b) Phase correlation.

and real/imaginary parts have also been determined through the Allan's variance. Furthermore, sensibility circles have been measured to determine the radiometric resolution. Moreover, the baseline response has been measured to characterize the antenna patterns, that the real and imaginary parts are orthogonal and to observe the sensibility to polarization changes in the transmitting antenna. Finally, the ECCOs have been determined to notice the contribution of correlation biases caused by waves emitted by the instrument itself and being collected by neighbour antennas. Although a single baseline has been tested to give us an idea of the instrument behavior. It is highly recommended to characterize the fully instrument in the anechoic chamber to determine the overall behavior of the instrument.

8.3 Experimental validation of the use of PRN for calibration of correlated radiometers

The performance of the proposed technique has been assessed by measuring the FWF and its value at the origin in three different ways: In order to compare and evaluate the performance of this technique, the first method, (ideal case), has been implemented injecting thermal noise [70] ["FWF(noise)", as shown in Fig. 5.3, with the switch in the position 1]. The FWF is computed directly from the cross-correlation of the output signals of each channel using Eqns. 5.1 and 5.2.

In the second method ["FWF(Y1 · Y2)"], the signal noise is replaced by a PRN signal (Fig. 5.3 with the switch in the position 2). The FWF is also computed using Eqns. 5.1 and 5.2. In the third method ["FWF(local)", in Fig. 5.4] the output signal of each channel

$y_i(n)$ and y_j (n) is correlated with a local replica of the PRN $[x(n)]$ to obtain $H_i(k)$ and $H_j(k)$ as in Eqn. 5.5. The FWF is then computed according to Eqn. 5.7. As an additional feature, this method allows also to make a diagnosis of the receivers' frequency response, which can be very helpful in monitoring the instrument's health.

This section presents the fundamentals of this new type of calibration implemented with standard laboratory instrumentation to demonstrate the concept. Once the technique is validated, it has been implemented in PAU-SA instrument where the hardware has been reduced, but performs the same functions with reduced dimensions and weight so that it can be incorporated within the instrument. The equivalent hardware in PAU-SA can be found in section 7.6 when describing the calibration subsystem. Figure 8.12 shows the experiment setup to validate the technique implemented with laboratory instrumentation. The PRN code is generated using a LFSR [100]. The selected length

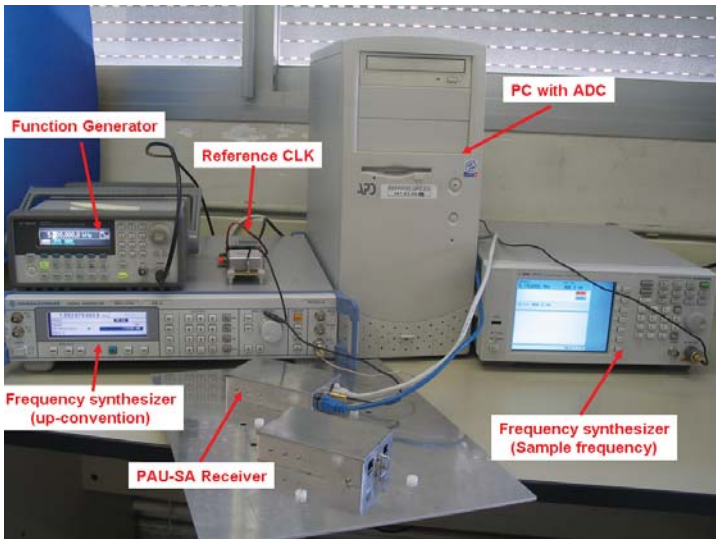

Figure 8.12. Laboratory set-up showing the instruments used in the experiment.

is 1,023 chips, which are recorded in an Agilent 33250A function generator, and upconverted using a Rodhe & Schwarz SMR40 frequency synthesizer. The parameters that can impact the estimation of the FWF are:

1. the SR defined as the ratio of the bandwidth of the PRN signal (B_{PRN}) and the receiver's low-pass equivalent bandwidth (B) [Eqn. 8.11]. The B_{PRN} is related to the sequence duration τ_{PRN}, and N_{chips} the number of chips (a chip is like a bit, but it does not carry any information) as shown in Eqn. 8.11:

$$SR = \frac{B_{PRN}}{B}, \tag{8.11}$$

and:

$$B_{PRN} = \frac{N_{chips}}{\tau_{PRN}}. \tag{8.12}$$

The higher the SR, the larger the bandwidth of the PRN signal spectrum, and the flatter is the spectrum within the receiver's bandwidth (Fig. 8.13). The minimum sampling frequency (fs) corresponds to one sample per chip $T_s = 1/B_{PRN}$.

2. the equivalent noise temperature of the PRN signal (T_{PRN}) at receivers' input, defined in terms of the PRN signal's amplitude (A) : $P_{PRN} = A^2/2k_B \cdot T_{PRN} \cdot B_{PRN}$, where PRN is the PRN signal power and k_B is the Boltzmann constant ($1.3806503 \cdot 10^{-23}$ J/ K). The values of T_{PRN} have been selected to be in the 6 K$\sim$ 65,000 K range,

3. the number of averages. In fact since the PRN sequences are deterministic, averaging the measured $\Gamma_{ij}(n)$ values (Eqn. 5.6), reduces the errors associated with the receiver's thermal noise ($k_B \cdot T_{REC} \cdot B$), being T_{REC} the receiver's noise temperature), and

4. the number of bits in the quantization process.

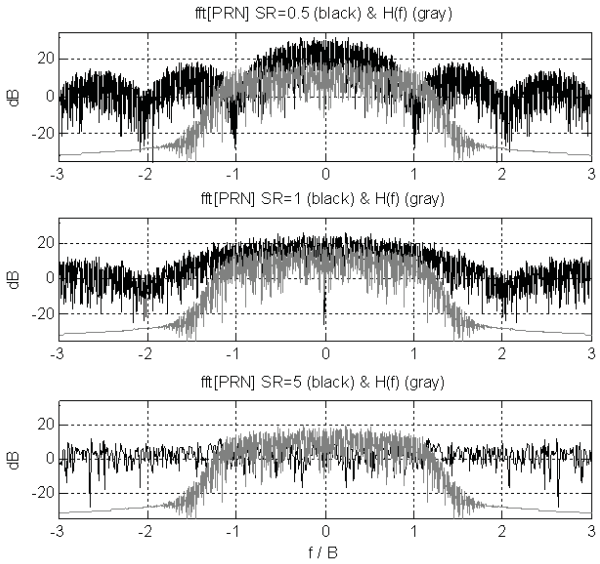

Figure 8.13. Equivalent low-pass spectrum of PRN sequence (black) with different SR and $H(f)$ estimated from noise (grey). Positive and negative frequencies plotted normalized to the bandwidth.

Without lost of generality of the proposed algorithms, these algorithms are tested using a PAU receivers [34] with the following parameters: gain $G = 112$ dB, noise figure $NF = 2.7$ dB ($T_{REC} = 250$ K), RF bandwidth $B = 2.2$ MHz low-pass equivalent bandwidth= 1.1 MHz, central frequency $f_0 = 1{,}575.42$ MHz, intermediate frequency $f_{IF} = 4.309$ MHz. Results are presented normalized to the receiver's bandwidth. In this set-up the SR can be easily modified by reading the look-up table in the function generator at different speed. If the whole table is read in $\tau_{PRN} = 1$ ms and $B_{PRN} = B$, then SR = 1 (Eqns. 8.11 and 8.12). The power level is adjusted with the frequency synthesizer. To minimize receiver's noise, 200 consecutive PRN sequences are averaged, i.e. the integration time is $T_i = 200\ \tau_{PRN}$.

In order to have a reference, Fig. 8.14 shows the results of the FWF(noise) implemented with block diagram presented in Fig. 5.3 with the switch in position 1, as a function of the input noise temperature T_N. As T_N approaches the physical temperature, the shape of the FWF degrades, since the noise introduced by the resistor in the

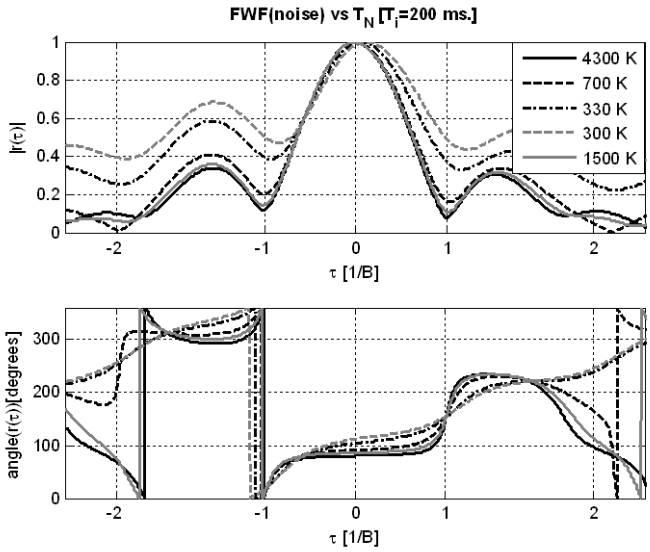

Figure 8.14. FWF estimated by cross-correlating receivers' outputs at different time lags when injecting thermal noise at different equivalent noise temperatures T_N [K].

Wilkinson power splitter, used to inject the noise to the two receiver chains, becomes comparable to the one injected (T_N) and it is 180º out-of-phase in each branch, leading to a zero cross-correlation. A too high T_N saturates the receiver and clips the signal. The best results are obtained for T_N / T_{REC} ranging between 2.7 and 16.7, and a value of 6 (T_N = 1,500 K) has been selected for all subsequent tests. Once the reference FWF has been determined, it is possible to analyze the FWF dependence on the three main parameters: SR, Signal-to-Noise Ratio (SNR) = $P_{in}/k_B \cdot T_{REC} \cdot B(T_{PRN}/T_{REC}, if B = B_{PRN})$ with $k_B \cdot T_{REC} \cdot B$ = -110 dBm, and the number of bits.

8.3.1 FWF dependence on SR

To determine the optimum SR value a sweep has been performed for both FWF(Y1 · Y2) and FWF(local) methods. Their performance has been analyzed and compared to the reference FWF(noise) (Figs. 8.15a and 8.15b). It is found that for the FWF(local) method SR≥ 1 is required to obtain a satisfactory FWF. The amplitude error does not improve significantly for SR > 1, but the phase error does, saturating above SR = 5. Slightly worse errors are obtained with the first method FWF(Y1 · Y2) and higher SR values are required to obtain comparable residual error.

8.3.2 FWF dependence on the signal input power

To determine the optimum power at receivers' input, the input power has been swept while keeping SR = 5 and $T_i = 200\tau_{PRN}$. Except at the lowest input power, the FWF(local) method outperforms the FWF(Y1 · Y2) one (Figs. 8.16a and 8.16b). Since the thermal noise present in the PRN signal being injected and the noise generated by the resistor of the Wilkinson power splitter, in fact, are completely uncorrelated with the local PRN

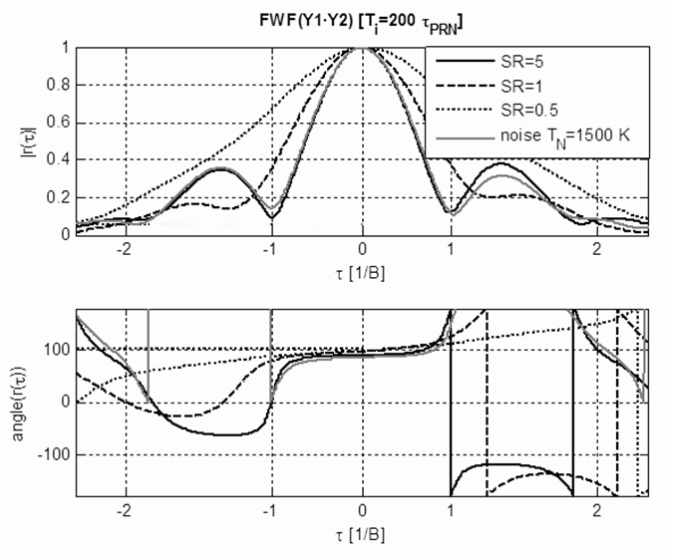

(a)

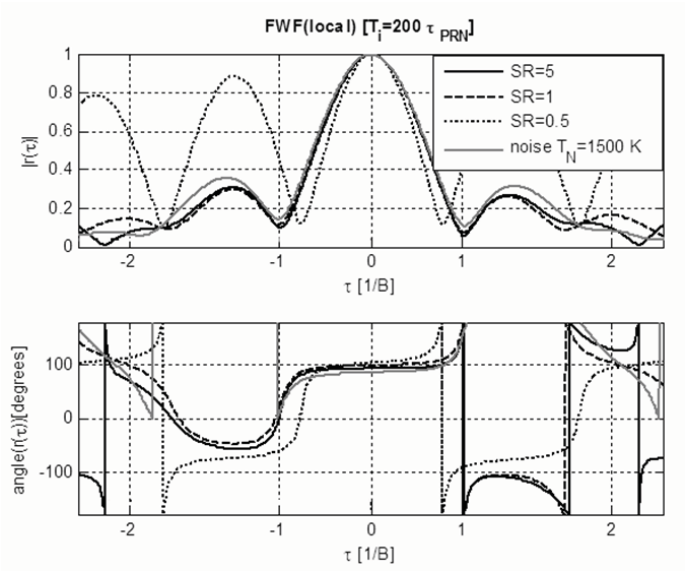

(b)

Figure 8.15. FWF estimated by cross-correlating receivers' outputs when the calibration signal is a PRN sequence FWF(Y1 · Y2) (Eqns. 5.1,5.2) and comparison with reference FWF computed with correlated noise with T_N = 1,500 K (Fig. 8.14), and b) FWF estimated by cross-correlating receivers' output with local replica of PRN sequence FWF(local) (Eqns. 5.3-5.7) and comparison with reference FWF computed with correlated noise with T_N = 1,500 K (Fig. 8.14). Note: time axis is normalized to $1/B$.

sequence. In this case to retrieve the FWF(local) it is necessary at least that SNR $\geq +1$ dB (Fig. 8.16a) and optimum values (amplitude error $< 2\%$ and phase error $< 5^o$ at $\tau = \pm T_S$) are obtained for SNR$\geq +11$ dB (Fig. 8.17a). For low input powers (SNR = -9 dB) the amplitude errors using the FWF(Y1 · Y2) method are smaller than using the

FWF(local) one, while phase errors are twice higher. When the input power increases both methods provide similar results (Figs. 8.17a and 8.17b).

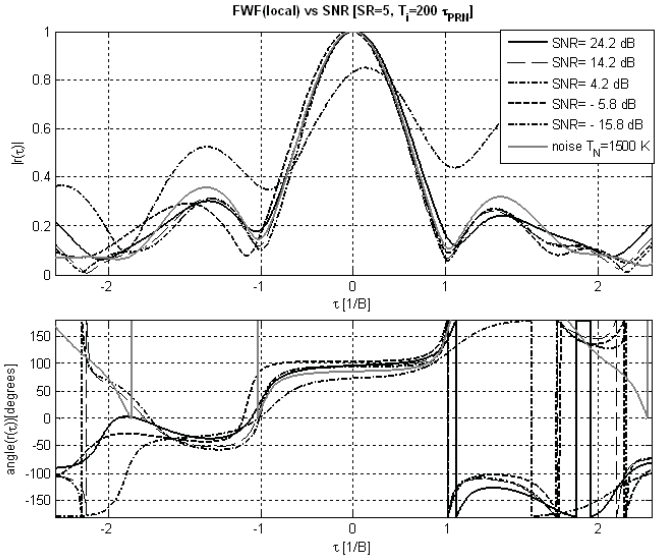

(a)

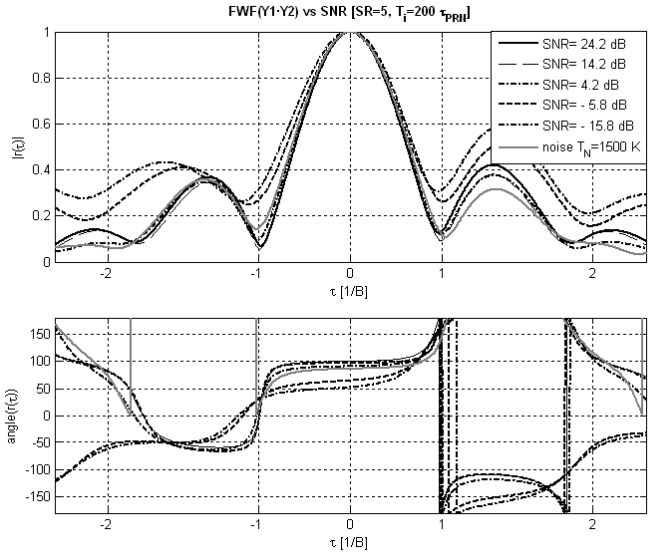

(b)

Figure 8.16. a) FWF estimated by cross-correlating receivers' outputs when the calibration signal is a PRN sequence FWF(local) (Eqns. 5.3-5.7) for different input powers and comparison with reference FWF computed with correlated noise with T_N = 1,500 K (Fig. 8.14), and b) FWF estimated by cross-correlating receivers' outputs when the calibration signal is a PRN sequence FWF(Y1·Y2) (Eqns. 5.1,5.2) for different input powers and comparison with reference FWF computed with correlated noise with T_N = 1,500 K (Fig. 8.14). Note: time axis normalized to $1/B$.

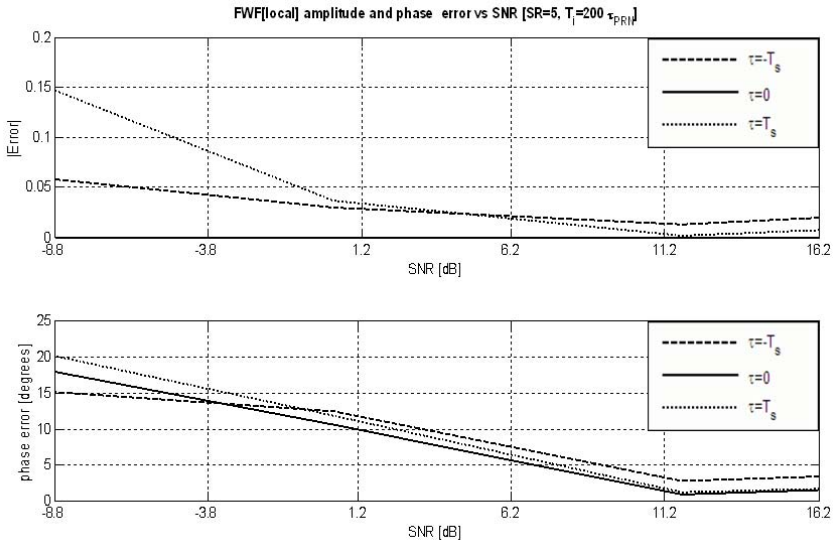

(a)

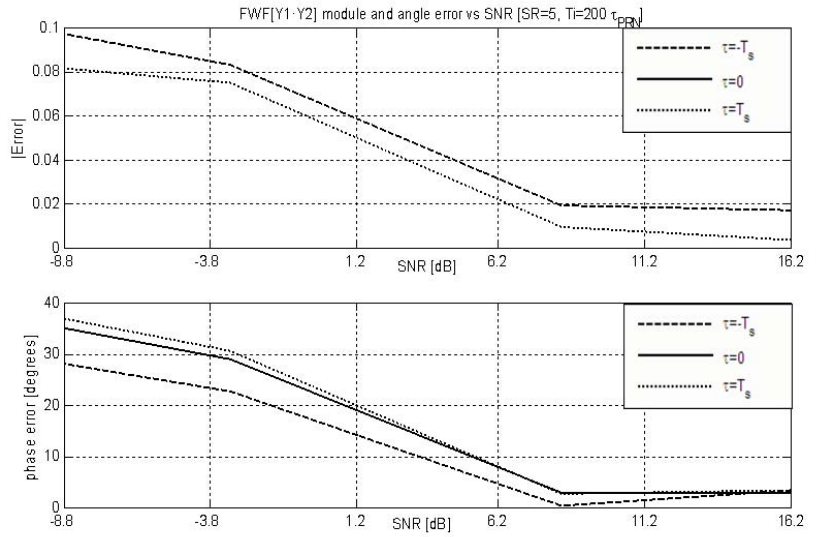

(b)

Figure 8.17. a) FWF amplitude and phase errors at $\tau = 0 \pm T_s$, when FWF is estimated by cross-correlating receivers' output with local replica of PRN sequence FWF(local) (Eqns. 5.3-5.7) for different input powers, and b) FWF amplitude and phase errors at $\tau = 0 \pm T_s$ when FWF is estimated by cross-correlating receivers' outputs when the calibration signal is a PRN sequence FWF(Y1·Y2) (Eqns. 5.1,5.2) for different input powers.

8.3.3 FWF dependence on the number of bits

Figs. 8.18a and 8.18b show the dependence of the estimated FWF as a function of the number of bits used to digitize the output signals from 1 to 12, while other parameters have been set to their optimum values: SNR $\geq +11$ dB, SR $= 5$ and $T_i = 200\tau_{PRN}$. As

it can be noticed, as in other systems [68,101,102] there is a negligible variation with the number of bits above 4 bits for both methods, and very good performance is achieved even with just 1 bit. As it can be noticed, the residual errors especially for the phase, are much smaller with the FWF(local) method (Fig. 8.19a), than with the FWF($Y1 \cdot Y2$) one (Fig. 8.19b).

As a summary, PRN signals can be successfully used to calibrate correlation radiometers. The best performance is achieved for T_i at least 200 realizations $\cdot$ PRN, and when the PRN signal bandwidth is about a factor 5 larger than the receiver's bandwidth (SR$\geq$ 5) and the SNR$\geq$ +11 dB, even when one bit correlators are used. The optimum values using 1bit/2 level correlators, SR = 5, SNR = 4.2 dB and T_i = 200 ms are: amplitude error $< 0.25\%$ at $\tau = 0, \pm T_s$, and phase error $< 1^o$ at $\tau = \pm T_s$ and $< 2^o$ at $\tau = \pm T_s$.

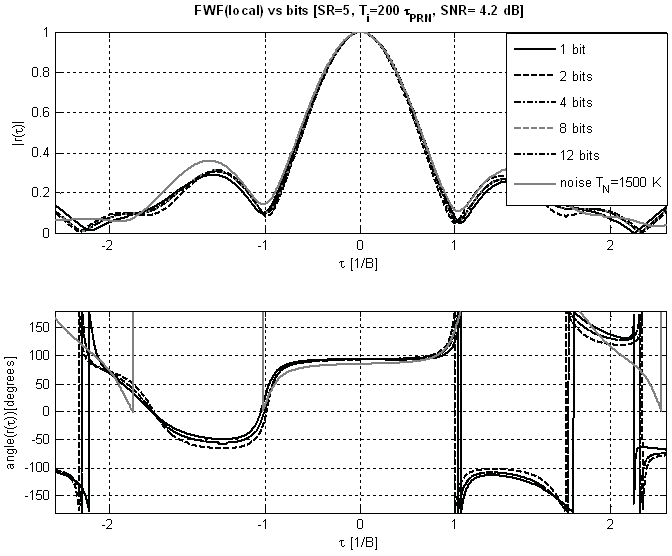

(a)

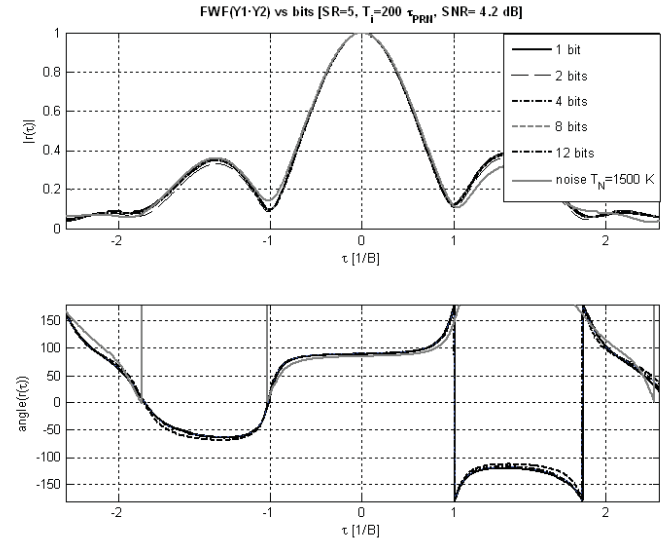

(b)

Figure 8.18. a) FWF estimated by cross-correlating receivers' output with local replica of PRN sequence FWF(local) (Eqns. 5.3-5.7) for different number of quantization bits and comparison with reference FWFcomputed with correlated noise with T_N = 1,500 K (Fig. 8.14)and b) FWF estimated by cross-correlating receivers' outputs when the calibration signal is a PRN sequence FWF(Y1·Y2) (Eqns. 5.1,5.2) for different number of quantization bits and comparison with reference FWF computed with correlated noise with T_N = 1,500 K (Fig. 8.14).

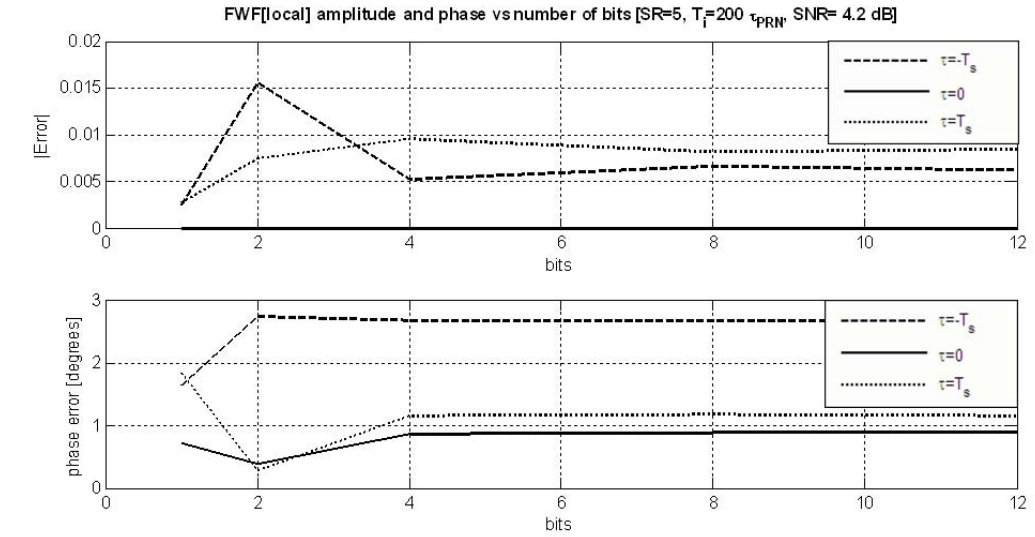

(a)

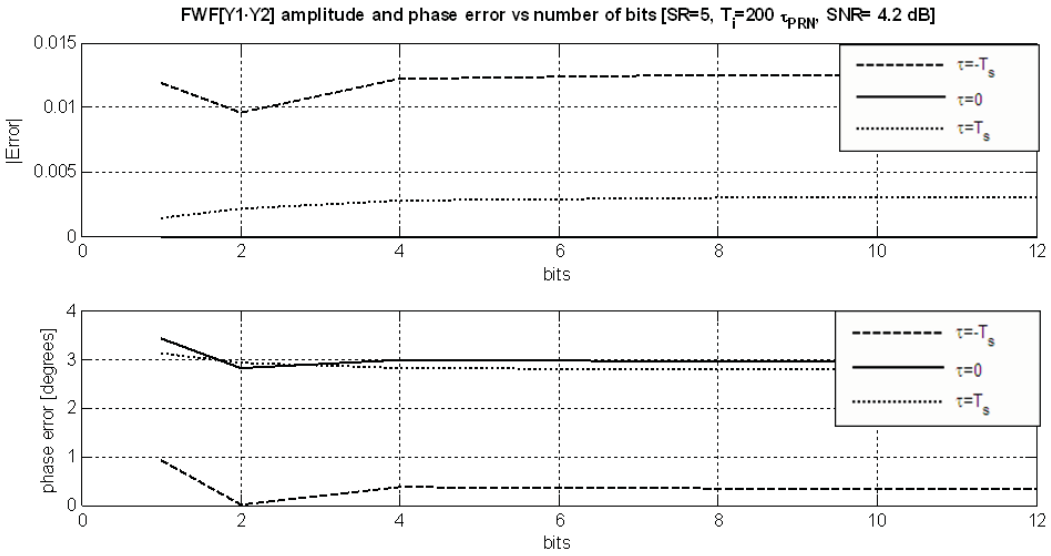

(b)

Figure 8.19. a) FWF amplitude and phase errors at $\tau = 0 \pm T_s$ as a function of the number of quantization bits when FWF is estimated by cross-correlating receivers' output a with local replica of PRN sequence FWF(local) (Eqns. 5.3-5.7),and b) FWF amplitude and phase errors at $\tau = 0 \pm T_s$ as a function of the quantization bits when FWF is estimated by cross-correlating receivers' outputs when the calibration signal is a PRN sequence FWF(Y1 · Y2) (Eqns. 5.1,5.2).

8.3.4 Conclusions

Correlation radiometers require the injection of known calibration signals. Currently these signals are generated by one or several noise sources and are distributed by a network of power splitters, which is bulky, difficult to equalize, and introduces additional noise. Aiming at alleviating these problems a new technique is presented. It consists of the centralized injection to all receivers of a deterministic PRN signal, providing complete baseline calibration. PRN signal exhibits a flat spectrum over the receivers' bandwidth, which makes possible to use those for calibration purposes instead of the usual thermal noise. Since the PRN signals are deterministic and known, new calibration approaches are feasible:

1. through the correlation of the output signals at different time lags, as it is usually done when noise is injected, but allowing a much easier distribution of the signal to all the receivers simultaneously, or

2. through the correlation of the output signals with a local replica of the PRN signal, leading to the estimation of the receivers' frequency responses and of the FWF. In this last case the distribution network has no influence on the correlation coefficient, adding correlated noise.

This technique has been verified experimentally to assess its performance and the optimum parameters to be used. Excellent performance has been demonstrated by comparing the FWF shape, and the amplitude and phase values at $\tau = 0, \pm T_s$ to the ones obtained using the injection of two levels of correlated noise [70]. The optimum parameters are: integration time at least 200 times the length of the sequence ($T_{\tau_{PRN}} = 200$ ms), PRN bandwidth larger than 5 times the receiver's bandwidth (SR$\geq$ 5), and the $P_{in}/k_B \cdot T_{REC} \cdot B \geq +11$ dB. The number of bits used turned out to only slightly affect the results and even if one-bit correlators are used, negligible system performance degradation has been noticed. The optimum values are: amplitude error < 0.25 % $\tau = 0, \pm T_s$, and phase error $< 1^o$ at $\tau = 0$ and $< 2^o$ at $\pm T_s$. Increasing the integration time above 200 ms will reduces the effect of receivers' noise in these estimates.

8.4 PAU-SA's test and experimental results

This section has been divided in two parts. Once all subsystems presented in chapter 7 have been individually checked and integrated in the instrument. The first part of this section is devoted to present the current status of the instrument, and to enumerate the problems with some parts of the instrument, how they are solved and how affect the instrument performance. Second part validates through experimental measurements the calibration, characterization, and imaging tests of the instrument performance. Calibration of instrumental offsets is performed by looking to a microwave absorber and the "cold" sky. Since the instrument operates in the GPS L1 band (f_{L1} = 1,575.42 MHz), satellites are imaged and a new way to compute the Flat Target Response has had to be devised. Internal phase/amplitude calibration is performed injecting pseudo-random noise signals. The different paths from the input switch to the antennas are calibrated by means of an external beacon. Differences in the propagation paths are accounted for by means of a near-field to far-field transformation. Finally, absolute amplitude calibration is achieved by imaging the GPS satellites constellation when pointing to the zenith. Evaluation of the images quality in terms of angular resolution, radiometric resolution and precision show the goodness of the techniques applied to compensate for instrumental errors and the imaging capabilities of the instrument.

8.4.1 PAU-SA's current state

Over the last five years the instrument has been successfully designed, implemented and assembled in the laboratory. This has been the most complicated part, the interconnection of a large number of control modules and the receivers working together. Concerning the hardware validation, all subsystems were checked independently and assembled all together to detect potential internal malfunction. Acquisition modes have been evaluated by checking the receiver internal switches (uncorrelated noise for offset calibration, correlated thermal noise or PRN signals for internal phase/amplitude calibration). This has been the most complicated part, the interconnection of a large number of control modules and the receivers working together. Finally, in July 2010, PAU-SA was installed in a trailer with a robotic mast that allows orienting it in arbitrary directions (Section 7.11). This has allowed testing the instrument in real conditions, including strong RFI at the GPS L1 band from some particular directions. Once the instrument was finished it underwent an exhaustive test process to validate the hardware and the software operation.

8.4.1.1 Detection of receiver's failure

In the process to check the receivers, the malfunction of three of them was detected. The methodology to detect the malfunction consisted of the injection to all receivers of uncorrelated noise (to detect saturated receivers), and correlated noise (to detect insensitive receivers), and to observe the visibility (V/H) matrices. Figures 8.20a and 8.20b show the viabilities matrices in the mode of correlated noise injection, where rows and columns represent the numbering of the 25 receivers.

To detect low sensitivity or insensitive receivers the injection of correlated noise was used. In the ideal case, but with high value (near the red color) visibilities matrices is

expected. In Fig. 8.20a it is possible to appreciate three horizontal and vertical blue lines (0's values) correspond with the receivers 9, 10 and 18. These receiver with absence of sensitivity have representation of 0's values in the spatial frequency coverage as shown in Figs 8.21a and 8.21b.

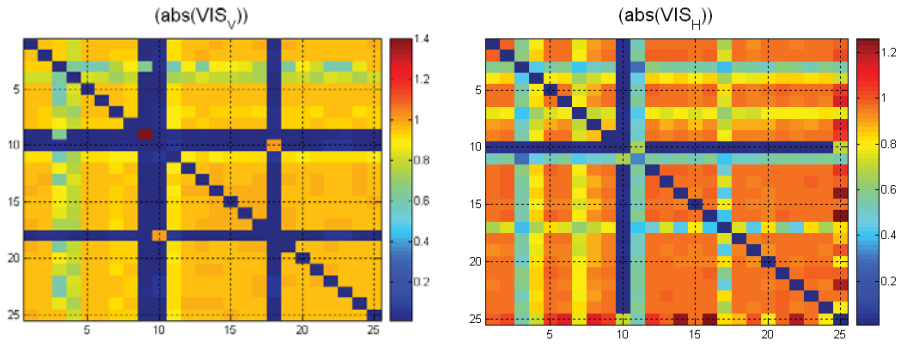

Figure 8.20. Absolute value of the visibility samples being the rows and columns the numbering of the 25 receivers, and the 0 values lines the insensitive correlations at a) V-pol, and b) H-pol.

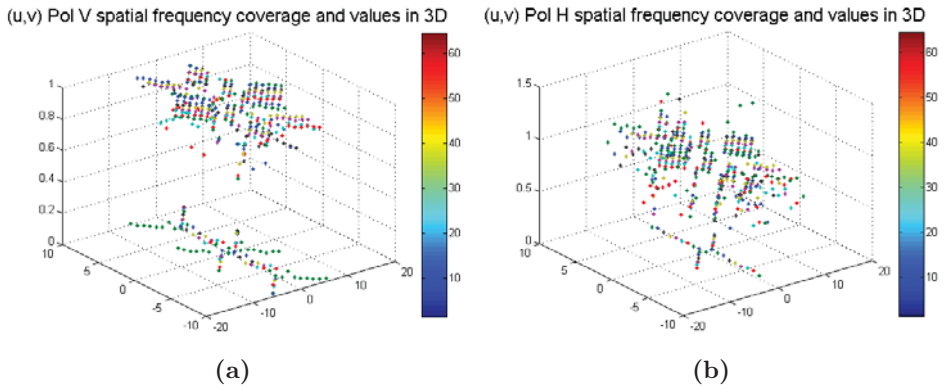

Figure 8.21. Representation of the visibility samples in the spatial frequency coverage of the a) V-pol, and b) H-pol.

Figures 8.22a to 8.22f show the impact of malfunction receivers in the spatial frequency coverage. On the contrary, to detect saturate receivers has used the injection of uncorrelated noise. In the ideal case, we expect a constant but with low value (near the blue color) visibilities matrices. Once the problematic receivers have been detected, these have been submitted to individual checking, concluding that the real problem was located inside the FPGA. It is due to the large number of lines to synchronization with the ADC. In these three cases (receivers involved) a synchronization instability was found due to the high occupation of the FPGA. For this reason we tried to compensate these synchronization instabilities, but the result was the deterioration of other receivers. Finally, the decision was the reduction of one element per arm (from 8 to 7 elements). The idea has been move at processing level the fault receivers at the end of each arm, so the malfunction receivers

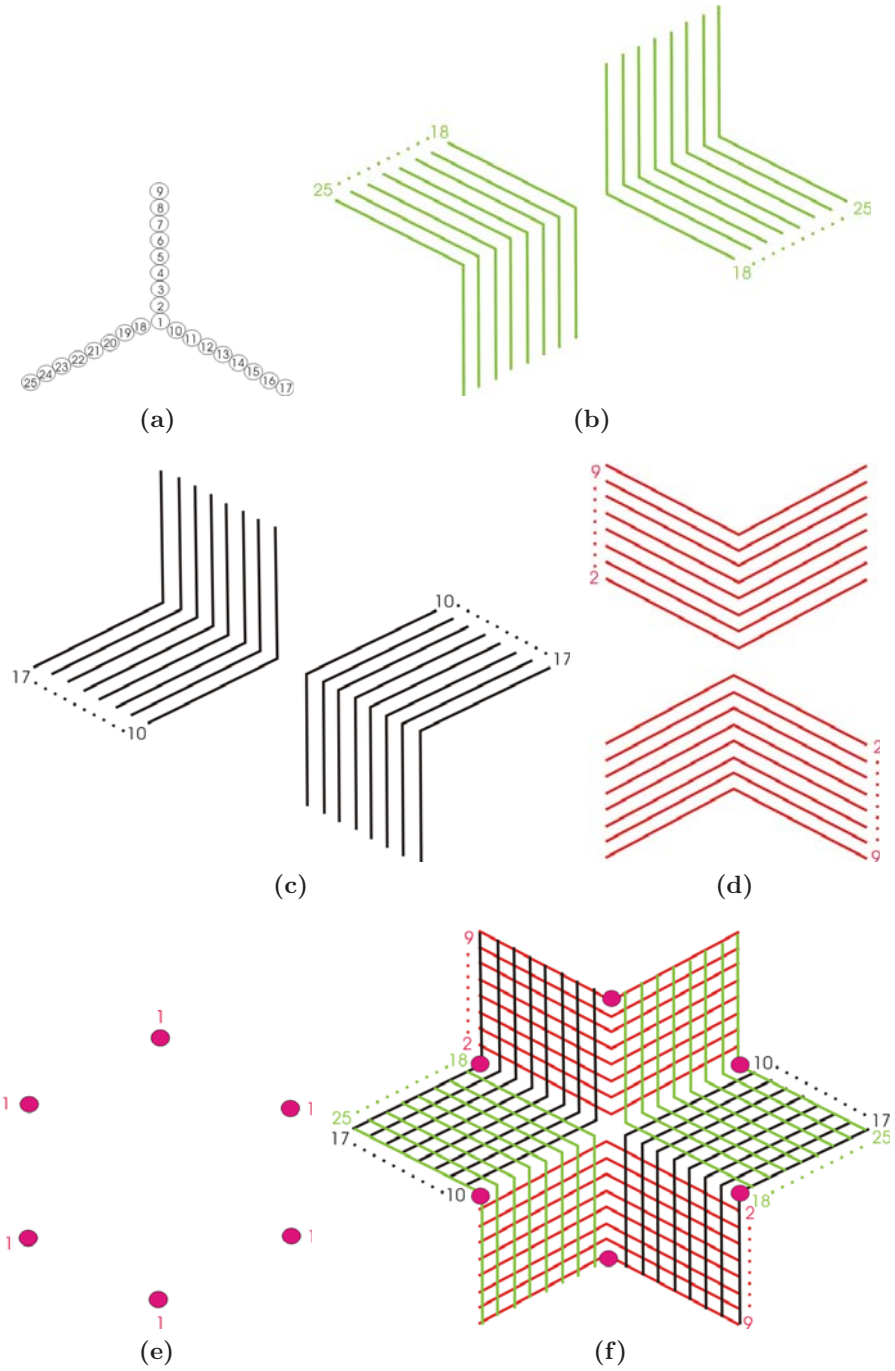

Figure 8.22. Representation of the impact of a malfunction receiver in the spatial frequency coverage a) PAU-SA's Y-shape array distribution, b) contribution receiver located in arm C (from 18 to 25), c) contribution receiver located in arm B (from 10 to 17), d) contribution receiver located in arm A (from 2 to 9), e) contribution of the central receiver, and f) combination of all contributions.

are relocated to the ends of each arm with less repercussion in the image reconstruction. By contrast, the elimination of one element per arm has an impact in the reduction of

the angular resolution.

8.4.1.2 Amplitude equalization

This section shows the power amplitude of each receiver at both polarizations (V / H) in order to check its behavior with different inputs. The goal of this test is to detect the malfunction of some receivers and to check the power level to determine the need for equalization. Figure 8.23a and 8.23b show the power level for external signal (antenna input). It consist of the injection of a external pattern signal, in the same way that used in the MBC method for the phase calibration process Fig 5.15. This signal has two power levels, RF ON and RF OFF. As expected in the most cases the power level RF ON is above the RF OFF. As it can be appreciate the receiver number 6 in polarization V has a malfunction since it work inversely to the power input. To detect the source of the problem the receiver was tested independently with proper operation, so the problem is focused in the (ADC channel or FPGA). The next test is focused with the injection of internal correlated noise (Noise source and PRN). It has two levels of power with an attenuator of (0 dB and 3 dB), Figs 8.23c and 8.23d. Despite it was calibrated to have the same power level in both correlated sources, it can observed that the power level with the PRN is larger than the Noise source, being necessary to compensate. In the same way as in the previous case, at v-polarization V, the receiver number 6 has the same behavior. The last test compares the external sources coming from the antennas (pattern signal and the absorber) with the internal uncorrelated signals Figs 8.23e and 8.23f. As expected with the MBC RF OFF, the absorber and the uncorrelated noise signals, signals have a lower power level than the MBC RF ON. In general terms, it is recommendable equalize the power amplitudes been necessary replace the manual adjustment by an electronically automatized process.

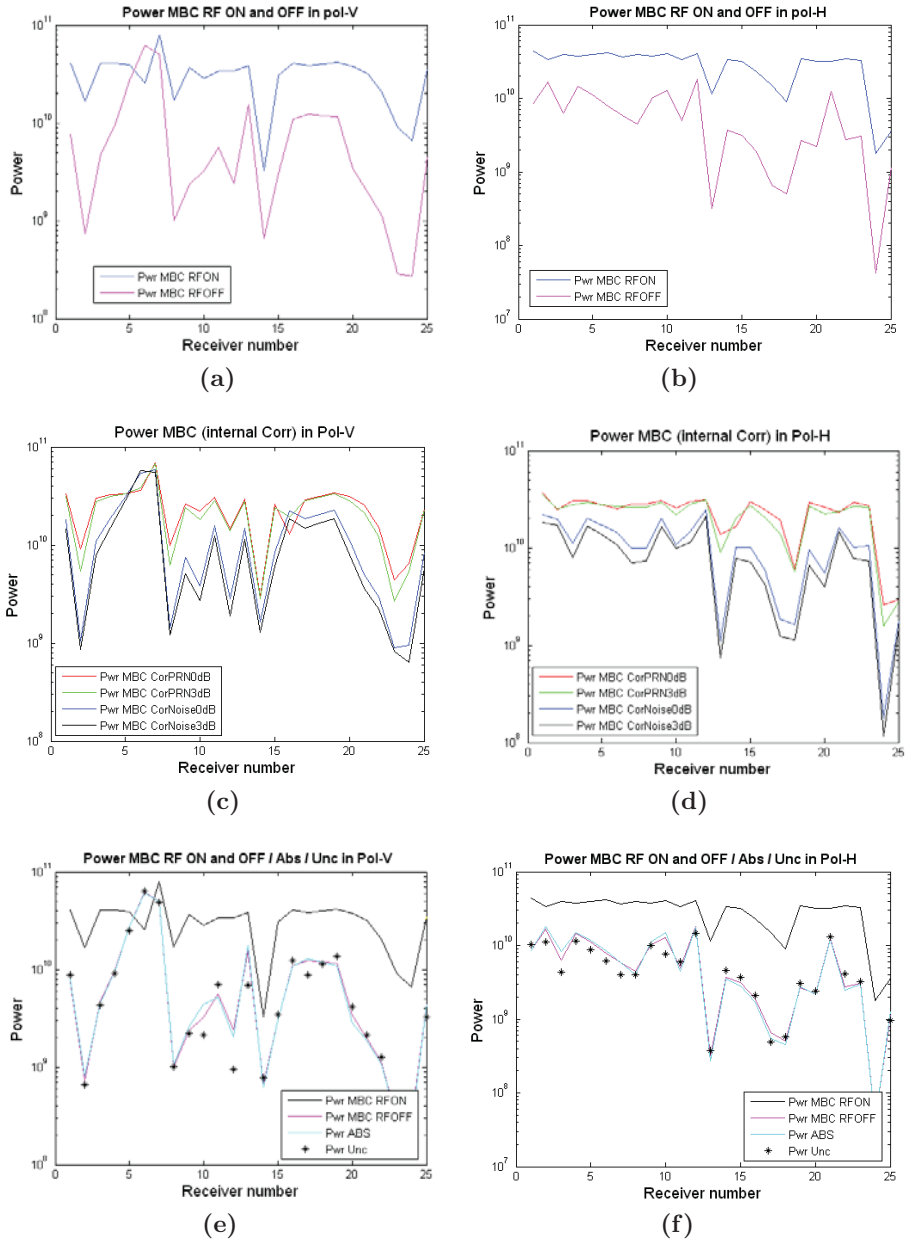

Figure 8.23. Power estimation test for all receivers with different injected signals, measurements are in AMUs. a) power response with an external reference RF ON and RF OFF, MBC method at V-pol, and b) H-pol, c) power response with correlated internal signals at 0 and 3 dB with (Noise Source and PRN) at V-pol, and d) H-pol, e) power response with different input signals (external with the MBC method / external with absorber / internal with uncorrelated signal) at V-pol, and f) H-pol.

8.4.2 Instrument characterization

8.4.2.1 Angular resolution

The angular resolution was experimentally obtained by measuring the response to a PRN point source (transmitter) located in different positions in the antenna boresight and its vicinities, and compared to the theoretical predictions (Eqn. 4.77 and [22]). Figure 8.24 shows the PAU-SA instrument in the top of the 8 m height robotic arm and the beacon. The PAU-SA instrument was moved $\pm 10^{o}$ and $\pm 20^{o}$ both in azimuth and elevation to confirm that the source was imaged in the right direction. Figures 8.25a to 8.25e show the imaged source using a hexagonal inverse Fourier transform [64] and a rectangular window. As predicted, the impulse response width is $\Delta\theta(\xi, \eta) \sim 5.7^{o}$, and it has six tails spaced 60^{o} each one, and peak side lobes $\sim$ -7 dB below the main peak, validating the concept of "equivalent array facto", since the whole interferometric array performs as a real aperture array with one element in each (u, v) position, except for the fact that the pattern does not have to be squared. Obviously, a simple way to reduce the side lobe level is by using a tapered window, at the expense of a wider synthetic beam. The positions of the PRN source are also correctly located. Figures 8.27a to 8.27d, show the test of the angular resolution transmitting two PRN sources at 10 m in the boresight and point sources separated from 1 to 4 m, Fig. 8.26. This test has been carry out using a rectangular window, the inverse Hexagonal Fourier Transform and no near-field to far-field correction. In Fig. 8.27a can be appreciate the angular resolution of the instrument coinciding with $\Delta\theta(\xi, \eta) \sim 5.7^{o}$. The effect of the no near-field compensation can be noticed specially in Fig. 8.27d, with the appearance of Y-shape in the point source. A simple way to reduce the side lobe level is by using a tapered window, at the expense of a wider synthetic beam. Fig 8.27a and Figs. 8.28a to 8.28d show the angular resolution at 1m with different windows. As expected the best results has been perform with the rectangular window. With the rest of windows the retrieved sources are overlapped, deteriorating the angular resolution.

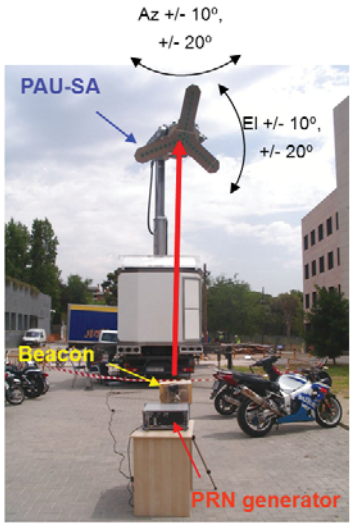

Figure 8.24. Angular resolution set up using a single PRN generator.

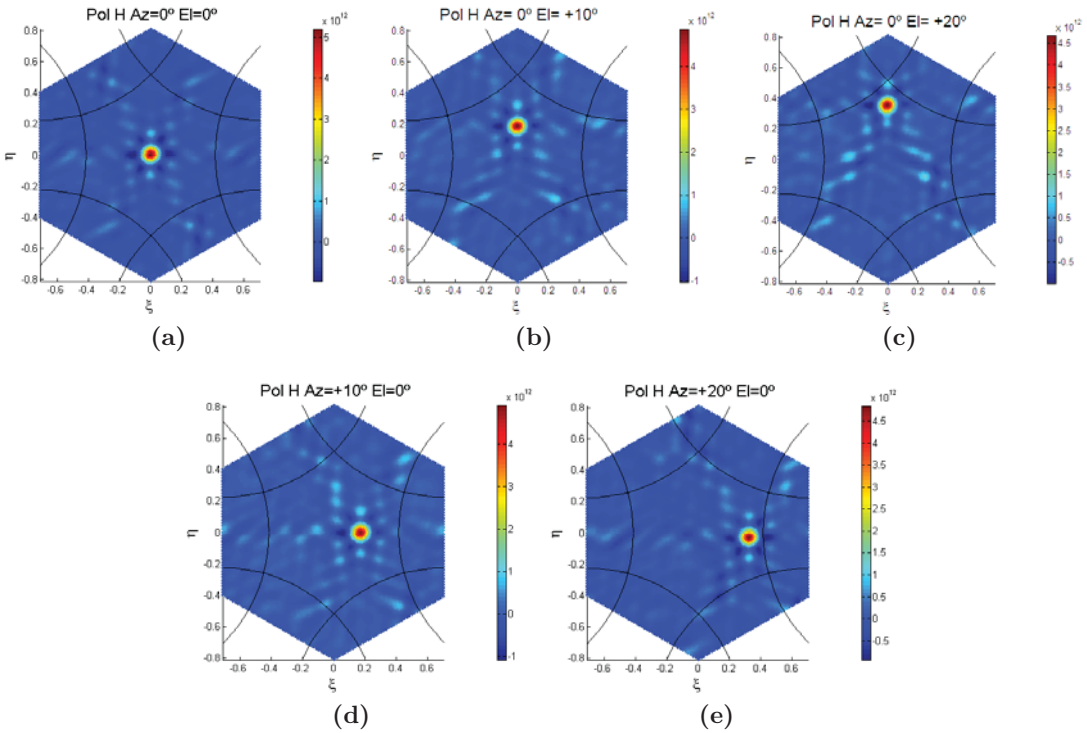

Figure 8.25. PRN source imaged (arbitrary units) using an inverse Hexagonal Fourier Transform and a rectangular window at horizontal polarization at: a) Az = 0º El = 0º, b) Az = +10º El = 0º, c) Az = +20º El = 0º, d) Az = +0º El = +10º, and e) Az = +0º El = +20º.

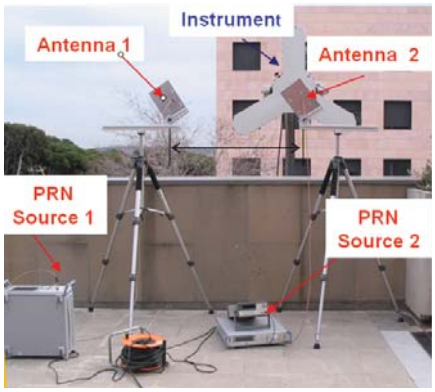

Figure 8.26. Angular resolution tests using two PRN generators.

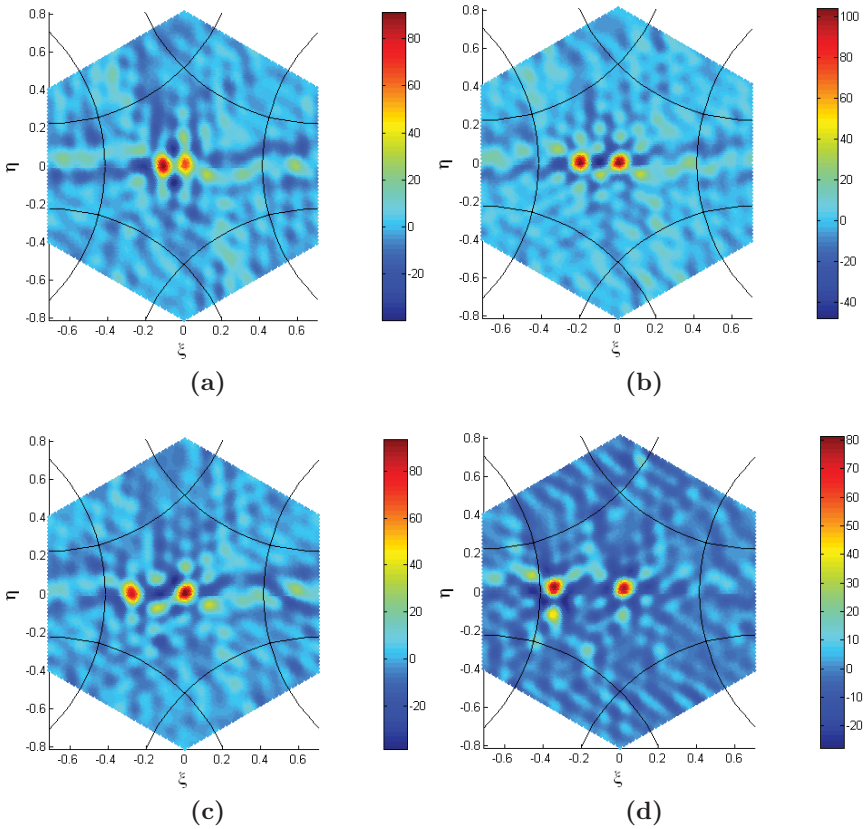

Figure 8.27. Two simultaneous PRN sources transmitted and being imaged in near-field (cannot be compensated if both are transmitting simultaneously), and using an inverse Hexagonal Fourier Transform and a rectangular window at horizontal polarization, spaced a) 1 m, b) 2 m, c) 3 m, and d) 4 m, at 10 m. The estimated angular resolution is $\Delta\theta(\xi, \eta) \sim 5.7^{\circ}$.

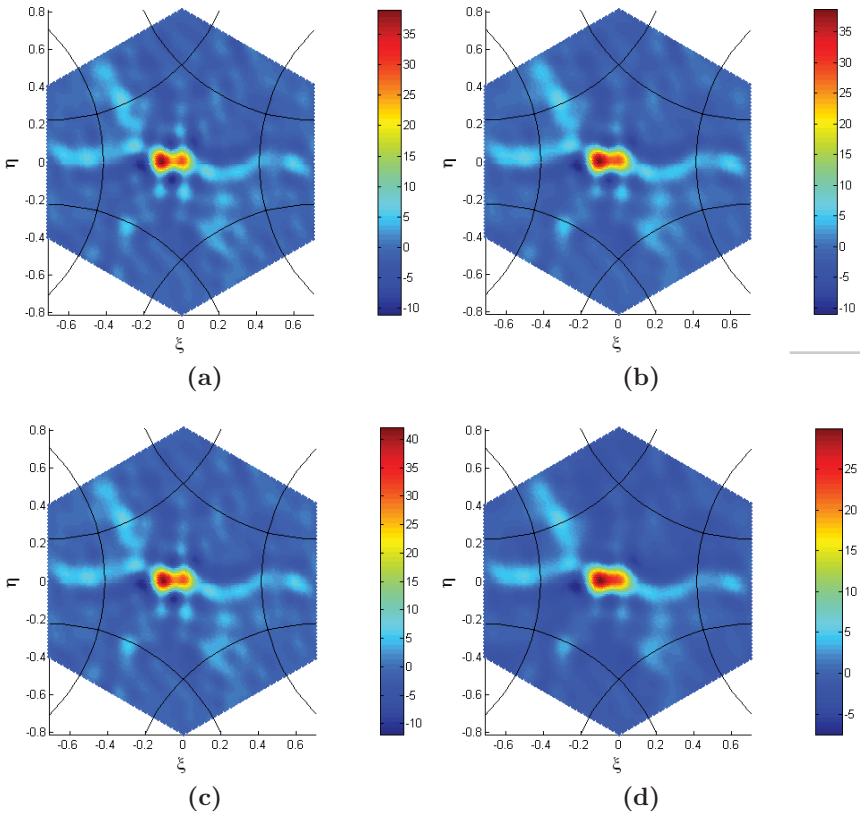

Figure 8.28. Two simultaneous PRN sources spaced 1 m being imaged in near-field (cannot be compensated if both are transmitting simultaneously), and using an inverse Hexagonal Fourier Transform at horizontal polarization using different windows a) triangular, b) Hanning, c) Hamming, and d) Blakman.

8.4.2.2 Radiometric resolution

The radiometric resolution is the minimum detectable change by the system, and it is usually defined as the standard deviation of the time fluctuations of a given observable. In a synthetic aperture interferometric radiometer, a single value is usually provided for all pixels in the image. In the case of PAU-SA was not clear how to evaluate this parameter, since the GPS satellites appear in all images. One way to assess the radiometric resolution, is to analyze the histogram of the differences between all the pixels in a given image, and the estimated the FTR (Section 5.5.1.3). Due to the presence of the GPS satellites being imaged, the histogram is not Gaussian, as it would be expected, and it is not symmetric around its peak value either. Figure 8.29 shows an example of such histogram. The tail corresponds to the differences between the GPS satellites and the FTR. Since the number of pixels "occupied" by GPS satellites and their tails is quite limited, without introducing a significant error, the mean of the histogram can be interpreted as the radiometric bias, and the standard deviation as the radiometric resolution. In our case, the average value of the 80 difference snap-shots (3 s integration time each one) has been evaluated, leading to: 1.91 K at both polarizations.

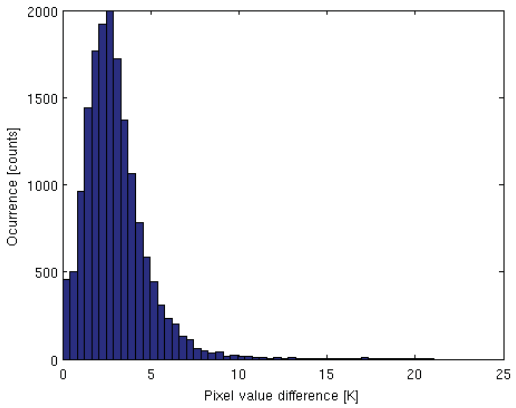

Figure 8.29. Sample histogram obtained as the difference between the zenith-looking images and the FTR obtained in Section 5.5.1.3. The tail corresponds to GPS satellites. Main bell corresponds to bias plus random errors.

8.4.2.3 Radiometric precision

The radiometric precision is defined as the systematic error in each pixel. Again, an average value is provided for the whole image, or at least for the significant part of it (the central part or alias-free field of view). A simple way to assess the radiometric precision is to compute the root mean squared value of the FTR (Figs. 5.18a and 5.18b) in a circle of (for example) radius 0.35 units (in the director cosines domain): $\sigma_v = 1.21$ K and $\sigma_h = 1.96$ K, respectively. The average values of the FTR in the same area are 5.40 K and 4.23 K at vertical and horizontal polarizations, which agree pretty well with the expected values of the sky/cosmic background (~ 2.7 K), plus the atmospheric contribution around the zenith (~ 2.1 K).

8.4.3 Imaging tests

During the "cold" sky-looking calibration, it was accidentally discovered that a number of moving spots appeared in the images. These spots correspond to the satellites of the GPS constellation, which were later used for our benefit for calibration purposes (Section 5.5.1.3). The imaging tests performed so far have consisted of looking to the zenith and imaging the evolution of the satellites of the GPS constellation. The imaging technique is a simple inverse hexagonal Fourier transform, followed by a compensation of the average estimated antenna pattern and the obliquity factor. In the reconstruction process the visibility samples have not been windowed, i.e. a rectangular window has been applied. Measurements were acquired every 11 minutes and consisted of a calibration using internal sources, followed by a zenith-looking measurement with an integration time of 3 s. Figure 8.30 shows the tracks of the GPS satellites and four snap-shots 22 min. apart, clearly showing their evolution. The color scale is in Kelvin, after absolute amplitude calibration as explained in section 5.5.1.3.

So far, all the results presented correspond to vertical polarization, rectangular window, except the results shown in Figs. 5.18b and 8.31b, which correspond to horizontal polarization. This is due to the failure of a number of receivers at horizontal polarization,

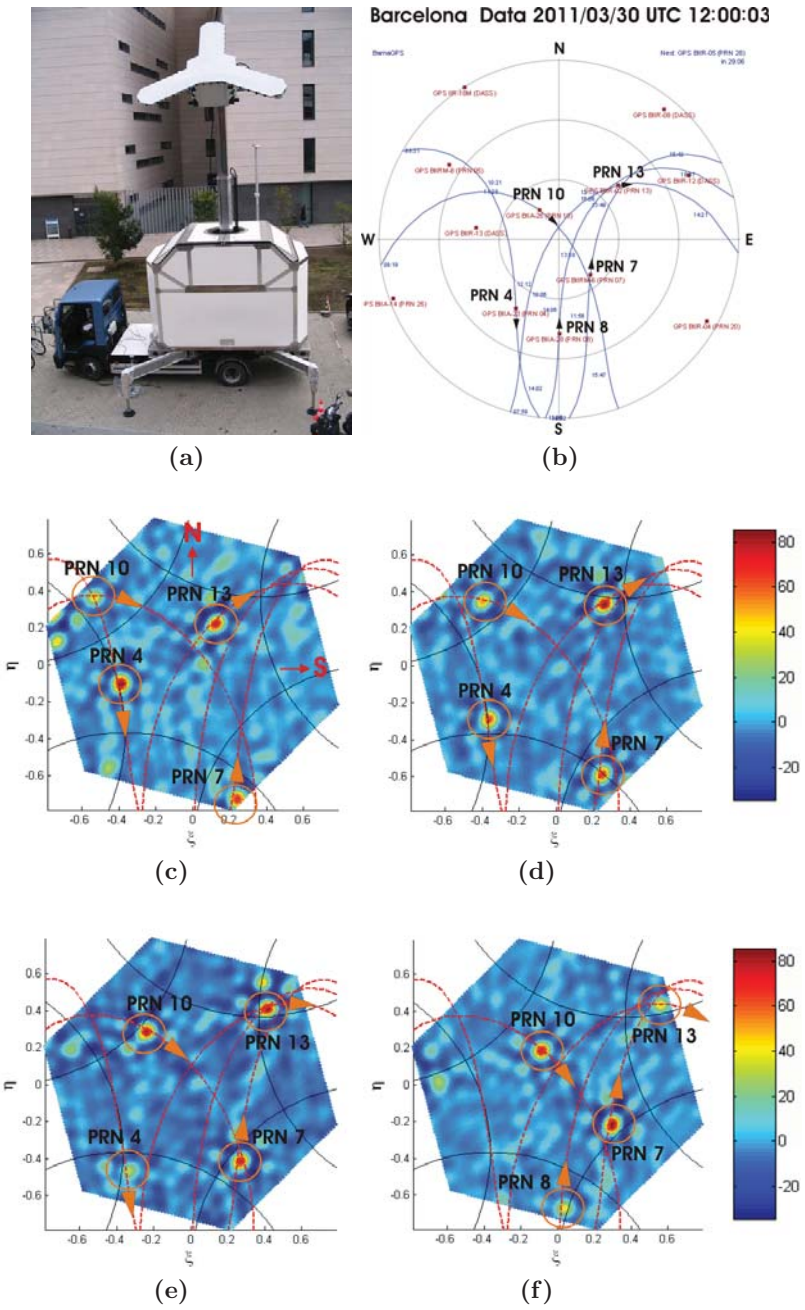

Figure 8.30. a) PAU-SA pointing to the GPS satellites, b) Map of GPS satellite paths as seen from the test location on March 30th, 2011. Sequential of images recovered by PAU-SA every 22 min: c) UTC 11:38:03, d) UTC 12:00:03 , e) UTC 12:22:03, f) UTC 12:44:03. Note: $\xi = 0, \eta \geq 0$ corresponds to the geographic north.

that prevented from retrieving nice-looking imagery at this polarization. A number of techniques have been tested to try to improve the quality of the retrieved images. These include:

- Interpolation (real and imaginary parts) of the visibility samples in the (u, v) space, without real success, and, assuming that the resulting image is the convolution of the original one and the distorted equivalent array factor or Point-Spread Function (PSF) in Optics, due to the failing elements) plus some noise:
- The Wiener and the regularized filter deconvolution algorithms [103, 104], which have been tested with some success and show very similar performance. Figure 8.31 shows the results of the application of the Wiener deconvolution algorithm at ver-

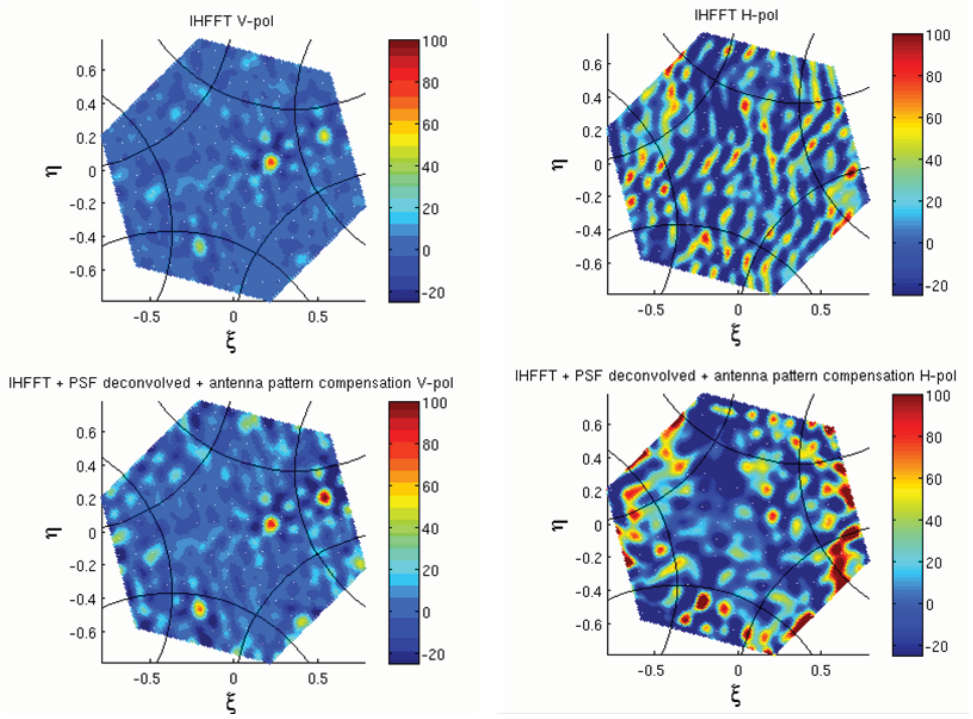

Figure 8.31. a) Vertical-polarization (top) retrieved and (bottom) deconvolved T_B images, and b) Horizontal-polarization(top) retrieved and (bottom) deconvolved T_B images.

tical and horizontal polarizations. At vertical polarization the improvement is very limited, or one would even see higher ripples in the image. At horizontal polarization, the improvement is strongly variable on the scene, and the best results are concentrated mostly in the alias-free field-of-view, where the ripples have been significantly reduced.

Unfortunately, the tests performed over large regions on the Earth, using real SMOS data in which artificial failing elements have been introduced, have not succeed to compensate for the antenna pattern errors, and therefore are not recommended here in general.

8.4.4 Summary and conclusions

This work has presented the calibration, performance, and imaging tests of the PAU-SA instrument. PAU-SA is a fully digital synthetic aperture radiometer designed and im-

plemented to test potential new improvements that could be applied in future missions. These include: digital I/Q down-conversion to avoid quadrature errors and achieve a perfect matching of the receivers' noise temperature and the frequency response in the in-phase and quadrature branches of each channel, digital filtering to achieve a quasi-perfect matching of receivers' frequency responses, because the narrowest one are digital and -by construction- identical, and digital estimation of the received power, avoiding thermal drifts in the detector diode, and the use of Pseudo-Random Noise signals for calibration purposes. Instrument offsets, phase and amplitude calibration have been explained, including the computation of the Flat Target Response in a new way to overcome the presence of the GPS satellites in the T_B images. The instrument performance has been evaluated in terms of the angular resolution ($\Delta\theta(\xi,\eta) \sim 5.7^{\text{o}}$), radiometric resolution (1.91 K at both polarizations), and radiometric precision ($\sigma_v = 1.21$ K and $\sigma_h = 1.96$ K). Finally, successful imaging tests of the satellites of the GPS constellation have been performed showing their relative movement around the sky zenith. Wiener and the regularized filter deconvolution algorithms have been tested to improve the image quality, specially when there are failing elements that distort the shape of the equivalent array factor or instrument's impulse response. Results exhibit some improvement for images consisting of point sources, but do not show any detectable improvement in extended sources (not shown, but tested with real SMOS data, simulating antenna failures). When it will be possible to move the trailer to the field, future research will include imaging of natural scenes that will hopefully be RFI free. Future research will also focus in improving the performance of image reconstruction algorithms in the presence of antenna failures.

Chapter 9

Conclusions, future research lines and contributions

This chapter is devoted to present the main conclusions of this Ph.D. research, in addition of the future research lines.

9.1 Conclusions and summary

The present Ph.D. thesis is the contribution to the development of a synthetic aperture radiometer under the frame of the PAU concept. It consists of measurements of the sea brightness temperature and reflected GNSS-R signals with the same receiver, in addition with an IR radiometer in order to improve of the retrieved SSS. Concerning to the design of the PAU-Synthetic Aperture (PAU-SA) radiometer part, it has been focused in the identification of critical elements in the MIRAS's design and introduce and test some potential improvements that could be eventually implemented in future MIRAS's versions of SMOS follow-on missions. Despite both instruments are Y-shaped arrays, there are several differences among them such as: the altitude, the arm size, the receiver topology, the processing unit, in addition to other parts, being unsuitable a direct comparison. For this reason this Ph.D. thesis is a proposal of a new instrument to test potential improvements for future interferometric radiometers, been divided in five parts.

The first part is devoted to present the motivations of the project, review of the PAU project, basic concepts in radiometry and interferometric radiometry. After a quick introduction to the interferometric radiometry in chapter 4, the first contribution has consisted of a new formulation of the theoretical angular resolution. Basically, it substituted the constant term of $\pi/2$ (Eqn. 4.77) found empirically by a new constant of $\pi/\sqrt{3}$ (Eqn. 4.79). This term is a conversion factor relating the areas of the external circle (ideal case) with the area of the star in the coverage of the synthetic aperture antenna, Fig. 4.12.

The second part, in chapter 5, presents a global description of the PAU-SA instrument. Moreover, a comparison table between MIRAS and PAU-SA is detailed, describing the main contributions in the PAU-SA instrument. These contributions have been focused on the replacement of analog by digital subsystems such as: I/Q down-conversion, digital filtering, full-matrix correlation (V, H and VH) and power estimation implemented in a FPGA. Due to the large number of these elements in the instrument, it is advisable to obtain quasi-perfect matching, mass reduction and minimize temperature and frequency drifts. Quadrature errors filter response matching, and temperature drifts can be minimized using digital techniques. Moreover, PAU-SA provides other improvements such as: non-sequential full-polarization receivers design, a dummy antenna at the end of each arm to improve the inter-antenna pattern similarity, reduction in the antenna spacing to increase the alias-free field of view, use of a centralized reference clock with internal LO generated in each receiver to minimize offsets, and the use of both a centralized noise source and the potential use of PRN for calibration purposes. This last, has been one of the most remarkable contributions in the hardware design since with this method it is possible to feed a large number of receivers using a centralized topology. PRNs are sequences of symbols with a long repetition period that have a flat spectrum over a bandwidth which is determined by the Symbol Rate, related with the speed of the code. The higher the SR, the larger the bandwidth of the PRN signal spectrum, and the flatter the spectrum is within the receiver's bandwidth so it looks like more white noise. Since the spectrum of PRN signals resembles that of thermal noise, they can be used to calibrate correlation radiometers. Moreover, one of the advantages of using PRN sequences as correlated "noise" sources for calibration is that they can be used to compute the frequency response of each receiver which can be interesting to check the instrument's

health. It consists of cross-correlating a baseband replica of the PRN signal injected, and the sampled output signals.

In PAU-SA, two of the parameters under discussion have been presented. The first one is the impact of the frequency operation on the radiometer part. Although the radiometry signal is approximate 23 dB above the reflectrometry signal, it has an impact on the radiometric measurements of about 220 K when the satellite point to the boresight, and in the best case of about 170 K when the satellite is located in the edge of the AF-FOV. For this reason, is mandatory point to the north for radiometric measurements where there are no GPS satellites due to their orbital distribution. The second one is the impact of the spatial decorrelation effect in the visibility function. Since the PAU-SA's dimension is 3 times smaller respect to MIRAS and the bandwidth is a factor of 10 smaller, the FWF is totally negligible.

After the PAU-SA's processing implementation description, the calibration process has been presented. Since some parameters of the instrument have been impossible to estimate directly, an alternative calibration has been proposed. Concerning the phase calibration an external signal is transmitted to the central array element and with combination of internal correlation signals; the physical paths are estimated and stored for future calibrations. In relation to the amplitude calibration, it is necessary to determine the system temperature in addition to the losses of the antennas, switches, etc. been necessary to characterize the instrument in an anechoic chamber, or calibrate the instrument with a pattern reference in the far field, as a scaling factor for all visibilities. Since the instrument has been impossible to characterize in an anechoic chamber, and the most of the time the GPS satellites are in the AF-FOV, these satellites have been used as signals of opportunity for the amplitude calibration. Finally, some PAU-SA's parameters have been determined such as: the AF-FOV with approximately 50º in the ξ plane, the angular resolution using a rectangular window with a $N_{EL} = 8$ and determined with the new formulation (Eqn. 4.79) of about 4.60º, and 5.25º using a $N_{EL} = 7$, among other parameters.

The third part is devoted to present the PAU-SA's physical modeling simulator. It is an end-to-end simulator trying to modeling the PAU-SA instrument, (radiometer part), as faithfully as possible. Since the instrumental errors can be introduced independently, it is possible to determine the impact of each one in image retrieved in order to improve the instrument continuously. In this it is possible simulate till nine point sources in both polarization and extended sources.

The fourth part presents the instrument description being extended in the section future research lines. This part has been the most complicated and where I have spent more time due to the high complexity of the hardware and coordination between us and the outsourced companies. In relation to the initial specifications of the design concerning sharing the central elements of the array for both radiometry and GNSS-R applications were postponed for simplification reasons, been possible to implement in the future. Meanwhile, a single receiver in arm C has been placed for the GNSS-R applications. Although there are lot of hardware, only the most remarkable conclusions are itemized.

- the impact of a dummy antenna at the end of each arm has been determined by simulations with the advantage to improve the patter array at the end of the arm but with the drawback of incorporate no operational antennas,

- the PAU-SA's receiver is a simplified version of PAU-RA. Since it has a large number of receivers 8 per arm plus one in the center, the pseudo-correlation topology has been discarded due to the limitation of I/O pins in the FPGA. For this reason a trade-off has been established between dual polarization (V/H) full time and receiver topology. The PAU-SA'receivers are the same of the PAU-RA, but mounting half of the components, having selecting a TPR topology. The three main keys of this receiver are: continuous acquisition, necessary for GNSS-R application, full-pol operation with continuous measurement of the radiometer, and reflectometer; and a three-stage down-converter with a centralized LO. All analog signals are downconverted from the L1 of GPS to 4.039 MHz. The receiver was carefully designed to preserve symmetry between both receiving branches, minimize cross-talk and interconnection routes. Taking into account that the operating frequency is the L1 band of GPS and many components are already available for commercial applications, some of them have been used for the implementation of this receiver. PAU-SA's receiver has a theoretical T_{REC} of 191 K, but the measurement value has been estimated with the Noise Analyzer of 250 K, probably due to losses in the switches,

- the base-band signals are digitalized at 8 bits in the ADC state using band-pass sampling in order to reduce the data throughput with a input rate approximately 2.4 Gb/s. All this information is sent to the FPGA, being possible to process thanks to the software reuse technique the three correlation matrices (V, H, and V/H) using 1 bit and the three power estimations using 8 bits,

- the calibration subsystem module, used to implement the correlation noise injection for calibration purposes, incorporate two methods: a classical noise source or the technique never used before using PRN signals. With this technique, it is possible to feed an independent number of receivers with a centralized configuration.

Finally, the fifth part presents the most relevant results during the instruments characterization. Because of an accident in the robotic arm early this year, the instrument has been disabled till the time of writing the Ph.D. thesis. The presented results have been performed in an urban environment, but a RFI-free environment is recommended to achieve future radiometric measurements.

The thermal control temperature of both the receiver (T_{ph}), and the ground plane has been determined. In both cases the central elements are hotter.

A representative baseline level in the anechoic chamber has successfully been calibrated, tested, and the baseline response measured. It is strongly recommended do these tests with the final instrument. In these tests have been possible to determine:

- baseline response has been measured in an anechoic chamber to characterize the ECCOs the antenna patterns of about (0.015, 0.055),

- determination of the optimum integration times through the Allan's variance, limited by the power estimation to 15 s.

- measurement of the sensibility circles to determine the radiometric sensitivity, detecting an estimated T_{REC} larger than 250 K,

- measurement of the baseline response observing that the real and imaginary parts are orthogonal and to observe the sensibility to polarization changes in the transmitting antenna,

- PRN signals behave as white noise and can be used for calibration purposes in correlation radiometers. The higher the symbol rate the flatter the spectrum (looks like more as white noise over the bandwidth). PRN has constant amplitude, and its input power can be much higher than in the case of noise injection (no clipping) being the calibration less sensitive to receiver's thermal noise. Moreover, the number of receivers using PRN injection is independent. Since PRN are deterministic signals, new calibration approaches are possible such as: determination of receivers' frequency responses and instrument's health. Experimental results have been performed with the next optimum parameters: PRN with SR > 5 (flat spectrum such as Noise Source). Estimation of FWF at $\tau = 0$ with 1B/2L (amplitude error $<$ 0.25% and phase error $< 1^{o}$).

PAU-SA instrument has been calibrated and experimental results have been achieved:

- phase, and offsets (without include the ECCOs) calibration have been performed successfully,

- GPS satellites have been used as amplitude calibration signals of opportunity, and the computation of Flat Target Response with the statistical operator mode as a way to mitigate the presence of GPS in the T_B images,

- instrument characterization has been focused in terms of the angular resolution ($\Delta\theta(\xi,\eta) \sim 5.7^{o}$) compared with ($\Delta\theta(\xi,\eta) \sim 5.25^{o}$) (theoretical method 2 and $N_{EL} = 7$ elements), radiometric resolution (1.91 K at both polarizations), and radiometric precision ($\sigma_v = 1.21$ K and $\sigma_h = 1.96$ K).

- Finally, results imaging recovery using PRN sequences as GPS C/A codes from a vector generator to test movements in azimuth and elevation and imaging real GPS satellites have been performed. A ground-based measurements campaign in a rural area is planned to test the whole system and validate the error budget of the calibration and imaging algorithms.

9.2 Future research lines

Although in this Ph.D. thesis it has been done a lot of work has been done a lot of work, it is recommendable to take into account the next research lines. The first part concerns to the global level, and the second part to the individual modules.

- it is strongly recommendable characterize the instrument inside an anechoic chamber, in a free of GPS satellites environment, to determine parameters such as: amplitude calibration, the ECCO offsets, the array pattern, and achieve radiometric measurements with a passive pattern,

- in a free from RFI enviroment, and pointing to the north (no GPS satellites), repeat radiometric measurements with the same passive patter, and verify with the results obtained in the anechoic chamber,

- incorporate the GNSS-R, and IR data with the radiometric measurements in order to retrieve the SSS. Measurement campaign in the mouth of a river where it is possible to appreciate a SSS gradient,

- in the PAU-SA's receiver, change the non-absorptive switches by absorptive to improve the ECCO offsets, reduce the NF improving the T_{REC}, and substitute the manual gain video amplifiers by programmable to equalize the channel automatically,

- in the ADC board array, wire individually each data and control (DCO and FCO) signals to the FPGA to solve the problem of de-synchronization,

- in the FPGA, update to anew developed board version, increasing: the I/O pins to wire each ADC data and control (DCO and FCO) signals directly with the FPGA, increase the number of slices to implement V/H polarization, the receiver's frequency response technique using PRN signals,

- in the calibration subsystems, substitute the fixed attenuator in the PRN generator module by a programmable one, in order to modify the power level if it is necessary,

- in the temperature control, improve the central air circulation, and train the PID to obtain a quick and better performance,

- in the computer and communication protocols, centralize the software of the simulator, the control of the instrument (robotic arm movements), and the data acquisition.

9.3 List of publications

This section is devoted to present the publications during the Ph.D. thesis. Publications are sorted in function of the participation, being classified in four groups: journal papers, main conference papers, participation in R & D projects, supervised master thesis, and patents.

JOURNAL PAPERS

- **I. Ramos-Perez**, X. Bosch-Lluis, A. Camps, N. Rodriguez-Alvarez, J.F. Marchan-Hernandez, E. Valencia, C. Vernich, S. de la Rosa, S. Pantoja, "Calibration of Correlation Radiometers Using Pseudo-Random Noise Signals" *Sensors Journal*, Vol. 9, pp. 6131-6149, 2009.

- **I. Ramos-Perez**, X. Bosch-Lluis, A. Camps, V. Gonzalez, N. Rodriguez-Alvarez, E. Valencia, and H. Park "Optimum Inter-calibration Time in Synthetic Aperture

Interferometric Radiometers: application to SMOS", *IEEE Transactions on Geociencie and Remote Sensing Letters* Volume: 9, Issue: 5 **(In press)**

- **I. Ramos-Perez**, G. Forte, A. Camps, X. Bosch-Lluis, E. Valencia, N. Rodriguez-Alvarez, H. Park, and M. Vall·llossera, "Calibration, performance, and imaging test of a fully digital synthetic aperture interferometric radiometric", *IEEE Journal of Selected Topics in applied Earth Observations and Remote Sensing* **(Submitted)**

- **I. Ramos-Perez**, A. Camps, X. Bosch-Lluis, N. Rodriguez-Alvarez, E. Valencia, H. Park, G.Forte, and M. Vall·llossera, "Passive Advanced Unit - Synthetic Aperture (PAU-SA): an instrument to test potential improvements for future interferometric radiometers" *Remote Sensing* **(Submitted)**

- X. Bosch-Lluis, **I. Ramos-Perez**, A. Camps, N. Rodriguez-Alvarez, E. Valencia, J.F. Marchan-Hernandez, "Common Mathematical Framework for Real and Synthetic Aperture Radiometers", *IEEE Transactions on Geoscience and Remote Sensing*, 2011, **(accepted)**

- X. Bosch-Lluis, **I. Ramos-Perez**, A. Camps, N. Rodriguez-Alvarez, E. Valencia, J.F. Marchan-Hernandez, "Description and Performance of an L-Band Radiometer with Digital Beamforming", *Remote Sensing*, Vol. 3, pp. 14-40, 2011.

- X. Bosch-Lluis, **I. Ramos-Perez**, A. Camps, N. Rodriguez-Alvarez, E. Valencia, H. Park, "A General Analysis of the Digitization Impact in Microwave Correlation Radiometers", *Sensors Journal*, vol. 11 n.6, pp. 6066-6087; 2011.

- A. Camps, X. Bosch-Lluis, **I. Ramos-Perez**, J. F. Marchan-Hernandez, B. Izquierdo, N. Rodriguez-Alvarez, "New Instrument Concepts for Ocean Sensing: Analysis of the PAU-Radiometer", *IEEE Transactions on Geoscience and Remote Sensing*, vol. 45 , no. 10, pp. 3180-319, 2007.

- X. Bosch-Lluis; A. Camps; **I. Ramos-Perez**; J. F. Marchán; N. Rodriguez-Alvarez; E. Valencia, "PAU/RAD: Design and Preliminary Calibration Results of a New L-Band Pseudo-Correlation Radiometer Concept" *Special issue Remote Sensing of Natural Resources and the Environment, Sensors Journal*, vol. 8 , pp. 4392-4412, 2008.

- N. Rodriguez-Alvarez, X. Bosch-Lluis, A. Camps, M. Vall-llossera, E. Valnecia, J.F. Marchan-Hernandez, **I. Ramos-Perez**, "Soil Moisture Retrieval Using GNSS-R Techniques: Experimental Results Over a Bare Soil Field", *IEEE Transactions on Geoscience and Remote Sensing*, Vol. 47, pp. 3616-3624, 2009.

- N. Rodriguez-Alvarez, A. Camps, M. Vall-llossera, X. Bosch-Lluis, A. Monerris, **I. Ramos-Perez**, E. Valencia, J. F. Marchan-Hernandez, J. Martinez-Fernandez, G. Baroncini-Turricchia, C. Perez-Gutierrez, and N. Sánchez, "Land Geophysical Parameters Retrieval Using the Interference Pattern GNSS-R Technique", *IEEE Transactions on Geoscience and Remote Sensing*, Vol. 49, n.1, pp. 71-84, 2011.

- E. Valencia, A. Camps, J.F. Marchan-Hernandez, X. Bosch-Lluis, N. Rodriguez-Alvarez, **I. Ramos-Perez**, "Advanced architectures for real-time Delay-Doppler Map GNSS-reflectomerters: The GPS refelctometer instrument for PAU griPAU)", *Advances In Space Research*, Vol. 46, pp. 196-207, 2010.

- J.F. Marchan-Hernandez, A. Camps, N. Rodriguez-Alvarez, E. Valencia, X. Bosch-Lluis, **I. Ramos-Perez**, "An Efficient Algorithm to the Simulation of Delay-Doppler Maps of Reflected Global Navigation Satellite System Signals", *IEEE Transactions on Geoscience and Remote Sensing*, Vol. 47, pp. 2733-2740, 2009.

- E. Valencia, A. Camps, J.F. Marchan-Hernandez, N. Rodriguez-Alvarez, **I. Ramos-Perez**, X. Bosch-Lluis, "Experimetnal Determination of the Sea Correlation Time Using GNSS-R Coherent Data", *IEEE Geoscience and Remote Sensing Letters*, Vol. 7, pp. 675-679, 2010.

- J. F. Marchan-Hernandez; N. Rodriguez-Alvarez; A. Camps; X. Bosch-Lluis; **I. Ramos-Perez**; E. Valencia, "Correction of the Sea State Impact in the L-Band Brightness Temperature by Means of Delay-Doppler Maps of Global Navigation Satellite Signals Reflected Over the Sea Surface", *IEEE Transactions on Geoscience and Remote Sensing*, vol. 46 , issue 10. Part 1. pp. 2914-2923, 2008.

- J.F. Marchan-Hernandez; A. Camps; N. Rodriguez-Alvarez; X. Bosch-Lluis; **I. Ramos-Perez**; E. Valencia, "PAU/GNSS-R: Implementation, Performance and First Results of a Real-Time Delay-Doppler Map Reflectometer Using Global Navigation Satellite System Signals" *Special issue Remote Sensing of Natural Resources and the Environment, Sensors Journa*l, vol. 8 , pp. 3005-3019, 2008.

- J.F. Marchan-Hernandez, A. Camps, N. Rodriguez-Alvarez, E. Valencia, X. Bosch-Lluis, **I. Ramos-Perez**, "An Efficient Algorithm to the Simulation of Delay-Doppler Maps of Reflected Global Navigation Satellite System Signals", *IEEE Transactions on Geoscience and Remote Sensing.* Vol 47, pp 2733-2740, 2009.

- N. Rodriguez-Alvarez, X. Bosch-Lluis, A. Camps, **I. Ramos-Perez**, E. Valencia, H. Park, M. Vall-llossera, "Vegetation Water Content Estimation Using GNSS Measurements," IEEE Geoscience and Remote Sensing Letters, 2011.

- N. Rodriguez-Alvarez, X. Bosch-Lluis, A. Camps, A. Aguasca, M. Vall-llossera, E. Valencia, **I. Ramos-Perez**, and H. Park, "Review of crop growth and soil moisture monitoring from a ground-based instrument implementing the Interference Pattern GNSS-R Technique", Radio Science, 46, RS0C03, 2011.

- E. Valencia, A. Camps, J.F. Marchan-Hernandez, H. Park, X. Bosch-Lluis, N. Rodriguez-Alvarez, **I. Ramos-Perez**, "Ocean Surface's Scattering Coefficient Retrieval by Delay-Doppler Map Inversion," IEEE Geoscience and Remote Sensing Letters, vol.8, no.4, pp.750-754, July 2011.

- E. Valencia, A. Camps, X. Bosch-Lluis, N. Rodriguez-Alvarez, **I. Ramos-Perez**, F. Eugenio, J. Marcello, "On the Use of GNSS-R Data to Correct L-Band Brightness Temperatures for Sea-State Effects: Results of the ALBATROSS Field Ex-

periments," IEEE Transactions on Geoscience and Remote Sensing, vol.49, no.9, pp.3225-3235, Sept. 2011.

- E. Valencia, A. Camps, N. Rodriguez-Alvarez, **I. Ramos-Perez**, X. Bosch-Lluis, and H. Park, "Improving the accuracy of sea surface salinity retrieval using GNSS-R data to correct the sea state effect", Radio Science, 46, RS0C02, 2011.

MAIN CONFERENCE PAPERS

- **I. Ramos-Perez**, X. Bosch-Lluis, A. Camps, J. F. Marchan-Hernandez, R. Prehn, B. Izquierdo, "Design of a Compact Dual-Polarization Receiver for Pseudo-Correlation Radiometers at L-Band", *Internacional Geoscience and Remote Sensing Symposium IGARSS 2006* , pp. 1172-1175, Denver, USA, 2006.

- **I. Ramos-Perez**, A. Camps, X. Bosch-Lluis, J. F. Marchan-Hernandez and N. Rodríguez-Álvarez, "Synthetic Aperture PAU: a new instrument to test potential improvements for future SMOSops", *Internacional Geoscience and Remote Sensing Symposium IGARSS 2007*, pp. 247-250, Barcelona, 2007.

- **I. Ramos-Perez**, X. Bosch-Lluis, A. Camps, N. Rodriguez-Alvarez, J.F. Marchan-Hernandez, E. Valencia, "Use of Pseudo-Random Noise Sequences in Microwave Radiometer Calibration", *Proceedings of the MicroRad*, Florence, Italy 2008 (CD-ROM).

- **I. Ramos-Perez**, E.Valencia , A. Camps, X. Bosch-Lluis, J. F. Marchan-Hernandez, N. Rodríguez-Álvarez, F. Canales-Contador, M. Donadio, "Initials Results of the Passive Advanced Unit - Synthetic Aperture (PAU-SA)", *Internacional Geoscience and Remote Sensing Symposium IGARSS 2008*, Vol. 2, pp- 1148-1151, Boston, USA, 2008.

- **I. Ramos-Perez**, X. Bosch-Lluis, A. Camps, E. Valencia, J.F. Marchan-Hernandez, N. Rodriguez-Alvarez, "Preliminary results of the Passive Advanced Unit Synthetic Aperture (PAU-SA)", *Internacional Geoscience and Remote Sensing Symposium IGARSS 2009*, Vol. 4, pp. 121 - 124, Cape Town, South Africa, 2009.

- **I. Ramos-Perez**, X. Bosch-Lluis , A. Camps, E. Valencia, J.F. Marchan-Hernandez, N. Rodriguez-Alvarez, F. Canales-Contador, "Integration and test results of the Passive Advanced Unit Synthetic Aperture (PAU-SA)", *Advanced RF Sensors and Remote Sensing Instruments 2009*, ESTEC, 2009.

- **I. Ramos-Perez**, X. Bosch-Lluis, A. Camps, E. Valencia, N. Rodriguez-Alvarez, M. Vall-llossera, "On-ground tests and measurements of the Passive Advanced Unit Synthetic Aperture (PAU-SA)", *Internacional Geoscience and Remote Sensing Symposium IGARSS 2010*, pp. 3114 - 3117, Honolulu, USA, 2010.

- **I. Ramos-Perez**, G. Forte, X. Bosch-Lluis , A. Camps, E. Valencia, N. Rodriguez-Alvarez, H. Park, and M. Vall·llossera, "First results of the PAU-SA synthetic aperture radiometer", *Internacional Geoscience and Remote Sensing Symposium IGARSS 2011* , pp 3633 - 3636, Vancouver, Canada, 2011.

9.4 Participation in R & D projects

- "PAU: Passive Advanced Unit for ocean monitoring" by European Science Foundation through EUropean Young Investigator (EURYI) award developed in Universitat Politècnica de Catalunya (2005-2010)

- AYA2008-05906-C02-01/ESP and ESP2007- 65667-C04-02.

9.5 Master thesis supervised during this Ph.D.

- E. Valencia i Domènech. " Implementació en FPGA d'una unitat de correladors I estimador de potència per a un radiòmetre de síntesi d'obertura" , Advisors: **I. Ramos-Perez**, and A. Camps, March 2007.

- F. Frascella. "Integration and Image Reconstruction Algorithms for an Aperture Synthesis Radiometer", Advisors: **I. Ramos-Perez**, and A. Camps, June 2007.

- P. Campigotto. "Integration and Calibration Algorithms for an Aperture Synthesis Radiometer", Advisors: **I. Ramos-Perez**, and A. Camps, June 2007.

- M. Donadio. "Implementation of Analog-Digital Array for Aperture Synthesis Radiometer", Advisors: **I. Ramos-Perez**, and A. Camps, January 2008.

- F.J. Canales Contador. "Análisis e integración de un radiometro de aperture sintética", Advisors: **I. Ramos-Perez**, and A. Camps, April 2009.

9.6 Patents

- Reasearchers: A. Camps, X. Bosch, J. F. Marchán, **I. Ramos-Perez** "Sistema híbrido Receptor de señales GNSS-Reflejadas/radiometro diferencial de pseudocorrelación para la observacion pasiva del océano" Identification Number: P-200602778, Priority country: Spain, Priority Data: 25/10/2006 Developed from: Universitat Politècnica de Catalunya, c/Jordi Girona 1-3, 08034 Barcelona, Spain.

- A. Camps, H. Park, J.F. Marchan-Hernandez, E. Valencia, N. Rodriguez-Alvarez, X. Bosch-Lluis, **I. Ramos-Perez**, "Algoritmos avanzados para el cálculo de mapas Delay Doppler (DDM)", (Software registration pending).
  [Advanced algorithms for the Delay Doppler Maps (DDM) computation.]

- A. Camps, A. Aguasca, R. Acevo-Herrera, X. Bosch-Lluis, **I. Ramos-Perez**, N. Rodriguez-Alvarez, E. Valencia, J.F. Marchan-Hernandez, H. Park, "Sistema aerotransportado para la medida de la humedad del terreno y el contenido de agua de la vegetación y método de implementación", Identification Number: P- 201131085, Priority country: Spain, Priority Data: 28/06/2011 Developed from: Universitat Politècnica de Catalunya, c/Jordi Girona 1-3, 08034 Barcelona, Spain.
  [An airborne system for soil moisture and vegetation water content measurement and implementation method.]

- A. Camps, A. Aguasca, N. Rodriguez-Alvarez, X. Bosch-Lluis, **I. Ramos-Perez**, J. F. Marchan-Hernandez, H. Park, "Sistema para la recuperación de parámetros geofísicos usando señales de satélites de navegación", Identification Number: P-201131082, Priority country: Spain, Priority Data: 28/06/2011 Developed from: Universitat Politècnica de Catalunya, c/Jordi Girona 1-3, 08034 Barcelona, Spain. [A system for geophysical parameters retrieval using navigation satellites' signals.]

Bibliography

[1] SMOS: ESA's Water Mission, *ESA SMOS Brochure, BR-224, 14*, 2004. [Online]. Available: http://www.esa.int/esapub/br/br224/br224.pdf

[2] C. T. Swift and R. E. Mcintosh, "Considerations for Microwave Remote Sensing of Ocean-Surface Salinity," *IEEE Transactions on Geoscience and Remote Sensing*, no. 4, pp. 480–491, 1983.

[3] United Nation Environmental Programme - Climate Retrieved. UNEP. November 2008. [Online]. Available: http://www.grida.no/climate/vital/32.htm

[4] Y. H. Kerr, P. Waldteufel, J.-P. Wigneron, S. Delwart, F. Cabot, J. Boutin, M.-J. Escorihuela, J. Font, N. Reul, C. Gruhier, S. E. Juglea, M. R. Drinkwater, A. Hahne, M. Martin-Neira, and S. Mecklenburg, "The SMOS Mission: New Tool for Monitoring Key Elements ofthe Global Water Cycle," *Proceedings of the IEEE*, vol. 98, no. 5, pp. 666–687, 2010.

[5] W. J. Emery and R. T. Wert, "Temperature-Salinity Curves in the Pacific and their Application to Dynamic Height Computation," *Journal of Physical Oceanography*, vol. 6, no. 4, pp. 613–617, 1976. [Online]. Available: http://journals.ametsoc.org/doi/abs/10.1175/1520-0485%281976%29006%3C0613%3ATSCITP%3E2.0.CO%3B2

[6] S. Michel, B. Chapron, J. Tournadre, and N. Reul, "Global Analysis of Sea Surface Salinity variability from Satellite Data," in *Oceans 2005 - Europe*, vol. 1, 2005, pp. 11 – 16 Vol. 1.

[7] S. Levitus, S. Boyer, M. Conkright, T. O'Brien, J. Antonov, and C. Stephens, "World Ocean Database 2009," *National Oceangraphic Data Center, NOAA / NODC*, 2009. [Online]. Available: http://www.nodc.noaa.gov/OC5/WOD09/pr_wod09.html

[8] G. C. Thomann, "Experimental Results of the Remote Sensing of Sea-Surface Salinity at 21-cm Wavelength," *IEEE Transactions on Geoscience Electronics*, vol. 14, no. 3, pp. 198–214, 1976.

[9] Global Earth Observation System of Systems. GEOSS. 2009-2011 Work Plan. [Online]. Available: http://www.earthobservations.org/geoss.shtml

[10] H. M. J. Barre, B. Duesmann, and Y. H. Kerr, "SMOS: The Mission and the System," *IEEE Transactions on Geoscience and Remote Sensing*, vol. 46, no. 3, pp. 587–593, 2008.

[11] D. M. Le Vine, G. S. E. Lagerloef, F. R. Colomb, S. H. Yueh, and F. A. Pellerano, "Aquarius: An Instrument to Monitor Sea Surface Salinity From Space," *IEEE Transactions on Geoscience and Remote Sensing*, vol. 45, no. 7, pp. 2040–2050, 2007.

[12] D. Entekhabi, E. G. Njoku, P. E. O'Neill, K. H. Kellogg, W. T. Crow, W. N. Edelstein, J. K. Entin, S. D. Goodman, T. J. Jackson, J. Johnson, J. Kimball, J. R. Piepmeier, R. D. Koster, N. Martin, K. C. McDonald, M. Moghaddam, S. Moran, R. Reichle, J. C. Shi, M. W. Spencer, S. W. Thurman, L. Tsang, and J. Van Zyl, "The Soil Moisture Active Passive (SMAP) Mission," *Proceedings of the IEEE*, vol. 98, no. 5, pp. 704–716, 2010.

[13] R. H. Dicke, "The Measurement of Thermal Radiation at Microwave Frequencies," *Review of Scientific Instruments*, vol. 17, no. 7, pp. 268–275, 1946. [Online]. Available: http://link.aip.org/link/?RSI/17/268/1

[14] E. R. Westwater, "The accuracy of water vapor and cloud liquid determination by dual-frequency ground-based microwave radiometry," *Radio Science*, vol. 13, no. 4, pp. 677–685, 1978. [Online]. Available: http://dx.doi.org/10.1029/RS013i004p00677

[15] B. Aja, E. Artal, L. de la Fuente, J. P. Pascual, A. Mediavilla, N. Roddis, D. Kettle, W. F. Winder, L. P. Cara, and P. de Paco, "Very low-noise differential radiometer at 30 GHz for the PLANCK LFI," *IEEE Transactions on Microwave Theory and Techniques*, vol. 53, no. 6, pp. 2050–2062, 2005.

[16] A. Prytz, M. L. Heron, D. M. Burrage, and M. Goodberlet, "Calibration of scanning low frequency microwave radiometer," in *Proc. OCEANS '02 MTS/IEEE*, vol. 4, 2002, pp. 2003–2007.

[17] R. M. Lerner and J. P. Hollinger, "Analysis of 1.4 GHz Radiometric measurements from Skylab," *Remote Sensing of Environment*, vol. 6, no. 4, pp. 251 – 269, 1977. [Online]. Available: http://www.sciencedirect.com/science/article/B6V6V-4894PB2-2/2/40f71958748eb92a4d9535e16cf8833a

[18] D. M. Le Vine and J. C. Good, "Aperture synthesis for microwave radiometers in space," NASA memorandum, NASA-TM-8503, 1983.

[19] P. J. Napier, A. R. Thompson, and R. D. Ekers, "The very large array: Design and performance of a modern synthesis radio telescope," *Proceedings of the IEEE*, vol. 71, no. 11, pp. 1295–1320, 1983.

[20] D. M. Le Vine, A. J. Griffis, C. T. Swift, and T. J. Jackson, "ESTAR: a synthetic aperture microwave radiometer for remote sensing applications," *Proceedings of the IEEE*, vol. 82, no. 12, pp. 1787–1801, 1994.

[21] D. M. Le Vine, "Synthetic aperture radiometer systems," in *Proc. IEEE MTT-S Int. Microwave Symp. Digest*, vol. 1, 1999, pp. 407–410.

[22] A. Camps, "Application of Interferometric Radiometry to Earth Observation," Ph.D. dissertation, Universitat Politècnica de Catalunya, 1996. [Online]. Available: http://www.tdx.cat/TDX-1020104-091741/

[23] C. S. Ruf, C. T. Swift, A. B. Tanner, and D. M. Le Vine, "Interferometric synthetic aperture microwave radiometry for the remote sensing of the Earth," *IEEE Transactions on Geoscience and Remote Sensing*, vol. 26, no. 5, pp. 597–611, 1988.

[24] J. Font, G. S. E. Lagerloef, D. M. Le Vine, A. Camps, and O.-Z. Zanife, "The determination of surface salinity with the European SMOS space mission," *IEEE Transactions on Geoscience and Remote Sensing*, vol. 42, no. 10, pp. 2196–2205, 2004.

[25] S. Zine, J. Boutin, J. Font, N. Reul, P. Waldteufel, C. Gabarro, J. Tenerelli, F. Petitcolin, J.-L. Vergely, M. Talone, and S. Delwart, "Overview of the SMOS Sea Surface Salinity Prototype Processor," *IEEE Transactions on Geoscience and Remote Sensing*, vol. 46, no. 3, pp. 621–645, 2008.

[26] K. D. McMullan, M. A. Brown, M. Martin-Neira, W. Rits, S. Ekholm, J. Marti, and J. Lemanczyk, "SMOS: The payload," *IEEE Transactions on Geoscience and Remote Sensing*, vol. 46, no. 3, pp. 594–605, 2008.

[27] R. Sabia, M. Caparrini, G. Ruffini, and Camps, "Potential Synergetic Use of GNSS-R Signals to Improve the Sea-State Correction in the Sea Surface Salinity Estimation: Application to the SMOS Mission," *IEEE Transactions on Geoscience and Remote Sensing*, vol. 45, no. 7, pp. 2088–2097, 2007.

[28] M. P. Clarizia, C. Gommenginger, S. Gleason, C. Galdi, and M. Unwin, "Global Navigation Satellite System-Reflectometry (GNSS-R) from the UK-DMC Satellite for Remote Sensing of the Ocean Surface," in *Proc. IEEE Int. Geoscience and Remote Sensing Symp. IGARSS 2008*, vol. 1, 2008.

[29] J. F. Marchan-Hernandez, E. Valencia, N. Rodriguez-Alvarez, I. Ramos-Perez, X. Bosch-Lluis, A. Camps, F. Eugenio, and J. Marcello, "Sea-State Determination Using GNSS-R Data," *IEEE Geoscience and Remote Sensing Letters*, vol. 7, no. 4, pp. 621–625, 2010.

[30] A. Camps, M. Caparrini, R. Sabia, and G. Ruffini, "Sea Surface Salinity Retrieval from Space: Potential Synergetic Use of GNSS-R Signals to Improve the Sea State Correction and Application to the SMOS Mission," in *Proc. IEEE MicroRad*, 2006, pp. 91–96.

[31] A. Camps, *Passive Advanced Unit (PAU): A hybrid L-band radiometer,GNSS-Reflectometer and IR-Radiometer for Passive Remote Sensing of the Ocean*, Project descriptions of the EURYI award winners 2004 Telecommunications Engineering Std., 2004. [Online]. Available: http://www.esf.org/activities/euryi/awards/2004.html

[32] M. Martín-Neira, "A Passive Reflectometry and Interferometry System (PARIS): Application to Ocean Altimetry," ESA Journal 1993, 17, 331-355, 17, 331-355.

[33] A. Camps, J. Marchan-Hernandez, I. Ramos-Perez, X. Bosch-Lluis, and R. Prehn, "New Radiometer Concepts for Ocean Remote Sensing: Description of the Passive Advanced Unit (PAU) for Ocean Monitoring," in *Proc. IEEE Int. Conf. Geoscience and Remote Sensing Symp. IGARSS 2006*, 2006, pp. 3988–3991.

[34] I. Ramos-Perez, X. Bosch-Lluis, A. Camps, J. F. Marchan-Hernandez, R. Prehn, and B. Izquierdo, "Design of a Compact Dual-Polarization Receiver for Pseudo-Correlation Radiometers at L-band," in *Proc. IEEE Int. Conf. Geoscience and Remote Sensing Symp. IGARSS 2006*, 2006, pp. 1172–1175.

[35] A. Camps, X. Bosch-Lluis, I. Ramos-Perez, J. Marchan-Hernandez, B. Izquierdo, and N. Rodriguez-Alvarez, "New Instrument Concepts for Ocean Sensing: Analysis of the PAU-Radiometer," *Geoscience and Remote Sensing, IEEE Transactions on*, vol. 45, no. 10, pp. 3180 –3192, 2007.

[36] E. Cardellach, "Sea Surface Determination using GNSS Reflected Signals," Ph.D. dissertation, Universitat Politecnica de Catalunya, Barcelona, 2002. [Online]. Available: http://www.grss-ieee.org/files/estel/CardellachPhD2002.pdf.gz

[37] X. Bosch-Lluis, A. Camps, I. Ramos-Perez, J. F. Marchan-Hernandez, N. Rodriguez-Alvarez, and E. Valencia, "PAU/RAD: Design and Preliminary Calibration Results of a New L-Band Pseudo-Correlation Radiometer Concept," *Sensors*, vol. 8, no. 7, pp. 4392–4412, 2008. [Online]. Available: http://www.mdpi.com/1424-8220/8/7/4392/

[38] X. Bosch-Lluis, "On the Desing of Microwave Radiometers with Digital Beamforming and Polarization Synthesis for Earth Obervation," Ph.D. dissertation, Universitat Politècnica de Catalunya, 2011.

[39] I. Ramos-Perez, A. Camps, X. Bosch-Lluis, J. F. Marchan-Hernandez, N. Rodriguez-Alvarez, E. Valencia, F. Frascella, P. Campigotto, and M. Donadio, "Synthetic Aperture PAU: a new instrument to test potential improvements for future SMOSops," in *Proc. IEEE Int. Geoscience and Remote Sensing Symp. IGARSS 2007*, 2007, pp. 247–250.

[40] J. Marchan-Hernandez, "Sea state determination using GNSS-R techniques: Contributions to the PAU instrument," Ph.D. dissertation, Universitat Politècnica de Catalunya, 2008.

[41] X. Bosch-Lluis, I. Ramos-Perez, A. Camps, J. F. Marchan-Hernandez, N. Rodriguez-Alvarez, E. Valencia, M. A. Guerrero, and J. M. Nieto, "Initial Results of a Digital Radiometer with Digital Beamforming," in *Proc. IEEE Int. Geoscience and Remote Sensing Symp. IGARSS 2008*, vol. 2, 2008.

[42] X. Bosch-Lluis, I. Ramos-Perez, A. Camps, N. Rodriguez-Alvarez, J. F. Marchan-Hernandez, E. Valencia, J. M. Nieto, and M. A. Guerrero, "Digital beamforming

analysis and performance for a digital L-band Pseudo-correlation radiometer," in *Proc. Geoscience and Remote Sensing Symp.,2009 IEEE Int.,IGARSS 2009*, vol. 5, 2009.

[43] I. Ramos-Perez, X. Bosch-Lluis, A. Camps, E. Valencia, N. Rodriguez-Alvarez, M. Vall-llossera, and G. Forte, "On-ground tests and measurements of the Passive Advanced Unit Synthetic Aperture (PAU-SA)," in *Proc. IEEE Int. Geoscience and Remote Sensing Symp. (IGARSS)*, 2010, pp. 3114–3117.

[44] A. Camps, A. Aguasca, X. Bosch-Lluis, J. F. Marchan-Hernandez, I. Ramos-Perez, Rodriguez-Alvarez, F. Bou, C. Ibanez, X. Banque, and R. Prehn, "PAU one-receiver ground-based and airbone instruments," in *Proc. IEEE Int. Geoscience and Remote Sensing Symp. IGARSS 2007*, 2007, pp. 2901–2904.

[45] N. Rodriguez-Alvarez, J. F. Marchan-Hernandez, A. Camps, X. Bosch-Lluis, E. Valencia, I. Ramos-Perez, M. Vall-Llossera, A. Monerris, J. Martinez-Fernandez, C. Perez-Gutierrez, G. Baroncini-Turricchia, N. Sanchez-Martin, and J. M. Nieto, "Topographic profile retrieval using the Interference Pattern GNSS-R technique," in *Proc. Geoscience and Remote Sensing Symp.,2009 IEEE Int.,IGARSS 2009*, vol. 3, 2009.

[46] E. Valencia, A. Camps, J. Marchan-Hernandez, X. Bosch-Lluis, N. Rodriguez-Alvarez, and I. Ramos-Perez, "Advanced architectures for real-time Delay-Doppler Map GNSS-reflectometers: The GPS reflectometer instrument for PAU (griPAU)," *Advances in Space Research*, vol. 46, no. 2, pp. 196 – 207, 2010, gNSS Remote Sensing-1. [Online]. Available: http://www.sciencedirect.com/science/article/B6V3S-4YC2XKJ-1/2/5dedb11859e320d7bb0099b264c87ca2

[47] E. Valencia, R. Acevo, X. Bosch-Lluis, A. Aguasca, N. Rodriguez-Alvarez, I. Ramos-Perez, J. F. Marchan-Hernandez, M. Glenat, F. Bou, and A. Camps, "Initial Results of an Airborne Light-Weight L-Band Radiometer," in *Proc. IEEE Int. Geoscience and Remote Sensing Symp. IGARSS 2008*, vol. 2, 2008.

[48] R. Acevo-Herrera, A. Aguasca, X. Bosch-Lluis, and A. Camps, "On the use of compact L-band Dicke radiometer (ARIEL) and UAV for soil moisture and salinity map retrieval: 2008/2009 field experiments," in *Proc. Geoscience and Remote Sensing Symp.,2009 IEEE Int.,IGARSS 2009*, vol. 4, 2009.

[49] J. M. Tarongi and A. Camps, "Multifrequency experimental radiometer with interference tracking for experiments over land and littoral: Meritxell," in *Proc. Geoscience and Remote Sensing Symp.,2009 IEEE Int.,IGARSS 2009*, vol. 4, 2009.

[50] N. Rodriguez-Alvarez, X. Bosch-Lluis, A. Camps, M. Vall-llossera, E. Valencia, J. F. Marchan-Hernandez, and I. Ramos-Perez, "Soil Moisture Retrieval Using GNSS-R Techniques: Experimental Results Over a Bare Soil Field," *IEEE Transactions on Geoscience and Remote Sensing*, vol. 47, no. 11, pp. 3616–3624, 2009.

[51] N. Rodriguez-Alvarez, A. Camps, M. Vall-llossera, X. Bosch-Lluis, A. Monerris, I. Ramos-Perez, E. Valencia, J. F. Marchan-Hernandez, J. Martinez-Fernandez,

G. Baroncini-Turricchia, C. Perez-Gutierrez, and N. Sanchez, "Land Geophysical Parameters Retrieval Using the Interference Pattern GNSS-R Technique," *IEEE Transactions on Geoscience and Remote Sensing*, vol. 49, no. 1, pp. 71–84, 2011.

[52] N. Rodriguez-Alvarez, X. Bosch-Lluis, R. Acevo, A. Aguasca, A. Camps, M. Vall-llossera, I. Ramos-Perez, and E. Valencia, "Study of maize plants effects in the retrieval of soil moisture using the interference pattern GNSS-R technique," in *Proc. IEEE Int. Geoscience and Remote Sensing Symp. (IGARSS)*, 2010, pp. 3813–3816.

[53] A. Monerris, N. Rodriguez-Alvarez, M. Vall-llossera, A. Camps, M. Piles, J. Martinez-Fernandez, N. Sanchez-Martin, C. Perez-Gutierrez, G. Baroncini-Turricchia, R. Acevo, and A. Aguasca, "The GPS and RAdiometric Joint Observations experiment at the REMEDHUS site (Zamora-Salamanca region, Spain)," in *Proc. Geoscience and Remote Sensing Symp.,2009 IEEE Int.,IGARSS 2009*, vol. 3, 2009.

[54] R. Acevo-Herrera, A. Aguasca, X. Bosch-Lluis, A. Camps, J. Martínez-Fernández, N. Sánchez-Martín, and C. Pérez-Gutiérrez, "Design and First Results of an UAV-Borne L-Band Radiometer for Multiple Monitoring Purposes," *Remote Sensing*, vol. 2, no. 7, pp. 1662–1679, 2010. [Online]. Available: http://www.mdpi.com/2072-4292/2/7/1662/

[55] S. Gleason, "Remote Sensing of Ocean, Ice and Land Surfaces Using Bistatically Scattered GNSS Signals From Low Earth Orbit," Ph.D. dissertation, University of Surrey, December 2006.

[56] A. Camps, N. Rodriguez-Alvarez, X. Bosch-Lluis, J. F. Marchan, I. Ramos-Perez, M. Segarra, L. Sagues, D. Tarrago, O. Cunado, R. Vilaseca, A. Tomas, J. Mas, and J. Guillamon, "PAU in SeoSAT: A proposed hybrid L-band microwave radiometer/GPS reflectometer to improve Sea Surface Salinity estimates from space," in *Proc. Microwave Radiometry and Remote Sensing of the Environment MICRORAD 2008*, 2008, pp. 1–4.

[57] F. T. Ulaby, R. K. Moore, and A. K. Fung, *Microwave Remote Sensing. Active and Passive Vol. 1. Fundemantals and Radiometry.* Artech House, 1981.

[58] ——, *Microwave Remote Sensing. Active and Passive Vol. 2. Fundemantals and Radiometry.* Artech House, 1981.

[59] J. Randa, Electronics, E. E. L. N. I. of Standards, and T. E. Division, *Recommended terminology for microwave radiometry*, ser. NIST technical note 1551. U.S. Dept. of Commerce, Technology Administration, National Institute of Standards and Technology, 2008. [Online]. Available: http://www.grss-ieee.org/wp-content/uploads/2009/09/TN1551.pdf

[60] N. Skou, B. Laursen, and S. Sobjaerg, "Polarimetric radiometer configurations: potential accuracy and sensitivity," *IEEE Transactions on Geoscience and Remote Sensing*, vol. 37, no. 5, pp. 2165–2171, 1999.

[61] J.W.Goodman, *Statistical Optics*. Wiley Interscience, 1985.

[62] I. Corbella, N. Duffo, M. Vall-llossera, A. Camps, and F. Torres, "The visibility function in interferometric aperture synthesis radiometry," *IEEE Transactions on Geoscience and Remote Sensing*, vol. 42, no. 8, pp. 1677–1682, 2004.

[63] J. C. Ehrhardt, "Hexagonal fast Fourier transform with rectangular output," *IEEE Transactions on Signal Processing*, vol. 41, no. 3, pp. 1469–1472, 1993.

[64] A. Camps, J. Bara, I. C. Sanahuja, and F. Torres, "The processing of hexagonally sampled signals with standard rectangular techniques: application to 2-D large aperture synthesis interferometric radiometers," *IEEE Transactions on Geoscience and Remote Sensing*, vol. 35, no. 1, pp. 183–190, 1997.

[65] Á. Aznar and et al., *Antenas*, ser. Politecnos Series. Edicions UPC, 2002.

[66] I. Ramos-Perez, X. Bosch-Lluis, A. Camps, J. F. Marchan-Hernandez, N. Rodriguez-Alvarez, and E. Valencia, "Use of Pseudo-Random Noise sequences in microwave radiometer calibration," in *Proc. Microwave Radiometry and Remote Sensing of the Environment MICRORAD 2008*, 2008, pp. 1–4.

[67] I. R. Pérez, X. Bosch-Lluis, A. Camps, N. R. Alvarez, J. F. M. Hernandez, E. V. Domènech, C. Vernich, S. de la Rosa, and S. Pantoja, "Calibration of Correlation Radiometers Using Pseudo-Random Noise Signals," *Sensors*, vol. 9, no. 8, pp. 6131–6149, 2009. [Online]. Available: http://www.mdpi.com/1424-8220/9/8/6131/

[68] R. A. Thompson and et al., *Interferometry and synthesis in radio astronomy*, 2nd ed. Wiley-Interscience, May 2001.

[69] A. Camps, F. Torres, P. Lopez-Dekker, and S. J. Frasier, "Redundant space calibration of hexagonal and Y-shaped beamforming radars and interferometric radiometers," *Int. J. Remote Sens*, vol. 24, p. 5183–5196, 2003.

[70] F. Torres, A. Camps, J. Bara, I. Corbella, and R. Ferrero, "On-board phase and modulus calibration of large aperture synthesis radiometers: study applied to MIRAS," *IEEE Transactions on Geoscience and Remote Sensing*, vol. 34, no. 4, pp. 1000–1009, 1996.

[71] A. B. Tanner, W. J. Wilson, P. P. Kangaslahti, B. H. Lambrigsten, S. J. Dinardo, J. R. Piepmeier, C. S. Ruf, S. Rogacki, S. M. Gross, and S. Musko, "Prototype development of a geostationary synthetic thinned aperture radiometer, GeoSTAR," in *Proc. IEEE Int. Geoscience and Remote Sensing Symp. IGARSS '04*, vol. 2, 2004, pp. 1256–1259.

[72] A. Carlstrom, J. Christensen, A. Emrich, and P. de Maagt, "Image Retrieval Simulations for the GEO Atmospheric Sounder (GAS)," in *Proc. IEEE Int. Geoscience and Remote Sensing Symp. IGARSS 2008*, vol. 2, 2008.

[73] F. Torres, A. Camps, and I. Bará, J. Corbella, "Impact of receiver errors on the radiometric resolution of large 2D aperture synthesis radiometers. Study applied to MIRAS," *Radio Sci*, vol. 32, pp. 629–642, 1997.

[74] I. Corbella, A. Camps, F. Torres, and J. Bara, "Analysis of noise-injection networks for interferometric-radiometer calibration," *IEEE Transactions on Microwave Theory and Techniques*, vol. 48, no. 4, pp. 545–552, 2000.

[75] M. A. Brown, F. Torres, I. Corbella, and A. Colliander, "SMOS Calibration," *IEEE Transactions on Geoscience and Remote Sensing*, vol. 46, no. 3, pp. 646–658, 2008.

[76] C. S. Ruf and J. Li, "A correlated noise calibration standard for interferometric, polarimetric, and autocorrelation microwave radiometers," *IEEE Transactions on Geoscience and Remote Sensing*, vol. 41, no. 10, pp. 2187–2196, 2003.

[77] D. Hagen, J.B.; Farley, "Digital correlation techniques in radio science," *Radio Sci*, vol. 8, p. 775–784, 1973.

[78] A. Camps, F. Torres, J. Bara, I. Corbella, and F. Monzon, "Automatic calibration of channels frequency response in interferometric radiometers," *Electronics Letters*, vol. 35, no. 2, pp. 115–116, 1999.

[79] J. G. Proakis and D. Manolakis, *Introduction to Digital Signal Processing.* New York: Macmillan Publishing Company, 1998.

[80] E. Dlala and A. Arkkio, "General formulation for the Newton-Raphson method and the fixed-point method in finite-element programs," in *Proc. XIX Int Electrical Machines (ICEM) Conf*, 2010, pp. 1–5.

[81] Martín-Neira, M. and Ribó, S. and Rautiainen, K., "0-1 Correction of Comparator Threshold in 1-bit Interferometric Radiometers," in *8th Specialist Meeting on Microwave Radiometry and Remote Sensing Applications. MicroRad 2004.*

[82] J. Font, A. Camps, A. Borges, M. Martin-Neira, J. Boutin, N. Reul, Y. H. Kerr, A. Hahne, and S. Mecklenburg, "SMOS: The Challenging Sea Surface Salinity Measurement From Space," *Proceedings of the IEEE*, vol. 98, no. 5, pp. 649–665, 2010.

[83] Y. H. Kerr, P. Waldteufel, J.-P. Wigneron, J. Martinuzzi, J. Font, and M. Berger, "Soil moisture retrieval from space: the Soil Moisture and Ocean Salinity (SMOS) mission," *IEEE Transactions on Geoscience and Remote Sensing*, vol. 39, no. 8, pp. 1729–1735, 2001.

[84] N. N. Duffo, I. Corbella, F. Torres, A. Camps, and M. Vall-llossera, "Advantages and Drawbacks of Near-field Characterization of Large Aperture Synthesis Radiometers." Rome, Italy: 8th Specialist Meeting on Microwave Radiometry and Remote Sensing Applications, February 2004.

[85] W. Lin, F. Corbella, N. Duffo, and M. Maetin-Neira, "Correction of Spatial Errors in SMOS Brightness Temperature Images," in *Proc. IEEE Int. Geoscience and Remote Sensing Symp. IGARSS 2011*, 2011.

[86] M. Martin-Neira, M. Suess, J. Kainulainen, and F. Martin-Porqueras, "The Flat Target Transformation," *IEEE Transactions on Geoscience and Remote Sensing*, vol. 46, no. 3, pp. 613–620, 2008.

[87] Anechoic Chamber . UPC-D3. 2011. [Online]. Available: http://www.upc.edu/pct/es/equip/506/camara-anecoica.html#

[88] E. D. Domingo, A. Broquetas, and S. V. Albareda, *Estudi mitjançant simulació de la radiometria interferomètrica de microones*, 1994, eusebi Daviu Domingo, Sergi Vilar Albareda ; director projecte: Antonio Broquetas Ibars; v. (paginació múltiple):il., gràf.;30 cm; Projecte final de carrera-Universitat Politècnica de Catalunya. Escola Tècnica Superior d'Enginyers de Telecomunicació de Barcelona, 1994; Bibliografia.

[89] (2002) Simulating Passive Microwave Radiometer Designs Using Simulink. [Online]. Available: http://eprints.jcu.edu.au/13672/1/13672_Burrage_et_al_2002.pdf

[90] C. A. Balanis, *Antenna Theory: Analysis and Design*, 3rd ed. Wiley-Interscience, Apr. 2005. [Online]. Available: http://www.amazon.ca/exec/obidos/redirect?tag=citeulike09-20&path=ASIN/047166782X

[91] SiGe GN3S Sampler v.2. [Online]. Available: http://www.sparkfun.com/products/8238

[92] A. Camps, J. Bara, F. Torres, and J. Romeu, "Impact of antenna errors on the radiometric accuracy of large aperture synthesis radiometers ," *Radio Science*, vol. vol 32 no.2, pp. 657–668, March-April 1997.

[93] A. Camps, F. Torres, I. Corbella, J. Bara, and J. De Paco, "Mutual coupling effects on antenna radiation pattern: an experimental study applied to interferometric radiometers," *Radio Science*, vol. vol 33 no.6, pp. 1543–1552, November-December 1998.

[94] I. Ramos-Perez, *Diseño e implanatción de un receptor para un radiometro de pseudo-correlación polarimetrico en banda L*, Final Project UPC, May 2005.

[95] M. Martín-Neira, P. Pironen, A. Camps, and L. Sempere-Payà, *Digital rms-voltage detector*, ESA/PAT/471.

[96] [Online]. Available: http://www.zarlink.com/zarlink/gp2015-datasheet-sept2007.pdf

[97] C. Paar and J. Pelzl, *Understanding Cryptography: A Textbook for Students and Practitioners*. Springer-Verlag New York Inc, 2010.

[98] G. Rau, R. Schieder, and B. Vowinkel, "Characterization and Measurement of Radiometer Stability," in *Proc. 14th European Microwave Conf*, 1984, pp. 248–253.

[99] D. W. Allan, "Statistics of atomic frequency standards," *Proceedings of the IEEE*, vol. 54, no. 2, pp. 221–230, 1966.

[100] R. Gold, "Optimal binary sequences for spread spectrum multiplexing (Corresp.)," *IEEE Transactions on Information Theory*, vol. 13, no. 4, pp. 619–621, 1967.

[101] A. Thompson, "Quantization Efficiency for Eight or More Sampling Levels," July 1998. [Online]. Available: http://www.alma.nrao.edu/memos/html-memos/alma220/memo220.html

[102] M. A. Fischman, A. W. England, and C. S. Ruf, "How digital correlation affects the fringe washing function in L-band aperture synthesis radiometry," *IEEE Transactions on Geoscience and Remote Sensing*, vol. 40, no. 3, pp. 671–679, 2002.

[103] R. C. Gonzalez and R. E. Woods, *Digital Image Processing*, 2nd ed. Boston, MA, USA: Addison-Wesley Longman Publishing Co., Inc., 2001.

[104] A. K. Jain, *Fundamentals of digital image processing*. Upper Saddle River, NJ, USA: Prentice-Hall, Inc., 1989.

List of Acronyms

AC alternating current

ADC Analog to Digital Converter

AF Array Factor

AF-FOV Alias-Free Field Of View

AGC Automatic Gain Control

ALBATROSS Advanced L-BAnd emissiviTy and Reflectivity Observations of the Sea Surface

AMU Arbitrary Measurement Unit

BPF Band Pass Filter

C/A Coarse Acquisition

CDMA Code Division Multiple Access

CESBIO Centre d'Etudes Spatiales de la BIOsphère

CNCS Correlated Noise Calibration Standards

CONAE Comisión Nacional de Actividades Espacieales

CPU Central Processing Unit

CSIC Consejo Superior de Investigaciones Científicas

CU Control Unit

CW Carrier Wave

DBF Digital Beam Former

DCU Digital Correlation Unit

DDC Digital Down Converter

DDM Delay-Doppler Map

DFT Discrete Fourier Transform

DR Dicke Radiometer

ECCO Empty Chamber Correlation Offset

EMC Electro Magnetic Compatibility

EMI Electro Magnetic Interference

ENR Excess Noise Ratio

ERIP Equivalent Radiated Isotropic Power

ESA European Space Agency

ESF European Science Foundation

ESTAR Electronically Steered Thinned Array Radiometer

ESTEC European Space Research and Technology Centre

EURYI European Young Investigator

FFT Fast Fourier Transformation

FOV Field Of View

FPGA Field Programmable Gate Array

FTR Flat Target Response

FWF Fringe-Wash Function

GAS Geostationary Earth Orbit Atmospheric Sounder

GeoSTAR Geostationary Synthetic Thinned Aperture Radiometer

GNSS Global Navigation Satellite System

GNSS-R Global Navigation Satellite System Reflectrometry

GPS Global Positioning System

GRAJO GPS and RAdiometric Joint Observations one-year experiment

griPAU GPS reflectometer instrument for PAU

GUI Graphical User Interface

HD Hard Disk

HFFT Hexagonal Fast Fourier Transformation

I/Q In-phase and Quadrature

I/O Input/Output

IC Integrated Circuit

ICM Institut de Ciències del Mar

IDFT Inverse Discrete Fourier Transform

IF Intermediate Frequency

IFFT Inverse Fast Fourier Transformation

IHFFT Inverse Hexagonal Fast Fourier Transformation

IIR Infinite Impulse Response

INTA Instituto Nacional de Tecnica Aeroespacial

IPT Interference Pattern Technique

IR Infrared Radiometer

LAURA L-Band AUtomatic Radiometer

LEO Low Earth Orbit

LFSR Linear Feedback Shift Register

LHCP Left Hand Circular Polarization

LICEF Light Cost Effective Front-end

LNA Low Noise Amplifier

LO Local Oscillator

LPF Low Pass Filter

MBC Multiple Baseline Calibration

MBE Mean Beam Effiency

MERITXELL Multi-frequency Experimental Radiometer With Interference Tracking For Experiments Over Land And Littoral

MIRAS Microwave Imaging Radiometer by Aperture Synthesis

NASA National Aeronautics and Space Administration

NF Noise Figure

NIR Noise Injection Radiometer

OCXO Oven Controlled Crystal Oscillator

PAU Passive Advanced Unit for ocean monitoring

PAU-OR PAU-One Receiver

PAU-ORA PAU-One Receiver Airborne

PAU-RA PAU-Real Aperture

PAU-RAD PAU-real aperture RADiometer part

PAU-SA Passive Advanced Unit Synthetic Aperture

PC Personal Computer

PIC Programmable Interrupt Controller

PID Proportional Integral Derivative

PIO Port Input Output

PLC Programmable Logic Controller

PLL Phase Lock Loop

PMS Power Measurement System

PR Polarimetric Radiometer

PRN Pseudo-Random Noise

PSF Point-Spread Function

psu practical salinity unit

RAM Random Access Memory

RF Radio Frequency

RFI Radio Frequency Interference

RHCP Right Hand Circular Polarization

rms root mean square

ROM Read Only Memory

RSC Redundant Space Calibration

RSLab Remote Sensing Lab

SAC-D Satélite de Aplicaciones Cientificas

SAW Surface Acoustic Wave

SeoSat Spanish Earth Observation Satellite

SLFMR Scanning Low Frequency Microwave Radiometer

SLL Side Lobe Level

SM Soil Moisture

SMAP Soil Moisture Active and Passive

SMIGOL Soil Moisture Interference-pattern GNSS Observations at L-band

SMOS Soil Moisture and Ocean Salinity

SNR Signal-to-Noise Ratio

SR Symbol Rate

SSD Solid-State Drive

SSS Sea Surface Salinity

SST Sea Surface Temperature

SWH Significant Wave Height

TPR Total Power Radiometer

TSC Theory of Signal and Communications

TTL Transistor–Transistor Logic

UART Universal Asynchronous Receiver/Transmitter

UPC Universitat Politècnica de Catalunya

USB Universal Serial Port

VNA Vector Network Analyzer

VNC Virtual Network Computing

V-pol Vertical polarization

WS Wind Speed